



저작자표시-비영리-변경금지 2.0 대한민국

이용자는 아래의 조건을 따르는 경우에 한하여 자유롭게

- 이 저작물을 복제, 배포, 전송, 전시, 공연 및 방송할 수 있습니다.

다음과 같은 조건을 따라야 합니다:



저작자표시. 귀하는 원저작자를 표시하여야 합니다.



비영리. 귀하는 이 저작물을 영리 목적으로 이용할 수 없습니다.



변경금지. 귀하는 이 저작물을 개작, 변형 또는 가공할 수 없습니다.

- 귀하는, 이 저작물의 재이용이나 배포의 경우, 이 저작물에 적용된 이용허락조건을 명확하게 나타내어야 합니다.
- 저작권자로부터 별도의 허가를 받으면 이러한 조건들은 적용되지 않습니다.

저작권법에 따른 이용자의 권리는 위의 내용에 의하여 영향을 받지 않습니다.

이것은 [이용허락규약\(Legal Code\)](#)을 이해하기 쉽게 요약한 것입니다.

[Disclaimer](#)

공학박사 학위논문

**Morphology and Chirality Control of
Plasmonic Nanoparticle
using Amino Acids and Peptides**

아미노산 및 펩타이드를 이용한
플라즈모닉 나노입자의 형태 및 카이랄성 제어

2019년 8월

서울대학교 대학원

재료공학부

안 효 용

Abstract

Morphology and Chirality Control of Plasmonic Nanoparticle using Amino Acids and Peptides

Hyo-Yong Ahn

Department of Materials Science and Engineering

The Graduate School

Seoul National University

Design and fabrication of nanostructure have been essential parts of nanomaterial researches as geometry is directly related to the material properties in nanoscale. From atoms to crystals and bulk materials, the morphology and chirality of optical materials are significant at various scales. For decades, nanostructured materials have led the field of nanophotonics due to exceptional light-matter interactions, but the formation of desired morphology and chirality in atomic to nanometer scale is still one of the most challenging issues in material science. So far, precise nanometer-level control and lower symmetry require state-of-the-art lithography techniques and macromolecular self-assembly scaffolds, but the complexity of the process, the limited resolution and stability, and the requirement for specialized facilities are major hindrances for the real applications. Therefore, developing an alternative method for nanostructure control is critical to addressing these limitations and providing a new direction. Through this research, we propose

that spontaneous growth of nanostructure such as colloidal synthesis can be a promising alternative for resolving the limitations mentioned above. In this thesis, we investigated a novel bottom-up and biomolecule-directed route for systematic morphology and chirality control of plasmonic nanoparticles.

Although numerous nanostructures have been achieved by colloidal synthesis of plasmonic nanoparticles for decades, the ultimate goal is a universal system capable of understanding and implementing thermodynamic and kinetic effect on nanocrystal growth. In addition, in terms of symmetry, intrinsic chiral nanocrystal has never been achieved due to the mirror-symmetric crystal structure of plasmonic metals. In order to build up a new strategy for the morphology and chirality control for plasmonic nanoparticle, we have first studied previous research on the bottom-up route for complex nanostructures in Chapter 2, by specifically focusing on the biomolecular pathway for inorganic chirality. Importantly, interfacing of biomolecule and naturally chiral inorganic surface give an important insight for the spontaneous formation chiral nanocrystal. Taking lessons from the chirality transfer at the atomic and molecular scale, we designed a novel synthesis platform for morphology control and chirality evolution, respectively presented in Chapter 3 and 4.

Based on the well-known seed-mediated synthesis, we developed various morphology of Au nanoparticles by the competitive effect of the capping agent, cetyltrimethylammonium bromide (CTAB), and reducing agent, ascorbic acid (AA). The ratio of CTAB and AA concentrations determined the Miller-indices of the exposed crystal facets, by changing relative growth rates along crystal orientations. As a result of the systematic control of CTAB and AA concentration, the morphology diagram of Au nanocrystal was constructed as a function of CTAB and AA concentration and specified the synthesis condition for low-Miller-index

exposed nanocrystal morphologies. Using this synthesis platform, it was possible to synthesize the rhombic dodecahedron and hexoctahedron morphology for the first time in CTAB-AA system. This study can provide a useful synthesis platform capable to control the exposed crystal surface of nanocrystal ranging from various low- to high-Miller-index planes, and corresponding nanocrystal morphology.

By introducing biomolecule as a chiral modifier in the control of morphology and crystal plane, we demonstrated the synthesis of uniform gold NPs with three-dimensional chiral morphology through the chemical synthesis route. Instead of using peptides as a template for chiral assembly, the enantioselective interaction between intrinsic chiral kink sites of high- Miller-index planes and thiol-containing chiral peptides directed the asymmetric growth of NPs. The evolution of chiral morphology was a result of the asymmetric growth of high-Miller-index planes, which have opposite chirality in the R and S atomic arrangement. Under normal growth conditions in this research, $\{321\}$ high-index planes are exposed to form differentiated stellated octahedral (or hexoctahedral) NPs. As naturally chiral surfaces with symmetric distribution confined to the single NP level, high-Miller-index NPs are a well-defined testbed for investigating chirality transfer from molecules to NP morphology. The high-Miller-index planes with kinked atom sites serve as asymmetric binding sites for the one enantiomer of cysteine or cysteine-containing peptides, providing enantioselective molecular orientation and reaction energetics. Detailed investigation on the high-Miller-index plane and molecular adsorption proved this mechanism for chirality development. Therefore, the addition of pure enantiomer peptides finally resulted in the evolution of left-right asymmetry in chiral helicoid morphology, featuring the twist in crystal facet boundaries between the R and S regions. The helicoid morphologies were carefully characterized by high-resolution imaging techniques and were revealed to be composed by a highly twisted chiral element. In terms of symmetry, the morphology of helicoid

nanoparticle has point chirality and belongs to the 432-point symmetry group, which is a new class of three-dimensional chiral geometry in the plasmonic nanostructure.

Intriguing optical properties of helicoid nanoparticles derived from the highly twisted feature of three-dimensional morphology was presented in Chapter 5. Compared to the reported bottom-up chiral nanostructure, helicoid Au nanoparticle exhibited remarkably strong plasmonic optical activity; dissymmetry factor of the randomly dispersed nanoparticle solution reached 0.2 at visible wavelengths. Theoretical calculation clarified that this optical activity is associated with the formation of strong chiral nearfield at chiral gap structure. Electromagnetic simulation for systematic geometrical variation of helicoid morphology suggested a general design strategy for high g -factors. Based on the wavelength-dependent polarization rotation ability, a solution of the helicoid III Au nanoparticle can modulate the color of transmitted light in a wide range of visible wavelengths. This color transformation operates in real-time by rotating a polarizer and can be observed in naked-eye, suggesting the possibility of optical applications such as a display. The chiroptical response of helicoid nanoparticles was further controlled by the resonance coupling with other plasmonic nanostructures. Spectral tuning in visible and NIR region was enabled by the Au and Ag metal deposition, and corresponding cross-polarized transmission of light covers a wide range in color space. We believe that this research may increase an understanding of plasmonic chiroptical phenomena and provide insight to develop novel polarization-based optical devices.

In conclusion, a novel bottom-up route for nanoscale morphology and chirality control was developed in this thesis. The biomolecular approach presented in this research for the evolution of chirality has a technological potential for the development of biomolecule-responsive and tunable metamaterials. Using this approach, chiral elements were arranged by 432-symmetry within only about 100-

nm cube-like structures, resulting in the three-dimensional, angle-insensitive plasmonic metamaterials. Further, the improved understanding of the interaction of biomolecules and inorganic materials could provide a breakthrough for designing chiral nanomaterials, and contribute to the advance of plasmonics, metamaterials, nanostructuring, and many related fields.

Keywords: plasmon, nanoparticle, morphology, chirality, peptide, high-index, colloidal synthesis

Student Number: 2013-20607

Contents

Chapter 1. Introduction	1
1.1 Structure-related optical property.....	1
1.2 Plasmonic nanostructure and metamaterial.....	5
1.3 Chirality and chiral plasmonic nanomaterial.....	19
1.4 Morphology and chirality control in nanoscale.....	24
1.5 Scope of thesis.....	31
1.6 Bibliography	35
Chapter 2. Biomolecular Pathway for Inorganic Chirality	41
2.1 Introduction	41
2.2 Biomolecule-enabled chiral assembly.....	49
2.2.1 Chiral nanostructures based on peptide assembly	49
2.2.2 DNA templates for chiral assembly of plasmonic nanostructures	54
2.2.3 Macromolecule-assisted chiral assembly of nanoparticles.....	62
2.3 Intrinsic chirality in inorganic material	64
2.4 Conclusion.....	75
2.5 Bibliography	76
Chapter 3. Morphology Control in Plasmonic Au Nanoparticle Synthesis.....	87

3.1	Introduction	87
3.2	Theoretical background.....	89
3.2.1	Mechanism of nanocrystal morphology control.....	89
3.2.2	Seed-mediated growth	94
3.3	Result and discussion	98
3.3.1	Synthesis of rhombic dodecahedral Au nanoparticles.....	98
3.3.2	Morphology diagram: Interplay between CTAB and ascorbic acid.....	102
3.3.3	Generality of morphology diagram	109
3.3.4	Two-step growth: High-Miller-index nanoparticles	117
3.4	Conclusion.....	120
3.5	Methods.....	121
3.6	Bibliography.....	123

Chapter 4. Peptide-Directed Synthesis of Plasmonic Helicoid Nanoparticle 131

4.1	Introduction	131
4.2	Result and discussion	132
4.2.1	Formation of chiral nanoparticles: 432 helicoid I and II.....	132
4.2.2	Mechanism of chirality evolution.....	148
4.2.3	Highly-twisted chiral morphology: 432 helicoid III.....	166
4.3	Conclusion.....	177
4.4	Methods.....	178
4.5	Bibliography.....	182

Chapter 5. Chiroptical Response of Plasmonic Helicoid Nanoparticles.....	187
5.1 Introduction	187
5.2 Theoretical background.....	190
5.2.1 Dielectric function of metal.....	190
5.2.2 Polarizability of metal nanostructure.....	192
5.2.3 Qualitative model for complex plasmonic response.....	194
5.2.4 Electrodynamic description for chiral nanomaterial	198
5.3 Results and discussion.....	201
5.3.1 Chiroptical spectroscopy analysis of Au helicoid nanoparticle	201
5.3.2 Electrodynamic simulation of Au helicoid nanoparticle	210
5.3.3 Polarization-based color modulation.....	224
5.3.4 Spectral tuning of metal-coated helicoid nanoparticles.....	227
5.4 Conclusion.....	237
5.5 Methods.....	238
5.6 Bibliography.....	243
 Chapter 6. Concluding Remarks.....	 247
국문 초록.....	251

List of Tables

Table 3.1 Synthesis routes based on a single-step, seed-mediated method for gold nanocrystals using a CTAB/AA system as the growth solution.	96
Table 3.2 Synthetic conditions based on a single-step, seed-mediated method for gold nanocrystals using a CTAB/AA system without any additives as the growth solution and the resulting major morphologies. The concentrations of seed were produced in two ways. Seed concentration produced by calculating ^a the total amount of gold ions in the seed solutions and the number of gold atoms in each seed or ^b the total amount of gold ions in the growth solutions and the number of gold atoms in a 46 nm cubic particle.	111
Table 5.1 Comparison of the g-factor of various chiral structures	209

List of Figures

- Figure 1.1 Structure-related optical property in the biological system. (a) Reflection of blue light from the wings of *Morpho didius* originated from the periodic structures of the wing scales. (b) The diverse coloration of peacock feather derived from the photonic crystal structure at the cortex surface with different periodicity. (c) The circularly polarized iridescence of jeweled beetles, *Chrysina gloriosa*, caused by helical cell arrangement. 2
- Figure 1.2 Optical response of metal nanoparticles. (a) Lycurgus cup (left) and stained glass of Chartres Cathedral (right) (b) Experimental and simulated scattering spectra of aluminum nanoparticles with different sizes, from 70 nm to 180 nm. (c) Simulated extinction (black), absorption (blue), and scattering (red) spectra of silver nanoparticles with various morphology. 4
- Figure 1.3 Schematic illustration of the sphere (a) and triangular prism (b) nanoparticles excited by the electric field of the incident light. The collective movements of electrons are resonant at optical frequencies and the surface charge and local electric field distribution depends on the shape of the nanoparticle: in the case of the sphere the field is distributed in a symmetric dipolar pattern, whereas in the case of the triangular shape there is charge and field concentration on the upper tip. 7
- Figure 1.4 Polarization-sensitive optical response using anisotropic plasmonic nanostructure. (a) Electroluminescence of LED active layer covered with plasmonic rectangular hole array structure. Three types of pixel structures consist of rectangular and square nanoholes construct a binary letter image encoded by polarization-sensitive luminescence. (b) White light interaction with anisotropic pixels where specific wavelengths of light are back-scattered with orthogonal polarization states. This configuration generates different scattering colors within each individual pixel. Polarization-sensitive dual-image can be embedded in high-resolution plasmonic color microprint. 9
- Figure 1.5 Local electric field amplitude distribution at plasmonic hotspot. (a, b)

Electric field profile showing strong field confinement at the tips of nanocrescent structure (a), and nanogap between nanotriangle (b).... 12

Figure 1.6 Single molecule SERS measurement using branched nanoparticle. (a) Single branched nanoparticle onto single molecules. For the branched nanoparticle, experimental and calculated EELS intensity mapping show high localization of electric field near the tip-end. (b) Bulk Raman spectrum of 15NAT molecules in aqueous solution (right scale), compared to the SERS spectrum (left scale) of the same molecules recorded by using the branched nanoparticle. (c) Single-particle SERS mapping recorded from a sample with less than 1 particle per μm^2 . . 13

Figure 1.7 Fluorescence enhancement near the gold particle. (a) Experimental arrangement. An 80nm gold particle is attached to the end of an etched glass tip and irradiated by a radially polarized laser beam. (b) Fluorescence rate as a function of particle-surface distance z for a vertically oriented molecule. (c) Experimental and theoretical fluorescence rate image of a single molecule acquired for $z \sim 2$ nm. The dip in the center indicates fluorescence quenching. 14

Figure 1.8 Plasmonic metasurface skin cloak. (a) Schematic view and working principle of a metasurface skin cloak. (b) Full-wave simulation results for the metasurface skin cloak, showing that the reflected light is almost completely recovered by the skin cloak as if there were no scattering object for both normal and oblique incidences. (c) Experimental demonstration of metasurface skin cloak for a 3D arbitrarily shaped object. 16

Figure 1.9 Optical negative-index material design. (a) Array of paired nanorods supporting antiparallel current modes. (b) Arrays of ellipsoidal voids in a pair of metal sheets with a negative index at about $\lambda = 2 \mu\text{m}$. (c) The nano-fishnet where the largest figure of merit $F = 3$ was obtained at $\lambda \approx 1.4 \mu\text{m}$ 17

Figure 1.10 (a) Slab of negative index material working as perfect lens. Light formerly diverging from a point source is set in reverse and converges back to a point. (b) Graded refractive index cloak guiding light around a hidden object. The field is excluded from the cloaked region but emerges from the cloaking sphere undisturbed. 18

- Figure 1.11 Chiral plasmonic nanostructure for polarization filter and negative-index. (a) Measured and calculated optical transmittance spectra of Au helix for circular polarization of the incoming light propagating along the axis. A large transmittance ratio results in the wavelength range from 3.5 to 7.5 μm . (b) Plasmonic chiral structure consisting of inductor-capacitor model which functions effectively as an electric dipole and a magnetic dipole forming an angle θ . Negative refractive index was achieved by LCP excitation in THz region..... 21
- Figure 1.12 Chiral nearfield and its application in chiral sensing. (a, b) Theoretical calculation and experimental measurement of chiral nearfield distribution. (c) CD spectra collected from left- and right-handed gammadion plasmonic nanostructure. Resonance shifts $\Delta\lambda_{\text{RH}}$ and $\Delta\lambda_{\text{LH}}$ caused by the adsorption of protein and exhibit different value, which indicates that optical dissymmetry occurs in opposite nanostructure. (d) $\Delta\Delta\lambda$ values for I, II and III modes for various proteins. Also shown are the effectively zero $\Delta\Delta\lambda$ values obtained from the (achiral) ethanol solvent..... 23
- Figure 1.13 Top-down fabrication of complex and chiral nanostructure. (a) 2D and quasi-3D chiral nanostructures fabricated by electron beam lithography. (b) Chiral kirigami nanostructure fabricated by focused ion beam lithography. (c) 3D helicoid nanostructure fabricated by direct laser writing..... 26
- Figure 1.14 Formation of inorganic nanocrystal. (a) LaMer curve describing three stages of metal nanocrystal formation in solution system. Stage I: atom producing, stage II: nucleation, and stage III: seed formation and growth. (b) Two-dimensional and (c) three-dimensional schematic Wulff construction to determine the equilibrium shape of a particle..... 28
- Figure 1.15 Chirality in natural organism. Starting from the stereocenter in small molecule, chirality exists in microscopic and macroscopic biological system and can be transferred across multiple length scales..... 30
- Figure 2.1 Integration of chiral biomolecules and achiral plasmonic building blocks into the chiral assembled nanostructures. 43
- Figure 2.2 Chiroptical response of chiral plasmonic assembly. (a) Schematic showing asymmetric circularly polarized light absorption of chiral

material. (b) Illustration of the plasmon hybridized model with the corresponding vector orientation of light. Different bonding and anti-bonding modes with split energy levels are created by plasmon coupling between two nanorods. The two different modes can be selectively excited by left or right circularly polarized light. 44

Figure 2.3 Intrinsic chiral morphology. (a) SEM images of chiral calcite microcrystal precipitated in the presence of L- or D-tartaric acid. (b) SEM images of chiral vaterite microcrystal precipitated in the presence of L- or D-cysteine. (c) TEM image and corresponding model of colloidal cinnabar (α -HgS) nanocrystals showing different twisting orientation depending on the chirality of penicillamine ligand. (d) Dark-field STEM image and tomography of colloidal chiral tellurium nanocrystal. 47

Figure 2.4 Formation of Chirality in Biology. (a) Helical *L. stagnalis* (left) and their embryos (right). Optical microscope and 3D-reconstruction image of dextral embryos and third cleavage in (i) four-cell stage, (ii) metaphase-anaphase, (iii) telophase, (iv) eight-cell stage. (b) Directional twisting of the whole body and cell arrangement of *Drosophila* lava as a result of actin filament gliding powered by Myo1D. (c) Model of chirality formation across multiple organization scales. 48

Figure 2.5 Peptide enabled chiral assembly. (a) TEM image and corresponding CD spectra of twisted gold nanorods oligomers generated by cysteine. (b) Self-assembled chiral gold nanorods induced by L-GSH or D-GSH and TEM image of the assembled nanochains coated with SiO₂ shells. (c) TEM images of T1 fibril biomolecules and gold nanoparticles (top) and the helical assemblies fabricated by electrostatically attaching the NPs onto fibrils (bottom) (d) Model and TEM images of the assembled gold nanoparticles through Cys-modified domain-swapped helical protein (DSD)-Gly hexamers on single-walled carbon nanotubes. 52

Figure 2.6 Peptide amphiphile template for chiral plasmonic nanostructure. (a) Double helical left-handed gold nanoparticles assembly templated by C₁₂-PEP_{Au} amphiphile peptides. TEM and electron tomography of enantiomeric gold nanoparticles double helices prepared by C₁₂-D-PEP_{Au} and C₁₂-L-PEP_{Au} templating. (b) TEM images and model of chiral NP assemblies templated via C₁₈-(PEP_{Au}M-ox)₂ superstructures with helical ribbon geometry. (c) Helical arrangement of NPs based on

self-assembled nucleobase–peptide conjugates (NPCs).....	53
Figure 2.7 Chiral assembly based on DNA linker and tile. (a) Schematic models and TEM images of enantiomeric plasmonic pyramid assemblies. (b) TEM and 3D TEM tomography images of the (-) enantiomer of twisted gold nanorods dimers. (c) Helical assembly of gold nanoparticles mediated by DNA tiles. By curling up the NP-modified tiles, the gold nanoparticles assembled into a spiral configuration.....	59
Figure 2.8 Rectangular DNA origami block for chiral plasmonic assembly. (a) Asymmetric plasmonic tetramer created by a rectangular DNA template with four defined binding sites, three on the top and one on the bottom. (b) Illustration of a two gold nanorods dimer assembly by bifacial DNA origami template. Schematic and TEM image of gold nanorods dimers with an “L” shape. (c) Schematic model and cryo-TEM image of helical superstructures of gold nanorods constructed by intercalating designed DNA origami between gold nanorods with an inter-rod angle of 45°.	60
Figure 2.9 DNA origami helix bundle for chiral plasmonic assembly (a) Left- and right-handed Au helices based on a DNA 24-helix bundle. (b) Reconfigurable twisted gold nanorods controlled by switchable DNA origami. The addition of DNA strands link the ends of two different helix bundles of DNA origami, generating opposite chiral structures.	61
Figure 2.10 Macromolecule assisted chiral assembly. (a) Plasmonic spirals based on phospholipid microtubule templates. (b) Chiral assembly of Au nanorods (AuNRs) induced by cellulose nanocrystals (CNC). Polarized optical microscope images and corresponding polarized two-photon-induced luminescence images prove the chiral nematic arrangement of both CNC and nanorods.	63
Figure 2.11 Intrinsic chiral crystal structures. (a) Natural quartz crystals with left- and right-handed morphology. (b) The chiral atomic arrangement of the trigonal α -HgS crystal. (c) Crystallographic point groups. Only eleven point groups are chiral, as highlighted as red.	65
Figure 2.12 Inorganic surface chirality. (a) Inorganic surface chirality defined on high-Miller-index planes, exposing crystalline atomic structures that lack mirror symmetry. (b) Definition of the absolute R and S conformation on the kink site.	66

Figure 2.13 Triangular diagram showing fcc metal polyhedrons bounded by different crystallographic facets.	68
Figure 2.14 High-Miller-index Au nanocrystal with concave rhombic dodecahedron shapes synthesized by benzenethiol derivative as a molecular encoder. According to the HRTEM analysis, the nanocrystal expose {331}, {221}, and {553} crystal planes.	69
Figure 2.15 Enantioselective interaction of cysteine on the achiral metal surface. (a) Schematic drawings of a cysteine molecule and the gold (110) surface, and STM images of cysteine dimers on gold (110), showing the asymmetric molecular arrangement. (b) STM images of monodispersed cysteine nanoclusters produced enantiomerically pure L- and D-cysteine, respectively.	72
Figure 2.16 Enantioselective binding of cysteine on the chiral high-index plane. (a) X-ray photoelectron diffraction patterns (top) and corresponding DFT calculation (bottom) for D- and L-cysteine adsorbed on the Au (17 11 9) ^S surface showing enantioselective adsorption geometry and binding strength (b) Schematic diagram of total energy of cysteine adsorbed on the Au (17 11 9) ^S for the transformation between cysteine-NH ₂ and cysteine-NH ₃	73
Figure 2.17 Formation of atomic-scale chiral geometry by chirality transfer. (a) STM image of chiral {3 1 17} facets of L-lysine/Cu(001) surface after thermal annealing. Surface reconstruction during the annealing process results in the formation of chiral {3 1 17} facets. (b) Electrodeposition of CuO from Cu(II)-(R,R)tartrate or Cu(II)-(S,S)tartrate results in the formation of enantiomorphic CuO 111 or CuO 111 surfaces, respectively.	74
Figure 3.1 Schematic of crystallographic planes for a face-centered-cubic metal. The red box shows the unit cell at the surface.	92
Figure 3.2 Schematic illustration showing (a) path of newly added atom and (b) total free energy plot depending on the structure	93
Figure 3.3 SEM micrographs of 40nm rhombic dodecahedral gold nanoparticles. (a) Low magnification SEM micrograph showing the assembly of rhombic dodecahedral particles. (b) High magnification SEM micrograph with illustrated images of rhombic dodecahedral nanoparticles.	100

Figure 3.4	TEM characterization of rhombic dodecahedral gold nanoparticles. (a) TEM micrograph with an illustrated model of a single rhombic dodecahedral particle. Inset is the corresponding SAED pattern of a rhombic dodecahedral particle along the [022] zone axis. (b) HRTEM micrograph of a rhombic dodecahedral gold nanoparticle. Inset is an overall image of particle and the corresponding FFT pattern of given lattice image. (c) TEM micrograph with an illustrated model of a single rhombic dodecahedral particle from another viewpoint. Inset is the corresponding SAED pattern. (d) SAED pattern along the [022] zone axis, which was obtained from the particle shown in the inset micrograph in the upper right corner. The red circle indicates a spot from a crossed shape, and its magnified image is located at the bottom right corner.	101
Figure 3.5	SEM micrographs of gold nanoparticles with varying the concentrations of CTAB and AA, ranging from 9 mM to 71 mM of AA and from 15 mM to 45 mM of CTAB.	106
Figure 3.6	SEM images of gold nanoparticles with varying AA concentration from 0.3 mM to 4.4 mM of AA and fixing CTAB concentration at 15 mM.	107
Figure 3.7	(a) Morphology diagram of gold nanoparticle shapes as a function of the CTAB and ascorbic acid concentrations. RD indicates rhombic dodecahedron. The small elliptical area near the y-axis represents the synthetic conditions of the rod and plates. (b)–(e) Representative SEM micrographs with illustrated images. (b) Rod and plate (length: 180 nm), (c) Cuboctahedron (40 nm), (d) Cube (46 nm), (e) Rhombic Dodecahedron (40 nm).	108
Figure 3.8	Estimation for the number of Au atoms in (a) 3.5 nm seed nanoparticle and (b) 46 nm cubic nanoparticle.	110
Figure 3.9	(a-c) SEM micrographs of gold nanoparticles with varying the concentrations of seed ([CTAB] = 15 mM, [AA] = 4.4 mM). The concentrations of seed particles in each growth solution were (a) 2 Cs (cuboctahedron, 34 nm), (b) Cs (cuboctahedron, 43 nm), (c) 0.5 Cs (cube, 61 nm). Cs means the original seed concentration. (d) UV-vis extinction spectra of (a) – (c). Each spectrum was normalized to its maximum value at resonance peak.	115

Figure 3.10 (a) Schematic of two-step growth (b) SEM and TEM image of synthesized hexoctahedron	119
Figure 4.1 (a) Extinction and (b) CD spectra of 432 helicoid I nanoparticles synthesized using L-Cys (black) and D-Cys (red).....	134
Figure 4.2 Opposite handedness of 3D plasmonic helicoids controlled by cysteine chirality transfer. (a) SEM image of synthesized L-Cys nanoparticles. Inset shows a highlighted edge tilted by $-\varphi$ degrees (solid line) with the vertices (red dots) and cubic outline (dashed line) indicated and viewed along the [100] (i) and [111] (ii) directions. (b) SEM image of synthesized D-Cys nanoparticles. The inset shows a highlighted edge, cubic outline (dashed line), and tilt angle ($+\varphi$ degrees).	135
Figure 4.3 Large-area SEM image of 432 helicoid I and corresponding 3D illustration.....	136
Figure 4.4 Characterization of high-Miller-index nanoparticle. (a) Schematic illustration of stellated octahedron differentiated with high-index facets, so-called hexoctahedron, consisting of $\{321\}^S$, (S-region, yellow) and $\{321\}^R$ (R-region, purple). Vertices of the [111], [100], and [110] directions are indicated as A, B, and C, respectively; A' and B' refer to the symmetric points of A and B, respectively. (b) Detailed illustration of $\{321\}$ subfacet differentiation. Each triangular facet of a stellated octahedron is divided into two convexed $\{321\}$ subfacets with R and S surface conformation, respectively. (c) SEM images showing detailed geometry of $\{321\}$ -enclosed nanoparticle.....	138
Figure 4.5 Identification of Miller-index for hexoctahedron nanoparticle. (a) Bright-field TEM image along [110] direction showing angles (α, β, γ) between eight outmost edges. (b) Calculated angles between outmost edges of $\{hkl\}$ -enclosed nanoparticle. The exposed facets were indexed as $\{321\}$	139
Figure 4.6 Comparison of atomic arrangement of the $(321)^R$ and $321S$ gold surfaces. Conformation at kink sites is defined by the rotational direction of low-index microfacets in (111) \rightarrow (100) \rightarrow (110) sequence; clockwise, R-region; counterclockwise, S-region.....	140
Figure 4.7 Mechanism of chirality evolution for 432 helicoid I. (a,b) Schematic (top) and SEM images (bottom) of R/S pairs showing the morphological	

development of 432 helicoid I in the presence of L-Cys and viewed along the [110] (a) and [100] (b) directions. Newly developed boundaries are indicated as a red patterned area with arrows, and each vertex is marked on the corresponding SEM image. (c) 3D model and SEM image of the final chiral shape. The newly formed R region is colored in red and the chiral element is indicated by a dashed line. 142

Figure 4.8 Time-dependent morphology transition of 432 helicoid I. (a) Schematic illustration of time-dependent evolution of 432 helicoid I. All models are viewed along [110] direction. Starting from {321}-indexed nanoparticle with the same ratio of R and S region, different R/S boundaries are split, thickened, and distorted. (b) SEM images of 432 helicoid I at different growth times. Developed chiral components in 432 helicoid I are highlighted with red..... 143

Figure 4.9 Mechanism of chirality evolution for 432 helicoid I. (a, b) Morphological development of 432 helicoid II in the presence of L-GSH viewed along the [110] (a) and [100] (b) directions. (c) Corresponding final chiral shape. Newly formed boundaries and pinwheel-like chiral elements of the final shape are colored in blue. Scale bar, 100 nm. 145

Figure 4.10 Time-dependent morphology transition of 432 helicoid II. (a) Schematic illustration of time-dependent evolution of 432 helicoid II. All models are viewed along [110] direction. Starting from {321}-indexed nanoparticle with the same ratio of R and S region, different R/S boundaries are split, thickened, and distorted. (b) SEM images of 432 helicoid II at different growth times. Developed chiral components in 432 helicoid II are highlighted with blue..... 146

Figure 4.11 Large-area SEM image of 432 helicoid II synthesized with L-GSH. 147

Figure 4.12 Atomic structure of chiral nanoparticle at initial stage. (a-c) SEM image (a) and TEM images (b, c) of chiral nanoparticle after 20-min growth. As the nanoparticle was oriented along $\langle 110 \rangle$ direction, the projected boundaries in TEM image consist of chirally distorted edges. HRTEM image of distorted edge corresponding to the red dotted box in (b). Atoms of microfacets are marked with colored spheres, and different colors are assigned to the Miller index of each microfacet. Based on microfacet nomenclature, the microstructure of (551) can be divided into three units of (111) and two units of (111). Inset: Corresponding

- FFT showing typical patterns along [110] zone. 149
- Figure 4.13 Adsorption energy difference of L-cysteine depending on the Miller index of surface. (a) Temperature-programmed desorption (TPD) spectra of L-Cys of helicoid I and low-index cube nanoparticle, monitoring of CO₂ (m/q=44 amu). As the temperature was raised at a heating rate of 3 K/min, helium carrier gas flowed over the dried nanoparticle sample. (b) Cyclic voltammograms for cube, high-index (stellated octahedron with differentiated {321} subfacets), and helicoid I with L-Cys measured in 0.1 M KOH-ethanol solution at a scan rate of 0.1 V/s. Negative peaks in -1.8 ~ -1.1 V originate from reductive desorption of L-Cys, and peaks at more negative potential indicates higher adsorption energy. 150
- Figure 4.14 Effect of functional group change in L-Cys. Comparison of g-factor and SEM image of synthesized nanoparticles with C-terminal blocked L-Cys (L-cysteine ethyl ester) (top), N-terminal blocked L-Cys (N-acetyl-L-cysteine) (middle), and L-Cys (bottom). C-blocked L-Cys changed the chiral morphology and decreased the CD intensity of the resulting nanoparticles. Nanoparticles produced with N-blocked L-Cys showed achiral morphology without observable CD signal. 152
- Figure 4.15 Schematic illustration showing asymmetric growth of R and S regions. Left: With the selective attachment of L-Cys in the R region, growth of the surface is inhibited, and the reduced growth results in a gradual increase of the area of the R region. Right: Corresponding surface region of the cross-section is indicated on rhombus ABA'B'. 153
- Figure 4.16 Effect of L-Cys and L-GSH concentrations on chiral morphology. (a, b) SEM images of chiral nanoparticles synthesized with different concentrations of Cys (a) and GSH (b). Highest g-factor was observed at optimum amino acid and peptide concentration (red color). At low concentration, only achiral nanoparticles were formed, but with incremental addition, chiral edges started to appear. An excess amount of molecule results in the overgrowth of edges and a significantly decreased CD signal, indicating that an optimal concentration exists for chirality formation. Scale bar, 100 nm. 155
- Figure 4.17 Quantification of adsorbed thiol molecule on helicoid nanoparticles. (a) Schematic experimental procedure for thiol quantification on Au

surface. The reduction of thiolate by NaBH₄ cleaved Au-S bond, and the thiol group of the released molecule spontaneously reacted with thiol-specific dye, producing a fluorescent derivative. Excitation and emission wavelengths were 405 nm and 535 nm, respectively. (b) Concentration curve from 0 to 5 μM for fluorometric assay of L-Cys. Linear fitting and corresponding R² value show good linearity within the measured range. (c) Measured surface density of L-Cys and L-GSH for 432 helicoid I and II, respectively. Surface coverage is calculated by previously reported surface density of L-Cys and L-GSH at the fully saturated monolayer condition. 156

Figure 4.18 Differential growth direction of 432 helicoid I and II at atomic level. (a) Schematic illustration of chirality formation on {321} nanoparticle. Boundary shifts of 432 helicoid I (L-Cys) and II (L-GSH) are indicated in red and blue, respectively. (b) Schematic (111) cross-section of (312)^S-(321)^R-(231)^S facets. Original and newly shifted R/S boundaries are indicated with dashed lines. (c) Atomic arrangement of (312)^S-(321)^R-(231)^S facets in (111) cross-section view. {321} surface consists of (111) terrace and alternating {100} and {110} microfacets. *AC* for 432 helicoid I shift in [101] direction and *AB* for 432 helicoid II shift in [011] direction, respectively. The differentiated growth directions at (312)^S and (231)^S, indicated with thick arrows, resulted in contrasting morphology of the chiral nanoparticles. 159

Figure 4.19 Effect of functional group change in L-GSH. (a) SEM image of synthesized nanoparticles prepared with L-glutathione ethyl ester (C-blocking), γE-C-A, E-C-G, and γE-C sequences. (b) SEM images of nanoparticles synthesized with different dipeptide sequences. Alanine (A), proline (P), cysteine (C), and tyrosine (Y) were added to the N-terminus of L-Cys, which dramatically modified the morphology of the resulting nanoparticle. 160

Figure 4.20 Temporal evolution of 432 helicoid I and II. (a) Increase in g-factor of 432 helicoid I (L-Cys) and II (L-GSH) with time. CD signal was measured, and normalized g-factor was displayed every 5 min during growth. (b) Amount of GSH adsorbed on 432 helicoid II at different growth times. For detailed quantification experiment of GSH on nanoparticle, see Method. 163

- Figure 4.21 Adsorption study of L-Cys and L-GSH on {321} nanoparticles. Different concentrations of L-Cys and L-GSH were added and aged for 2 h, and the amount of adsorbate was measured by subtracting the L-Cys concentration in the supernatant from the initial concentration. 164
- Figure 4.22 3D atomic model of L-Cys and L-GSH on Au (321)^R. (a, b) Molecular configuration of L-Cys (a) and L-GSH (b) anchored on the kinks of the Au (321)^R surface along the top view (left) and tilted angle view (right). Simple fitting of molecules around the (321)^R kink seems to indicate that L-Cys interacts with a single kink via two anchoring sites (Au-S*: 2.75 Å, Au-N*: 2.56 Å), whereas L-GSH interacts with multiple kinks located in different terrace layers via three anchoring sites (Au-S*: 2.72 Å, Au-N*: 2.62 Å, Au-O*: 2.64 Å). Color codes for each atom are Au (yellow, terrace; orange, kink), S (purple), N (light blue), O (red), C (gray), and H (white). 165
- Figure 4.23 Morphology of 432 helicoid III. (a) SEM image of 432 helicoid III nanoparticles evolved from an octahedron seed. (b) 3D models and corresponding SEM images of 432 helicoid III oriented in various directions. Scale bar, 100 nm..... 168
- Figure 4.24 Large-area SEM image of 432 helicoid III nanoparticles synthesized using octahedral seed and L-GSH. 169
- Figure 4.25 Effect of different seed shapes on chirality evolution. (a, b) SEM images of 432 helicoid II nanoparticles synthesized in the presence of L-GSH with cube seeds (a) or octahedron seeds (b) at different reaction times. In the case of octahedron seeds, more protruding edges of nanoparticles were created in the [100] direction compared to cube seeds in the early stages (10 and 20 min) of synthesis. The fast evolution of edges induces the formation of highly twisted arms and is a critical determinant of further growth. 170
- Figure 4.26 Tilt series of HAADF-STEM for 432 helicoid III. (a) HAADF-STEM images and corresponding 3D models of 432 helicoid III at different tilting angles. Front faces of 432 helicoid III are indicated with yellow in 3D models. Red dotted lines show the cubic outline. (b) Magnified STEM images showing the chiral carved gap with depth of about 50 nm. 171

- Figure 4.27 Characterization of interior gap using helium ion microscopy. Helium ion microscopy (HIM) secondary electron (SE) image of 432 helicoid III by He^+ -ion milling process. Original pinwheel-like structure of 432 helicoid III is highlighted in yellow. Exposure to He^+ ion beam with acceleration voltage of 30 keV and beam current of 0.733 pA allows visualization of the interior parts of the curved surfaces, as indicated by red arrows. 172
- Figure 4.28 Miller-index analysis of 432 helicoid III based on 3D modeling. (a-c) Modeling of 432 helicoid III surface. Magnified SEM image of 432 helicoid III (a), corresponding 3D model (b), and interpolated curved surface (c) of 432 helicoid III. Curved outlines of chiral arm at the front and side face are indicated by green and red lines, respectively, and internal boundary is indicated by blue dotted line. 3D curved surface model of 432 helicoid III was constructed by the interpolation of surface outlines. (d) Distribution of Miller index on the modeled surface. Miller indices were calculated from a normal vector at each point of the surface. 173
- Figure 4.29 Optical activity of 432 helicoid III. (a) Measured CD and extinction spectra of 432 helicoid III. (b) Comparison of CD response of the synthesized helicoid structures and other nanoparticles..... 174
- Figure 4.30 Symmetry aspect of 432 helicoid structure. (a) Comparison of symmetry elements for achiral hexoctahedral nanoparticle (top) and helicoid nanoparticle (bottom). (b) Rotation symmetry of 432 helicoid nanoparticle along $\langle 100 \rangle$ (blue) and $\langle 111 \rangle$ (red) directions..... 176
- Figure 5.1 Plasmon hybridization scheme for complex and resonance-coupled plasmonic nanostructure. (a) Resonance coupling of end-to-end aligned Au nanorods dimer separated by a small gap. (b) Plasmonic Born-Kuhn model composed of 90° -twisted nanorods dimer. Hybridized plasmon mode excited by LCP and RCP corresponds to bonding and anti-bonding, respectively. 197
- Figure 5.2 Chiroptical response of three 432 helicoid nanoparticles. (a) Schematic and SEM image of (a) 432 helicoid I, (b) 432 helicoid II, (c) 432 helicoid III nanoparticles. (d) Corresponding g-factor spectra of 432 helicoid I, II, and III solutions. 202

Figure 5.3 Reciprocity of CD measurement in 432 helicoid III. (a,b) CD spectra of 432 helicoid III nanoparticles dispersed in aqueous solution (a) and deposited on glass substrate (b). In both cases, CD measurements in forward and backward direction of samples produced identical responses.....	204
Figure 5.4 Circular dichroism (CD) and optical rotatory dispersion (ORD) spectra of 432 helicoid III nanoparticles.	206
Figure 5.5 Finite-difference time-domain (FDTD) simulation. (a) 3D model and orientation of 432 helicoid III. (b) Orientation-averaged CD spectrum (CD_{Ω} , black solid line) and CD spectra calculated at selected orientations (dots). CD_{Ω} is averaged over 756 discrete orientations. CD spectrum at a single orientation resembles CD_{Ω} with some deviations.....	212
Figure 5.6 (a) Experimental CD and extinction spectra of 432 helicoid III. (b) Theoretical calculation of CD and extinction spectra of 432 helicoid III based on finite-difference time-domain method.....	213
Figure 5.7 (a) CD and extinction spectra calculated for the helicoid III nanoparticle with a normal incidence of circularly polarized light. (b) Electric- and (c) magnetic-field intensities on an illuminated helicoid surface upon normal incidence of LCP and RCP light at 650 nm. The asymmetric field distribution of the (d) electric and (e) magnetic fields are displayed by the differences in these fields under excitation by left circularly polarized (LCP) and right circularly polarized (RCP) light.	215
Figure 5.8 FDTD simulation on 432 helicoid III with different chiral gap geometry. Calculated g-factors of chiral nanoparticles corresponding to models (sample 1–19) using parameterized chiral nanoparticles. Chiral nanoparticles with different (sample 1–3) edge lengths (L) of 100–200 nm; (sample 4–7) gap widths (w) of 10–40 nm; (sample 8–15) gap depths (d) of 30–100 nm; and (sample 16–19) gap angles (t) of 30–75°. Default parameters are edge length of 150 nm, gap width of 20 nm, gap depth of 70 nm, and gap angle of 60°.....	218
Figure 5.9 Correlation of chiroptical response and gap width. (a, b) Calculated absorbance and CD of chiral nanoparticles (sample 7: L150, w40, d70, t60), (sample 12: L150, w20, d70, t60), and (sample 14: L150, w20, d90,	

t60) using $N = 10^{15} \text{ m}^{-3}$ and $l = 10^{-3} \text{ m}$. (c–e) Calculated electric field intensity on the illuminated face ($z = -75 \text{ nm}$) at RCP illumination at the first CD peak of 600 nm, 670 nm, and 720 nm, respectively. 219

Figure 5.10 FDTD simulation on differently modified 432 helicoid III. Calculated g-factors of chiral nanoparticles corresponding to models (sample 20–32) using chiral nanoparticles with various geometry changes. (sample 20–22) Chiral nanoparticles with increasing curvatures from (sample 20) to (sample 22); (sample 23–26) Chiral nanoparticles with aspect ratio of (sample 23) 1 to (sample 26) 3; (27–31) chiral nanoparticles with hollow structures constructed by removing cubic domains with side lengths of (sample 27) 70 nm to (sample 31) 130 nm. Default size of chiral nanoparticles in (sample 20–31) is 150 nm. (sample 32) Planar-triangle-based chiral nanoparticle with edge length of 150 nm. 220

Figure 5.11 Effect of structure deviation on optical activity. Calculated CD signals of chiral nanoparticles with morphological deviation. With the addition of a spherical bump, changes in chiral structure were created, and the model with different bump locations was analyzed. 223

Figure 5.12 Visible light polarization control by 432 helicoid III solution. (a) Experimental setup used for polarimeter measurements with 561, 635, 658, and 690 nm laser source. (b) Polarization ellipses at each wavelength are expressed by ellipticity (χ) and azimuthal rotation (ψ); $\chi = 1.7^\circ$, $\psi = -7.9^\circ$ at 561 nm; $\chi = -28.7^\circ$, $\psi = 2.6^\circ$ at 635 nm; $\chi = -20.7^\circ$, $\psi = 26.6^\circ$ at 658 nm; and $\chi = -4.8^\circ$, $\psi = 29.0^\circ$ at 690 nm. (c) Photographs of achiral (left) and 432 helicoid III (right) solutions showing transmitted light under cross-polarized conditions. 225

Figure 5.13 Transmitted color modulation by a dispersed solution of 432 helicoid. (a) SEM images and (b) corresponding CD spectra of 432 helicoid III nanoparticles with different sizes controlled by seed concentrations. Increasing nanoparticle size resulted in a red shift in plasmon resonance. The wavelengths λ_{max} at maximum CD intensity are indicated in the images. (c) Polarization-resolved colors of light transmitted through seven different 432 helicoid III solutions containing different λ_{max} values. The rotational angle of the analyzer was increased from -10° to 10° (see Methods). Angle 0° , which is indicated by a dashed box, represents cross-polarized conditions. (d) Color transition patterns of 432 helicoid

III nanoparticles traced on CIE 1931 color space. The white triangle indicates the RGB boundary.	226
Figure 5.14 Fabrication of metal-deposited helicoid III nanoparticle. (a) Schematic of metal deposition process on the nanoparticle-coated substrate. (b) TEM image of mPEG-SH (MW=5000) modified helicoid III nanoparticle. (c) SEM images of Au deposited helicoid nanoparticle with a thickness of 30 nm. Upper right: SEM image of topmost surface of Au coated helicoid III nanoparticle. Lower right: SEM image of a hole of the metal thin-film was formed at the lower side of the nanoparticle, captured after the detachment of nanoparticle. (d) TEM image of Ag deposited helicoid nanoparticle (Ag thickness: 30 nm).	229
Figure 5.15 Chiroptical spectral tuning of 432 helicoid III nanoparticles. CD spectra of (a) Au-deposited and (b) Ag-deposited helicoid III nanoparticle substrate with metal thickness of 10 nm to 50 nm.	232
Figure 5.16 FDTD simulation of metal-deposited helicoid nanoparticle. (a,b) Absorption cross-section (a) and differential absorption cross-section between the case of LCP and RCP excitation (b). (c) The difference of nearfield distribution in the case of LCP and RCP excitation, at 850 nm. Time-averaged electric field was measured at nanogap region ($z = 20$ nm).	233
Figure 5.17 Transmitted color modulation by metal-deposited 432 helicoid III substrate. (a) Calculated polarization-resolved color transition and (b) corresponding trajectory on CIE 1931 color space for the light transmitted through Au-deposited 432 helicoid III substrate. (c) Calculated polarization-resolved color transition and (d) corresponding trajectory on color space for Ag-deposited 432 helicoid III substrate. The black dotted line indicates color coverage for bare 432 helicoid III solution.	236

Chapter 1. Introduction

1.1 Structure-related optical property

From atoms to crystals and bulk materials, the structure of optical materials is significant at various scales. Controlling the structure is one of the effective ways to achieve the desired optical properties.¹⁻⁴ We can easily find optical phenomena due to these microscopic structures in natural materials and organisms. For example, the butterfly (*Morpho didius*) that can be seen in nature is shining a vivid blue light despite the absence of pigment molecules (Figure 1.1a).^{5,6} This unique color comes from a unique microstructure that can be seen on the surface of a butterfly wing. Regularly arranged patterns interfere with incoming visible light, so only light of a particular wavelength can be reflected, and the rest is absorbed or transmitted. These patterns can be found in a wide variety of natural organisms such as peacock feathers (Figure 1.1b)⁷ and beetle shells (Figure 1.1c)⁸, as well as in mineral structures such as opals⁹. The definitive cause of this phenomenon is due to the photonic crystal structure in which the dielectric materials are regularly arranged to induce interference and diffraction of light, and the resulting color is called structural color.¹⁰ Such a photonic crystal can be applied not only to reflect a specific color but also to design various optical devices, such as optical waveguides,¹¹ lasers,¹² and optical switches.¹³ In order for a photonic crystal structure to operate in the visible light region, the periodicity of the structure must have a wavelength and comparable several hundred-nanometer levels. Thus, precise control of nanostructures at the level of hundreds of nanometers is critical for achieving the desired optical properties in the visible region.

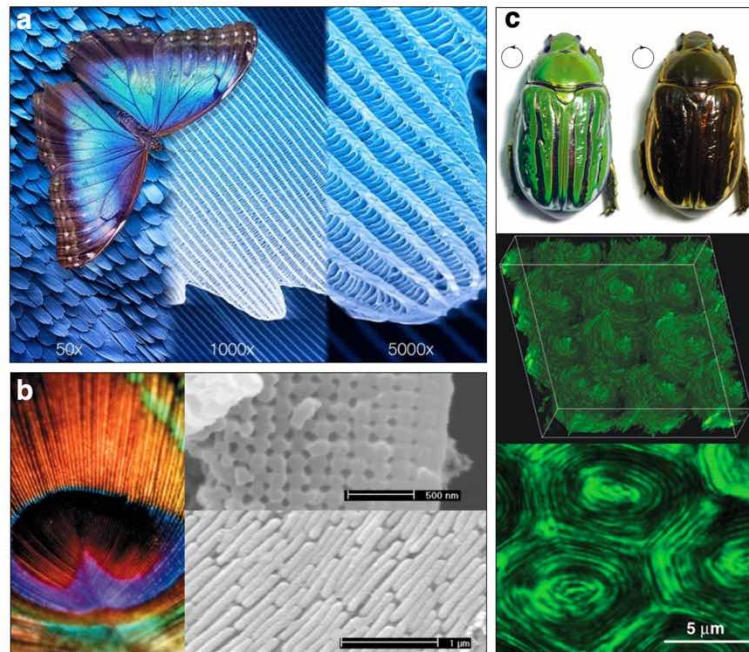


Figure 1.1 Structure-related optical property in the biological system. (a) Reflection of blue light from the wings of *Morpho didius* originated from the periodic structures of the wing scales. (b) The diverse coloration of peacock feather derived from the photonic crystal structure at the cortex surface with different periodicity. (c) The circularly polarized iridescence of jeweled beetles, *Chrysina gloriosa*, caused by helical cell arrangement.

Furthermore, metallic materials can interact with light at the smaller length scale even under the 100-nm. Along with many other physical properties, highly conductive metallic materials such as gold, silver, copper, or aluminum, have different optical properties from the dielectric materials. One of the well-known examples is that they show high reflectivity in the visible range, working as efficient materials for mirrors with various types. In the subwavelength scale, metal nanoparticles can exhibit unique optical properties in the visible range, such as a sharp and strong absorption in the visible and near-IR regime, which is not observed in bulk size (Figure 1.2). This phenomenon can be found in the brilliant coloration in some historical relics, such as Lycurgus cup in 4th-century and various stained glasses in medieval ages, which resulted from the presence of metal impurities in the glass (Figure 1.2a). Interestingly, the wavelength, bandwidth, and overall spectral shape of the absorption band are not only dependent on materials but structural parameters of the metal nanoparticles such as size, morphology, and symmetry (Figure 1.2b, 1.2c). Furthermore, a rigorous design of metallic nanostructure enables a wide variety of unique optical effects, including extraordinary light transmission, strong enhancement in the local electromagnetic field, negative refraction of light, and gigantic optical activity.

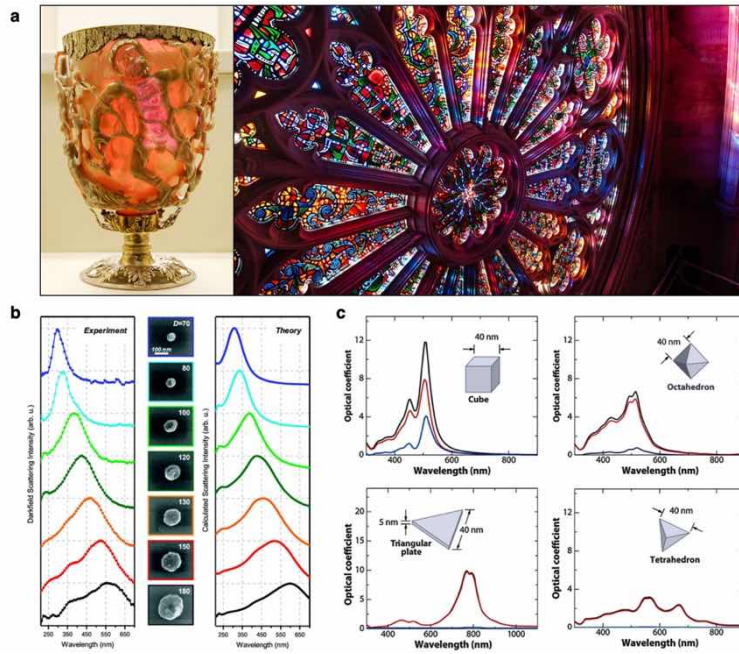


Figure 1.2 Optical response of metal nanoparticles. (a) Lycurgus cup (left) and stained glass of Chartres Cathedral (right) (b) Experimental and simulated scattering spectra of aluminum nanoparticles with different sizes, from 70 nm to 180 nm. (c) Simulated extinction (black), absorption (blue), and scattering (red) spectra of silver nanoparticles with various morphology.

1.2 Plasmonic nanostructure and metamaterial

In metallic materials, free electrons can move in the spaces between fixed positive ions maintaining overall neutrality. This state can be called a free-electron plasma. The optical properties of metallic materials are governed by the response of this free electron plasma. When the oscillating electromagnetic wave interacts with the metal, the delocalized electrons of metal can be fluctuated and physically displaced from the lattice of positive metal ions. This collective movement of electron clouds in the metal nanoparticle is short-lived because the Coulombic attraction from the positive metal ions can work as a restoring force to pull the delocalized electron back to initial position. The simultaneous action of the oscillating electric field from incident light and Coulomb attraction from metal ions, acting as a sinusoidal driving force and restoring force, respectively, enable the harmonic oscillation of plasma in the metal nanoparticle. Consequently, resonant conditions can be achieved by the in-phase coupling of oscillating plasma and incident electromagnetic field. At this frequency, the interaction of metal nanostructure and incident electromagnetic field can be maximized, causing the largest absorption and charge displacement. As the dimensions of the nanoparticle are too small compared with the wavelength of the incident light, this collective oscillating plasma in the metal nanoparticle is called a localized surface plasmon resonance (LSPR).

The confinement of plasma oscillation in subwavelength volumes results in an oscillating electromagnetic field to be located in close proximity to the surface of the nanoparticle. Interestingly, as surface plasmon are confined to the nanoparticle geometry, the LSPR conditions depend not only on the material property of metal and the surrounding medium but also on the structural parameters of nanoparticles

such as size and morphology. Variations of the structural parameters change the resonant frequency of plasmon oscillation and further give rise to different resonant modes denoted as a dipole, quadrupole, octupole, and higher multipoles. Each mode of plasmon resonance can build different patterns of surface charge distribution, and thus a characteristic electric field distribution around the nanoparticle. Figure 1.3 schematically shows the effect of morphology on surface charge and electric field distribution of plasmonic nanoparticles as a response to the external electric field.¹⁴ Compared to the spherical case, triangular nanoparticle shows a concentration of charge at the sharp tip and corresponding asymmetry in the electric field. This morphology dependency may appear as a more complex feature in nanoparticles with anisotropic and more intricate structures such as ellipsoid, rod, polyhedron, and even branched structure. The resonances of those cases can be described by plasmon hybridization between oscillations of the different structural components of the nanoparticle.

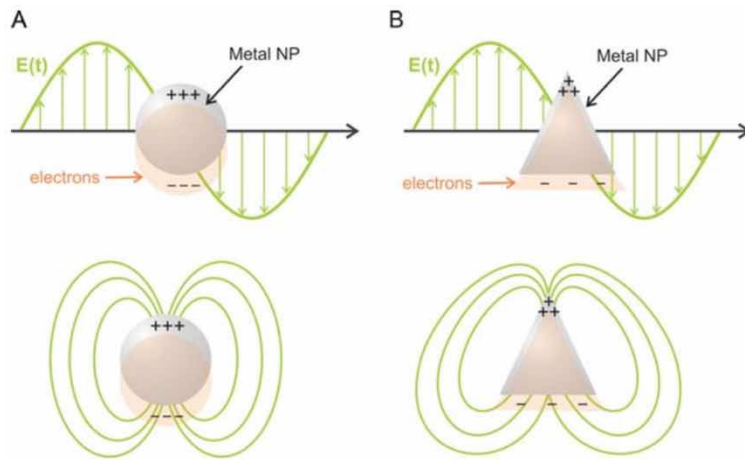


Figure 1.3 Schematic illustration of the sphere (a) and triangular prism (b) nanoparticles excited by the electric field of the incident light. The collective movements of electrons are resonant at optical frequencies and the surface charge and local electric field distribution depends on the shape of the nanoparticle: in the case of the sphere the field is distributed in a symmetric dipolar pattern, whereas in the case of the triangular shape there is charge and field concentration on the upper tip.

For the metal nanoparticles with anisotropic ellipsoid or rod structures, the LSPR condition can be separated in two different spectral positions, corresponding to the longitudinal and transverse oscillations of its electron clouds along the major or minor axis, respectively.¹ Compared to the isotropic spherical nanoparticles with the same volume, the resonance due to longitudinal oscillations of rod-shaped nanoparticles can exhibit a significant spectral red-shift. For the metal nanoparticles with the high aspect ratio, their plasmon resonances can be extended to the near-infrared region of the spectrum due to the lowered frequency. The resonance separation between the minor axis and the major axis due to this anisotropic structure can actually bring about the directionality of optical response with respect to the polarization angle of the incident light. Tailored resonances depending on the polarization of incident illumination can be integrated into the single-layer architecture, generate color variations under orthogonal polarizations with spatial resolutions approaching the diffraction limit (Figure 1.4).¹⁵⁻¹⁷ In particular, adjusting the polarization direction of light can change the optical response in real-time, and the integration with conventional liquid crystal devices may produce an active color modulating device. Such polarization-sensitive spectral tuning is an attractive strategy for high-density multiplexed optical information storage or active display materials.

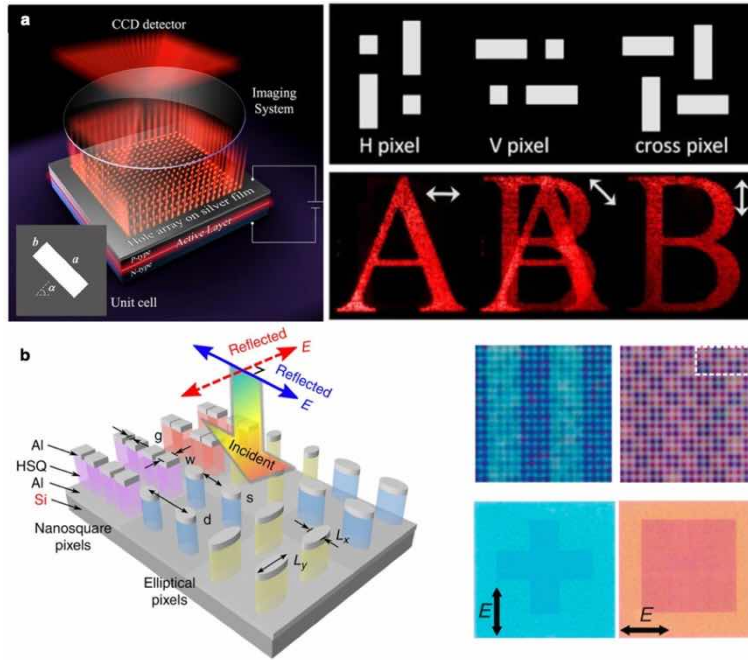


Figure 1.4 Polarization-sensitive optical response using anisotropic plasmonic nanostructure. (a) Electroluminescence of LED active layer covered with plasmonic rectangular hole array structure. Three types of pixel structures consist of rectangular and square nanoholes construct a binary letter image encoded by polarization-sensitive luminescence. (b) White light interaction with anisotropic pixels where specific wavelengths of light are back-scattered with orthogonal polarization states. This configuration generates different scattering colors within each individual pixel. Polarization-sensitive dual-image can be embedded in high-resolution plasmonic color microprint.

Furthermore, on the microscopic scale, the oscillation of localized surface plasmon can induce optical phenomena in near-field regimes that are closely related to the nanoparticle morphology. When the plasmon nanoparticle is excited by light, the intensity of electromagnetic field in the vicinity of the nanostructure may increase in order of $10^1\sim 10^2$ compared to the initial intensity of light as a result of resonance. More amplified electromagnetic radiation in order of 10^3 can occur at the sharp tip (Figure 1.5a),¹⁸ which is believed to be due to the lightning rod effect and can also be achieved in the bow-tie structure with small spacing between opposing nanotriangles (Figure 1.5b).¹⁹ These areas of the strong electric field are often called “hot spot”, and the morphology control of plasmonic nanostructure determine the location and distribution of this hot spot with subwavelength precision.

The generation of plasmonic hot spots with the concentrated electromagnetic field is advantageous for various plasmon-enhanced spectroscopic techniques. By the rational design of electromagnetic field-enhancing nanostructures, the optical signals from the nearby molecules can be amplified by several orders of magnitude, and even single-molecule detection is possible. In surface-enhanced Raman scattering (SERS), extremely strong Raman scattering can be observed from molecules in the vicinity of metal nanostructure at plasmon resonance condition. The intensity of Raman scattering is proportional to that of the local electric field at the incident wavelength $I(\lambda) = |E(\lambda)|^2$ and at the Stokes-shifted wavelength $I(\lambda') = |E(\lambda')|^2$, and the Raman enhancement factor is usually approximated to be proportional to the 4th power of the local electric field at the incident frequency.²⁰ The strongest enhancement of Raman scattering can occur under conditions where both incident and scattered light can be strongly enhanced. Therefore, the LSPR conditions of the nanoparticles should be tuned to cover both incident and Stokes-shifted wavelengths. With the proper design of nanostructures, the local field can be strongly enhanced, and the SERS signals can be observed from even single-molecules (Figure 1.6).²¹

Meanwhile, the interaction between strongly confined field at the hot spot and the various fluorophores may amplify or quench the photoluminescence at their absorption and emission wavelengths (Figure 1.7).²² Plasmon-induced modification of the excitation and decay dynamics can be described by using absorption and emission electric dipole moments of fluorophores.²³ Under the enhanced electromagnetic field near the plasmonic nanostructure, the excitation rate of a fluorophore at the absorption wavelength can increase. After excitation, plasmon-enhanced field modifies quantum yield, by increasing local density of optical state and changing radiative and non-radiative decay rate. In addition to these two factors, strong quenching of radiative transitions may occur for fluorophores close to metal surface ($d < 15$ nm). Therefore, placing the fluorophore and nanoparticle at optimal distance can induce strong enhancement of the fluorescence signal by the plasmons. Harnessing the plasmon-enhanced spectroscopic strategies are essential for biosensor applications, which enable to detect tiny amounts of biomarkers or pathogens by amplifying signals of the analyte molecules.

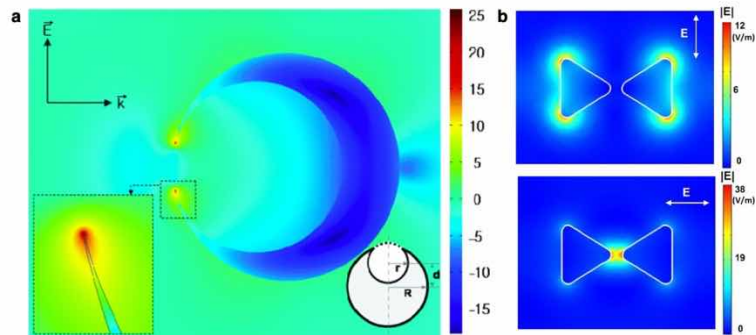


Figure 1.5 Local electric field amplitude distribution at plasmonic hotspot. (a, b) Electric field profile showing strong field confinement at the tips of nanocrescent structure (a), and nanogap between nanotriangle (b).

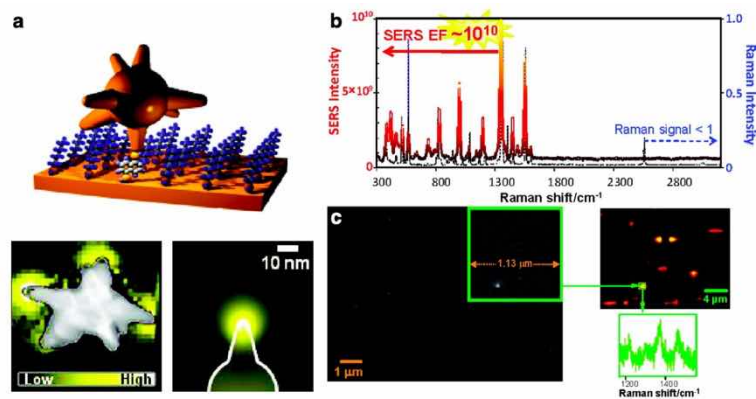


Figure 1.6 Single molecule SERS measurement using branched nanoparticle. (a) Single branched nanoparticle onto single molecules. For the branched nanoparticle, experimental and calculated EELS intensity mapping show high localization of electric field near the tip-end. (b) Bulk Raman spectrum of 15NAT molecules in aqueous solution (right scale), compared to the SERS spectrum (left scale) of the same molecules recorded by using the branched nanoparticle. (c) Single-particle SERS mapping recorded from a sample with less than 1 particle per μm^2 .

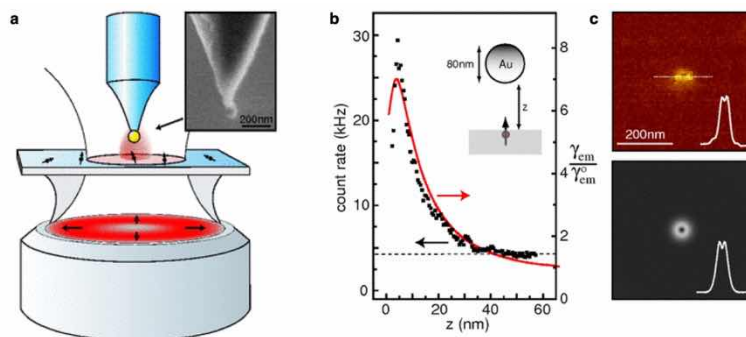


Figure 1.7 Fluorescence enhancement near the gold particle. (a) Experimental arrangement. An 80nm gold particle is attached to the end of an etched glass tip and irradiated by a radially polarized laser beam. (b) Fluorescence rate as a function of particle-surface distance z for a vertically oriented molecule. (c) Experimental and theoretical fluorescence rate image of a single molecule acquired for $z \sim 2$ nm. The dip in the center indicates fluorescence quenching.

The interaction of the plasmonic nanostructure with light can be applied not only to the improvement of the optical function but to the design of a new optical element that was not present in the natural world, called metamaterial. The optical properties of the metamaterials are governed by the smallest building block, the meta-atom, with precise shape, geometry, size, orientation, and arrangement pattern. Well-designed plasmonic nanostructure arrays can control phase delays locally rather than simply reflect light (Figure 1.8).²⁴ This artificial design can be used to directly control the wavefront when the incident light is transmitted or reflected, and it is also possible to control the propagation of the light behaves as if it was reflected from a planar surface even though the light is originally reflected from the protruded object. These materials are highly applicable as cloaking materials that can make an object invisible. Furthermore, attempts have been made to realize negative refractive index materials that are not present in nature by precisely controlling the optical response of plasmon nanostructures.²⁵ Several designs for the negative-index material in optical frequency were suggested (Figure 1.9).²⁶⁻²⁸ The direction of light propagation between the two materials can be changed by the refraction phenomenon, and in the case of negative refraction, the light is bent in a direction opposite to that of the natural material, and furthermore, subwavelength focusing becomes possible (Figure 1.10a).²⁹ Precise control of this propagation direction can be applied to making a three-dimensional cloaking medium (Figure 1.10b).³⁰

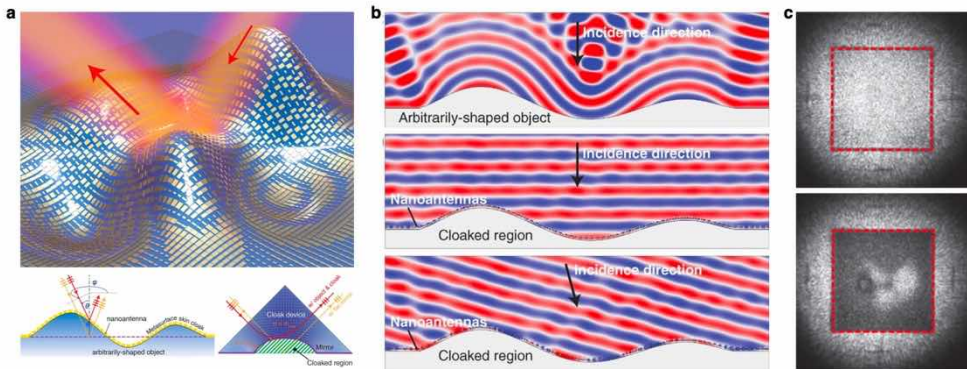


Figure 1.8 Plasmonic metasurface skin cloak. (a) Schematic view and working principle of a metasurface skin cloak. (b) Full-wave simulation results for the metasurface skin cloak, showing that the reflected light is almost completely recovered by the skin cloak as if there were no scattering object for both normal and oblique incidences. (c) Experimental demonstration of metasurface skin cloak for a 3D arbitrarily shaped object.

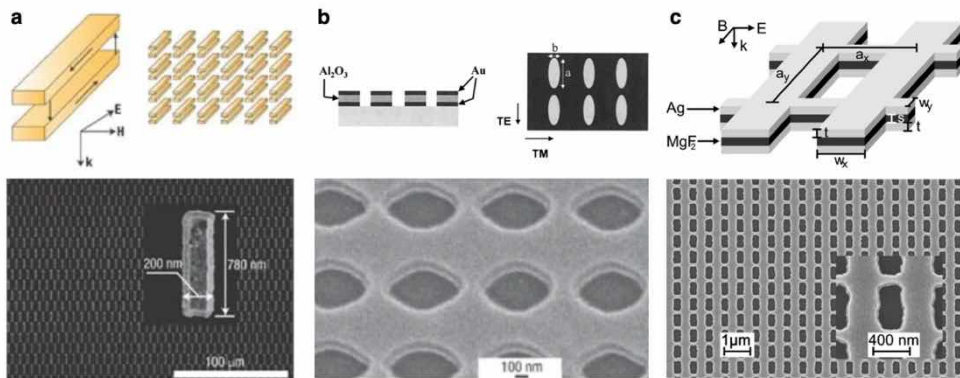


Figure 1.9 Optical negative-index material design. (a) Array of paired nanorods supporting antiparallel current modes. (b) Arrays of ellipsoidal voids in a pair of metal sheets with a negative index at about $\lambda = 2 \mu\text{m}$. (c) The nano-fishnet where the largest figure of merit $F = 3$ was obtained at $\lambda \approx 1.4 \mu\text{m}$.

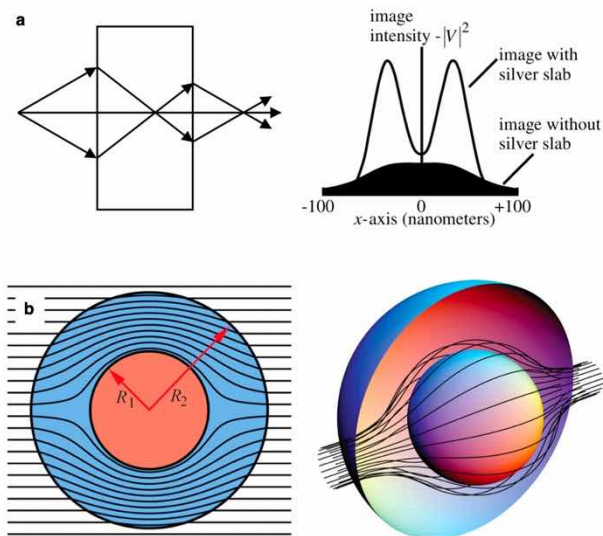


Figure 1.10 (a) Slab of negative index material working as perfect lens. Light formerly diverging from a point source is set in reverse and converges back to a point. (b) Graded refractive index cloak guiding light around a hidden object. The field is excluded from the cloaked region but emerges from the cloaking sphere undisturbed.

1.3 Chirality and chiral plasmonic nanomaterial

Chirality is a three-dimensional geometric property which is a structure cannot overlap to its mirror image and is easily found in various biological systems or biomolecules. For example, the chirality in biological system exists on a variety of length scales ranging from the smallest molecules (amino acids and sugars), supra-molecules (peptides, proteins, and DNA), virus and helical microbe to the macroscopic chirality. In 1848, Luis Pasteur explained the optical activity—the light-matter interaction in chiral materials.³¹ Based on careful observation of well-separated (+)- and (-)- tartaric acid (TA), he suggested that TA has non-superimposable configuration with its mirror-image and rationalized that this chiral structure is the origin of the opposite optical rotation caused by (+)- and (-)- TA molecules. Ever since his pioneering insight into the chiral structure and its optical activity, great scientific effort has been dedicated to investigation of the chirality of matter. Spatially different arrangements in chiral structures lead to unequal interactions with left-handed (LCP) and right-handed circularly polarized (RCP) light that possesses rotational vectors perpendicular to the direction of propagation of light in space. Therefore, amino acids or helical proteins, as representative chiral entities, produce distinctive circular dichroism (CD) response that can be measured as the difference in the absorption of LCP and RCP. Based on this distinctive characteristic, the chiroptical response of biomolecules has been used as a valuable tool for understanding and detecting structural changes in the biological field, where myriads of chiral examples are known.

The effort to understand the optical response of chiral structures over the past centuries has extended to the artificial design of chiral materials. The integration of an asymmetric structure with a plasmonic material is essential for this purpose, as plasmonic material exhibits intense structure-related optical properties originating from maximized light-matter interaction. Typically, the Au helical nanostructure exhibits a very large contrast in transmission for the handedness of the incoming circular polarization (Figure 1.11a).³² Therefore, this chiral plasmonic structure can be directly used to make a polarization-selective filter using a single layer thin-film of a few hundred nanometers or less. In addition, J. Pendry suggests that negative refraction can be achieved by the chiral materials, which have different refractive indices between LCP and RCP via relation $n_{\pm} = \sqrt{\epsilon \cdot \mu} \pm \kappa$.³³ Here, κ is chirality parameter, and + refers to RCP and – refers to LCP, respectively. Using this concept, several groups demonstrated chiral negative index material in GHz and THz regime (Figure 1.11b).^{34,35} Recently, there have been attempts to achieve the negative refraction in NIR and visible range via chiral plasmonic materials.

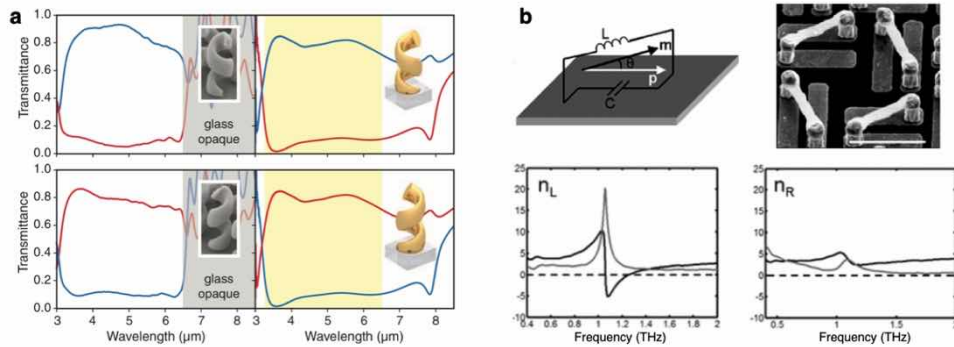


Figure 1.11 Chiral plasmonic nanostructure for polarization filter and negative-index. (a) Measured and calculated optical transmittance spectra of Au helix for circular polarization of the incoming light propagating along the axis. A large transmittance ratio results in the wavelength range from 3.5 to 7.5 μm . (b) Plasmonic chiral structure consisting of inductor-capacitor model which functions effectively as an electric dipole and a magnetic dipole forming an angle θ . Negative refractive index was achieved by LCP excitation in THz region.

At the microscopic level, chiral plasmonic nanostructure strongly distorts electromagnetic nearfield, and the electric field and the magnetic field are cross-coupled locally to form a twisted field (Figure 1.12a, b).^{36,37} This region is called the "superchiral field", and recent studies have shown that the chiral signal of the molecule is amplified in the superchiral field region.³⁸ Based on this concept, Kadodwala and coworkers reported the Au gammadion nanostructures that can distinguish the secondary structure of protein, and this chiral spectroscopy methodology has been adapted to analyze the molecular fingerprint closely related to the 3D structure of biomolecules.³⁹ Another important direction is polarization-selective wavefront control and beam steering via elaborate design of chiral nanoarray, called geometric phase metasurface.^{40,41} For the nanorods pattern, spatially controlled rotation angles within a single wavelength scale can produce a space-variant phase delay for the incident circular polarization. This phenomenon finally results in changes in propagation direction due to the generation of slanted wavefront. This concept can be applied to the polarization-selective hologram device because the handedness of circular polarization can determine the diffraction direction of the light. Circular and spiral design of the space-variant phase delay can be further adapted to the multiplexed optical communication by giving the orbital angular momentum of light.⁴²

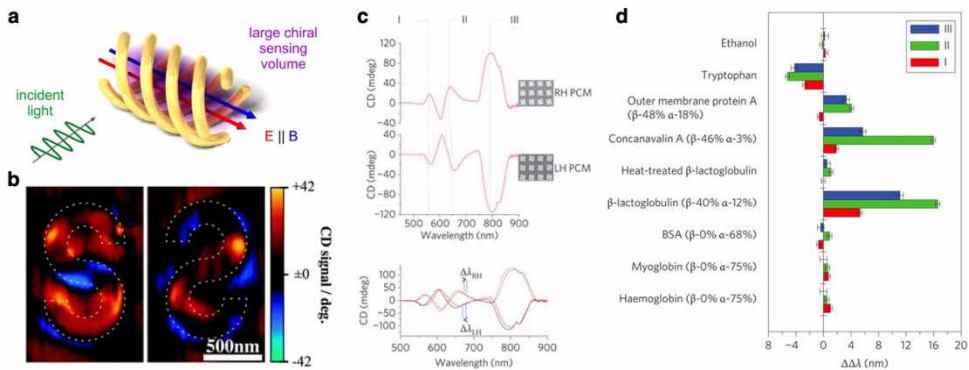


Figure 1.12 Chiral nearfield and its application in chiral sensing. (a, b) Theoretical calculation and experimental measurement of chiral nearfield distribution. (c) CD spectra collected from left- and right-handed gammadion plasmonic nanostructure. Resonance shifts $\Delta\lambda_{RH}$ and $\Delta\lambda_{LH}$ caused by the adsorption of protein and exhibit different value, which indicates that optical dissymmetry occurs in opposite nanostructure. (d) $\Delta\Delta\lambda$ values for I, II and III modes for various proteins. Also shown are the effectively zero $\Delta\Delta\lambda$ values obtained from the (achiral) ethanol solvent.

1.4 Morphology and chirality control in nanoscale

As shown in the previous examples, the ability of plasmonic nanostructures to manipulate light at nanoscale has resulted in extensive applications in optical fields. Since their plasmonic properties can be delicately tuned and significantly enhanced by controlling the nanostructure, the morphogenesis in the range of nanoscale is prerequisite for optical application.

Fabrication of nanometer-scale plasmonic materials has been done by conventional nanopatterning strategies, such as electron beam lithography (EBL) and focused ion beam (FIB) lithography. These methods are superior to demonstrate proof-of-concept research to realize the theoretically designed structure due to the ease of programming desired structures: nanopatterns are generated through a direct writing process, producing a complete arbitrary structure regardless of anisotropy, symmetry-breaking, and chirality (Figure 1.13a, b).⁴³⁻⁴⁵ Nanopatterns made by EBL and FIB are specialized on 2D structures, because they are projected on planar substrate and resist layer. Therefore, these methods are suitable to fabricate monolayer 2D plasmonic nanostructures, which is mainly used as building blocks of metasurface. However, in order to overcome fundamental limitations of 2D plasmonic nanostructures including angle dependency, non-reciprocity, and difficulty to control the bulk characteristics, the 3D plasmonic nanostructure is strongly required. Recently, several studies have been carried out to improve existing 2D nanopatterning method, by stacking several layers.⁴⁴ Although this approach has succeeded to construct layered quasi-3D structures, still it is difficult to realize a true 3D structure, because flexibility in the structural design along the z-direction is relatively low. Therefore, there has been strong desire for a method that can directly produce the 3D morphology in nanoscale. The direct laser writing method is one of

the candidates for the 3D nanofabrication. In this method, a photoresist matrix was exposed to a pulsed laser with a tiny focus made by two-photon absorption, and nanostructures can be directly patterned according to movement of the focal point along x-, y-, and z-axes. In this way, a continuous structure with arbitrary 3D morphology can be obtained, and the fabrication of even helix structure and gyroid structure with 3D chirality were possible (Figure 1.13c).³² Despite this utility in 3D nanofabrication, there were several limitations such as restricted pool of resist materials for the two-photon photolithography and spatial resolution with several hundred nanometers which is relatively low compared to 2D lithography techniques. Although the direct patterning using electrons, ions, and photons is superior to obtain the desired nanostructure, one of the critical weakness is slow fabrication process, which restricts the overall pattern size in micrometer scale. For the practical large-scale fabrication, alternative methods such as nanoimprint lithography (NIL) and various self-assembling methods have been studied to produce bulk-scale plasmonic nanopattern.^{46,47} In the NIL method, a master with pre-patterned nanostructure is replicated to the soft or curable material. Because this method can physically imprint the structure, it is possible to produce a nanopattern below the diffraction limit of light with a large area. In addition, the ordering of self-assembled structure can be also applied to the periodic nanostructures.

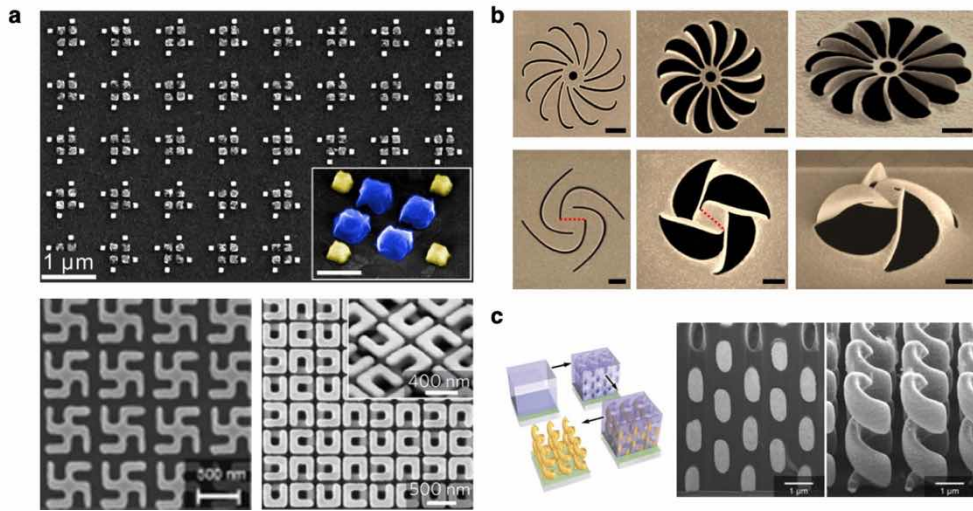


Figure 1.13 Top-down fabrication of complex and chiral nanostructure. (a) 2D and quasi-3D chiral nanostructures fabricated by electron beam lithography. (b) Chiral kirigami nanostructure fabricated by focused ion beam lithography. (c) 3D helicoid nanostructure fabricated by direct laser writing.

Top-down strategy using hard materials is particularly advantageous for fabrication with complex and low symmetry geometries such as chiral nanostructures. However, the complexity of the process, the trade-off between resolution and structural diversity, and the requirements for specialized facilities are major hindrances for the real applications. Therefore, developing an alternative method for making chiral nanostructure is critical to addressing these limitations and providing a new direction in the nanophotonics and material science. In this context, spontaneous formation and control of morphology and chirality at the nanometer level can develop a new class of nanomaterial which provide a novel bottom-up pathway to overcome the aforementioned technical challenges and suggest fundamental principle of nanostructure design.

One of the representative methods is the colloidal synthesis of nanocrystals. Until now, enormous geometries including from simple sphere⁴⁸ and rods⁴⁹ to complex polyhedron,⁵⁰ branched structure,⁵¹ concave structure,⁵² and hollow structures⁵³ have spontaneously formed via colloidal synthesis. At the early stage of colloidal synthesis, inorganic atoms are supplied from a precursor, and nucleation of crystal seed occurs (Figure 1.14a).⁵⁴ Subsequently, continuous bottom-up assembly of atoms to the seed and subsequent growth results in the formation of nanocrystal. Interestingly, during the synthesis, final morphology of the nanocrystal is mainly determined by the thermodynamic and kinetic parameters (Figure 1.14b, 1.14c).⁵⁵ In particular, understanding the surface energy and growth factors of the nanocrystals enable colloidal morphology control and tailored bottom-up nanostructures.

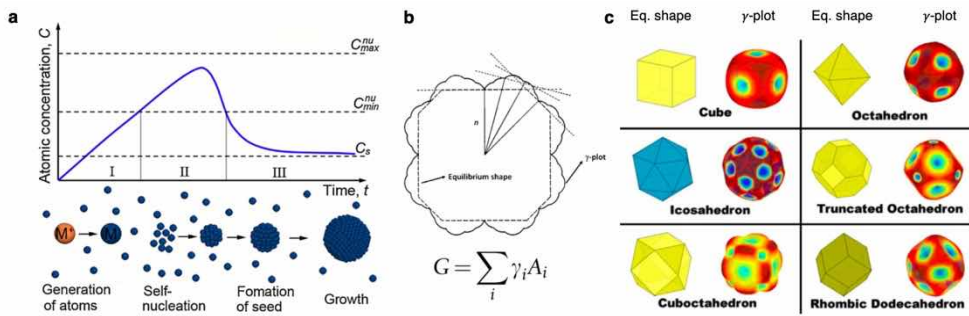


Figure 1.14 Formation of inorganic nanocrystal. (a) LaMer curve describing three stages of metal nanocrystal formation in solution system. Stage I: atom producing, stage II: nucleation, and stage III: seed formation and growth. (b) Two-dimensional and (c) three-dimensional schematic Wulff construction to determine the equilibrium shape of a particle.

Another interesting example is the left-right asymmetry in living organisms, which give us a useful insight for chirality. Left-right asymmetry in biological system is a consequence of the hierarchical chirality transfer throughout the multiple length scales. For instance, helical and spiral structures found in gastropod shells,⁵⁶ larvae,⁵⁷ and plant tendrils⁵⁸ are formed by the twisted arrangement of cells at the early developmental stage. Driving force of this twisting is the distortion of cell morphology induced by the chirality of subcellular macromolecules such as actin, microtubule, myosin, and other various proteins. Chirality of macromolecules is originated from the small biomolecules such as amino acid and sugars, which have chiral centers in their molecular structures (Figure 1.15). During dynamic process of the biological system development where the living organisms are self-assembled from the molecular level and developed into larger structures, chirality is transferred from the molecular encoder to the macroscopic left-right asymmetry.

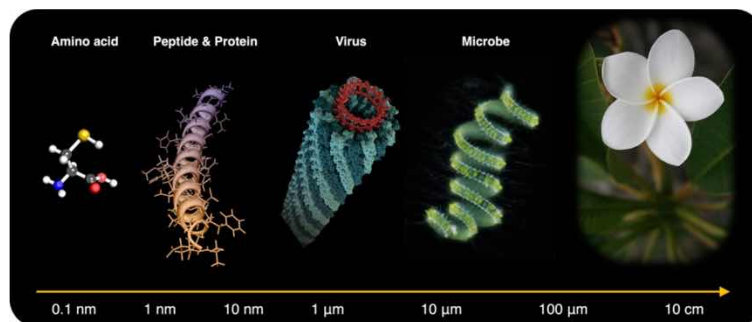


Figure 1.15 Chirality in natural organism. Starting from the stereocenter in small molecule, chirality exists in microscopic and macroscopic biological system and can be transferred across multiple length scales

1.5 Scope of thesis

The overall goal of this thesis is to develop a novel bottom-up route for nanoscale morphology and chirality control using plasmonic materials. Based on the lessons from nanocrystal synthesis and biological left-right asymmetry, this thesis focused on the following problems:

- 1) How to control the morphology of plasmonic nanoparticle during the colloidal synthesis?
- 2) How to develop and control chiral geometry of colloidal nanoparticle using naturally achiral metals?
- 3) How to understand the optical response of complex chiral plasmonic nanostructures?

To address these questions, the aims of this thesis are given as follows:

In Chapter 2, prior to the main research, previous research trends on the biomolecule-induced chirality was introduced. Thanks to intrinsic chirality of biomolecule, various studies have attempted to implement chirality via interfacing of inorganic material and biomolecule. Biomolecules can be self-assembled in chiral geometry, and most researches focused on making chiral assembly structures using achiral plasmonic building blocks, providing chiral structures such as helix, twisted rod, and asymmetric pyramid. On the other hand, chiral geometry of the plasmonic metal itself is one of the important scientific challenges in bottom-up synthesis. In the latter part of this chapter, the concept of inorganic chirality defined on the high-Miller-index plane and their interfacing with biomolecules were introduced. We believe that chirality transfer at interface provides a new principle of chiral

nanofabrication, which is a theoretical background of peptide-directed synthesis of chiral nanoparticle in following Chapter 4.

In Chapter 3, a systematic morphology control of plasmonic Au nanoparticle was described. For the first time, the morphology diagram was constructed as a function of cetyltrimethylammonium bromide (CTAB) and ascorbic acid (AA) concentration. Although CTAB and AA have been used in many gold synthetic protocols as a well-known ligand and reducing agent, the mutual interaction to control the shapes of gold nanoparticles has not been investigated fully. In most cases, the results still remain phenomenological and are hard to be predicted and translated into new synthesis developments. We have chosen the CTAB-AA system to study the role of thermodynamic stabilization and kinetic growth and successfully synthesized low-Miller-index exposed various polyhedral nanoparticles. Based upon the constructed morphology diagram, we further advanced the low-index seed morphology into the high-Miller-index exposed nanoparticles. This result was the first demonstration of $\{hkl\}$ -index-plane exposed hexoctahedral nanoparticle in CTAB-AA system, which is important for chirality transfer. Based on this research, bottom-up control of plasmonic nanostructure was achieved, and a background for the synthesis of chiral nanoparticle was provided.

In Chapter 4, we developed a strategy for synthesizing chiral gold nanoparticles that involves using amino acids and peptides to control the optical activity, handedness and chiral plasmonic resonance of the nanoparticles. The key requirement for achieving such chiral structures is the formation of high-Miller-index surfaces that are intrinsically chiral, owing to the presence of ‘kink’ sites in the nanoparticles during growth. The presence of chiral components at the inorganic surface of the nanoparticles and in the amino acids and peptides results in enantioselective interactions at the interface between these elements: these

interactions lead to asymmetric evolution of the nanoparticles. To understand chirality evolution mechanism at the molecular level, detailed analyses on the high-Miller-index plane and molecular adsorption were conducted. The helicoid morphologies that consist of highly twisted chiral elements were carefully characterized by high-resolution imaging techniques using electron microscopy and helium ion microscopy. The chiral structure of helicoid nanoparticle belongs to the 432-symmetry group and contain opposite rotation in single nanoparticle, which is achieved for the first time in plasmonic nanostructure. The insights from this research will increase the fundamental understanding of chirality transfer phenomena and aid in development of the artificial chirality in plasmonic metamaterials.

In Chapter 5, the optical properties of chiral helicoid nanoparticles were studied. In the first part of this chapter, we studied the theoretical consideration for optical and chiroptical property of metallic nanomaterial. To describe the electromagnetic response of chiral plasmonic material, chiral analogue of plasmon hybridization model was briefly explained. In comparison with collective chiral assembly, we highlighted the strong chiroptical response of the continuous chiral geometry. In the latter part of this chapter, we discussed the chiroptical property of chiral helicoid nanostructures. 432-helicoid nanoparticles showed strong optical dissymmetry with g-factor of 0.2 at visible wavelengths. Using numerical simulation, we found that the underlying mechanism of strong optical dissymmetry was strong chiral plasmonic resonance occurring at the chiral gap structure. By adjusting geometrical parameter in simulation, design of helicoid geometry with the strongest optical dissymmetry was studied. As a practical optical application, a dynamic modulation of transmission color in wide range was demonstrated on the basis of the wavelength-dependent polarization rotation ability of helicoid nanoparticles. This intriguing chiroptical response can be further controlled by the post-synthesis metal

deposition strategy. Formation of the plasmonic metal thin-film on the substrate and helicoid nanoparticle enabled a dramatic spectral tuning for the chiroptical response. We believe that 432-helicoid nanoparticle will aid in the rational design of three-dimensional chiral nanostructures for use in advanced optical applications such as chiral sensing, display, and encryption technology.

1.6 Bibliography

1. Maier, S. A. *Plasmonics: Fundamentals and Applications*; Springer US: New York, NY, 2007.
2. Joannopoulos, J. D.; Johnson, S. G.; Winn, J. N.; Meade, R. D.; Sjödaahl, C. J. *Photonic Crystals: Molding the Flow of Light*; Princeton University Press: Princeton, 2011.
3. Gramotnev, D. K.; Bozhevolnyi, S. I. Nanofocusing of Electromagnetic Radiation. *Nat. Photonics* **2014**, *8* (1), 13–22.
4. Schuller, J. A.; Barnard, E. S.; Cai, W.; Jun, Y. C.; White, J. S.; Brongersma, M. L. Plasmonics for Extreme Light Concentration and Manipulation. *Nat. Mater.* **2010**, *9* (3), 193–204.
5. Parker, A. R.; Townley, H. E. Biomimetics of Photonic Nanostructures. *Nat. Nanotechnol.* **2007**, *2* (6), 347–353.
6. Vukusic, P.; Sambles, J. R. Photonic Structures in Biology. *Nature* **2003**, *424* (6950), 852–855.
7. Zi, J.; Yu, X.; Li, Y.; Hu, X.; Xu, C.; Wang, X.; Liu, X.; Fu, R. Coloration Strategies in Peacock Feathers. *Proc. Natl. Acad. Sci.* **2003**, *100* (22), 12576–12578.
8. Sharma, V.; Crne, M.; Park, J. O.; Srinivasarao, M. Structural Origin of Circularly Polarized Iridescence in Jeweled Beetles. *Science* **2009**, *325* (5939), 449–451.
9. Blaaderen, A. v. MATERIALS SCIENCE:Opals in a New Light. *Science* **1998**, *282* (5390), 887–888.
10. Zhao, Y.; Xie, Z.; Gu, H.; Zhu, C.; Gu, Z. Bio-Inspired Variable Structural Color Materials. *Chem. Soc. Rev.* **2012**, *41* (8), 3297.
11. Baba, T. Slow Light in Photonic Crystals. *Nat. Photonics* **2008**, *2* (8), 465–473.
12. Altug, H.; Englund, D.; Vučković, J. Ultrafast Photonic Crystal Nanocavity Laser. *Nat. Phys.* **2006**, *2* (7), 484–488.
13. Almeida, V. R.; Barrios, C. A.; Panepucci, R. R.; Lipson, M. All-Optical Control of Light on a Silicon Chip. *Nature* **2004**, *431* (7012), 1081–1084.

14. Coronado, E. A.; Encina, E. R.; Stefani, F. D. Optical Properties of Metallic Nanoparticles: Manipulating Light, Heat and Forces at the Nanoscale. *Nanoscale* **2011**, *3* (10), 4042.
15. Goh, X. M.; Zheng, Y.; Tan, S. J.; Zhang, L.; Kumar, K.; Qiu, C.-W.; Yang, J. K. W. Three-Dimensional Plasmonic Stereoscopic Prints in Full Colour. *Nat. Commun.* **2014**, *5* (1), 5361.
16. Wang, L.; Li, T.; Guo, R. Y.; Xia, W.; Xu, X. G.; Zhu, S. N. Active Display and Encoding by Integrated Plasmonic Polarizer on Light-Emitting-Diode. *Sci. Rep.* **2013**, *3* (1), 2603.
17. Ellenbogen, T.; Seo, K.; Crozier, K. B. Chromatic Plasmonic Polarizers for Active Visible Color Filtering and Polarimetry. *Nano Lett.* **2012**, *12* (2), 1026–1031.
18. Yu, L.; Liu, G. L.; Kim, J.; Mejia, Y. X.; Lee, L. P. Nanophotonic Crescent Moon Structures with Sharp Edge for Ultrasensitive Biomolecular Detection by Local Electromagnetic Field Enhancement Effect. *Nano Lett.* **2005**, *5* (1), 119–124.
19. Wang, Q.; Liu, L.; Wang, Y.; Liu, P.; Jiang, H.; Xu, Z.; Ma, Z.; Oren, S.; Chow, E. K. C.; Lu, M.; et al. Tunable Optical Nanoantennas Incorporating Bowtie Nanoantenna Arrays with Stimuli-Responsive Polymer. *Sci. Rep.* **2016**, *5* (1), 18567.
20. Willets, K. A.; Van Duyne, R. P. Localized Surface Plasmon Resonance Spectroscopy and Sensing. *Annu. Rev. Phys. Chem.* **2007**, *58* (1), 267–297.
21. Rodríguez-Lorenzo, L.; Álvarez-Puebla, R. A.; Pastoriza-Santos, I.; Mazzucco, S.; Stéphan, O.; Kociak, M.; Liz-Marzán, L. M.; García de Abajo, F. J. Zeptomol Detection Through Controlled Ultrasensitive Surface-Enhanced Raman Scattering. *J. Am. Chem. Soc.* **2009**, *131* (13), 4616–4618.
22. Anger, P.; Bharadwaj, P.; Novotny, L. Enhancement and Quenching of Single-Molecule Fluorescence. *Phys. Rev. Lett.* **2006**, *96* (11), 113002.
23. Ford, G. W.; Weber, W. H. Electromagnetic Interactions of Molecules with Metal Surfaces. *Phys. Rep.* **1984**, *113* (4), 195–287.
24. Ni, X.; Wong, Z. J.; Mrejen, M.; Wang, Y.; Zhang, X. An Ultrathin Invisibility Skin Cloak for Visible Light. *Science* **2015**, *349* (6254), 1310–1314.

25. Shalaev, V. M. Optical Negative-Index Metamaterials. *Nat. Photonics* **2007**, *1* (1), 41–48.
26. Zhang, S.; Fan, W.; Malloy, K. J.; Brueck, S. R. J.; Panoiu, N. C.; Osgood, R. M. Demonstration of Metal-Dielectric Negative-Index Metamaterials with Improved Performance at Optical Frequencies. *J. Opt. Soc. Am. B* **2006**, *23* (3), 434.
27. Dolling, G.; Enkrich, C.; Wegener, M.; Soukoulis, C. M.; Linden, S. Low-Loss Negative-Index Metamaterial at Telecommunication Wavelengths. *Opt. Lett.* **2006**, *31* (12), 1800.
28. Shalaev, V. M.; Cai, W.; Chettiar, U. K.; Yuan, H.-K.; Sarychev, A. K.; Drachev, V. P.; Kildishev, A. V. Negative Index of Refraction in Optical Metamaterials. *Opt. Lett.* **2005**, *30* (24), 3356.
29. Pendry, J. B. Negative Refraction Makes a Perfect Lens. *Phys. Rev. Lett.* **2000**, *85* (18), 3966–3969.
30. Pendry, J. B. Controlling Electromagnetic Fields. *Science* **2006**, *312* (5781), 1780–1782.
31. Pasteur, L. Recherches Sur Les Propriétés Spécifiques Des Deux Acides Qui Composent l'acide Racémique. *Ann. Chim. Phys. Sér.* **1848**, *3*, 442–459.
32. Gansel, J. K.; Thiel, M.; Rill, M. S.; Decker, M.; Bade, K.; Saile, V.; von Freymann, G.; Linden, S.; Wegener, M. Gold Helix Photonic Metamaterial as Broadband Circular Polarizer. *Science* **2009**, *325* (5947), 1513–1515.
33. Pendry, J. B. A Chiral Route to Negative Refraction. *Science* **2004**, *306* (5700), 1353–1355.
34. Plum, E.; Zhou, J.; Dong, J.; Fedotov, V. A.; Koschny, T.; Soukoulis, C. M.; Zheludev, N. I. Metamaterial with Negative Index Due to Chirality. *Phys. Rev. B* **2009**, *79* (3), 035407.
35. Zhang, S.; Park, Y.-S.; Li, J.; Lu, X.; Zhang, W.; Zhang, X. Negative Refractive Index in Chiral Metamaterials. *Phys. Rev. Lett.* **2009**, *102* (2), 023901.
36. Narushima, T.; Okamoto, H. Circular Dichroism Nano-Imaging of Two-Dimensional Chiral Metal Nanostructures. *Phys. Chem. Chem. Phys.* **2013**, *15* (33), 13805.
37. Schäferling, M.; Yin, X.; Engheta, N.; Giessen, H. Helical Plasmonic

- Nanostructures as Prototypical Chiral Near-Field Sources. *ACS Photonics* **2014**, *1* (6), 530–537.
38. Tang, Y.; Cohen, A. E. Optical Chirality and Its Interaction with Matter. *Phys. Rev. Lett.* **2010**, *104* (16), 163901.
 39. Hendry, E.; Carpy, T.; Johnston, J.; Popland, M.; Mikhaylovskiy, R. V.; Laphorn, A. J.; Kelly, S. M.; Barron, L. D.; Gadegaard, N.; Kadodwala, M. Ultrasensitive Detection and Characterization of Biomolecules Using Superchiral Fields. *Nat. Nanotechnol.* **2010**, *5* (11), 783–787.
 40. Zheng, G.; Mühlenbernd, H.; Kenney, M.; Li, G.; Zentgraf, T.; Zhang, S. Metasurface Holograms Reaching 80% Efficiency. *Nat. Nanotechnol.* **2015**, *10* (4), 308–312.
 41. Yu, N.; Genevet, P.; Kats, M. A.; Aieta, F.; Tetienne, J.-P.; Capasso, F.; Gaburro, Z. Light Propagation with Phase Discontinuities: Generalized Laws of Reflection and Refraction. *Science* **2011**, *334* (6054), 333–337.
 42. Karimi, E.; Schulz, S. A.; De Leon, I.; Qassim, H.; Upham, J.; Boyd, R. W. Generating Optical Orbital Angular Momentum at Visible Wavelengths Using a Plasmonic Metasurface. *Light Sci. Appl.* **2014**, *3* (5), e167–e167.
 43. Liu, Z.; Du, H.; Li, J.; Lu, L.; Li, Z.-Y.; Fang, N. X. Nano-Kirigami with Giant Optical Chirality. *Sci. Adv.* **2018**, *4* (7), eaat4436.
 44. Soukoulis, C. M.; Wegener, M. Past Achievements and Future Challenges in the Development of Three-Dimensional Photonic Metamaterials. *Nat. Photonics* **2011**, *5* (9), 523–530.
 45. Duan, X.; Kamin, S.; Sterl, F.; Giessen, H.; Liu, N. Hydrogen-Regulated Chiral Nanoplasmonics. *Nano Lett.* **2016**, *16* (2), 1462–1466.
 46. Traub, M. C.; Longsine, W.; Truskett, V. N. Advances in Nanoimprint Lithography. *Annu. Rev. Chem. Biomol. Eng.* **2016**, *7* (1), 583–604.
 47. Burckel, D. B.; Wendt, J. R.; Ten Eyck, G. A.; Ellis, A. R.; Brener, I.; Sinclair, M. B. Fabrication of 3D Metamaterial Resonators Using Self-Aligned Membrane Projection Lithography. *Adv. Mater.* **2010**, *22* (29), 3171–3175.
 48. Stöber, W.; Fink, A.; Bohn, E. Controlled Growth of Monodisperse Silica Spheres in the Micron Size Range. *J. Colloid Interface Sci.* **1968**, *26* (1), 62–69.
 49. Hinman, J. G.; Stork, A. J.; Varnell, J. A.; Gewirth, A. A.; Murphy, C. J.

- Seed Mediated Growth of Gold Nanorods: Towards Nanorod Matryoshkas. *Faraday Discuss.* **2016**, *191*, 9–33.
50. Quan, Z.; Wang, Y.; Fang, J. High-Index Faceted Noble Metal Nanocrystals. *Acc. Chem. Res.* **2013**, *46* (2), 191–202.
 51. Bakr, O. M.; Wunsch, B. H.; Stellacci, F. High-Yield Synthesis of Multi-Branched Urchin-Like Gold Nanoparticles. *Chem. Mater.* **2006**, *18* (14), 3297–3301.
 52. Zhang, H.; Jin, M.; Xia, Y. Noble-Metal Nanocrystals with Concave Surfaces: Synthesis and Applications. *Angew. Chem. Int. Ed.* **2012**, *51* (31), 7656–7673.
 53. Wang, X.; Feng, J.; Bai, Y.; Zhang, Q.; Yin, Y. Synthesis, Properties, and Applications of Hollow Micro-/Nanostructures. *Chem. Rev.* **2016**, *116* (18), 10983–11060.
 54. You, H.; Fang, J. Particle-Mediated Nucleation and Growth of Solution-Synthesized Metal Nanocrystals: A New Story beyond the LaMer Curve. *Nano Today* **2016**, *11* (2), 145–167.
 55. Guisbiers, G.; José-Yacamán, M. Use of Chemical Functionalities to Control Stability of Nanoparticles. In *Encyclopedia of Interfacial Chemistry*; Elsevier, 2018; pp 875–885.
 56. Shibasaki, Y.; Shimizu, M.; Kuroda, R. Body Handedness Is Directed by Genetically Determined Cytoskeletal Dynamics in the Early Embryo. *Curr. Biol.* **2004**, *14* (16), 1462–1467.
 57. Lebreton, G.; Géminard, C.; Lapraz, F.; Pyrpassopoulos, S.; Cerezo, D.; Spéder, P.; Ostap, E. M.; Noselli, S. Molecular to Organismal Chirality Is Induced by the Conserved Myosin 1D. *Science* **2018**, *362* (6417), 949–952.
 58. Wang, J.-S.; Wang, G.; Feng, X.-Q.; Kitamura, T.; Kang, Y.-L.; Yu, S.-W.; Qin, Q.-H. Hierarchical Chirality Transfer in the Growth of Towel Gourd Tendrils. *Sci. Rep.* **2013**, *3* (1), 3102.

Chapter 2. Biomolecular Pathway for Inorganic

Chirality

2.1 Introduction

The three-dimensional (3D) chirality has previously existed in only organic molecules and bio-organisms, but now it is adapted to the nanophotonics and plasmonics field, raising an extra degree of freedom to control light. Recently, efforts have been made to create plasmonic nanostructures with chiral geometries. Top-down fabrication processes exemplified by electron beam lithography, glancing angle deposition, and direct laser writing provides ways to incorporate chiral structures into plasmonic materials.^{1,2} Although the fabrication of chiral plasmonic nanostructures is an active area of research, strategies for the direct fabrication of single chiral particles are limited due to the difficulty in controlling the shape of the particles with nanometer-scale precision. On the other hand, the biomolecule-assisted strategies can provide elaborate spatial control and flexibility as well as new chiral geometries. As a representative strategy, the biomolecule-enabled assembly has a considerable advantage for handling 3D chiral nanostructure as biomolecules are superior to constructing asymmetric geometry. In addition, nanoscale control over the position of building blocks can be achieved by utilizing a programmable sequence of peptide or DNA. Remarkably, the entire process of biomolecule-enabled assembly can be spontaneously performed in solution phase, providing a capability for large scale production. Representative structures such as helical assemblies of protein, twisted angle imposed by peptide interaction, and asymmetric tetramer provided by DNA origami enable the fabrication of 3D chiral geometries of

nanoparticle ensembles through bio-templates, giving rise to strong optical activity (Figure 2.1).

In plasmonic nanoparticle assemblies, plasmonic coupling occurs between adjacent particles, and this coupling imparts complex near- and far-field optical properties, distinct from those of the individual nanoparticles. As many previous studies have pointed out, plasmonic coupling in nanoparticle assemblies is extremely sensitive to the geometrical parameters, such as the size, shape, spatial separation, and arrangement of the constituent nanoparticles.³⁻⁵ Notably, for assemblies with a non-centrosymmetric geometry, there is a strong correlation between the plasmonic coupling and the polarization direction of the incident light used to excite a specific resonance mode. For example, when 1D chain-like assemblies were subjected to linear polarization, strong plasmonic coupling and enhanced near-field were developed in the case where the polarization axis was fitted with the aligned direction of the nanoparticles. Likewise, plasmonic nanoparticle assemblies with chiral spatial arrangements exhibit different optical responses with respect to the handedness of circularly polarized light (CPL) at the visible frequency (Figure 2.2a). According to the theoretical model, this optical activity of chiral plasmonic assemblies arises from Coulombic interactions among the constituent nanoparticles, which splits the resonance into collective bonding and anti-bonding modes (Figure 2.2b).⁶⁻⁸ To excite these chiral collective modes, the arrangement of dipole moments in each resonance mode must be fitted to the direction of the rotating vector in the circularly polarized light. Therefore, the resulting asymmetric interaction with LCP and RCP leads to a chiroptical response of the chiral plasmonic assembly. In this sense, precise control of the chiral plasmonic assembly can be used to manipulate the overall chiroptical response, and further, to enable unique optical applications.

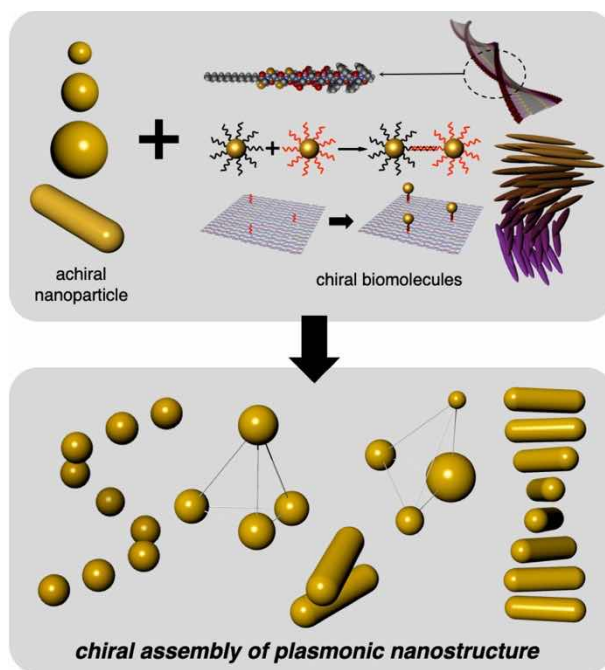


Figure 2.1 Integration of chiral biomolecules and achiral plasmonic building blocks into the chiral assembled nanostructures.

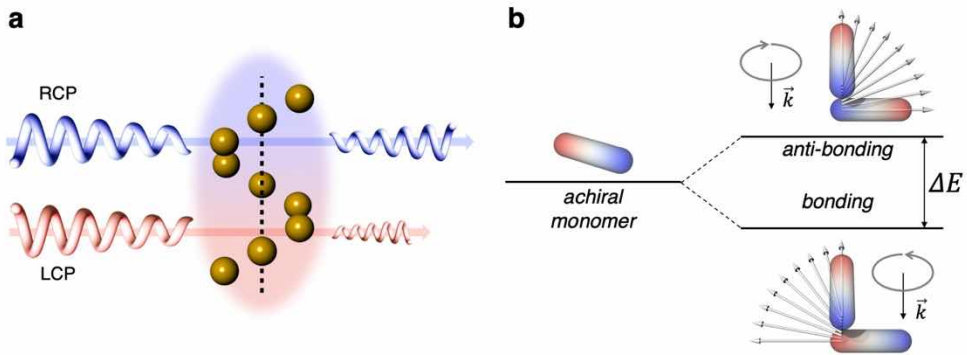


Figure 2.2 Chiroptical response of chiral plasmonic assembly. (a) Schematic showing asymmetric circularly polarized light absorption of chiral material. (b) Illustration of the plasmon hybridized model with the corresponding vector orientation of light. Different bonding and anti-bonding modes with split energy levels are created by plasmon coupling between two nanorods. The two different modes can be selectively excited by left or right circularly polarized light.

Continuously connected 3D chiral morphology, rather than a chiral ensemble of achiral morphology, can amplify the plasmonic chiroptical responses. The strong chiroptical response of continuous chiral plasmonic nanostructures came from the contribution of multiple resonance modes,⁹ which is distinct from that of chiral assembly attributed to the dipolar Coulombic interactions between building blocks.⁸ In addition to the optical retardation effect, structural instability of conjugated molecules in various environments such as organic solvent, biofluid with high ionic strength, and dried condition, can be problematic for the future application. As an alternative chiral nanostructure, the continuous chiral structure is more advantageous in terms of structural stability and stronger chiroptical signal. However, the fabrication of continuous chiral structures using inorganic material remains a challenge. Although intrinsic chiral morphology at the single-particle level had been reported first on micrometer-sized biomineral precipitates (Figure 2.3a)^{10,11} and a few nanomaterials with chiral crystal structures (Figure 2.3b),^{12,13} chirality evolution in plasmonic materials has never been achieved at the nanometer range.

In this regard, nature's strategy for chirality evolution offers important lessons for understanding the process of intrinsically forming and changing chirality in artificial systems. Even though the process of forming asymmetry and chirality is complex and involves multiscale origins in biological systems, one convincing explanation is that the chirality of a microscopic unit produces collective chirality in a higher-order structure.¹⁴⁻¹⁷ In this description, the chiral encoder at the molecular scale, from the chiral center in small molecules to the higher-order structures of biomacromolecules, can induce chirality in a cell by mediating the asymmetric interaction. Subsequently, the chiral encoders at various biological scales can lead to the asymmetric structure of organisms via continuous and transient actions on growth. For example, the left-right asymmetry in a spiral-shaped organism such as snails and gastropods are derived from spiral cleavage during early embryonic

development. Cytoskeletal structures in blastomeres, called mitotic spindles, are slanted clockwise in the four-cell stage, and a twisted arrangement of cells occurs in the following eight-cell stage (Figure 2.4a).¹⁸ Furthermore, a recent biological study on the left-right asymmetry of *Drosophila* highlighted the importance of the molecular motor myosin 1D, which generates chirality from the molecular level to the asymmetry in the organism and their behavior (Figure 2.4b).¹⁹ The asymmetry emerges from the chiral interaction of myosin 1D and F-actin, which mediate the counterclockwise circular gliding of the actin filaments. The chirality encoded at the molecular level continuously induces the directional twisting of cells, single organs, and the whole body of the organism (Figure 2.4c). Several key features that we can learn from biological examples are: 1) hierarchical assembly that results in macroscopic chirality, 2) molecular encoders that play a role in multiple scales, and 3) time-dependent development that gradually induces chirality. In this chapter, the biomolecular strategy for inorganic chirality from collective chiral ensemble to the intrinsic chirality evolution are presented.

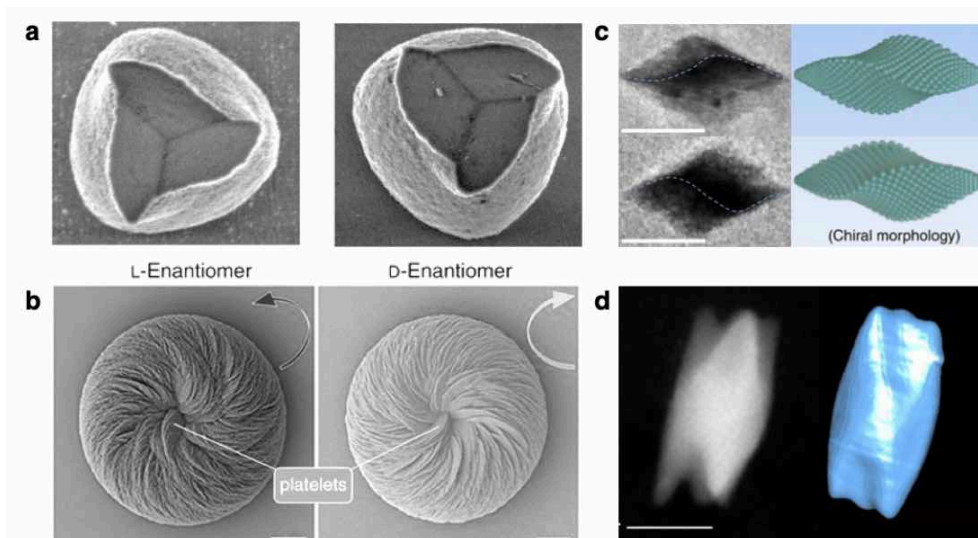


Figure 2.3 Intrinsic chiral morphology. (a) SEM images of chiral calcite microcrystal precipitated in the presence of L- or D-tartaric acid. (b) SEM images of chiral vaterite microcrystal precipitated in the presence of L- or D-cysteine. (c) TEM image and corresponding model of colloidal cinnabar (α -HgS) nanocrystals showing different twisting orientation depending on the chirality of penicillamine ligand. (d) Dark-field STEM image and tomography of colloidal chiral tellurium nanocrystal.

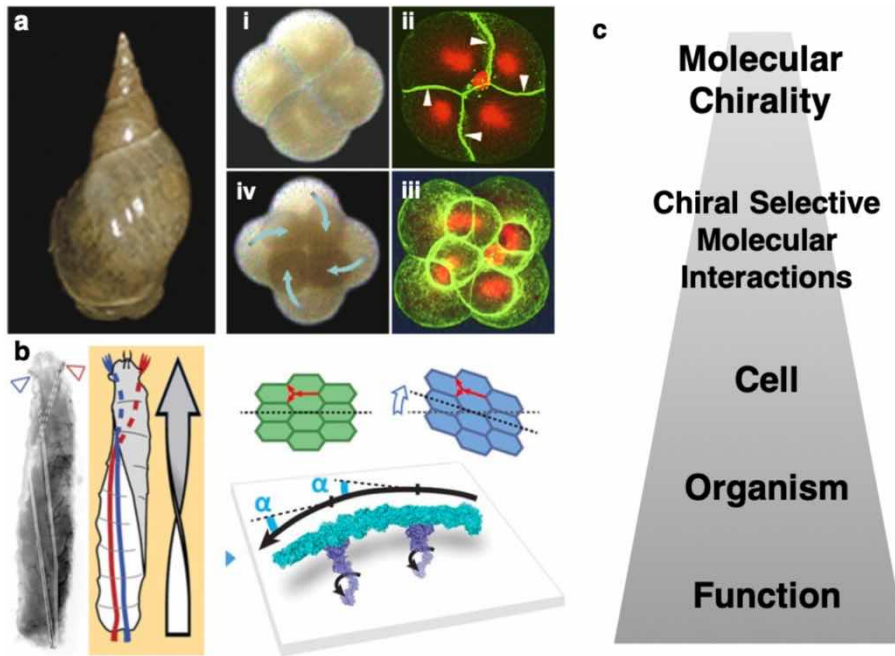


Figure 2.4 Formation of Chirality in Biology. (a) Helical *L. stagnalis* (left) and their embryos (right). Optical microscope and 3D-reconstruction image of dextral embryos and third cleavage in (i) four-cell stage, (ii) metaphase-anaphase, (iii) telophase, (iv) eight-cell stage. (b) Directional twisting of the whole body and cell arrangement of *Drosophila* lava as a result of actin filament gliding powered by Myo1D. (c) Model of chirality formation across multiple organization scales.

2.2 Biomolecule-enabled chiral assembly

2.2.1 Chiral nanostructures based on peptide assembly

Peptides, oligomeric or polymeric biomolecules composed of amino acid chains, have been considered as viable candidates for the formation of chiral plasmonic nanostructured materials. The sequence of the constituent amino acids significantly influences the properties of the peptide and can be engineered to produce unique self-assemblies, such as amyloid structures, alpha-helical coiled-coil, and peptide amphiphile assemblies.^{20,21} During the self-assembly process, the innate chirality of the peptides directs their stereochemical configurations, which strongly influences the formation of the chiral nanostructures.²² Notably, peptides can be employed for recognizing and generating inorganic materials,²³ and this strategy allows the inorganic building blocks to replicate the chiral arrangement of the peptide-templated nanostructures. In this regard, peptide-based materials can provide a route for the rational design of chiral plasmonic nanostructures.

Smallest building blocks of a biological entity, such as amino acids and oligopeptides, can be used to render optical activity in plasmonic nanoparticle assemblies. Despite the size mismatch between these small biomolecules and plasmonic nanoparticles, several recent studies have reported chiroptical responses of plasmonic nanoparticle oligomers with biomolecules such as cysteine and glutathione. Ma and coworkers reported that for the assembly of anisotropic nanoparticle, the small dihedral angle between adjacent nanoparticles can break the symmetry of side-by-side assembly, which is a source of chirality.²⁴ In this context, Wu and coworkers developed Au NRs oligomer with chiral configuration by cysteine-induced symmetry breaking (Figure 2.5a).²⁵ Due to the cooperative

interaction of the cysteine and the surfactant bilayer, twisted conformation and resulting chiroptical signal was developed. In addition to the small amino acid, Liu and coworkers demonstrated that a helical glutathione (GSH) oligomer, i.e., a tripeptide with the γ Glu-Cys-Gly sequence, led to the end-to-end assembly of Au NRs with a chiral configuration (Figure 2.5b).²⁶ Formation of the helical glutathione oligomer, expedited by the hydrophobic confinement of the surfactant micelle, induced the formation of a right-handed or left-handed end-to-end crossed assembly depending on the chirality of glutathione. A helical assembly of gold nanoparticles (Au NPs) was first demonstrated by Wang and coworkers, based on a self-assembling peptide scaffold using de novo designed T1 peptide (with the RGYFWAGDYNYF sequence) (Figure 2.5c).²⁷ Electrostatic interaction of positively charged T1 nanofibril and a negatively charged Au NPs forms the precipitates comprised of a self-assembled nanostructure from the single to double-helical arrays. More systematically, the computational sequence design and screening for peptide self-assembly was successfully employed to construct a virus-like helical scaffold, and subsequently, a helical assembly of Au NPs (Figure 2.5d).²⁸

Peptide amphiphiles (PA), particularly alkyl-chain terminated lipopeptides, can provide greater systematic control of the peptide-based scaffold for helical assemblies of inorganic materials. General molecular structure of PA consists of a self-assembling domain and a recognition domain,^{29,30} which control the overall structures of the hierarchical assemblies³¹ and the incorporate nanoparticles into the scaffold,^{30,32} respectively. The explicit roles of each domain that coexist in the peptide amphiphile monomer can facilitate the formation of complex nanostructures, including helical geometries. Several studies have reported plasmonic helical nanostructures obtained via the PA-based platform.³³⁻³⁸ Rosi and co-workers adopted the alkyl-chain terminated oligopeptide, C₁₁H₂₃-AYSSGAPPMPF (C₁₂-PEP_{Au}), in the construction of a highly ordered double-helical array superstructure

of Au NPs (Figure 2.6a).³³ The AYSSGAPPMPF (PEP_{Au}) peptide strongly interact with an Ag and Au,³⁹ and specific AYSS segment attributed to the beta-sheet formation and subsequently supramolecular twisted ribbon morphology. Reaction parameters, additives, aliphatic chain length, and absolute configuration were manipulated for the tailored helical pitch, interparticle spacing, and handedness of helix.³⁴⁻³⁶ Furthermore, partial oxidation of functional groups produced a single-helical ordering rather than a double-helix (Figure 2.6b).³⁷ As a derivative of PA, an amphiphilic nucleobase-peptide conjugate (NPC) with amyloid-like diphenylalanine moiety was also adopted to induce the helical assembly of plasmonic NPs (Figure 2.6c).³⁸

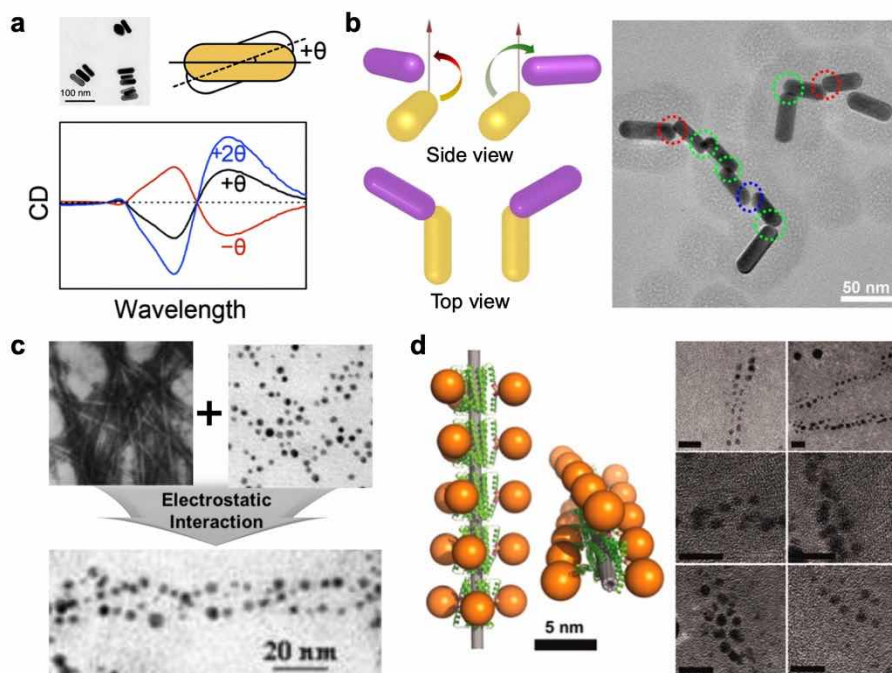


Figure 2.5 Peptide enabled chiral assembly. (a) TEM image and corresponding CD spectra of twisted gold nanorods oligomers generated by cysteine. (b) Self-assembled chiral gold nanorods induced by L-GSH or D-GSH and TEM image of the assembled nanochains coated with SiO₂ shells. (c) TEM images of T1 fibril biomolecules and gold nanoparticles (top) and the helical assemblies fabricated by electrostatically attaching the NPs onto fibrils (bottom) (d) Model and TEM images of the assembled gold nanoparticles through Cys-modified domain-swapped helical protein (DSD)-Gly hexamers on single-walled carbon nanotubes.

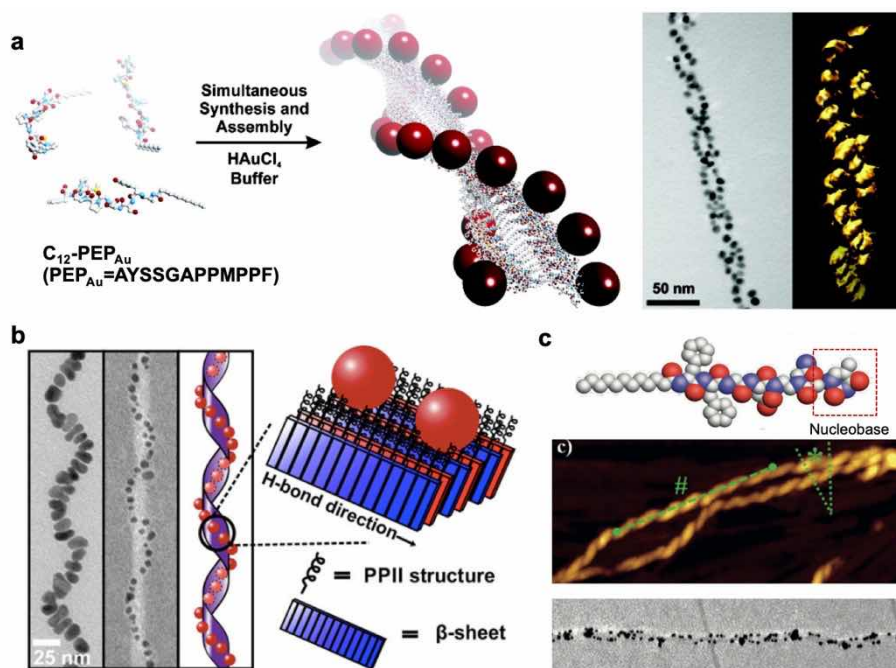


Figure 2.6 Peptide amphiphile template for chiral plasmonic nanostructure. (a) Double helical left-handed gold nanoparticles assembly templated by C_{12} -PEP_{Au} amphiphile peptides. TEM and electron tomography of enantiomeric gold nanoparticles double helices prepared by C_{12} -D-PEP_{Au} and C_{12} -L-PEP_{Au} templating. (b) TEM images and model of chiral NP assemblies templated via C_{18} -(PEP_{Au}M-ox)₂ superstructures with helical ribbon geometry. (c) Helical arrangement of NPs based on self-assembled nucleobase-peptide conjugates (NPCs).

2.2.2 DNA templates for chiral assembly of plasmonic nanostructures

DNA nanotechnology is a powerful tool for fabricating exquisite nanostructures.⁴⁰⁻⁴³ By taking advantage of the hybridization capability of the DNA scaffold, NPs could be treated as artificially engineered atoms that can be constructed into complex structures, analogous to organic molecule synthesis. With this excellent platform, various design concepts and methodologies initially developed for DNA nanotechnology have been successfully extended to metallic nanostructure systems. The optical activity can be achieved in materials by incorporating various structural features, such as twisted constituents, asymmetric tetramers, spirals, and helical structures. Specifically, breaking the geometrical symmetry is considered as the first step in achieving chiroptical properties as the CD response originates from non-equivalent light-matter coupling under LCP and RCP. In this regard, DNA technology, which is effective for constructing predesigned nanoarchitectures, provides a viable route for accomplishing asymmetric chiral structures.

The complementary pairing of DNA provides considerable advantages in the construction of nanostructures by offering programmability with predictable geometry. Kotov and coworkers suggested the potential of DNA-NP conjugates for chiral assemblies⁴⁴ utilizing direct polymerase chain reaction (PCR) on the surface of the Au NPs. The Au NPs are connected by complementary pairing, and various chiral structures, such as dimers, trimers, tetramers, superstructures, and heterochains were generated.⁴⁴⁻⁴⁶ Similarly, premade single-stranded DNA was also used to construct the chiral tetrahedron structure of R or S configuration instead of PCR(Figure 2.7a).^{47,48} For this tetrahedral structure, it was revealed that all NP

constituents contribute to the chiroptical activity and provided a route for tuning the chiroptical bands. In addition, chirogenesis in plasmonic nanostructures can also be accomplished with simple, twisted anisotropic building blocks.^{24,49} The two Au NRs were assembled into a side-by-side arrangement and conformational torsion of the two adjacent NRs was imposed by the DNA trigger.²⁴ In an extension of this study, heterodimer structure comprising AuNRs and ellipsoidal NPs was utilized to achieve chiral structure (Figure 2.7b).⁴⁹ In addition to tetramers and twist structures, various innovative nanostructures have also been demonstrated, such as a heterogeneous core–satellite, Au or Ag shell-coated DNA-bridged dimers, Ag core–Au shell tetramers, and propeller-like AuNRs-upconversion nanoparticle structures.^{50–53} The unique ability of DNA to reversibly de-hybridize and re-hybridize makes it an attractive tool for biosensor research.^{54,55} Because only the asymmetrically coupled plasmonic nanoparticles in close proximity in the nanostructure give rise to a CD response, the conjugated nanoparticle can act as an optical transducer for conformational change via reconfiguration or dissociation of the DNA frame. Using this concept, detection of 3.4 aM DNA and 0.073 fmol/10 µg miRNA was reported, where the detection limit was significantly enhanced relative to that of other conventional techniques.^{54,55}

The recognition and assembly properties of DNA scaffolds have been utilized to fabricate more complex architectures.^{56,57} The DNA structuring process with several types of designed motifs leads to two-dimensional tile structures, which further developed into well-defined DNA polyhedral or hierarchical 3D nanostructures.⁴² Yan and coworkers rationally designed nanotubes for a variety of 3D chiral nanostructures (Figure 2.7c).⁵⁸ DNA tiles, consisting of a long array of repeating planar double-crossover tiles, are used to construct a helical assembly of nanoparticles on a tubular structure. Gold nanoparticles were conjugated on the first DNA tile and a stem-loop structure that provides steric counterbalance was located

in the third tile. Depending on the degree of twisting of the nanotube, nanoparticle assemblies with a ring, single spiral, double spiral, and multiple nested spiral configurations were created. As an alternative strategy for helix formation, Willner and coworkers utilized a different scaffold comprising self-assembled DNA barrels to create helical assemblies.⁵⁹ The plasmonic helical assembly was produced by the conjugation of gold nanoparticle at the tethering strands, which exhibited a typical peak-dip (bisignate) signal in the visible region of the CD spectrum.

In comparison with the tile assembly method, scaffolded DNA origami has been shown to provide more precisely controlled geometric structures.⁴³ With the periodic crossover of several short DNA strands on the single-stranded viral DNA, the DNA scaffold can be folded into predesigned nanostructures. Ding and coworkers used 2D rectangular origami block to construct 3D helical nanostructure.⁶⁰ By taking advantage of the addressable binding sites in DNA origami, two linear chains of nanoparticles diagonally aligned. Then, subsequent rolling and stapling of the block produced tubular scaffolds with a helicoid array of NPs. As another approach that uses a rectangular origami block, the asymmetric tetrahedral arrangement was demonstrated by utilizing both sides of the origami as binding sites for Au NPs (Figure 2.8a).⁶¹ The relative position of single NP on bottom-side to the top-side NPs can be precisely determined by the sequence engineering, which provides a versatile platform for the true structure-related chiroptical property. In a further study by Dai et al., the size and distance between spherical nanoparticles of an asymmetric tetramer were specifically modulated to systematically engineer the chiral optical properties.⁶² Stacking rectangular origami blocks is advantageous for assembling large anisotropic nanostructures. Wang and coworkers formed numerous Au NRs assemblies by employing precisely designed bifacial DNA origami scaffolds, from the twisted patterns of Au NRs dimer (Figure 2.8b) to the helical arrangement of oligomers (Figure 2.8c).^{63,64}

Recently, another approach Shen et al. employed bifacial origami to further construct heterogeneous AuNR@AuNP helices by winding the origami around the Au NR and attaching eight Au NPs on the same origami.⁶⁵ DNA helix bundles is another class of stable DNA origami structure, which can be adapted to create well-defined helical plasmonic structures. Liedl and coworkers utilized 24-helix bundles designed to provide 9 helical decoration sites (Figure 2.9a).^{66,67} Gold nanoparticles with a diameter of 10 nm were attached along with the DNA template through linker strands and finally constructed helical assembly of plasmonic nanoparticles with 2-nm precision and high yield. The helical nanostructure gave rise to a strong characteristic bisignate CD peak centered around the plasmonic resonance frequency. Importantly, in this research, optical rotatory dispersion of the nanohelices was first visualized in a macroscopic optical polarization experiment. Opposite color changes in solutions containing left-handed and right-handed nanohelices were clearly manifested under polarization-resolved transmission conditions. In an extension of this study, Urban et al. reported the hierarchical assembly of DNA origami-based Au nanohelices into toroidal geometry. They utilized curved helix bundle as monomers, and four origami monomers were joined to create a complete DNA origami ring with helical NP binding.⁶⁸ Gang and coworkers reported the novel design of octahedral DNA frames based on a 6-helix bundle with six independent binding sites to produce chiroptical response.⁶⁹

The unique feature of consecutive hybridization and dehybridization of DNA offers exciting opportunities to impart reconfigurability to the nanosystems controlled by DNA input. Kuzyk et al. presented reconfigurable 3D chiral plasmonic nanostructure which is powered by DNA (Figure 2.9b).⁷⁰ In this approach, two Au NRs were located on two different 14-helix bundles, where the intermediate point was tied by a flexible linker and each end of the helix bundle has a locking moiety. Sequential hybridization and dehybridization of the DNA locks permitted reversible

manipulation of the absolute configuration and generated a characteristic CD peak with on or off cycling. On the basis of the similar constructional design, various programmed active plasmonic systems were further demonstrated via modification of DNA trigger by the same group.^{71,72} Another dynamic manipulation of the plasmonic system called "plasmonic walker" was also achieved by Liu and coworkers.⁷³ In this system, sequential detaching and attaching process along the track of the binding site makes the AuNR roll, making fully tunable optical responses.

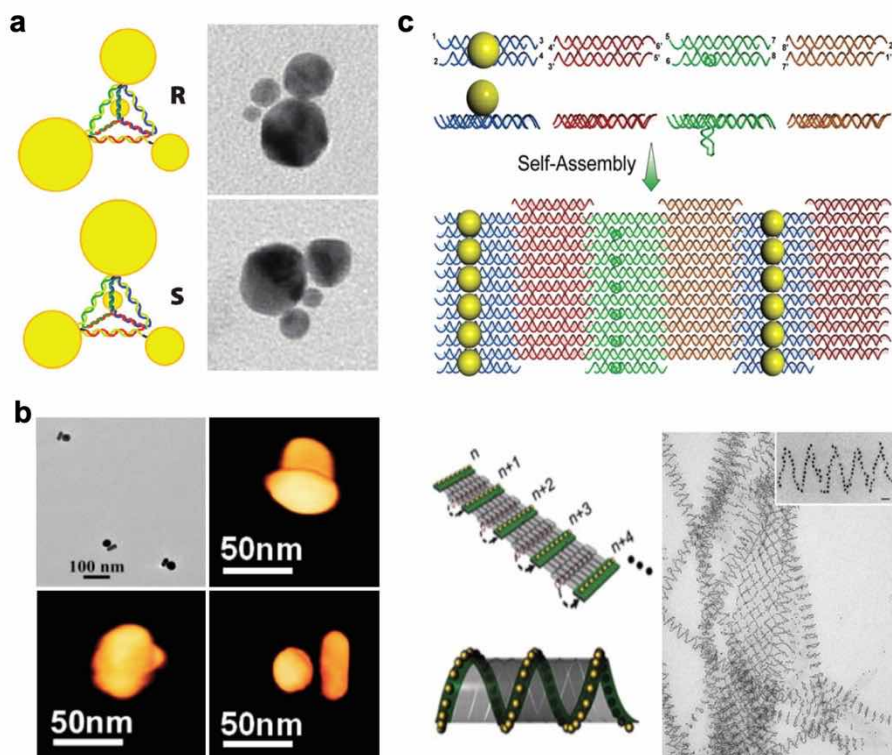


Figure 2.7 Chiral assembly based on DNA linker and tile. (a) Schematic models and TEM images of enantiomeric plasmonic pyramid assemblies. (b) TEM and 3D TEM tomography images of the (-) enantiomer of twisted gold nanorods dimers. (c) Helical assembly of gold nanoparticles mediated by DNA tiles. By curling up the NP-modified tiles, the gold nanoparticles assembled into a spiral configuration.

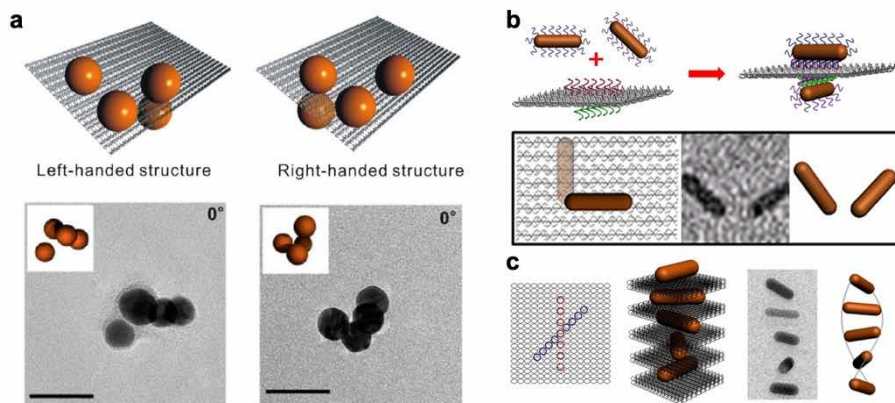


Figure 2.8 Rectangular DNA origami block for chiral plasmonic assembly. (a) Asymmetric plasmonic tetramer created by a rectangular DNA template with four defined binding sites, three on the top and one on the bottom. (b) Illustration of a two gold nanorods dimer assembly by bifacial DNA origami template. Schematic and TEM image of gold nanorods dimers with an “L” shape. (c) Schematic model and cryo-TEM image of helical superstructures of gold nanorods constructed by intercalating designed DNA origami between gold nanorods with an inter-rod angle of 45° .

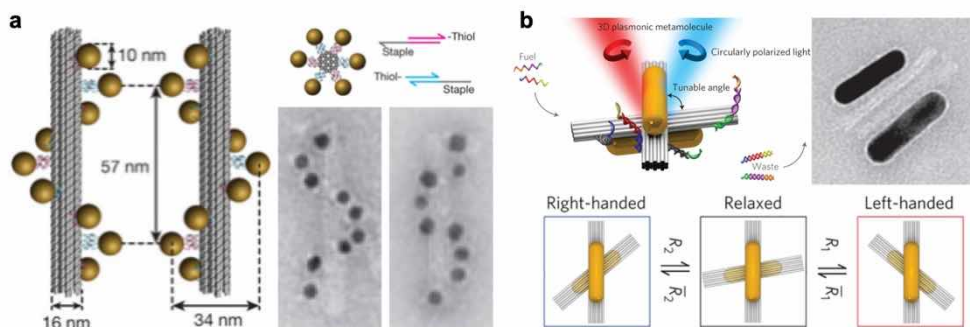


Figure 2.9 DNA origami helix bundle for chiral plasmonic assembly (a) Left- and right-handed Au helices based on a DNA 24-helix bundle. (b) Reconfigurable twisted gold nanorods controlled by switchable DNA origami. The addition of DNA strands link the ends of two different helix bundles of DNA origami, generating opposite chiral structures.

2.2.3 Macromolecule-assisted chiral assembly of nanoparticles

Macromolecular mesoscale self-assembly, featuring molecular packing on multiple length scales, is an emerging area of research in which the spontaneous associations of individual macromolecular species lead to supramolecular structures. Biomacromolecules such as proteins, DNA, polysaccharides, and lipids generally assemble into supramolecular complexes that function as biological devices such as ribosomes, membranes, and organelles.⁷⁴ Over the past decade, a wealth of macromolecular structures has been used as templates or host matrices to achieve chiral structures. Phospholipids, which are composed of three essential parts, a polar head group, one or more hydrophobic tails, and a backbone structure, have been assembled into several structures such as micelles, bilayers, tubules, and ribbons. Because cylindrical microtubules and ribbons can be formed by rolling up lipid bilayers, these species adopt intrinsic helical structures. For example, in 2003, a metallic Cu helical structure was fabricated via the selective electroless metallization of a phospholipid microtubule template (Figure 2.10a).⁷⁵ Later, Chung and Xu group a supramolecular templating approach using a phospholipid helical ribbon to generate tightly coupled⁷⁶ and loosely coupled⁷⁷ chiral assemblies of AuNRs, respectively, where both cases exhibited collective chiroptical responses. Another remarkable example of macroscopic chiral structures is chiral nematic, also called cholesteric, liquid-crystals.^{78,79} Highly crystalline, negatively charged, high-aspect-ratio cellulose nanocrystals (CNCs) were assembled into a chiral nematic phase in aqueous solution and the structure was maintained after drying. The hybrid system can potentially couple the chiroptical property of the host matrix with the intrinsic optical properties of the NPs, leading to distinct plasmon-induced chiroptical properties. Au NPs, Au NRs, and silver nanowires (Ag NWs) have been incorporated

into the CNC matrix, providing plasmonic CD responses and polarization-sensitive contrast in optical microscopy (Figure 2.10b).

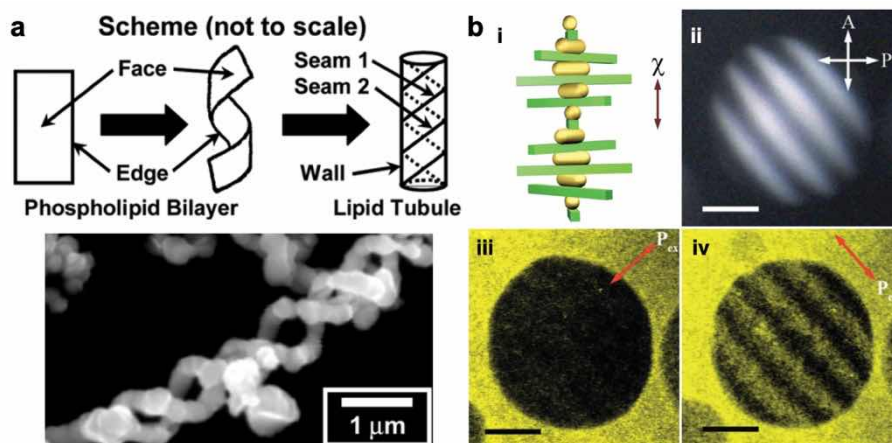


Figure 2.10 Macromolecule assisted chiral assembly. (a) Plasmonic spirals based on phospholipid microtubule templates. (b) Chiral assembly of Au nanorods (AuNRs) induced by cellulose nanocrystals (CNC). Polarized optical microscope images and corresponding polarized two-photon-induced luminescence images prove the chiral nematic arrangement of both CNC and nanorods.

2.3 Intrinsic chirality in inorganic material

The evolution of chirality in inorganic materials is one of the most significant challenges in material science because of the high degree of symmetry developed in typical inorganic crystal structures. Few types of intrinsically chiral crystals that exhibit enantiomorphic crystallographic symmetry, such as α -quartz (α -SiO₂, Figure 2.11a),⁸⁰ sodium chlorate (NaClO₃),⁸¹ cinnabar (α -HgS, Figure 2.11b),⁸² and selenium,⁸³ have an inorganic chirality from their atomic arrangement. According to three-dimensional point group symmetry, only 11 of the 32 crystallographic point groups (triclinic 1; monoclinic 2; orthorhombic 222; trigonal 3 and 32; tetragonal 4 and 422; hexagonal 6 and 622; cubic 23 and 432), which do not have mirrors, inversion, or improper rotation symmetry, can be chiral (Figure 2.11c). However, including plasmonic gold, silver, copper, and aluminum, all metals have highly symmetric face-centered cubic, body-centered cubic, or hexagonal closed-packed crystal structures and are consequently achiral in bulk structure. As a breakthrough for the chirality evolution in achiral metals, a novel concept of inorganic surface chirality defined on the crystalline surface was proposed.⁸⁴⁻⁸⁶ This concept, proposed by Gellman⁸⁴ and Attard,⁸⁵ describes the chirality at all $\{hkl\}$ ($h \neq k \neq l \neq 0$) high-Miller-index surfaces consisting of the atomic kinked site made by the intersection of a low-index $\{111\}$ terrace, $\{100\}$ step, and $\{110\}$ step (Figure 2.12a). This “naturally chiral surface” is non-superimposable on its mirror image; and on the kinked atom, if the ordering of low-index crystal planes $\{111\} \rightarrow \{100\} \rightarrow \{110\}$ is oriented clockwise(counterclockwise), the surface can be denoted as R(S) (Figure 2.12b).

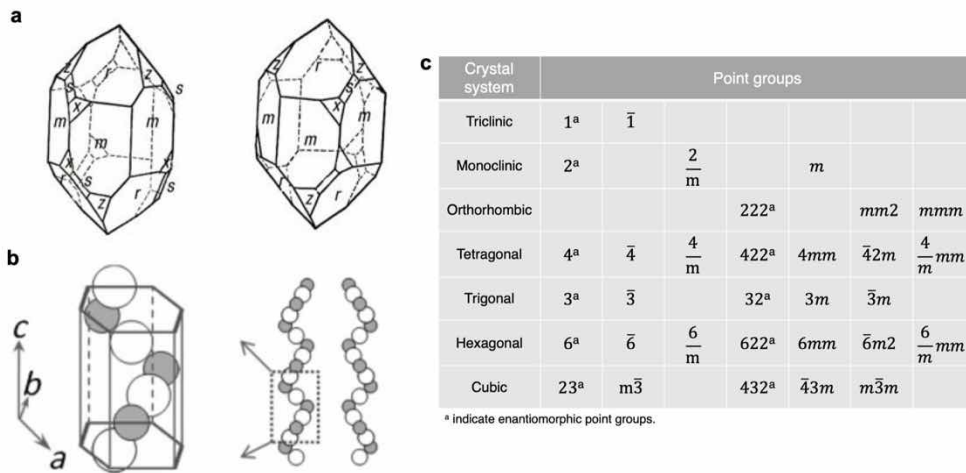


Figure 2.11 Intrinsic chiral crystal structures. (a) Natural quartz crystals with left- and right-handed morphology. (b) The chiral atomic arrangement of the trigonal α -HgS crystal. (c) Crystallographic point groups. Only eleven point groups are chiral, as highlighted as red.

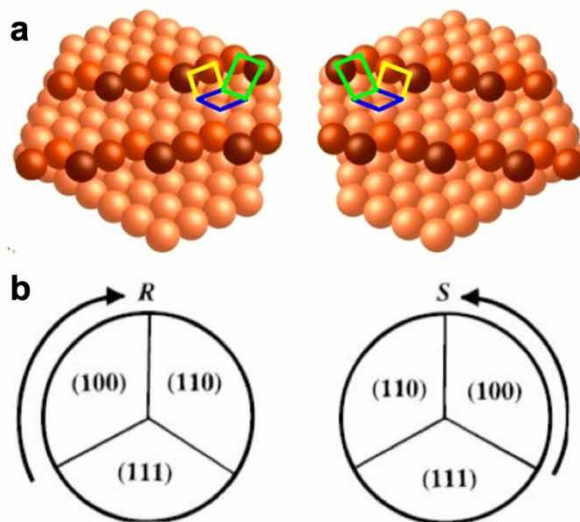


Figure 2.12 Inorganic surface chirality. (a) Inorganic surface chirality defined on high-Miller-index planes, exposing crystalline atomic structures that lack mirror symmetry. (b) Definition of the absolute R and S conformation on the kink site.

As described above, the chirality of inorganic materials can be defined at the atomic surface level. However, in order to expand chirality to nanoscale morphology, the exposed crystal planes, especially high index planes and the resulting morphology (Figure 2.13), should be controlled at the NP level. Several methods have been proposed to generate a stable high-Miller-index NP that can expose naturally chiral surfaces on crystal facets.⁸⁷⁻⁸⁹ i) Fast reduction kinetics can promote the growth of high-curvature morphology, consisting of high-Miller-index planes. Temperature and the concentration of reducing agents can be modulated to produce a hexoctahedral shape with $\{321\}$ planes⁹⁰ and concave trisoctahedral shapes with $\{221\}$, $\{331\}$, and $\{221\}$ planes.⁹¹ ii) Surface passivation with metal ions is adapted to stabilize the high-Miller-index planes. The addition of Ag(I) ions resulted in the formation of underpotential deposition (UPD) layers and stabilized $\{311\}$ ⁹² and $\{720\}$ ⁹³ planes, and the coexistence of other metal ions such as Pd(II) gradually change the morphology and exposed planes.⁹⁴ iii) The rational design of small organic ligands adsorbed on the NP surface induced the formation of high-Miller-index planes. For example, methylamines were adapted to synthesize concave nanocrystals composed of $\{411\}$ planes.⁹⁵ Recently, the Nam group used benzenethiol derivatives as the Au NP shape modifier and stabilizer.⁹⁶ Strong Au-S bonding and the aromatic geometry of 4-aminothiophenol promoted selective growth on the edges of a cuboctahedron to produce a concave rhombic dodecahedron shape containing various high index facets, such as $\{331\}$, $\{221\}$, and $\{553\}$ (Figure 2.14). In aid of strategies based on the seed-mediated synthesis, the exposed high index plane can be controlled and stabilized in single plasmonic nanomaterials.

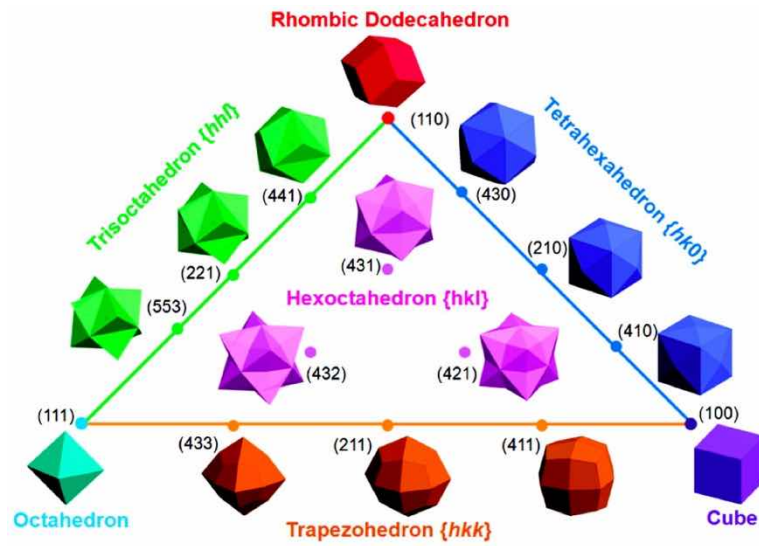


Figure 2.13 Triangular diagram showing fcc metal polyhedrons bounded by different crystallographic facets.

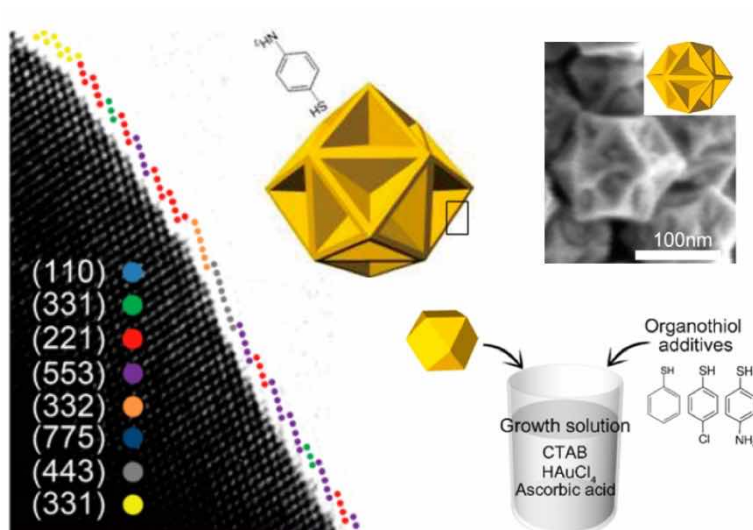


Figure 2.14 High-Miller-index Au nanocrystal with concave rhombic dodecahedron shapes synthesized by benzenethiol derivative as a molecular encoder. According to the HRTEM analysis, the nanocrystal expose {331}, {221}, and {553} crystal planes.

Although most of the synthetic protocols developed for plasmonic NPs are based on the addition of achiral metal ions and organic molecules, there is growing evidence for the chiral-specific interaction of chiral molecules and high-Miller-index planes. As shown in the biological examples, one or several specific encoders control the interaction at the molecular level for the initiation of chirality and continue to be dynamically involved during the development of chirality at the macroscopic scale. Thus, a natural question is how to realize this principle synthetically or to translate similar mechanisms into chiral plasmonic nanostructures. Indeed, there are recent examples that suggest the possibility of applying chiral encoders, such as amino acids and peptides, in inorganic materials from the atomic surface.

At the microscopic atomic surface, the chiral interaction of amino acids and peptides with inorganic materials emerges as the energetics of molecular adsorption and desorption and their relative orientation.⁹⁷⁻⁹⁹ The adsorption of a chiral molecule on an achiral single crystalline surface breaks the symmetry of the surface and creates a chiral configuration. Besenbacher and coworkers reported STM observation results that cysteine formed an asymmetric dimer arrangement even on achiral Au{110} surfaces (Figure 2.16a), and further induced the formation of chiral clusters (Figure 2.16b).^{100,101} Moreover, a chiral atomic arrangement around the kinked site of a high-Miller-index plane provides an inherently asymmetric environment that allows inorganic enantioselective binding. The interaction between a variety of amino acids and the single crystalline high-Miller-index surfaces of noble metals such as Pt, Cu, and Au has been extensively studied.^{84,85,102-105} Interestingly, according to the experiments and simulation by Greber and coworkers, the kinked sites of Au can discriminate enantiomers of cysteine. X-ray photoelectron diffraction analysis proved that the D-cysteine and L-cysteine adsorbed on the Au(111) kinked site showed molecular orientations in different directions (Figure 2.16a), and density functional theory simulation suggested that D-cysteine binds

more strongly than L-cysteine at 140 meV.¹⁰² A definitive cause of this selectivity was the hydrogenated form of adsorbed cysteine, which provided an adsorption geometry that allowed D-cysteine to bind more strongly than L-cysteine (Figure 2.16b).¹⁰³

Interestingly, this asymmetric environment at the crystalline surface offers control over atomic-scale chiral geometry in inorganic materials. In the presence of chiral molecules adsorbed on the surface, an achiral single crystal surface undergoes a reconstruction process and ultimately exposes a chiral high index plane, which can persist even if the chiral molecules were to be removed (Figure 2.17a).¹⁰⁶ Furthermore, Switzer et al. reported that chiral tartrate ions can induce the evolution of chirality in copper oxide film during the electrodeposition process of copper oxide on an achiral gold surface (Figure 2.17b).¹⁰⁷ These reports suggest a perspective that chirality can be transferred from the molecule to the inorganic material. The integration of chirality at atomic crystal planes with nanocrystal shape control based on crystallography parameters may further provide a potential to overcome the mismatch in length scale between atoms and nanocrystal.

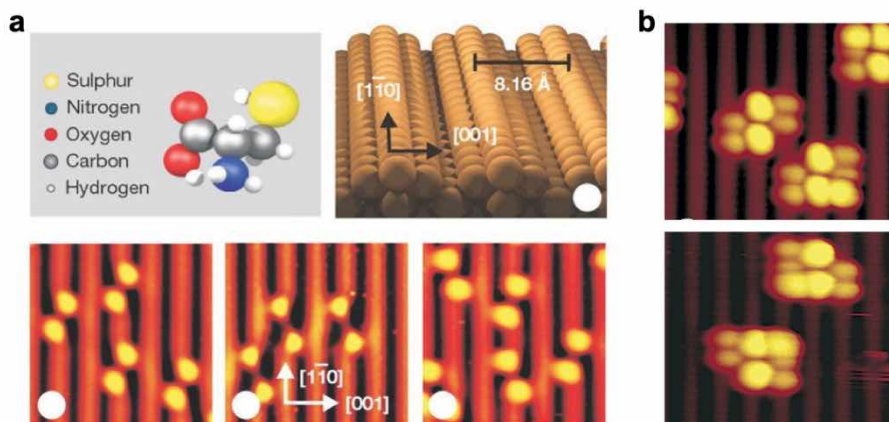


Figure 2.15 Enantioselective interaction of cysteine on the achiral metal surface. (a) Schematic drawings of a cysteine molecule and the gold (110) surface, and STM images of cysteine dimers on gold (110), showing the asymmetric molecular arrangement. (b) STM images of monodispersed cysteine nanoclusters produced enantiomerically pure L- and D-cysteine, respectively.

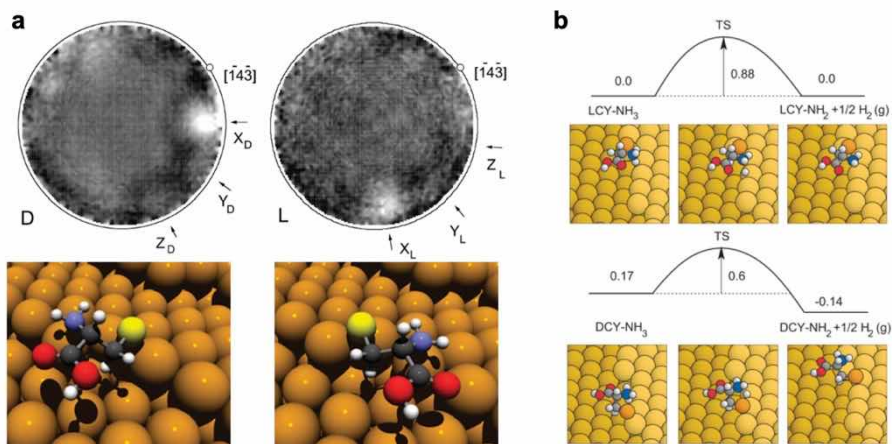


Figure 2.16 Enantioselective binding of cysteine on the chiral high-index plane. (a) X-ray photoelectron diffraction patterns (top) and corresponding DFT calculation (bottom) for D- and L-cysteine adsorbed on the Au (17 11 9)^S surface showing enantioselective adsorption geometry and binding strength (b) Schematic diagram of total energy of cysteine adsorbed on the Au (17 11 9)^S for the transformation between cysteine-NH₂ and cysteine-NH₃.

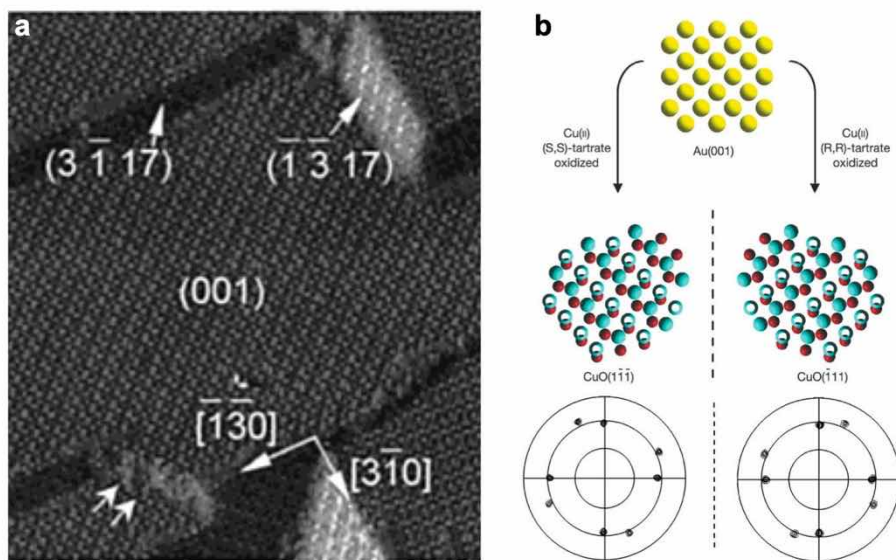


Figure 2.17 Formation of atomic-scale chiral geometry by chirality transfer. (a) STM image of chiral $\{3\ 1\ \bar{1}7\}$ facets of L-lysine/Cu(001) surface after thermal annealing. Surface reconstruction during the annealing process results in the formation of chiral $\{3\ 1\ \bar{1}7\}$ facets. (b) Electrodeposition of CuO from Cu(II)-(R,R)tartrate or Cu(II)-(S,S)tartrate results in the formation of enantiomorphic CuO($\bar{1}11$) or CuO($1\bar{1}\bar{1}$) surfaces, respectively.

2.4 Conclusion

The naturally occurring chirality in biological macromolecules, such as peptides and DNA, provides an excellent template for dissymmetric structure controlled at the nanoscale and can produce sophisticated 3D plasmonic nanostructures. There are still many possibilities that biomolecule hybrid artificial plasmonic structures with extremely strong optical activity is to be found. Numerous biomolecules such as virus, actin filaments, surface layer proteins, and higher levels of the organization can be exploited for compelling chiral templates. This soft method can be an efficient route for the chiral nanostructure with a 3D geometrical feature. In addition, the intrinsic chiral nanostructure of inorganic materials can be more advantageous in terms of strong chiroptical response and structural stability, despite the difficulty in fabrication. In order to induce the chirality in plasmonic metals, the concept of inorganic surface chirality play a crucial role in generating the asymmetric environment at the interface between the chiral molecule and high-Miller-index crystal plane. We believe that the chirality transfer phenomena in the atomic scale reported so far can be extended to develop the 3D chiral morphology in the nanoscale.

2.5 Bibliography

1. Mark, A. G.; Gibbs, J. G.; Lee, T. C.; Fischer, P. Hybrid Nanocolloids with Programmed Three-Dimensional Shape and Material Composition. *Nat. Mater.* **2013**.
2. Soukoulis, C. M.; Wegener, M. Past Achievements and Future Challenges in the Development of Three-Dimensional Photonic Metamaterials. *Nature Photonics*. 2011.
3. Ma, W.; Xu, L.; De Moura, A. F.; Wu, X.; Kuang, H.; Xu, C.; Kotov, N. A. Chiral Inorganic Nanostructures. *Chemical Reviews*. 2017.
4. Jones, M. R.; Osberg, K. D.; Macfarlane, R. J.; Langille, M. R.; Mirkin, C. A. Templated Techniques for the Synthesis and Assembly of Plasmonic Nanostructures. *Chem. Rev.* **2011**.
5. Halas, N. J.; Lal, S.; Chang, W.-S.; Link, S.; Nordlander, P. Plasmons in Strongly Coupled Metallic Nanostructures. *Chem. Rev.* **2011**.
6. Nordlander, P.; Oubre, C.; Prodan, E.; Li, K.; Stockman, M. I. Plasmon Hybridization in Nanoparticle Dimers. *Nano Lett.* **2004**.
7. Auguie, B.; Alonso-Gómez, J. L.; Guerrero-Martínez, A.; Liz-Marzán, L. M. Fingers Crossed: Optical Activity of a Chiral Dimer of Plasmonic Nanorods. *J. Phys. Chem. Lett.* **2011**.
8. Fan, Z.; Govorov, A. O. Plasmonic Circular Dichroism of Chiral Metal Nanoparticle Assemblies. *Nano Lett.* **2010**.
9. Fan, Z.; Govorov, A. O. Chiral Nanocrystals: Plasmonic Spectra and Circular Dichroism. *Nano Lett.* **2012**.
10. Jiang, W.; Pacella, M. S.; Vali, H.; Gray, J. J.; McKee, M. D. Chiral Switching in Biomineral Suprastructures Induced by Homochiral L-Amino Acid. *Sci. Adv.* **2018**.
11. Kulp, E. A.; Switzer, J. A. Electrochemical Biomineralization: The Deposition of Calcite with Chiral Morphologies. *J. Am. Chem. Soc.* **2007**.
12. Wang, P. P.; Yu, S. J.; Govorov, A. O.; Ouyang, M. Cooperative Expression of Atomic Chirality in Inorganic Nanostructures. *Nat. Commun.* **2017**.

13. Ben-Moshe, A.; Wolf, S. G.; Sadan, M. B.; Houben, L.; Fan, Z.; Govorov, A. O.; Markovich, G. Enantioselective Control of Lattice and Shape Chirality in Inorganic Nanostructures Using Chiral Biomolecules. *Nat. Commun.* **2014**.
14. Levin, M. Left–Right Asymmetry in Embryonic Development: A Comprehensive Review. *Mech. Dev.* **2005**, *122* (1), 3–25.
15. Inaki, M.; Liu, J.; Matsuno, K. Cell Chirality: Its Origin and Roles in Left–Right Asymmetric Development. *Philos. Trans. R. Soc. B* **2016**, *371* (1710), 20150403.
16. Tee, Y. H.; Shemesh, T.; Thiagarajan, V.; Hariadi, R. F.; Anderson, K. L.; Page, C.; Volkmann, N.; Hanein, D.; Sivaramakrishnan, S.; Kozlov, M. M.; et al. Cellular Chirality Arising from the Self-Organization of the Actin Cytoskeleton. *Nat. Cell Biol.* **2015**, *17* (4), 445–457.
17. Brown, N. A.; Wolpert, L. The Development of Handedness in Left/Right Asymmetry. *Development* **1990**, *109* (1), 1–9.
18. Shibazaki, Y.; Shimizu, M.; Kuroda, R. Body Handedness Is Directed by Genetically Determined Cytoskeletal Dynamics in the Early Embryo. *Curr. Biol.* **2004**, *14* (16), 1462–1467.
19. Lebreton, G.; Géminard, C.; Lapraz, F.; Pyrpassopoulos, S.; Cerezo, D.; Spéder, P.; Ostap, E. M.; Noselli, S. Molecular to Organismal Chirality Is Induced by the Conserved Myosin 1D. *Science* **2018**, *362* (6417), 949–952.
20. Zhang, S. Fabrication of Novel Biomaterials through Molecular Self-Assembly. *Nature Biotechnology*. 2003.
21. Woolfson, D. N.; Mahmoud, Z. N. More than Just Bare Scaffolds: Towards Multi-Component and Decorated Fibrous Biomaterials. *Chemical Society Reviews*. 2010.
22. Aggeli, A.; Nyrkova, I. A.; Bell, M.; Harding, R.; Carrick, L.; McLeish, T. C. B.; Semenov, A. N.; Boden, N. Hierarchical Self-Assembly of Chiral Rod-like Molecules as a Model for Peptide -Sheet Tapes, Ribbons, Fibrils, and Fibers. *Proc. Natl. Acad. Sci.* **2001**.
23. Lee, J. Y.; Choo, J. E.; Choi, Y. S.; Park, J. B.; Min, D. S.; Lee, S. J.; Rhyu, H. K.; Jo, I. H.; Chung, C. P.; Park, Y. J. Assembly of Collagen-Binding Peptide with Collagen as a Bioactive Scaffold for Osteogenesis in Vitro and in Vivo. *Biomaterials* **2007**.

24. Ma, W.; Kuang, H.; Wang, L.; Xu, L.; Chang, W. S.; Zhang, H.; Sun, M.; Zhu, Y.; Zhao, Y.; Liu, L.; et al. Chiral Plasmonics of Self-Assembled Nanorod Dimers. *Sci. Rep.* **2013**.
25. Hou, S.; Zhang, H.; Yan, J.; Ji, Y.; Wen, T.; Liu, W.; Hu, Z.; Wu, X. Plasmonic Circular Dichroism in Side-by-Side Oligomers of Gold Nanorods: The Influence of Chiral Molecule Location and Interparticle Distance. *Phys. Chem. Chem. Phys.* **2015**.
26. Lu, J.; Chang, Y. X.; Zhang, N. N.; Wei, Y.; Li, A. J.; Tai, J.; Xue, Y.; Wang, Z. Y.; Yang, Y.; Zhao, L.; et al. Chiral Plasmonic Nanochains via the Self-Assembly of Gold Nanorods and Helical Glutathione Oligomers Facilitated by Cetyltrimethylammonium Bromide Micelles. *ACS Nano* **2017**.
27. Fu, X.; Wang, Y.; Huang, L.; Sha, Y.; Gui, L.; Lai, L.; Tang, Y. Assemblies of Metal Nanoparticles and Self-Assembled Peptide Fibrils - Formation of Double Helical and Single-Chain Arrays of Metal Nanoparticles. *Adv. Mater.* **2003**.
28. Grigoryan, G.; Kim, Y. H.; Acharya, R.; Axelrod, K.; Jain, R. M.; Willis, L.; Drndic, M.; Kikkawa, J. M.; DeGrado, W. F. Computational Design of Virus-like Protein Assemblies on Carbon Nanotube Surfaces. *Science* **2011**.
29. Zhao, X.; Pan, F.; Xu, H.; Yaseen, M.; Shan, H.; Hauser, C. A. E.; Zhang, S.; Lu, J. R. Molecular Self-Assembly and Applications of Designer Peptide Amphiphiles. *Chemical Society Reviews*. 2010.
30. Hartgerink, J. D.; Beniash, E.; Stupp, S. I. Self-Assembly and Mineralization of Peptide-Amphiphile Nanofibers. *Science* **2001**.
31. Fleming, S.; Ulijn, R. V. Design of Nanostructures Based on Aromatic Peptide Amphiphiles. *Chemical Society Reviews*. 2014.
32. Silva, G. A.; Czeisler, C.; Niece, K. L.; Beniash, E.; Harrington, D. A.; Kessler, J. A.; Stupp, S. I. Selective Differentiation of Neural Progenitor Cells by High-Epitope Density Nanofibers. *Science* **2004**.
33. Chen, C. L.; Zhang, P.; Rosi, N. L. A New Peptide-Based Method for the Design and Synthesis of Nanoparticle Superstructures: Construction of Highly Ordered Gold Nanoparticle Double Helices. *J. Am. Chem. Soc.* **2008**.
34. Chen, C. L.; Rosi, N. L. Preparation of Unique 1-D Nanoparticle Superstructures and Tailoring Their Structural Features. *J. Am. Chem. Soc.*

2010.

35. Merg, A. D.; Slocik, J.; Blaber, M. G.; Schatz, G. C.; Naik, R.; Rosi, N. L. Adjusting the Metrics of 1-D Helical Gold Nanoparticle Superstructures Using Multivalent Peptide Conjugates. *Langmuir* **2015**.
36. Song, C.; Blaber, M. G.; Zhao, G.; Zhang, P.; Fry, H. C.; Schatz, G. C.; Rosi, N. L. Tailorable Plasmonic Circular Dichroism Properties of Helical Nanoparticle Superstructures. *Nano Lett.* **2013**.
37. Merg, A. D.; Boatz, J. C.; Mandal, A.; Zhao, G.; Mokashi-Punekar, S.; Liu, C.; Wang, X.; Zhang, P.; Van Der Wel, P. C. A.; Rosi, N. L. Peptide-Directed Assembly of Single-Helical Gold Nanoparticle Superstructures Exhibiting Intense Chiroptical Activity. *J. Am. Chem. Soc.* **2016**.
38. Lin, Y.; Pashuck, E. T.; Thomas, M. R.; Amdursky, N.; Wang, S. T.; Chow, L. W.; Stevens, M. M. Plasmonic Chirality Imprinting on Nucleobase-Displaying Supramolecular Nanohelices by Metal–Nucleobase Recognition. *Angew. Chem. Int. Ed.* **2017**.
39. Naik, R. R.; Stringer, S. J.; Agarwal, G.; Jones, S. E.; Stone, M. O. Biomimetic Synthesis and Patterning of Silver Nanoparticles. *Nat. Mater.* **2002**.
40. Alivisatos, A. P.; Johnsson, K. P.; Peng, X.; Wilson, T. E.; Loweth, C. J.; Bruchez, M. P.; Schultz, P. G. Organization of “nanocrystal Molecules” Using DNA. *Nature* **1996**.
41. Mirkin, C. A.; Letsinger, R. L.; Mucic, R. C.; Storhoff, J. J. A DNA-Based Method for Rationally Assembling Nanoparticles into Macroscopic Materials. *Nature* **1996**.
42. Seeman, N. C. DNA in a Material World. *Nature* **2003**, *421* (6921), 427–431.
43. Rothemund, P. W. K. Folding DNA to Create Nanoscale Shapes and Patterns. *Nature* **2006**.
44. Chen, W.; Bian, A.; Agarwal, A.; Liu, L.; Shen, H.; Wang, L.; Xu, C.; Kotov, N. A. Nanoparticle Superstructures Made by Polymerase Chain Reaction: Collective Interactions of Nanoparticles and a New Principle for Chiral Materials. *Nano Lett.* **2009**.
45. Zhao, Y.; Xu, L.; Liz-Marzán, L. M.; Kuang, H.; Ma, W.; Asenjo-García, A.; García De Abajo, F. J.; Kotov, N. A.; Wang, L.; Xu, C. Alternating

- Plasmonic Nanoparticle Heterochains Made by Polymerase Chain Reaction and Their Optical Properties. *J. Phys. Chem. Lett.* **2013**.
46. Zhao, Y.; Xu, L.; Kuang, H.; Wang, L.; Xu, C. Asymmetric and Symmetric PCR of Gold Nanoparticles: A Pathway to Scaled-up Self-Assembly with Tunable Chirality. *J. Mater. Chem.* **2012**.
 47. Yan, W.; Xu, L.; Xu, C.; Ma, W.; Kuang, H.; Wang, L.; Kotov, N. A. Self-Assembly of Chiral Nanoparticle Pyramids with Strong R/S Optical Activity. *J. Am. Chem. Soc.* **2012**.
 48. Mastroianni, A. J.; Claridge, S. A.; Paul Alivisatos, A. Pyramidal and Chiral Groupings of Gold Nanocrystals Assembled Using DNA Scaffolds. *J. Am. Chem. Soc.* **2009**.
 49. Hao, C.; Xu, L.; Ma, W.; Wang, L.; Kuang, H.; Xu, C. Assembled Plasmonic Asymmetric Heterodimers with Tailorable Chiroptical Response. *Small* **2014**.
 50. Xu, L.; Hao, C.; Yin, H.; Liu, L.; Ma, W.; Wang, L.; Kuang, H.; Xu, C. Plasmonic Core-Satellites Nanostructures with High Chirality and Bioproperty. *J. Phys. Chem. Lett.* **2013**.
 51. Zhao, Y.; Xu, L.; Ma, W.; Wang, L.; Kuang, H.; Xu, C.; Kotov, N. A. Shell-Engineered Chiroplasmonic Assemblies of Nanoparticles for Zeptomolar DNA Detection. *Nano Lett.* **2014**.
 52. Zhao, Y.; Yang, Y.; Zhao, J.; Weng, P.; Pang, Q.; Song, Q. Dynamic Chiral Nanoparticle Assemblies and Specific Chiroplasmonic Analysis of Cancer Cells. *Adv. Mater.* **2016**.
 53. Wu, X.; Xu, L.; Ma, W.; Liu, L.; Kuang, H.; Kotov, N. A.; Xu, C. Propeller-Like Nanorod-Upconversion Nanoparticle Assemblies with Intense Chiroptical Activity and Luminescence Enhancement in Aqueous Phase. *Adv. Mater.* **2016**.
 54. Yan, W.; Xu, L.; Ma, W.; Liu, L.; Wang, L.; Kuang, H.; Xu, C. Pyramidal Sensor Platform with Reversible Chiroptical Signals for DNA Detection. *Small* **2014**.
 55. Li, S.; Xu, L.; Ma, W.; Wu, X.; Sun, M.; Kuang, H.; Wang, L.; Kotov, N. A.; Xu, C. Dual-Mode Ultrasensitive Quantification of MicroRNA in Living Cells by Chiroplasmonic Nanopyramids Self-Assembled from Gold and Upconversion Nanoparticles. *J. Am. Chem. Soc.* **2016**.

56. Seeman, N. C. Nucleic Acid Junctions and Lattices. *J. Theor. Biol.* **1982**.
57. Chen, J.; Seeman, N. C. Synthesis from DNA of a Molecule with the Connectivity of a Cube. *Nature* **1991**.
58. Sharma, J.; Chhabra, R.; Cheng, A.; Brownell, J.; Liu, Y.; Yan, H. Control of Self-Assembly of DNA Tubules through Integration of Gold Nanoparticles. *Science* **2009**.
59. Cecconello, A.; Kahn, J. S.; Lu, C. H.; Khosravi Khorashad, L.; Govorov, A. O.; Willner, I. DNA Scaffolds for the Dictated Assembly of Left-/Right-Handed Plasmonic Au NP Helices with Programmed Chiro-Optical Properties. *J. Am. Chem. Soc.* **2016**.
60. Shen, X.; Song, C.; Wang, J.; Shi, D.; Wang, Z.; Liu, N.; Ding, B. Rolling up Gold Nanoparticle-Dressed Dna Origami into Three-Dimensional Plasmonic Chiral Nanostructures. *J. Am. Chem. Soc.* **2012**.
61. Shen, X.; Asenjo-Garcia, A.; Liu, Q.; Jiang, Q.; García De Abajo, F. J.; Liu, N.; Ding, B. Three-Dimensional Plasmonic Chiral Tetramers Assembled by DNA Origami. *Nano Lett.* **2013**.
62. Dai, G.; Lu, X.; Chen, Z.; Meng, C.; Ni, W.; Wang, Q. DNA Origami-Directed, Discrete Three-Dimensional Plasmonic Tetrahedron Nanoarchitectures with Tailored Optical Chirality. *ACS Appl. Mater. Interfaces* **2014**.
63. Lan, X.; Chen, Z.; Dai, G.; Lu, X.; Ni, W.; Wang, Q. Bifacial DNA Origami-Directed Discrete, Three-Dimensional, Anisotropic Plasmonic Nanoarchitectures with Tailored Optical Chirality. *J. Am. Chem. Soc.* **2013**.
64. Lan, X.; Lu, X.; Shen, C.; Ke, Y.; Ni, W.; Wang, Q. Au Nanorod Helical Superstructures with Designed Chirality. *J. Am. Chem. Soc.* **2015**.
65. Shen, C.; Lan, X.; Zhu, C.; Zhang, W.; Wang, L.; Wang, Q. Spiral Patterning of Au Nanoparticles on Au Nanorod Surface to Form Chiral AuNR@AuNP Helical Superstructures Templated by DNA Origami. *Adv. Mater.* **2017**.
66. Kuzyk, A.; Schreiber, R.; Fan, Z.; Pardatscher, G.; Roller, E. M.; Högele, A.; Simmel, F. C.; Govorov, A. O.; Liedl, T. DNA-Based Self-Assembly of Chiral Plasmonic Nanostructures with Tailored Optical Response. *Nature* **2012**.
67. Schreiber, R.; Luong, N.; Fan, Z.; Kuzyk, A.; Nickels, P. C.; Zhang, T.;

- Smith, D. M.; Yurke, B.; Kuang, W.; Govorov, A. O.; et al. Chiral Plasmonic DNA Nanostructures with Switchable Circular Dichroism. *Nat. Commun.* **2013**.
68. Urban, M. J.; Dutta, P. K.; Wang, P.; Duan, X.; Shen, X.; Ding, B.; Ke, Y.; Liu, N. Plasmonic Toroidal Metamolecules Assembled by DNA Origami. *J. Am. Chem. Soc.* **2016**.
69. Tian, Y.; Wang, T.; Liu, W.; Xin, H. L.; Li, H.; Ke, Y.; Shih, W. M.; Gang, O. Prescribed Nanoparticle Cluster Architectures and Low-Dimensional Arrays Built Using Octahedral DNA Origami Frames. *Nat. Nanotechnol.* **2015**.
70. Kuzyk, A.; Schreiber, R.; Zhang, H.; Govorov, A. O.; Liedl, T.; Liu, N. Reconfigurable 3D Plasmonic Metamolecules. *Nat. Mater.* **2014**.
71. Kuzyk, A.; Urban, M. J.; Idili, A.; Ricci, F.; Liu, N. Selective Control of Reconfigurable Chiral Plasmonic Metamolecules. *Sci. Adv.* **2017**.
72. Kuzyk, A.; Yang, Y.; Duan, X.; Stoll, S.; Govorov, A. O.; Sugiyama, H.; Endo, M.; Liu, N. A Light-Driven Three-Dimensional Plasmonic Nanosystem That Translates Molecular Motion into Reversible Chiroptical Function. *Nat. Commun.* **2016**.
73. Zhou, C.; Duan, X.; Liu, N. A Plasmonic Nanorod That Walks on DNA Origami. *Nat. Commun.* **2015**.
74. Zhao, Y.; Sakai, F.; Su, L.; Liu, Y.; Wei, K.; Chen, G.; Jiang, M. Progressive Macromolecular Self-Assembly: From Biomimetic Chemistry to Bio-Inspired Materials. *Advanced Materials*. 2013.
75. Price, R. R.; Dressick, W. J.; Singh, A. Fabrication of Nanoscale Metallic Spirals Using Phospholipid Microtubule Organizational Templates. *J. Am. Chem. Soc.* **2003**.
76. Wang, R. Y.; Wang, H.; Wu, X.; Ji, Y.; Wang, P.; Qu, Y.; Chung, T. S. Chiral Assembly of Gold Nanorods with Collective Plasmonic Circular Dichroism Response. *Soft Matter* **2011**.
77. Wang, P.; Chen, L.; Wang, R.; Ji, Y.; Zhai, D.; Wu, X.; Liu, Y.; Chen, K.; Xu, H. Giant Optical Activity from the Radiative Electromagnetic Interactions in Plasmonic Nanoantennas. *Nanoscale* **2013**.
78. Liu, Q.; Campbell, M. G.; Evans, J. S.; Smalyukh, I. I. Orientationally Ordered Colloidal Co-Dispersions of Gold Nanorods and Cellulose

- Nanocrystals. *Adv. Mater.* **2014**.
79. Querejeta-Fernández, A.; Chauve, G.; Methot, M.; Bouchard, J.; Kumacheva, E. Chiral Plasmonic Films Formed by Gold Nanorods and Cellulose Nanocrystals. *J. Am. Chem. Soc.* **2014**.
 80. Hazen, R. M.; Sholl, D. S. Chiral Selection on Inorganic Crystalline Surfaces. *Nat. Mater.* **2003**, 2 (6), 367–374.
 81. Ramachandran, G. N.; Chandrasekaran, K. S. The Absolute Configuration of Sodium Chlorate. *Acta Crystallogr.* **1957**, 10 (10), 671–675.
 82. Ben-Moshe, A.; Govorov, A. O.; Markovich, G. Enantioselective Synthesis of Intrinsically Chiral Mercury Sulfide Nanocrystals. *Angew. Chem. Int. Ed.* **2013**, 52 (4), 1275–1279.
 83. Saeva, F. D.; Olin, G. R.; Chu, J. Y. C. Circular Dichroism of Trigonal Selenium Formed in a Chiral Polymer Matrix. *Mol. Cryst. Liq. Cryst.* **1977**, 41 (1), 5–9.
 84. McFadden, C. F.; Cremer, P. S.; Gellman, A. J. Adsorption of Chiral Alcohols on “Chiral” Metal Surfaces. *Langmuir* **1996**, 12 (10), 2483–2487.
 85. Ahmadi, A.; Attard, G.; Feliu, J.; Rodes, A. Surface Reactivity at “Chiral” Platinum Surfaces. *Langmuir* **1999**, 15 (7), 2420–2424.
 86. Sholl, D. S.; Asthagiri, A.; Power, T. D. Naturally Chiral Metal Surfaces as Enantiospecific Adsorbents. *J. Phys. Chem. B* **2001**, 105 (21), 4771–4782.
 87. Quan, Z.; Wang, Y.; Fang, J. High-Index Faceted Noble Metal Nanocrystals. *Acc. Chem. Res.* **2013**, 46 (2), 191–202.
 88. Zhang, H.; Jin, M.; Xia, Y. Noble-Metal Nanocrystals with Concave Surfaces: Synthesis and Applications. *Angew. Chem. Int. Ed.* **2012**, 51 (31), 7656–7673.
 89. Chen, Q.; Jia, Y.; Xie, S.; Xie, Z. Well-Faceted Noble-Metal Nanocrystals with Nonconvex Polyhedral Shapes. *Chem. Soc. Rev.* **2016**, 45 (11), 3207–3220.
 90. Hong, J. W.; Lee, S.-U.; Lee, Y. W.; Han, S. W. Hexoctahedral Au Nanocrystals with High-Index Facets and Their Optical and Surface-Enhanced Raman Scattering Properties. *J. Am. Chem. Soc.* **2012**, 134 (10), 4565–4568.
 91. Yu, Y.; Zhang, Q.; Lu, X.; Lee, J. Y. Seed-Mediated Synthesis of

- Monodisperse Concave Trisoctahedral Gold Nanocrystals with Controllable Sizes. *J. Phys. Chem. C* **2010**, *114* (25), 11119–11126.
92. Grzelczak, M.; Sánchez-Iglesias, A.; Heidari, H.; Bals, S.; Pastoriza-Santos, I.; Pérez-Juste, J.; Liz-Marzán, L. M. Silver Ions Direct Twin-Plane Formation during the Overgrowth of Single-Crystal Gold Nanoparticles. *ACS Omega* **2016**, *1* (2), 177–181.
 93. Langille, M. R.; Personick, M. L.; Zhang, J.; Mirkin, C. A. Defining Rules for the Shape Evolution of Gold Nanoparticles. *J. Am. Chem. Soc.* **2012**, *134* (35), 14542–14554.
 94. Tran, T. T.; Lu, X. Synergistic Effect of Ag and Pd Ions on Shape-Selective Growth of Polyhedral Au Nanocrystals with High-Index Facets. *J. Phys. Chem. C* **2011**, *115* (9), 3638–3645.
 95. Huang, X.; Zhao, Z.; Fan, J.; Tan, Y.; Zheng, N. Amine-Assisted Synthesis of Concave Polyhedral Platinum Nanocrystals Having {411} High-Index Facets. *J. Am. Chem. Soc.* **2011**, *133* (13), 4718–4721.
 96. Lee, H. E.; Yang, K. D.; Yoon, S. M.; Ahn, H. Y.; Lee, Y. Y.; Chang, H.; Jeong, D. H.; Lee, Y. S.; Kim, M. Y.; Nam, K. T. Concave Rhombic Dodecahedral Au Nanocatalyst with Multiple High-Index Facets for CO₂ Reduction. *ACS Nano* **2015**, *9* (8), 8384–8393.
 97. Horvath, J. D.; Gellman, A. J. Naturally Chiral Surfaces. *Top. Catal.* **2003**, *25* (1–4), 9–15.
 98. Mallat, T.; Orglmeister, E.; Baiker, A. Asymmetric Catalysis at Chiral Metal Surfaces. *Chem. Rev.* **2007**, *107* (11), 4863–4890.
 99. Gellman, A. J. Chiral Surfaces: Accomplishments and Challenges. *ACS Nano* **2010**, *4* (1), 5–10.
 100. Kühnle, A.; Linderoth, T. R.; Hammer, B.; Besenbacher, F. Chiral Recognition in Dimerization of Adsorbed Cysteine Observed by Scanning Tunneling Microscopy. *Nature* **2002**, *415* (6874), 891–893.
 101. Kühnle, A.; Linderoth, T. R.; Besenbacher, F. Self-Assembly of Monodispersed, Chiral Nanoclusters of Cysteine on the Au(110)-(1 × 2) Surface. *J. Am. Chem. Soc.* **2003**, *125* (48), 14680–14681.
 102. Greber, T.; Šljivančanin, Ž.; Schillinger, R.; Wider, J.; Hammer, B. Chiral Recognition of Organic Molecules by Atomic Kinks on Surfaces. *Phys. Rev. Lett.* **2006**, *96* (5), 056103.

103. Schillinger, R.; Šljivančanin, Ž.; Hammer, B.; Greber, T. Probing Enantioselectivity with X-Ray Photoelectron Spectroscopy and Density Functional Theory. *Phys. Rev. Lett.* **2007**, *98* (13), 136102.
104. Gellman, A. J.; Huang, Y.; Feng, X.; Pushkarev, V. V.; Holsclaw, B.; Mhatre, B. S. Superenantioselective Chiral Surface Explosions. *J. Am. Chem. Soc.* **2013**, *135* (51), 19208–19214.
105. Yun, Y.; Gellman, A. J. Adsorption-Induced Auto-Amplification of Enantiomeric Excess on an Achiral Surface. *Nat. Chem.* **2015**, *7* (6), 520–525.
106. Zhao, X. Fabricating Homochiral Facets on Cu(001) with L-Lysine. *J. Am. Chem. Soc.* **2000**, *122* (50), 12584–12585.
107. Switzer, J. A.; Kothari, H. M.; Poizot, P.; Nakanishi, S.; Bohannon, E. W. Enantiospecific Electrodeposition of a Chiral Catalyst. *Nature* **2003**, *425* (6957), 490–493.

Chapter 3. Morphology Control in Plasmonic Au Nanoparticle Synthesis

3.1 Introduction

Morphology control of gold nanoparticles is a significant issue because the geometry of surface and entire particles is directly correlated with intrinsic properties of nanoparticles.¹ For the past decades, morphology dependent properties of gold nanoparticles were utilized for use in a wide range of applications such as catalysis,²⁻⁴ sensing,⁵⁻⁹ and therapeutic agent,^{10,11} and particularly their unique optical features from surface plasmon phenomena were compelling interests. By controlling morphology of gold nanoparticles, their plasmonic properties can be changed and enhanced for the wide range of uses such as chemical and biomedical sensing.⁵⁻⁹ Therefore, there have been many efforts to advance synthetic methods that easily control the shape evolution of gold nanoparticles.¹²⁻¹⁵

For the facile control of nanoparticle morphology, the seed-mediated method is regarded as one of the most well-defined approaches.¹⁶⁻¹⁸ In the seed-mediated method, nanocrystal formation undergoes two stages of seed nucleation and subsequent growth. The advantage of the seed-mediated method is that the parameters that directly affect the shape evolution can be easily and precisely tuned to obtain the desired size and morphology.^{17,18} For example, parameters such as the condition of seed particle,¹⁹ composition of the growth solution,^{20,21} temperature,²² and pH²³ can be modified to synthesize various shapes. Although various shapes have been obtained using the seed-mediated methods, further understanding of the

correlation between CTAB and AA is required to precisely control the final shape of nanoparticles.

Herein, we investigated the relationship between the capping agent and the reducing agent in a simplified system of CTAB and AA. Series of gold nanoparticle synthesis were executed by varying the compositions of CTAB and AA. In the synthesis of gold nanoparticles with tailored morphologies, it has been accepted that the CTAB/AA system has limitations because of the strong binding of bromide ions.²⁴ Therefore, alternative methods have been developed that use different ligands and include other additives, such as halides and silver ions, to control the synthetic process.²⁴⁻²⁶ However, we showed that cuboctahedral, cubic, and rhombic dodecahedral nanocrystals were synthesized when the concentrations of CTAB and AA were precisely adjusted. Furthermore, we demonstrated that the rhombic dodecahedral shape was kinetically synthesized in a highly concentrated region of AA in our system. To our knowledge, there is no prior report about the synthesis of rhombic dodecahedra with or without additives in the CTAB/AA system. Based upon these results, a morphology diagram was constructed as a function of the concentrations of CTAB and AA. This diagram represents the tendency of specific morphology formation; thus, we suggest that the ratio of the CTAB and AA concentrations plays a crucial role in the shape evolution of gold nanoparticles.

3.2 Theoretical background

3.2.1 Mechanism of nanocrystal morphology control

Surface energy consideration is an integral part of understanding and manipulating the morphology of metal nanoparticle. The morphology of nanoparticle is defined by relative growth rate of each crystallographic plane. In order to control the relative growth of surface, thus achieve desired morphology, energy term of surface formation needs to be considered. The surface energies of planes are described by the Gibbs free energy per unit area. The summation of the bulk Gibbs free energy and the surface free energy describes the total Gibbs free energy in the nanoparticles as follows:

$$dG = dG_{bulk} + \gamma dA \quad (2.1)$$

where γ is the specific surface free energy per unit area and A is the surface area. The specific surface free energy of crystallographic plane is expressed as follows:

$$\gamma = \frac{1}{2} N_B \varepsilon \rho_A \quad (2.2)$$

where N_B is the number of broken bonds per surface unit cell, ε is the bond strength, ρ_A is the number of surface atoms per unit area. This surface free energy (γ) can be understood as the increase in free energy per unit area when a new surface is created. As each material has unique intrinsic anisotropy in atomic arrangement, resulting surface energy of the various crystal planes are different each other. In the case of face-centered cube (fcc) lattice, the surface free energy shows following order:

$$\gamma_{111} < \gamma_{100} < \gamma_{110} \quad (2.3)$$

When atoms are tightly bound to each other, the generation of a new crystal surface is only enabled by the dissociation of the bonds between atoms. In this sense, the surface free energy is related to the energy expenses for dissociating the bonds, which is calculated by the number and strength of bonds at the exposed crystal surface. As shown in Figure 3.1,²⁷ depending on the crystallographic plane, the number of bonds determined by the atomic arrangement of that plane. Compared to the (111) and (100), the (110) plane has one additional broken bond between the a' and b' site from the subsurface. Therefore, this surface exhibits higher surface energy than other (111) or (100) surface.

When the atom is newly added to the nanoparticle, it undergoes two paths, deposition and diffusion. During the growth of nanoparticles, if deposited adatoms can move to the most stable site by the surface diffusion process (global minimum), this results in equilibrium shape which is dependent on the surface free energy of nanocrystals. However, in many cases, the existence of activation barriers during surface diffusion process results in the nanocrystal morphology of the local minima (Figure 3.2b),²⁷ leading to the formation of different product which is not perfectly matched with the thermodynamic equilibrium shape. The growth pathway of the nanoparticle and their resulting morphology are strongly dependent on the competition of atom deposition and surface diffusion. Deposition rate of atoms is directly correlated with the rate of metal atom supply in the solution, in which the rate V calculated by the molar concentration of precursor $[A]$ and reducing agent $[B]$ and reaction constant k , as follows:

$$V = k[A]^x[B]^y \quad (2.4)$$

where x and y correspond to the reaction orders for A and B , respectively. In the practical synthesis reaction, the rate of deposition can be controlled by various routes such as reagent type, concentration, and reaction temperature. The rate of surface

diffusion which is directly related to diffusion coefficient D can be described as follows:

$$D = D_0 \exp(-E_{diff}/RT) \quad (2.5)$$

where D_0 is constant, E_{diff} is energy barrier for diffusion process, R is gas constant, and T is temperature. Various factors can be attributed to E_{diff} such as the type of crystal plane, binding strength, the accessibility of atom deposition, and the gradient of chemical potential near the surface. By considering these factors, one can carefully achieve the synthesis of the desired morphology.

In this work, we are mainly focused on the gold nanostructures prepared in the solution phase methods. The scope of this thesis is engineering the shape of particles, and assembly of nanoparticles to intensify optical property. In here, we are going to review the aqueous synthesis methods for creating nanoparticles, assembling methods of nanoparticles, and optical properties with interesting applications.

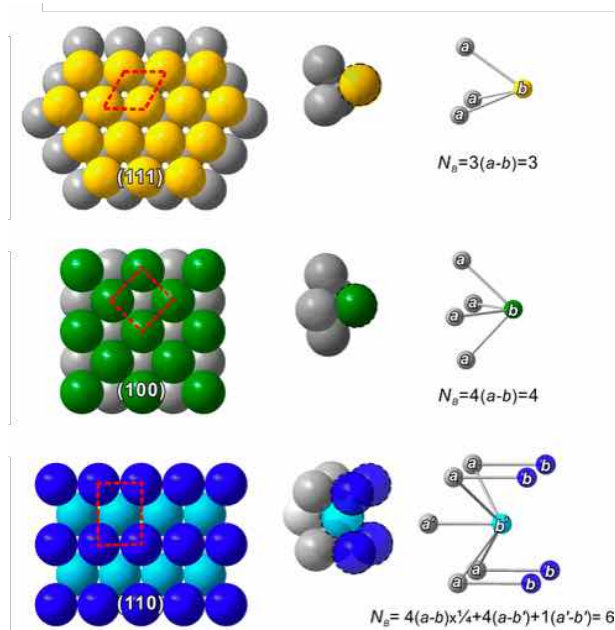


Figure 3.1 Schematic of crystallographic planes for a face-centered-cubic metal. The red box shows the unit cell at the surface.

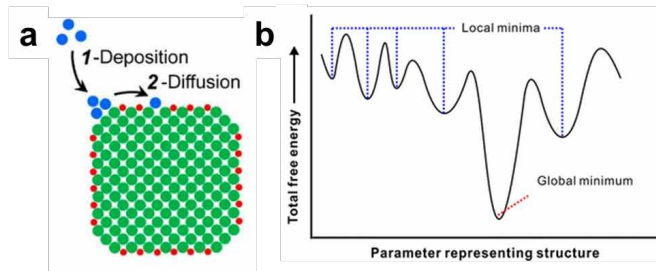


Figure 3.2 Schematic illustration showing (a) path of newly added atom and (b) total free energy plot depending on the structure

3.2.2 Seed-mediated growth

For the homogeneous nucleation, careful control of reaction condition such as reagent concentration and temperature are necessary because nucleation and growth occurred in the same one reactor, and it is not easy to avoid secondary nucleation events. On the other hand, the heterogeneous reaction using pre-defined seed particles synthesized in a separate reaction is more advantageous for morphology control due to the significantly lower activation energy for metal reduction. Therefore, in the heterogeneous reaction, the addition of seed nanoparticle facilitates the reduction of metal ions, and continuous overgrowth process under the various reaction conditions allows for a wide range of nanoparticles with diverse size and morphology. Murphy group have shown that the isolation of nucleation and growth stages can be easily achieved by using the pre-synthesized seed and have successfully controlled the size and morphology of Au nanoparticles, which is called “seed-mediated method.”^{28,29} In the typical seed-mediated method synthesis, small Au seeds (3-5 nm in diameter) are added to the growth solution which contains Au precursor, CTAB capping agent, and ascorbic acid. Ascorbic acid, which is mild reducing agent, reduces Au(III) in solution only to its single oxidation state, Au(I), but cannot change into gold atom. Thus, the nucleation and growth only can be proceeded by attachment of gold ions onto the injected preformed seed nanoparticle. The morphology control of the nanoparticle is enabled by carefully controlling the reaction condition of the separated growth stage. Reducing power of the ascorbic acid in this step is only strong enough for the deposition of metal atoms on preformed nuclei. Therefore, the advantage of using seed-mediated growth to prepare larger particle is that greater control can be achieved over the size of grown nanoparticles.

As one of the strategies to modify the growth stage of gold nanoparticles, the composition of the growth solution has been varied for systematic study of shape control. The growth solution includes two major components, the capping agent and the reducing agent, and diverse combinations of these agents have been investigated.³⁰⁻⁴⁰ For example, capping agents that have quaternary ammonium heads^{30,31,33-35} are frequently adopted as well as citrate,³⁶⁻³⁸ and sulfate^{32,39,40}; chemicals such as citrate, and ascorbic acid^{24,31,41} have been used for reducing gold precursors; and other techniques^{13-15,42} for reducing these precursors can be used. Additionally, certain additives can be included in the growth system to induce shape-directing effects. Table 3.1 describes previous gold nanoparticle synthesis routes using a well-known ligand and reducing agent, the cetyltrimethylammonium bromide (CTAB) and ascorbic acid (AA) system.

Table 3.1 Synthesis routes based on a single-step, seed-mediated method for gold nanocrystals using a CTAB/AA system as the growth solution.

Gold seed condition	Additives	Particle shape	Ref.
Citrate capped seed (~3.5 nm)	-	rod (AR 5) ^a	43
	-	sphere (5.5 nm, 8 nm)	44
	AgNO ₃	multi-branched shape, bipyramid, rod	45
	AgNO ₃ , HCl	Bipyramid	23
	AgNO ₃ , cyclohexane, acetone	spheroid to rod (AR 1 - 10), ϕ -shape	30
	KI	sphere (50 nm)	46
	KI	triangular prism	21
	KI, NaOH, NaCl	Plates	47
	Pluronic F-127	rod (AR 4.2 - 5.4)	48
	Pluronic F-127, AgNO ₃	rod (AR 12 - 21)	48
	HCl, HNO ₃ , H ₂ SO ₄	wire (~5 μ m)	49
CTAB capped seed (<5 nm)	-	rod (AR 6 - 33)	41
	-	cube, hexagon, triangle, star-shape	12
	KI	rod to dumbbell shape	16
	AgNO ₃	rod (AR 2 - 4)	50
	AgNO ₃	cube, tetrapod, branched shape	12

		AgNO ₃ , NaBr	cube, ϕ -shape	51
		AgNO ₃ , HCl	rod (AR 2 - 5)	23
		AgNO ₃ , HCl	elongated tetrahexahedron	52
		Pb(NO ₃) ₂	rod (AR ~7)	53
		Cu(NO ₃) ₂	octahedron, cuboctahedron, triangle	53
		AgNO ₃	sphere (30 nm)	54
		CuSO ₄	cuboid, decahedron	55
		Aromatic additives, HCl, AgNO ₃	rod (AR 8 - 20)	56
	Commercially supplied seed (10 nm)	AgNO ₃	star-shape	57
	SDS capped seed (~10 nm)	AgNO ₃	star-shape	58
Large seed	Citrate capped (20 nm)	-	large tetrapod	12
	CTAB capped (50 nm)	-	sphere (115 - 850 nm)	46
	CTAC capped (40 nm)	-	octahedron, cube, trisoctahedron	20

3.3 Result and discussion

3.3.1 Synthesis of rhombic dodecahedral Au nanoparticles

Rhombic dodecahedral gold nanoparticles were grown from spherical seeds. We synthesized spherical seeds using an aqueous solution containing HAuCl_4 and CTAB. The gold precursor was reduced by NaBH_4 , and spherical seeds whose diameter was smaller than 5 nm were prepared. After the seed solution was diluted in deionized water (1:10), 1.6 mL of 100 mM CTAB, 0.25 mL of 10 mM HAuCl_4 , 0.95 mL of 400 mM AA, and 5 μL of the diluted seed solution were added to 8 mL of deionized water in sequence. These growth solutions were aged for 15 min at 28 °C to grow gold nanoparticles, after which the solution became red in color.

Figure 3.3a shows an SEM micrograph of well-ordered rhombic dodecahedral nanoparticles on a silicon wafer. This ordered assembly represents the high synthetic yield and uniform size of the resultant particles. Average yield of the rhombic dodecahedral nanoparticles was 85%. The particles were hexagonally arrayed, which is typically observed for uniform-sized rhombic dodecahedral nanoparticles.^{25,33} Figure 3.3b shows magnified SEM micrographs with illustrated models taken in various directions. Each set of a particle image and model is well-fitted to the geometry of a rhombic dodecahedron that consists of 12 identical rhombic faces. The edge length of a single rhombic dodecahedral nanoparticle was 25 nm with a diameter of 40 nm, and these particles were synthesized with good monodispersity. Their good monodispersity originates from the nature of the seed-mediated method, which makes particles of uniform size during the growth stage.^{59,60}

Figure 3.4a shows a TEM micrograph and the SAED pattern of a nanoparticle that proves the geometry of nanoparticles. In Figure 3.4a, a rhombic

dodecahedral particle lies on the substrate and shows elongated hexagonal outline with a flat rhombic face looking upward. The SAED pattern was obtained by an electron beam that penetrated perpendicular to upper rhombic face. This diffraction pattern exhibits a typical tendency of gold single crystal along the $\{110\}$ zone axis and well-matched with the geometry of the rhombic dodecahedral gold nanocrystal.⁶¹ Figure 3.4b is high-resolution TEM micrograph and its fast Fourier transform (FFT) pattern which shows lattice image projected along $\langle 110 \rangle$ direction. Figure 3.4c is a TEM micrograph and the corresponding SAED pattern along another direction. The midpoint vertex of the particle is one of the vertices in the $\langle 100 \rangle$ direction of rhombic dodecahedral gold nanocrystal. Interestingly, several diffraction spots in Figure 3.4d are not concentrated at the center of each spot but rather are separated into five spots so that they appear to be crossed shapes. Such spot patterns were also observed for the gold rhombic dodecahedral particles synthesized by Park et al. and Huang et al.,^{31,62} which may have resulted from double diffraction.^{63,64} This distinctive pattern can be regarded as evidence for the synthesis of rhombic dodecahedral gold nanoparticles.³¹

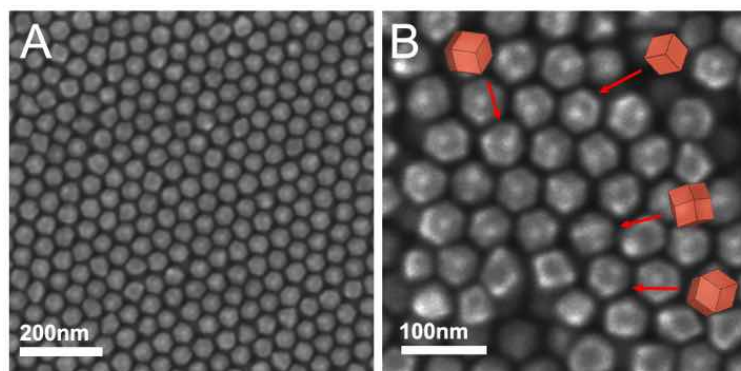


Figure 3.3 SEM micrographs of 40nm rhombic dodecahedral gold nanoparticles. (a) Low magnification SEM micrograph showing the assembly of rhombic dodecahedral particles. (b) High magnification SEM micrograph with illustrated images of rhombic dodecahedral nanoparticles.

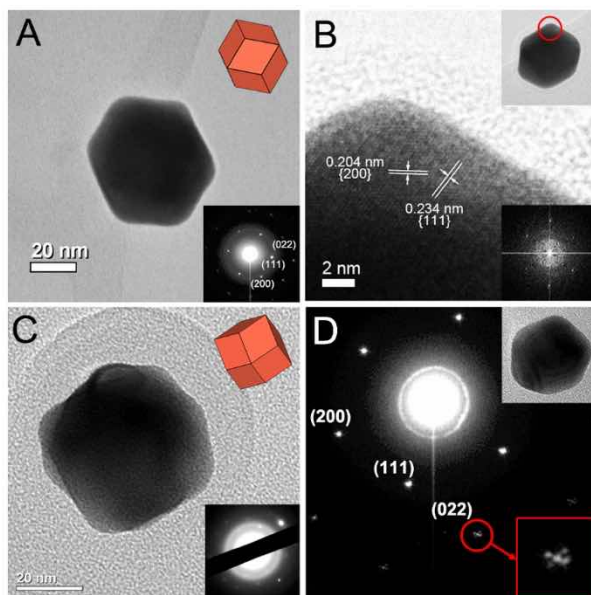


Figure 3.4 TEM characterization of rhombic dodecahedral gold nanoparticles. (a) TEM micrograph with an illustrated model of a single rhombic dodecahedral particle. Inset is the corresponding SAED pattern of a rhombic dodecahedral particle along the $[02\bar{2}]$ zone axis. (b) HRTEM micrograph of a rhombic dodecahedral gold nanoparticle. Inset is an overall image of particle and the corresponding FFT pattern of given lattice image. (c) TEM micrograph with an illustrated model of a single rhombic dodecahedral particle from another viewpoint. Inset is the corresponding SAED pattern. (d) SAED pattern along the $[02\bar{2}]$ zone axis, which was obtained from the particle shown in the inset micrograph in the upper right corner. The red circle indicates a spot from a crossed shape, and its magnified image is located at the bottom right corner.

3.3.2 Morphology diagram: Interplay between CTAB and ascorbic acid

Key parameters determining the particle shape during the formation of gold nanoparticles were the compositions of CTAB and AA. To explain how the shape evolution was affected by the composition of the growth solution, we performed experiments that systematically adjusted the CTAB and AA concentrations at the growth stage. The concentration of CTAB was changed from 15 mM to 45 mM, and that of AA was changed from 3mM to 71mM. Figure 3.5 shows SEM micrographs of resulting particle shapes that obtained from 9 mM to 71 mM of AA. In this region, spherical seeds grew to cuboctahedral, cubic, and rhombic dodecahedral shape. When [AA] was lower than 3 mM, however, a rod shape of gold nanoparticles was observed with triangular or hexagonal plates (Figure 3.6), which was typically reported in the synthesis of a gold nanorod shape without silver.

For the clear description of shape evolution trends of gold nanoparticles, a morphology diagram (Figure 3.7a) was constructed as a function of [CTAB] and [AA] in growth solution. The shaded areas indicate the concentration ranges of resulting particle shapes, and the approximate borders between the areas are drawn. Figures 3.7b–3.7e are representative SEM micrographs of rod, cuboctahedral, cubic and rhombic dodecahedral nanocrystals accompanied by illustrated images. The diameter of a cuboctahedron particle was 40 nm and the edge length of a cubic particle was 46 nm.

Focusing on the effect of CTAB, we found that with increasing CTAB concentration, cubes were easily synthesized at a wider range of AA concentrations. A cubic shape was obtained for AA concentrations of 9 mM to 18 mM at a CTAB concentration of 15 mM, which is shown in Figure 3.7d. When the CTAB

concentration increased to 30 mM, a cubic shape was formed for AA concentrations from 18 mM to 35 mM, which is a wider range than the case of 15 mM CTAB. At 45 mM CTAB, cubes were formed, and no other morphologies were found above 35 mM AA under our experimental conditions. This observation supports that CTAB promotes the formation of cubic particles via a stabilizing effect which was widely reported by many researchers. Murphy et al. reported that CTAB tends to bind preferentially to {100} planes and reduces their surface energy.⁶⁵ To further understand the effect of CTAB, the concept of halide adlayers was introduced. Halide anions such as Cl⁻, Br⁻ in solution readily adsorb to the gold surface, and the positively charged ammonium head of CTAB adsorbs to the negatively charged adlayer via electrostatic forces.^{66,67} Consequently, the halide ions, which directly bind to the gold surface, induce CTAB to build surfactant layer which hinders the reduction of gold ions onto surface of gold nanoparticles. Also, it has been reported that the bromide ion, in particular, passivates {100} facets of gold.^{33,65,68} Therefore, the tendency of cube formation described in Figure 3.7a can be explained by considering the bromide ions of CTAB which influence the {100} facets.

For a fixed concentration of CTAB, it was observed that the final shape of gold nanoparticles was determined by the concentration of AA. At a CTAB concentration of 15 mM, the final shape variously changed in sequence from a cuboctahedron to a cube and finally to a rhombic dodecahedron as the AA concentration increased from 3 mM to 71 mM. A similar tendency was also demonstrated at 30 mM CTAB. To account for this tendency, the correlation of AA with CTAB should be considered. Although CTAB stabilizes the {100} planes of the gold surface, AA accelerates the reduction of gold ions and influences the kinetic growth of nanoparticles. Previous studies suggested that AA facilitates the reduction of metal nanoparticles and the formation of kinetically driven shapes.^{20,69} When CTAB and AA coexist in the growth solution, it was well known that their

competition affects the difference in the relative growth rate along a specific crystallographic direction for each gold nanoparticle.⁷⁰ By controlling the relative growth rate, various shapes of metal nanocrystals can be synthesized,^{17,50,71} and here we observed the diverse shape evolution that depends on the concentrations of CTAB and AA. In the presence of CTAB, the {100} facets have the lowest surface energy among low index facets due to the binding effect of CTAB.^{12,65,72} When the concentration of AA is low and the reduction rate slows, growth rate along the <100> direction becomes lower than other directions because {100} facets are strongly bound by CTAB, causing the disappearance of other facets. Finally, the gold nanocrystals grow to the cubic shape enveloped with {100} facets. At high AA concentrations above 27 mM, however, rhombic dodecahedral gold nanocrystals were synthesized exposing {110} facets. This result implies that AA kinetically encourages the formation of {110} facets by accelerating growth along the <100> direction.

If AA concentration is lower than that of cube formation, the final product can be an intermediate shape of cubic nanoparticles due to slow reduction rate. 40 nm cuboctahedral gold nanoparticles (Figure 3.7c) were found when the AA concentration was 9 mM, which exposing {111} facets and {100} facets simultaneously. At such low [AA] condition, growth rate of gold nanoparticles becomes slower and addition of gold atoms along the specific growth direction decreases. In fact, it was reported that cuboctahedral nanoparticles were found in the intermediate stage of cube formation, and a metal atom addition along <111> direction lead to the formation of cube.⁷² Thus, the lower AA concentration retarded the growth along <111> direction and caused the formation of cuboctahedral gold nanoparticles.

Collectively, Figure 3.7 represents the morphology diagram as a function of CTAB and AA and demonstrates that the competition of CTAB and AA affects the morphology formation. As the CTAB concentration increases, it is difficult to accelerate the reduction rate of gold atoms because of increased the steric hindrance of surfactant bilayer. On this account, it is insufficient to synthesize rhombic dodecahedral shape when [CTAB] was 45 mM, even though the AA concentration increased to 71 mM. Instead of various shapes, the cubic shape with stable {100} planes was synthesized dominantly in a wider range of the AA concentration. At the lower CTAB concentration, however, the reduction rate can be increased easily as the AA concentration increases and consequently various morphologies including the kinetically driven rhombic dodecahedral shape were obtained. Therefore, the concentration of AA should be adjusted simultaneously with the CTAB concentration to obtain desired morphology. Our study emphasizes the importance of relative ratio of CTAB and AA in controlling the shape evolution of gold nanoparticles. By using this concept along with the morphology diagram, a final morphology of a specific composition can be predicted.

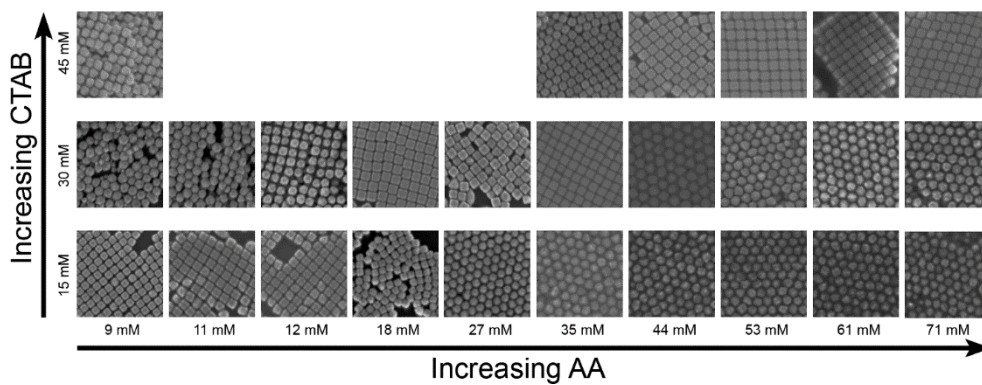


Figure 3.5 SEM micrographs of gold nanoparticles with varying the concentrations of CTAB and AA, ranging from 9 mM to 71 mM of AA and from 15 mM to 45 mM of CTAB.

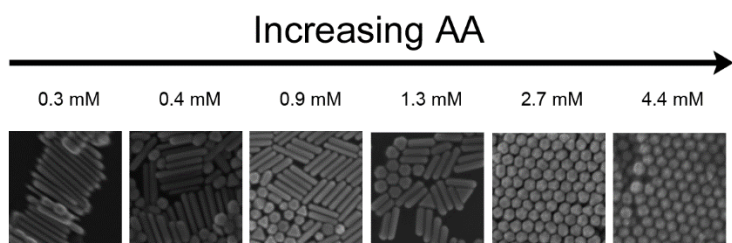


Figure 3.6 SEM images of gold nanoparticles with varying AA concentration from 0.3 mM to 4.4 mM of AA and fixing CTAB concentration at 15 mM.

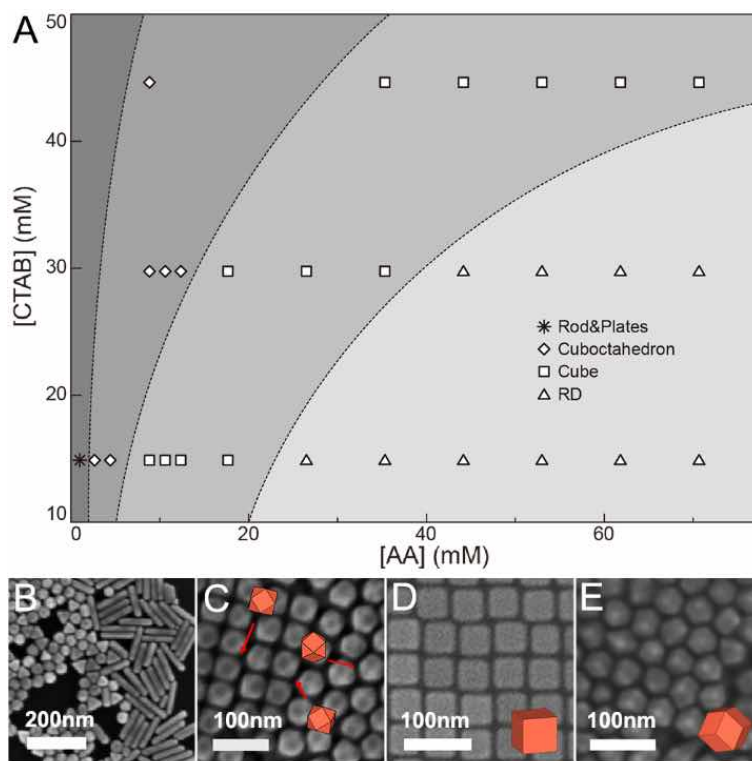


Figure 3.7 (a) Morphology diagram of gold nanoparticle shapes as a function of the CTAB and ascorbic acid concentrations. RD indicates rhombic dodecahedron. The small elliptical area near the y-axis represents the synthetic conditions of the rod and plates. (b) –(e) Representative SEM micrographs with illustrated images. (b) Rod and plate (length: 180 nm), (c) Cuboctahedron (40 nm), (d) Cube (46 nm), (e) Rhombic Dodecahedron (40 nm).

3.3.3 Generality of morphology diagram

The morphology diagram constructed here can be used to explain the previous results obtained by others, thus proving its generality. In Table 3.2, we summarized the compositions of other systems previously reported and those of the current study. For the estimation of seed concentration, we assumed that all Au ions in the seed solution were consumed during the formation of seed particles and the diameter of each particle is 3.5 nm. The crystal structure of gold is face-centered cubic, so each unit cell contains 4 atoms of gold. The lattice parameter of gold is 0.40786 nm and thereby the number of atoms in the unit volume and in each particle can be calculated. According to the calculated result, a 3.5 nm seed particle consists of 1324 gold atoms. Finally, the particle concentration of the seed solution is produced from dividing the molar concentration of Au ions by 1324, and $[Au_{seed}]$ of the growth solution is 1.03×10^{-8} mM (Figure 3.8a). In addition, concentration of seed was obtained from calculating the number of gold atoms contained in the 46 nm cubic gold nanoparticles. We assumed that all the gold ions were consumed in the growth solution for formation of cubic nanoparticles. The crystal structure of gold is face-centered cubic, and each unit cell contains 4 atoms of gold. The lattice parameter of gold is 0.40786 nm and thereby the number of atoms in the unit volume can be calculated. According to the calculated result, a 46 nm cubic particle consists of 5738523 gold atoms. Finally, the particle concentration of the seed solution is produced from dividing the molar concentration of Au ions by 5738523, and then $[Au_{seed}]$ of the growth solution is 3.24×10^{-8} mM (Figure 3.8b).

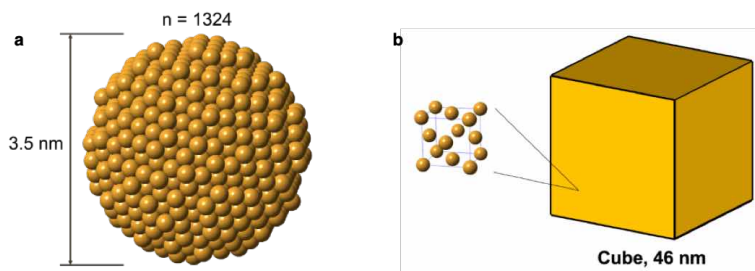


Figure 3.8 Estimation for the number of Au atoms in (a) 3.5 nm seed nanoparticle and (b) 46 nm cubic nanoparticle.

Table 3.2 Synthetic conditions based on a single-step, seed-mediated method for gold nanocrystals using a CTAB/AA system without any additives as the growth solution and the resulting major morphologies. The concentrations of seed were produced in two ways. Seed concentration produced by calculating ^a the total amount of gold ions in the seed solutions and the number of gold atoms in each seed or ^b the total amount of gold ions in the growth solutions and the number of gold atoms in a 46 nm cubic particle.

Ref.	[Au _{seed}] (mM)	[CTAB] (mM)	[AA] (mM)	[CTAB]/[AA]	Particle shape
		15	0.3 - 0.9	17 - 50	rod
		15	0.9 - 1.3	12 - 17	hexagon and triangle
		15	3 - 5	3.37 - 5.61	
		30	9 - 11	2.41 - 3.37	cuboctahedron
This work	^a 1.03 x 10 ⁻⁸	45	9	5.05	
	^b 3.24 x 10 ⁻⁸	15	9 - 18	0.84 - 1.68	
		30	18 - 35	0.84 - 1.68	cube
		45	35 - 71	0.63 - 1.26	
		15	26 - 71	0.21 - 0.56	
		30	44 - 53	0.56 - 0.67	RD
⁴⁴	4.7 x 10 ⁻⁵	59.7	0.5	119.4	sphere (5.5 nm)
	1.88 x 10 ⁻⁵	71.6	0.5	143.2	sphere (8 nm)
⁴³	4.69 x 10 ⁻⁷	99.3	0.5	198.6	rod (74 nm x 16 nm)
⁴¹	1 x 10 ⁻⁶	95	0.64	148.43	rod (475 nm x 15 nm)

	1×10^{-6}	95	3	31.7	rod (90 nm x 15 nm)
	3×10^{-6}	95	3	31.7	rod (75 nm x 10 nm)
	5×10^{-6}	95	3	31.7	rod (50 nm x 10 nm)
	2.49×10^{-8}	16	3	5.33	hexagon (70 nm)
12	2.49×10^{-8}	16	6	2.67	cube (66 nm)
	2.49×10^{-8}	16	12	1.33	star-shape (66 nm)
	2.49×10^{-7}	16	6	2.67	triangle (35 nm)

Several papers reported that a rod shape was formed at high concentration of CTAB (95 - 99.3 mM) and low concentration of AA (0.5 - 3 mM). Due to the high concentration of CTAB the value of ratio $[CTAB]/[AA]$ is large (31-148). This is well-matched with our value ($[CTAB]/[AA]$: 17 - 50) where rod is synthesized in our morphology diagram. From this result, it is concluded that rod shape is formed at high concentration of CTAB and high value of $[CTAB]/[AA]$. On the other hand, when the $[CTAB]/[AA]$ is low, various shapes can be formed. In our experimental condition, cuboctahedron ($[CTAB]/[AA]$: 3.37 - 5.61), cube ($[CTAB]/[AA]$: 0.84 - 1.68), and RD ($[CTAB]/[AA]$: 0.21 - 0.56) shape were synthesized. Also, various shapes reported in the Ref. 12 which is similar to our $[CTAB]$ range, and shape transition trend from hexagon to cube is similar to that of our study. However, the concentration range for each shape is slightly deviating from our system. For example, the 66 nm cube was obtained when $[CTAB]/[AA]$ ratio was 2.67 in Ref. 12, but this ratio corresponds to the cuboctahedron in our system. We believe that this discrepancy originates from different seed concentration because the amount of CTAB and AA associated per particle at the given seed concentration changed. Therefore, we think that different seed concentration results in such a shift in the concentration range of our morphology diagram.

In order to prove the effect of seed concentration, we performed experiments by varying the concentration of seeds in the condition of $[CTAB] = 15$ mM and $[AA] = 4.4$ mM where the cuboctahedral nanoparticles were synthesized. We set the higher and lower concentration of seeds than the initial concentration used in the morphology diagram because the seed concentration can be calculated to be 1.03×10^{-8} or 3.24×10^{-8} depending on the assumption described in experimental section. Even though these values are in the same order of magnitude, the effect on the growth stage is significant so that the resulting morphology can be very different. Figure 3.9a, 3.9b, and 3.9c are results of particles obtained in the cuboctahedron

synthetic composition at high seed concentration (2 Cs), standard (Cs), and lower concentration (0.5 Cs) respectively (Cs means the original seed concentration). In the case of higher concentration of seed, small size of cuboctahedron shape was formed (Figure 3.9a). We think that small size was formed due to the higher concentration of seed and the cuboctahedron shape was achieved due to the reduced effect of CTAB and AA. On the other hand, when we decreased the seed concentration, a cubic shape with large diameter was obtained. We believe that this is due to the increased CTAB and AA effect on each particle. The diameters of synthesized particles were 34 nm, 43 nm, and 61 nm at the seed concentration of 2 Cs, Cs, and 0.5 Cs respectively. Figure 3.9d is the UV/vis spectra of each particle. In the case of the lower seed concentration, synthesized particles became larger with the diameter of 61 nm and consequently, resonance peak position was red-shifted. It is noticeable that we successfully synthesized 61 nm Cube at 0.5 Cs using the same [CTAB] and [AA] condition that produced 40 nm cuboctahedron at Cs. Indeed, synthesized 61 nm cube is similar to the 66 nm cube in the Ref. 12, which was synthesized at the seed concentration of 2.49×10^{-8} using the concentration of CTAB (16 mM) and AA (6 mM). This result supports that concentration range in the morphology diagram can shift depending on the seed concentration. It suggests that our morphology diagram can be generalized and extended, and it explains the overall trends of morphology changes observed by others. However, for further generalization of the morphology diagram suggested in here, the seed concentration should be considered as another important parameter. A three-dimensional diagram as a function of [CTAB], [AA], and $[Au_{\text{seed}}]$ will improve understanding the interplay of all these parameters in morphology control.

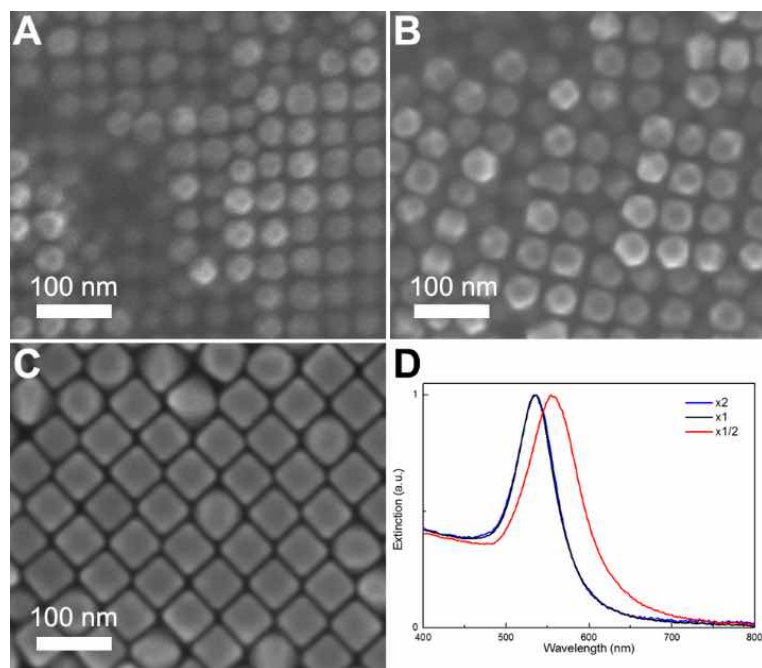


Figure 3.9 (a-c) SEM micrographs of gold nanoparticles with varying the concentrations of seed ($[CTAB] = 15 \text{ mM}$, $[AA] = 4.4 \text{ mM}$). The concentrations of seed particles in each growth solution were (a) 2 Cs (cuboctahedron, 34 nm), (b) Cs (cuboctahedron, 43 nm), (c) 0.5 Cs (cube, 61 nm). Cs means the original seed concentration. (d) UV-vis extinction spectra of (a) – (c). Each spectrum was normalized to its maximum value at resonance peak.

One of the interesting features of our study is the simplicity of the CTAB/AA system without using any additives. Commonly, it has been reported that it is difficult to control and synthesize uniform shapes at high concentrations of bromide ion due to its strong binding to the gold surface.⁴¹ In order to circumvent the strong binding of bromide ions, CTAC which had chloride counterions with small amount of bromide ion has been introduced instead of CTAB.⁴¹ Here, we demonstrate that various shapes of gold nanoparticles can be synthesized only using CTAB and AA. Modulating the ratio between CTAB and AA allows modification of the relative growth rate along directions. Using simple CTAB and AA system can facilitate the shape control of gold nanoparticles and our morphology diagram will be useful to predict desired morphology.

3.3.4 Two-step growth: High-Miller-index nanoparticles

As an extension of systematic morphology control, a nanocrystal morphology with exposing high-Miller-index planes can be synthesized in our CTAB and AA system. High-index nanoparticles can have more extended categories of polyhedral morphologies than those of low-index nanoparticles, which are more beneficial to various applications. Sharp or concave morphology of high-index nanoparticles is more advantageous to capture the light into the nanoscale region, and low-coordination atoms on the surface of those nanoparticles usually have increased catalytic activity. However, since high-index crystal plane is more unstable than the low-index planes, colloidal synthesis of the high-index nanoparticles is relatively difficult. In particular, for the $\{hkl\}$ -indexed planes, exposure of unstable kink site is the most unfavorable situation in terms of surface energy. Previously studies on the synthesis of high index nanoparticles required a harsh reaction condition such as periodic potential⁷³ or high-temperature conditions,⁷⁴ or surface passivation using metal and halide ions as secondary additives.²⁰ In addition, if the seed particles have well-defined morphology and crystal planes themselves, the further growth of nanocrystal can manipulate the overall morphology of the nanocrystal after the final step. For example, spherical Au nanoparticles with 18-nm diameter can grow into the Au nanorods,¹⁹ and further overgrowth of this nanorods can produce the nanoparticles with different morphology and material composition.^{75,76} The anisotropic morphology of the seed nanorods changed the overgrowth kinetics.

Here, we synthesized $\{hkl\}$ -exposed high-index nanoparticles by two-step growth method featuring the re-growth of the low-index nanoparticles with a well-defined polyhedral shape as seeds. Starting from the $\{100\}$ -exposed cubic seed, second-step growth was carried out at a high growth rate, and it was possible to

synthesize high-index nanoparticles (Figure 3.10a). According to the SEM images, the synthesized nanoparticles are highly monodispersed (Figure 3.10b) and show crystal facets split into 48 planes, which corresponds to $\{hkl\}$ -exposed hexoctahedron morphology. TEM images obtained along the $[111]$, $[100]$, and $[110]$ zone axis proved that the projected outlines of the nanoparticles are well-fitted to the ideal hexoctahedron shapes. As the seed already contains pre-formed facet, we can manipulate growth direction resulting in more complex structure. From this result, it is suggested that the surface structure of the seed-mediate the overgrowth morphology and the facile formation of high-index nanoparticles.

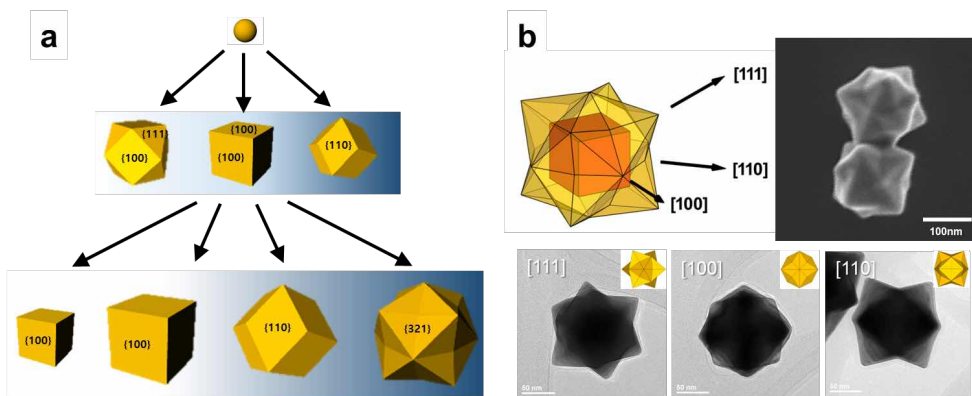


Figure 3.10 (a) Schematic of two-step growth (b) SEM and TEM image of synthesized hexooctahedron

3.4 Conclusion

In conclusion, uniform rhombic dodecahedral gold nanoparticles, which were enclosed by {110} facets, were synthesized in a simple system consisting of CTAB and AA. To further understand the relationship between CTAB and AA, a series of experiments was carried out, and cuboctahedral and cubic nanocrystals were also obtained. Based on these observations, a morphology diagram that shows the trends in shape evolution was constructed as a function of the concentrations of CTAB and AA. This diagram implies that CTAB affects the {100} gold surface and suppresses growth on that plane and that AA promotes the growth of gold nanoparticles, especially along the $\langle 100 \rangle$ direction. As a result of the cooperative effects of CTAB and AA, the final shape of the gold nanoparticles is determined by the ratio of CTAB and AA concentrations. We believe that improved understanding of gold nanoparticle synthesis with a simple CTAB/AA system will contribute to the sensible design of morphologies. Our morphology diagram can be used to predict and create various other morphologies of nanoparticles that may be difficult to achieve using a conventional approach.

3.5 Methods

Chemicals

Gold(III) chloride trihydrate ($\text{HAuCl}_4 \cdot 3\text{H}_2\text{O}$: 99.9%), sodium borohydride (NaBH_4 : 99%), cetyltrimethylammonium bromide (CTAB: 99%) and L-ascorbic acid (AA: 99%) were purchased from Sigma-Aldrich and were used without further purification. High purity deionized water ($18.2 \text{ M}\Omega \text{ cm}^{-1}$) was used in all of the procedures.

Preparation of nanocrystals with various shapes

The different-shaped gold nanoparticles produced here were prepared by the modification of the seeded growth method.^{12,72} Firstly, gold seeds were synthesized by the rapid reduction of gold salts. 0.25 mL of HAuCl_4 (10 mM) was added into 7.5 mL of aqueous solution consisting of CTAB (100 mM), and the transparent solution turned to yellow. Then, 0.8 mL of NaBH_4 (10 mM) was injected and the color of the solution instantly changed to dark brown. Followed by rapid mixing for 2 min, the seed solution was kept at 28 °C for 3 h to decompose the remaining NaBH_4 . The solution was diluted (1 : 10) in deionized water for the synthesis of larger particles.

The formation of gold nanoparticles with various shapes was controlled by the concentrations of CTAB and AA in the growth solution. Typically, a growth solution was prepared by adding HAuCl_4 (10 mM, 0.2 mL) and AA (0.95 mL) into a solution of CTAB (1.6 mL) in DI water (8 mL). Different concentrations of CTAB (100 mM, 200 mM, 300 mM) and AA (5 mM–800 mM) were used for the different morphologies of gold nanoparticles to be synthesized. For example, 50 mM, 100 mM or 400 mM of AA was injected into the growth solutions for the cuboctahedron,

cube and rhombic dodecahedron respectively after adding CTAB (100 mM) to the growth solution. The formation of each shape of gold nanoparticles was performed by adding 5 μL of diluted Au seeds to the growth solution. The growth solution was thoroughly mixed and left undisturbed for 15 min. The resultant nanocrystals were centrifuged to remove excess reagents and were additionally washed and redispersed in water.

Characterization

Scanning electron microscopy (SEM) micrographs were obtained using a Zeiss Supra 55 VP instrument operating at 2 kV. The samples were prepared by dropping colloidal solutions onto silicon wafers. Transmission electron microscopy (TEM) micrographs and selected area electron diffraction (SAED) patterns were obtained using a JEOL JEM-3000F FEG TEM instrument. UV/Vis extinction spectra were taken using a Thermo Scientific NanoDrop 2000c UV/Vis Spectrophotometer in the 220–840 nm wavelength region.

3.6 Bibliography

1. Tao, A. R.; Habas, S.; Yang, P. Shape Control of Colloidal Metal Nanocrystals. *Small* **2008**, *4* (3), 310–325.
2. Schimpf, S.; Lucas, M.; Mohr, C.; Rodemerck, U.; Brückner, A.; Radnik, J.; Hofmeister, H.; Claus, P. Supported Gold Nanoparticles: In-Depth Catalyst Characterization and Application in Hydrogenation and Oxidation Reactions. *Catal. Today* **2002**, *72* (1–2), 63–78.
3. Haruta, M.; Tsubota, S.; Kobayashi, T.; Kageyama, H.; Genet, M. J.; Delmon, B. Low-Temperature Oxidation of CO over Gold Supported on TiO₂, α -Fe₂O₃, and Co₃O₄. *J. Catal.* **1993**, *144* (1), 175–192.
4. Turner, M.; Golovko, V. B.; Vaughan, O. P. H.; Abdulkin, P.; Berenguer-Murcia, A.; Tikhov, M. S.; Johnson, B. F. G.; Lambert, R. M. Selective Oxidation with Dioxygen by Gold Nanoparticle Catalysts Derived from 55-Atom Clusters. *Nature* **2008**, *454* (7207), 981–983.
5. Xia, Y.; Xiong, Y.; Lim, B.; Skrabalak, S. E. Shape-Controlled Synthesis of Metal Nanocrystals: Simple Chemistry Meets Complex Physics? *Angew. Chem. Int. Ed.* **2009**, *48* (1), 60–103.
6. Jones, M. R.; Osberg, K. D.; Macfarlane, R. J.; Langille, M. R.; Mirkin, C. A. Templated Techniques for the Synthesis and Assembly of Plasmonic Nanostructures. *Chem. Rev.* **2011**, *111* (6), 3736–3827.
7. Dreaden, E. C.; Alkilany, A. M.; Huang, X.; Murphy, C. J.; El-Sayed, M. A. The Golden Age: Gold Nanoparticles for Biomedicine. *Chem. Soc. Rev.* **2012**, *41* (7), 2740–2779.
8. Huang, X.; Jain, P. K.; El-Sayed, I. H.; El-Sayed, M. A. Gold Nanoparticles: Interesting Optical Properties and Recent Applications in Cancer Diagnostics and Therapy. *Nanomedicine* **2007**, *2* (5), 681–693.
9. Wu, D.-Y.; Liu, X.-M.; Duan, S.; Xu, X.; Ren, B.; Lin, S.-H.; Tian, Z.-Q. Chemical Enhancement Effects in SERS Spectra: A Quantum Chemical Study of Pyridine Interacting with Copper, Silver, Gold and Platinum Metals. *J. Phys. Chem. C* **2008**, *112* (11), 4195–4204.
10. Dreaden, E. C.; Mackey, M. A.; Huang, X.; Kang, B.; El-Sayed, M. A. Beating Cancer in Multiple Ways Using Nanogold. *Chem. Soc. Rev.* **2011**, *40* (7), 3391.

11. Wang, L.; Liu, Y.; Li, W.; Jiang, X.; Ji, Y.; Wu, X.; Xu, L.; Qiu, Y.; Zhao, K.; Wei, T.; et al. Selective Targeting of Gold Nanorods at the Mitochondria of Cancer Cells: Implications for Cancer Therapy. *Nano Lett.* **2011**, *11* (2), 772–780.
12. Sau, T. K.; Murphy, C. J. Room Temperature, High-Yield Synthesis of Multiple Shapes of Gold Nanoparticles in Aqueous Solution. *J. Am. Chem. Soc.* **2004**, *126* (28), 8648–8649.
13. Yu; Chang, S.-S.; Lee, C.-L.; Wang, C. R. C. Gold Nanorods: Electrochemical Synthesis and Optical Properties. *J. Phys. Chem. B* **1997**, *101* (34), 6661–6664.
14. Torigoe, K.; Esumi, K. Preparation of Colloidal Gold by Photoreduction of Tetracyanoaurate(1-)-Cationic Surfactant Complexes. *Langmuir* **1992**, *8* (1), 59–63.
15. Zhang, J.; Du, J.; Han, B.; Liu, Z.; Jiang, T.; Zhang, Z. Sonochemical Formation of Single-Crystalline Gold Nanobelts. *Angew. Chem. Int. Ed.* **2006**, *45* (7), 1116–1119.
16. Grzelczak, M.; Sánchez-Iglesias, A.; Rodríguez-González, B.; Alvarez-Puebla, R.; Pérez-Juste, J.; Liz-Marzán, L. M. Influence of Iodide Ions on the Growth of Gold Nanorods: Tuning Tip Curvature and Surface Plasmon Resonance. *Adv. Funct. Mater.* **2008**, *18* (23), 3780–3786.
17. Murphy, C. J.; Thompson, L. B.; Alkilany, A. M.; Sisco, P. N.; Boulos, S. P.; Sivapalan, S. T.; Yang, J. A.; Chernak, D. J.; Huang, J. The Many Faces of Gold Nanorods. *J. Phys. Chem. Lett.* **2010**, *1* (19), 2867–2875.
18. Lohse, S. E.; Murphy, C. J. The Quest for Shape Control: A History of Gold Nanorod Synthesis. *Chem. Mater.* **2013**, *25* (8), 1250–1261.
19. Gole, A.; Murphy, C. J. Seed-Mediated Synthesis of Gold Nanorods: Role of the Size and Nature of the Seed. *Chem. Mater.* **2004**, *16* (19), 3633–3640.
20. Langille, M. R.; Personick, M. L.; Zhang, J.; Mirkin, C. A. Defining Rules for the Shape Evolution of Gold Nanoparticles. *J. Am. Chem. Soc.* **2012**, *134* (35), 14542–14554.
21. Ha, T. H.; Koo, H.-J.; Chung, B. H. Shape-Controlled Syntheses of Gold Nanoprisms and Nanorods Influenced by Specific Adsorption of Halide Ions. *J. Phys. Chem. C* **2007**, *111* (3), 1123–1130.

22. Xiong, Y.; Cai, H.; Yin, Y.; Xia, Y. Synthesis and Characterization of Fivefold Twinned Nanorods and Right Bipyramids of Palladium. *Chem. Phys. Lett.* **2007**, *440* (4–6), 273–278.
23. Liu, M.; Guyot-Sionnest, P. Mechanism of Silver(I)-Assisted Growth of Gold Nanorods and Bipyramids. *J. Phys. Chem. B* **2005**, *109* (47), 22192–22200.
24. Personick, M. L.; Langille, M. R.; Zhang, J.; Harris, N.; Schatz, G. C.; Mirkin, C. A. Synthesis and Isolation of {110}-Faceted Gold Bipyramids and Rhombic Dodecahedra. *J. Am. Chem. Soc.* **2011**, *133* (16), 6170–6173.
25. Personick, M. L.; Langille, M. R.; Zhang, J.; Mirkin, C. A. Shape Control of Gold Nanoparticles by Silver Underpotential Deposition. *Nano Lett.* **2011**, *11* (8), 3394–3398.
26. Chung, P.-J.; Lyu, L.-M.; Huang, M. H. Seed-Mediated and Iodide-Assisted Synthesis of Gold Nanocrystals with Systematic Shape Evolution from Rhombic Dodecahedral to Octahedral Structures. *Chem. - A Eur. J.* **2011**, *17* (35), 9746–9752.
27. Xia, Y.; Xia, X.; Peng, H.-C. Shape-Controlled Synthesis of Colloidal Metal Nanocrystals: Thermodynamic versus Kinetic Products. *J. Am. Chem. Soc.* **2015**, *137* (25), 7947–7966.
28. Jana, N. R.; Gearheart, L.; Murphy, C. J. Wet Chemical Synthesis of Silver Nanorods and Nanowires of Controllable Aspect Ratio. *Chem. Commun.* **2001**, No. 7, 617–618.
29. Murphy, C. J.; Jana, N. R. Controlling the Aspect Ratio of Inorganic Nanorods and Nanowires. *Adv. Mater.* **2002**.
30. Jana, N. R.; Gearheart, L.; Murphy, C. J. Seed-Mediated Growth Approach for Shape-Controlled Synthesis of Spheroidal and Rod-like Gold Nanoparticles Using a Surfactant Template. *Adv. Mater.* **2001**, *13* (18), 1389–1393.
31. Wu, H.-L.; Kuo, C.-H.; Huang, M. H. Seed-Mediated Synthesis of Gold Nanocrystals with Systematic Shape Evolution from Cubic to Trisoctahedral and Rhombic Dodecahedral Structures. *Langmuir* **2010**, *26* (14), 12307–12313.
32. Di Gianvincenzo, P.; Marradi, M.; Martínez-Ávila, O. M.; Bedoya, L. M.; Alcamí, J.; Penadés, S. Gold Nanoparticles Capped with Sulfate-Ended Ligands as Anti-HIV Agents. *Bioorg. Med. Chem. Lett.* **2010**, *20* (9), 2718–

2721.

33. Niu, W.; Zheng, S.; Wang, D.; Liu, X.; Li, H.; Han, S.; Chen, J.; Tang, Z.; Xu, G. Selective Synthesis of Single-Crystalline Rhombic Dodecahedral, Octahedral, and Cubic Gold Nanocrystals. *J. Am. Chem. Soc.* **2009**, *131* (2), 697–703.
34. Gao, J.; Bender, C. M.; Murphy, C. J. Dependence of the Gold Nanorod Aspect Ratio on the Nature of the Directing Surfactant in Aqueous Solution. *Langmuir* **2003**, *19* (21), 9065–9070.
35. Kou, X.; Ni, W.; Tsung, C.-K.; Chan, K.; Lin, H.-Q.; Stucky, G. D.; Wang, J. Growth of Gold Bipyramids with Improved Yield and Their Curvature-Directed Oxidation. *Small* **2007**, *3* (12), 2103–2113.
36. Ji, X.; Song, X.; Li, J.; Bai, Y.; Yang, W.; Peng, X. Size Control of Gold Nanocrystals in Citrate Reduction: The Third Role of Citrate. *J. Am. Chem. Soc.* **2007**, *129* (45), 13939–13948.
37. Turkevich, J.; Stevenson, P. C.; Hillier, J. A Study of the Nucleation and Growth Processes in the Synthesis of Colloidal Gold. *Discussions of the Faraday Society*. 1951.
38. Xie, W.; Su, L.; Donfack, P.; Shen, A.; Zhou, X.; Sackmann, M.; Materny, A.; Hu, J. Synthesis of Gold Nanopeanuts by Citrate Reduction of Gold Chloride on Gold–Silver Core–Shell Nanoparticles. *Chem. Commun.* **2009**, No. 35, 5263.
39. Kuo, C.-H.; Huang, M. H. Synthesis of Branched Gold Nanocrystals by a Seeding Growth Approach. *Langmuir* **2005**, *21* (5), 2012–2016.
40. Kuo, C.-H.; Chiang, T.-F.; Chen, L.-J.; Huang, M. H. Synthesis of Highly Faceted Pentagonal- and Hexagonal-Shaped Gold Nanoparticles with Controlled Sizes by Sodium Dodecyl Sulfate. *Langmuir* **2004**, *20* (18), 7820–7824.
41. Sau, T. K.; Murphy, C. J. Seeded High Yield Synthesis of Short Au Nanorods in Aqueous Solution. *Langmuir* **2004**, *20* (15), 6414–6420.
42. Zhou, M.; Bron, M.; Schuhmann, W. Controlled Synthesis of Gold Nanostructures by a Thermal Approach. *J. Nanosci. Nanotechnol.* **2008**, *8* (7), 3465–3472.
43. Jana, N. R.; Gearheart, L.; Murphy, C. J. Wet Chemical Synthesis of High Aspect Ratio Cylindrical Gold Nanorods. *J. Phys. Chem. B* **2001**, *105* (19),

4065–4067.

44. Jana, N. R.; Gearheart, L.; Murphy, C. J. Seeding Growth for Size Control of 5–40 Nm Diameter Gold Nanoparticles. *Langmuir* **2001**, *17* (22), 6782–6786.
45. Chen, H. M.; Liu, R.-S.; Tsai, D. P. A Versatile Route to the Controlled Synthesis of Gold Nanostructures. *Cryst. Growth Des.* **2009**, *9* (5), 2079–2087.
46. Pazos-Perez, N.; Garcia de Abajo, F. J.; Fery, A.; Alvarez-Puebla, R. A. From Nano to Micro: Synthesis and Optical Properties of Homogeneous Spheroidal Gold Particles and Their Superlattices. *Langmuir* **2012**, *28* (24), 8909–8914.
47. Fan, X.; Guo, Z. R.; Hong, J. M.; Zhang, Y.; Zhang, J. N.; Gu, N. Size-Controlled Growth of Colloidal Gold Nanoplates and Their High-Purity Acquisition. *Nanotechnology* **2010**, *21* (10), 105602.
48. Iqbal, M.; Chung, Y.-I.; Tae, G. An Enhanced Synthesis of Gold Nanorods by the Addition of Pluronic (F-127) via a Seed Mediated Growth Process. *J. Mater. Chem.* **2007**, *17* (4), 335–342.
49. Kim, F.; Sohn, K.; Wu, J.; Huang, J. Chemical Synthesis of Gold Nanowires in Acidic Solutions. *J. Am. Chem. Soc.* **2008**, *130* (44), 14442–14443.
50. Nikoobakht, B.; El-Sayed, M. A. Preparation and Growth Mechanism of Gold Nanorods (NRs) Using Seed-Mediated Growth Method. *Chem. Mater.* **2003**, *15* (10), 1957–1962.
51. Sau, T. K.; Murphy, C. J. Role of Ions in the Colloidal Synthesis of Gold Nanowires. *Philos. Mag.* **2007**, *87* (14–15), 2143–2158.
52. Ming, T.; Feng, W.; Tang, Q.; Wang, F.; Sun, L.; Wang, J.; Yan, C. Growth of Tetrahedral Gold Nanocrystals with High-Index Facets. *J. Am. Chem. Soc.* **2009**, *131* (45), 16350–16351.
53. Keul, H. A.; Möller, M.; Bockstaller, M. R. Selective Exposition of High and Low Density Crystal Facets of Gold Nanocrystals Using the Seeded-Growth Technique. *CrystEngComm* **2011**, *13* (3), 850–856.
54. Narayanan, R.; Lipert, R. J.; Porter, M. D. Cetyltrimethylammonium Bromide-Modified Spherical and Cube-Like Gold Nanoparticles as Extrinsic Raman Labels in Surface-Enhanced Raman Spectroscopy Based

- Heterogeneous Immunoassays. *Anal. Chem.* **2008**, *80* (6), 2265–2271.
55. Sun, J.; Guan, M.; Shang, T.; Gao, C.; Xu, Z.; Zhu, J. Selective Synthesis of Gold Cuboid and Decahedral Nanoparticles Regulated and Controlled by Cu²⁺ Ions. *Cryst. Growth Des.* **2008**, *8* (3), 906–910.
 56. Ye, X.; Jin, L.; Caglayan, H.; Chen, J.; Xing, G.; Zheng, C.; Doan-Nguyen, V.; Kang, Y.; Engheta, N.; Kagan, C. R.; et al. Improved Size-Tunable Synthesis of Monodisperse Gold Nanorods through the Use of Aromatic Additives. *ACS Nano* **2012**, *6* (3), 2804–2817.
 57. Nehl, C. L.; Liao, H.; Hafner, J. H. Optical Properties of Star-Shaped Gold Nanoparticles. *Nano Lett.* **2006**, *6* (4), 683–688.
 58. Sahoo, G. P.; Bar, H.; Bhui, D. K.; Sarkar, P.; Samanta, S.; Pyne, S.; Ash, S.; Misra, A. Synthesis and Photo Physical Properties of Star Shaped Gold Nanoparticles. *Colloids Surf. A* **2011**, *375* (1–3), 30–34.
 59. Peng, X.; Wickham, J.; Alivisatos, A. P. Kinetics of II-VI and III-V Colloidal Semiconductor Nanocrystal Growth: “Focusing” of Size Distributions. *J. Am. Chem. Soc.* **1998**, *120* (21), 5343–5344.
 60. Reiss, H. The Growth of Uniform Colloidal Dispersions. *J. Chem. Phys.* **1951**, *19* (4), 482–487.
 61. Wang, Z. L. *Reflection Electron Microscopy and Spectroscopy for Surface Analysis*; Cambridge University Press: Cambridge, 1996.
 62. Choi, K. W.; Kim, D. Y.; Zhong, X.-L.; Li, Z.-Y.; Im, S. H.; Park, O. O. Robust Synthesis of Gold Rhombic Dodecahedra with Well-Controlled Sizes and Their Optical Properties. *CrystEngComm* **2013**, *15* (2), 252–258.
 63. Monzen, R.; Seo, T.; Sakai, T.; Watanabe, C. Precipitation Processes in a Cu–0.9 Mass% Be Single Crystal. *Mater. Trans.* **2006**, *47* (12), 2925–2934.
 64. Williams, D. B.; Carter, C. B. *Transmission Electron Microscopy*; Springer US: Boston, MA, 2009.
 65. Johnson, C. J.; Dujardin, E.; Davis, S. A.; Murphy, C. J.; Mann, S. Growth and Form of Gold Nanorods Prepared by Seed-Mediated, Surfactant-Directed Synthesis. *J. Mater. Chem.* **2002**, *12* (6), 1765–1770.
 66. Magnussen, O. M. Ordered Anion Adlayers on Metal Electrode Surfaces. *Chem. Rev.* **2002**, *102* (3), 679–726.

67. Velegol, S. B.; Fleming, B. D.; Biggs, S.; Wanless, E. J.; Tilton, R. D. Counterion Effects on Hexadecyltrimethylammonium Surfactant Adsorption and Self-Assembly on Silica. *Langmuir* **2000**, *16* (6), 2548–2556.
68. Garg, N.; Scholl, C.; Mohanty, A.; Jin, R. The Role of Bromide Ions in Seeding Growth of Au Nanorods. *Langmuir* **2010**, *26* (12), 10271–10276.
69. Lee, Y. W.; Kim, D.; Hong, J. W.; Kang, S. W.; Lee, S. B.; Han, S. W. Kinetically Controlled Growth of Polyhedral Bimetallic Alloy Nanocrystals Exclusively Bound by High-Index Facets: Au-Pd Hexoctahedra. *Small* **2013**, *9* (5), 660–665.
70. Petroski, J. M.; Wang, Z. L.; Green, T. C.; El-Sayed, M. A. Kinetically Controlled Growth and Shape Formation Mechanism of Platinum Nanoparticles. *J. Phys. Chem. B* **1998**, *102* (18), 3316–3320.
71. Grzelczak, M.; Pérez-Juste, J.; Mulvaney, P.; Liz-Marzán, L. M. Shape Control in Gold Nanoparticle Synthesis. *Chem. Soc. Rev.* **2008**, *37* (9), 1783.
72. Dovgolevsky, E.; Haick, H. Direct Observation of the Transition Point Between Quasi-Spherical and Cubic Nanoparticles in a Two-Step Seed-Mediated Growth Method. *Small* **2008**, *4* (11), 2059–2066.
73. Tian, N.; Zhou, Z.-Y.; Sun, S.-G.; Ding, Y.; Wang, Z. L. Synthesis of Tetrahedral Platinum Nanocrystals with High-Index Facets and High Electro-Oxidation Activity. *Science* **2007**, *316* (5825), 732–735.
74. Hong, J. W.; Lee, S.-U.; Lee, Y. W.; Han, S. W. Hexoctahedral Au Nanocrystals with High-Index Facets and Their Optical and Surface-Enhanced Raman Scattering Properties. *J. Am. Chem. Soc.* **2012**, *134* (10), 4565–4568.
75. Kou, X.; Zhang, S.; Yang, Z.; Tsung, C.-K.; Stucky, G. D.; Sun, L.; Wang, J.; Yan, C. Glutathione- and Cysteine-Induced Transverse Overgrowth on Gold Nanorods. *J. Am. Chem. Soc.* **2007**, *129* (20), 6402–6404.
76. Xiang, Y.; Wu, X.; Liu, D.; Jiang, X.; Chu, W.; Li, Z.; Ma, Y.; Zhou, W.; Xie, S. Formation of Rectangularly Shaped Pd/Au Bimetallic Nanorods: Evidence for Competing Growth of the Pd Shell between the {110} and {100} Side Facets of Au Nanorods. *Nano Lett.* **2006**, *6* (10), 2290–2294.

Chapter 4. Peptide-Directed Synthesis of Plasmonic Helicoid Nanoparticle

4.1 Introduction

Chirality is of importance not only due to enantioselective activity in biochemical reactions,¹ but also the recent development of chiral metamaterials with exceptional light-manipulating capabilities, including polarization control,²⁻⁴ negative refractive index,⁵ and chiral sensing.⁶ To produce chiral nanostructures, nanofabrication techniques such as lithography⁷ and molecular self-assembly⁸⁻¹¹ are required; however, to date, large-scale and facile fabrication methods for three-dimensional chiral structures remain a challenge. In this regard, chirality transfer represents a simpler and more efficient pathway to controlling the chiral morphology.¹²⁻¹⁸ Although a few pioneering studies^{12,19} have described the transfer of molecular chirality into micrometer-sized helical ceramic crystals, this phenomenon has not yet been implemented for metal nanoparticles in the 100-nm range. Here, we developed a novel synthetic strategy for chiral gold nanoparticles that involves amino acid and peptides to enable the control of optical activity, handedness, and wavelength dependence. The key requirement for achieving unique chiral structures is the formation of high-Miller-index $\{hkl\}$ surfaces ($h \neq k \neq l \neq 0$) that are intrinsically chiral owing to the presence of kink sites²⁰⁻²² in the nanoparticles during particle growth. Due to the chiral counterparts in the inorganic surface and molecules, enantioselective interaction occurs at the interface resulting in the asymmetrical evolution of nanoparticles and formation of a novel helicoid morphology composed of highly twisted chiral elements. We anticipate that our ‘amino acid/peptide-encoded’ strategy will aid in the rational design and fabrication

of chiral nanostructures for use in novel applications as three-dimensional chiral metamaterials.

4.2 Result and discussion

4.2.1 Formation of chiral nanoparticles: 432 helicoid I and II

To control the chiral morphology of gold nanoparticles through molecular interactions of amino acid or peptides with high-index surfaces, an aqueous-based, two-step growth method with organothiols additives was devised. As the first step, low-index plane exposed (LIPE) gold nanoparticles with uniform size were synthesized using the well-established seed-mediated method.^{23–25} In the second step, cysteine or cysteine-based peptides with a chiral conformation were used to ‘encode’ chirality into the gold nanoparticles. The molecules were added to the growth solution where the pre-synthesized LIPE gold nanoparticles evolved into high-index plane exposed (HIPE) nanoparticles with the reduction of Au⁺ ions (see Methods for detailed experimental procedure). Au-S bonding and interaction of other functional groups in the amino acid or peptides involve in the nanoparticle growth process with chiral selectivity. Peptide-sequence-specific interaction has been investigated for the nanomaterial growth and optical property control.^{26–29} Changes in the growth components, such as the peptide sequence and concentration, and seed morphology affected the growth kinetics and induced the dynamic morphological evolution of LIPE gold seed nanoparticles into chiral nanoparticles.

Circular dichroism (CD) and scanning electron microscopy (SEM) analyses confirmed the synthesis of chiral plasmonic nanoparticles. Notably, the conformation of the molecule used for the synthesis controlled the handedness of the

resulting nanoparticles. Depending on whether L- or D- amino acids were added during the nanoparticle growth process, the opposite rotational direction in nanoparticle form was observed, thus exhibiting the exact opposite chiroptical responses. For example, when L-cysteine (L-Cys) and D-cysteine (D-Cys) were used as an additive, the extinction spectrum of the synthesized nanoparticles was identical and was dependent only on the overall particle size (Figure 4.1a). However, the measured CD spectra were inverted with respect to each other but had the same peak positions at 569 and 699 nm (Figure 4.1b). In both cases, the outline morphologies of the synthesized nanoparticles were cube-like with a side length of 150 nm. A unique feature of the synthesized L-Cys and D-Cys nanoparticles is that the vertices were protruded and the edges, which typically bridge the two vertices in a cube, were split into two. As shown in the inset of Figure 4.2a (i and ii), the two split edges are pointed toward opposite directions with $-\phi$ degree tilt and become protruded. In the case of nanoparticles synthesized with D-Cys, the split edges were tilted in the opposite direction at $+\phi$ degree (Figure 4.2b). Along the [111] view, the tilted edges protruded as tripods at each vertex of a cube, thereby contributing to the chirality of the synthesized gold nanoparticles (Figure 4.2a, inset ii). The tripods with 40-nm thickness and 100-nm length are assembled, making nano-gaps inside a helicoid cube. The right-handed chiral structures synthesized using L-Cys as an additive exhibited increased absorption of left-circular polarized light at 569 nm, whereas an opposite chiroptical response was observed for the left-handed chiral structures synthesized using D-Cys. The yield of the chiral nanoparticles using this synthesis approach was $\sim 81\%$ ($N = 989$, Figure 4.3)

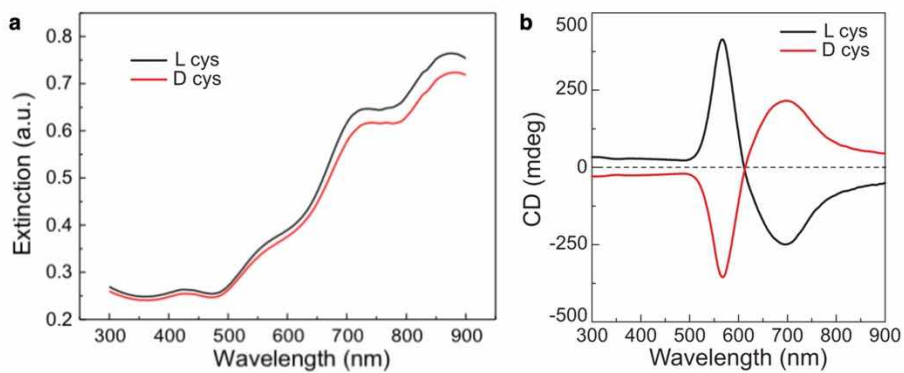


Figure 4.1 (a) Extinction and (b) CD spectra of 432 helicoid I nanoparticles synthesized using L-Cys (black) and D-Cys (red).

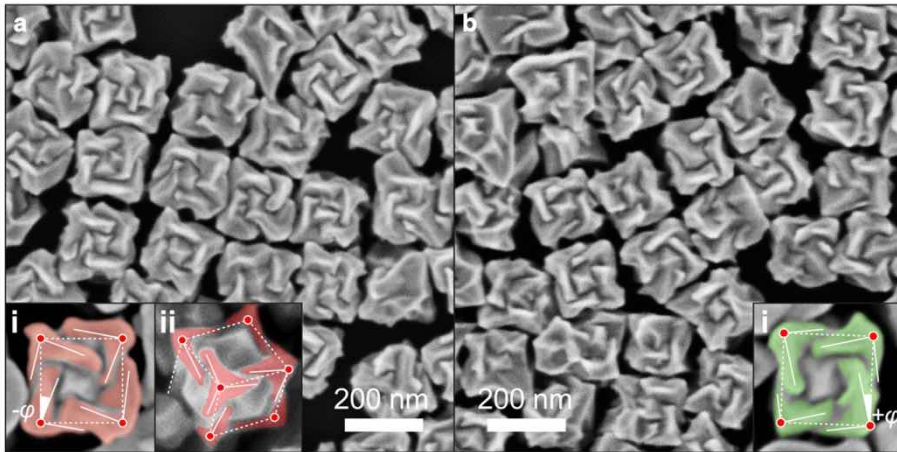


Figure 4.2 Opposite handedness of 3D plasmonic helicoids controlled by cysteine chirality transfer. (a) SEM image of synthesized L-Cys nanoparticles. Inset shows a highlighted edge tilted by $-\varphi$ degrees (solid line) with the vertices (red dots) and cubic outline (dashed line) indicated and viewed along the $[100]$ (i) and $[111]$ (ii) directions. (b) SEM image of synthesized D-Cys nanoparticles. The inset shows a highlighted edge, cubic outline (dashed line), and tilt angle ($+\varphi$ degrees).



Figure 4.3 Large-area SEM image of 432 helicoid I and corresponding 3D illustration.

Chiral morphology development can be understood by the different growth rates of the two oppositely chiral high-index planes in the presence of L- or D-Cys. In the present growth condition, the absence of cysteine resulted in a stellated octahedron that was differentiated with $\{321\}$ subfacets, called hexoctahedron (Figure. 4.4). The synthesis method reported here can be further utilized to modify other stellated shape nanostructures.^{30,31} $\{321\}$ indexing was assigned by analyzing the relative angles of each edge in the TEM image (Figure. 4.5). This shape has $4/m\bar{3}2/m$ point group symmetry defined by 48 equal triangular faces, which can be clearly visualized from differently positioned multiple particles by SEM (Figure 4.4c). The $\{321\}$ facet is comprised of R (clockwise rotation, $(321)^R$) or S (counterclockwise rotation, $(32\bar{1})^S$) conformation, which is defined by the rotational direction of the low-index microfacets of (100), (110), and (111) at the kink sites (Figure. 4.6).²⁰⁻²² In Figure. 4.4, the pairs of $\{hkl\}$ planes with R/S conformation (rhombus $ABA'B'$) are indicated as purple and yellow areas. R and S triangular regions are alternating, and their distribution is basically symmetrical and achiral. It was observed that the chiral morphologies developed by the shifting and tilting of specific R/S boundaries. The detailed analysis of time-dependent evolution in the case of L-Cys is as follows.

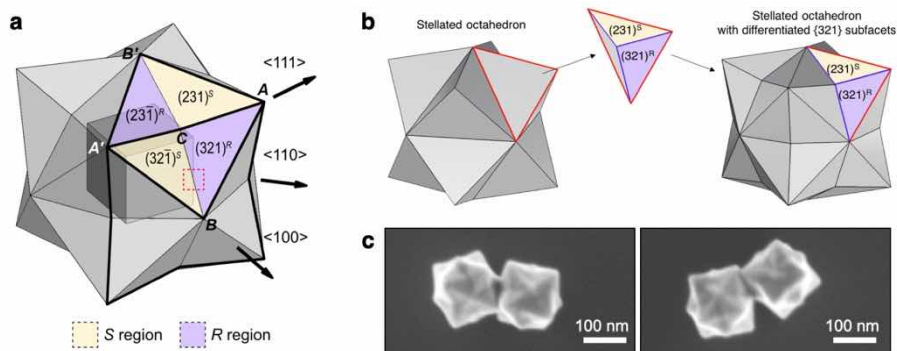


Figure 4.4 Characterization of high-Miller-index nanoparticle. (a) Schematic illustration of stellated octahedron differentiated with high-index facets, so-called hexooctahedron, consisting of $\{321\}^S$, (S-region, yellow) and $\{321\}^R$ (R-region, purple). Vertices of the $[111]$, $[100]$, and $[110]$ directions are indicated as A, B, and C, respectively; A' and B' refer to the symmetric points of A and B, respectively. (b) Detailed illustration of $\{321\}$ subfacet differentiation. Each triangular facet of a stellated octahedron is divided into two convex $\{321\}$ subfacets with R and S surface conformation, respectively. (c) SEM images showing detailed geometry of $\{321\}$ -enclosed nanoparticle.

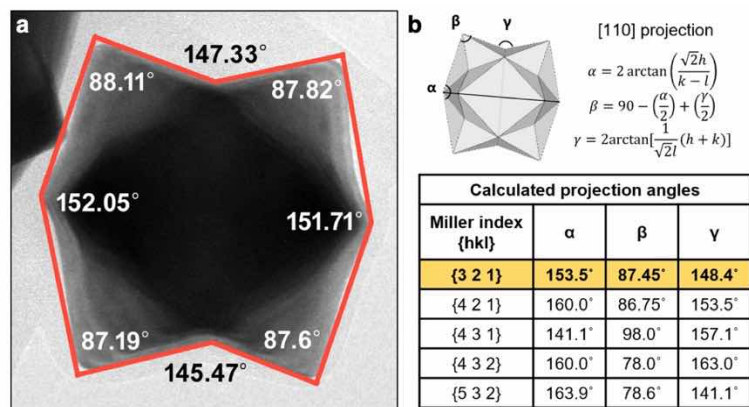


Figure 4.5 Identification of Miller-index for hexoctahedron nanoparticle. (a) Bright-field TEM image along [110] direction showing angles (α , β , γ) between eight outmost edges. (b) Calculated angles between outmost edges of {hkl}-enclosed nanoparticle. The exposed facets were indexed as {321}.

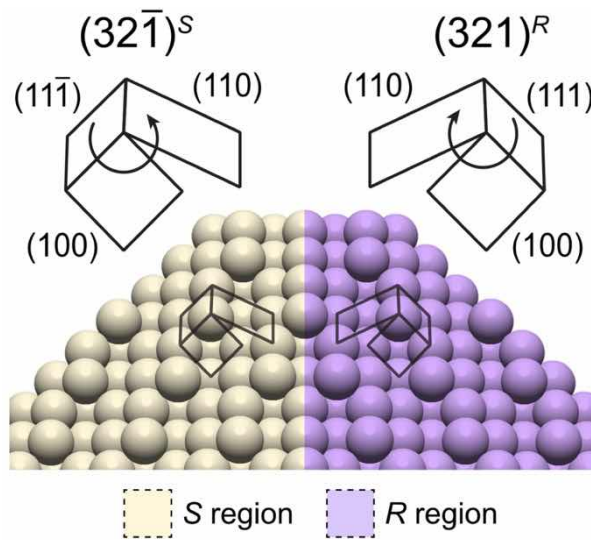


Figure 4.6 Comparison of atomic arrangement of the $(321)^R$ and $(32\bar{1})^S$ gold surfaces. Conformation at kink sites is defined by the rotational direction of low-index microfacets in $(111) \rightarrow (100) \rightarrow (110)$ sequence; clockwise, R -region; counterclockwise, S -region.

The addition of LIPE cube-shaped seeds into the second-step solution containing L-Cys begins the growth. In order to monitor morphology evolution at each time, the reaction was stopped by centrifugation and washing (from 10 min to 120 min). The underlying mechanism of the evolution is most clearly evident in the 20-min case, in which the chiral structures start to develop for the next 20 min (Figure 4.7 and 4.8). For clear visualization, the rhombus $ABA'B'$, which is composed of two sets of R and S regions, is schematically displayed (Figure 4.7, top row) and marked with red dots and dotted white lines in the corresponding SEM images (Figure 4.7, bottom row). Among the R/S boundaries, significant changes, such as split, movement, and overgrowth, were found in \overline{AC} and $\overline{A'C}$ of the rhombus $ABA'B'$, and the 12 equivalent boundaries were changed in the same manner. Both \overline{AC} and $\overline{A'C}$ were tilted by $-\varphi$ degree toward the S regions and protruded with distortion, as indicated by the red-patterned area and arrows in Figure 4.7a and 4.7b. In $[111]$ and $[100]$ directions, the chiral elements formed three- and four-fold symmetry, respectively. As shown in the sequential images of the growth process (Figure 4.8), the twisted edges continued to become thick, laterally growing and evolving into the final morphology, in which the elongated edges were twisted inward (Figure 4.7c). As the mirror symmetry of the R/S region is broken by the distortion, $4/m\bar{3}2/m$ point group symmetry of the stellated octahedron was changed to 432 symmetry. Thus, this chiral morphology was designated as '432 helicoid I'. In case of D-Cys, in the R/S boundary, both \overline{AC} and $\overline{A'C}$ were tilted by $+\varphi$ degree toward the R regions, resulting in the opposite chiral 432 helicoid I.

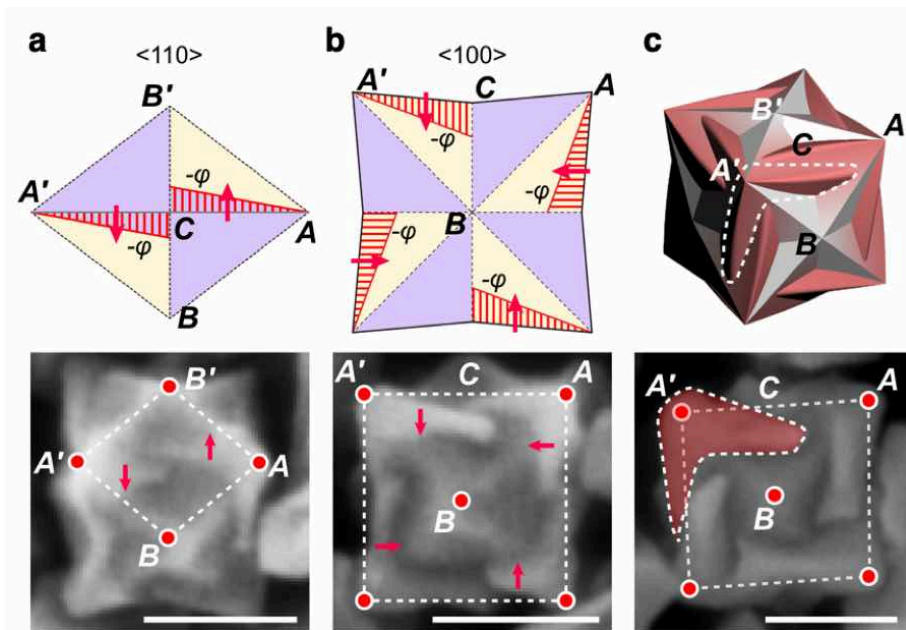


Figure 4.7 Mechanism of chirality evolution for 432 helicoid I. (a,b) Schematic (top) and SEM images (bottom) of R/S pairs showing the morphological development of 432 helicoid I in the presence of L-Cys and viewed along the $[110]$ (a) and $[100]$ (b) directions. Newly developed boundaries are indicated as a red patterned area with arrows, and each vertex is marked on the corresponding SEM image. (c) 3D model and SEM image of the final chiral shape. The newly formed R region is colored in red and the chiral element is indicated by a dashed line.

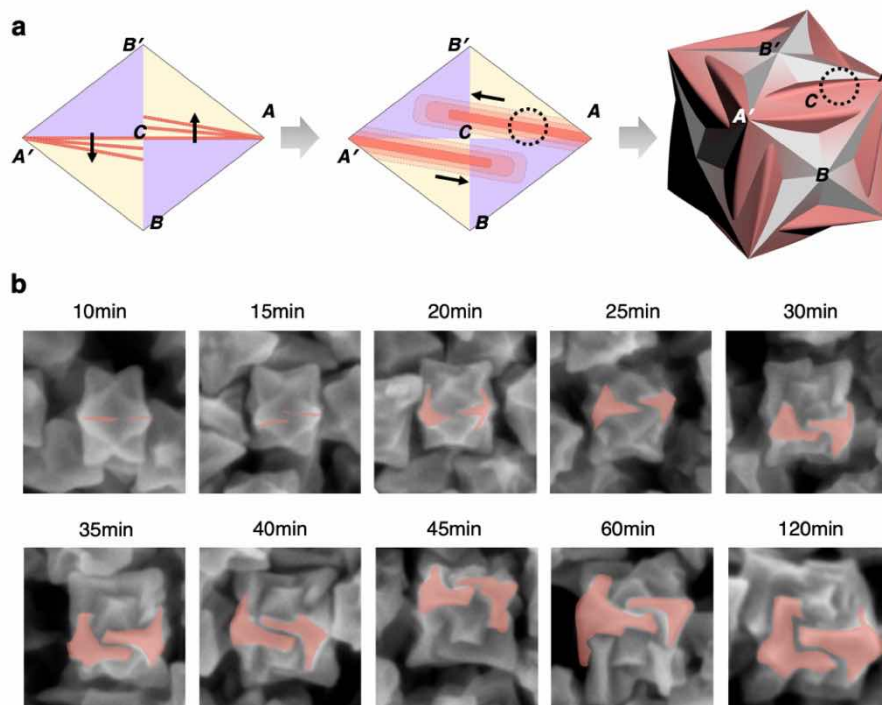


Figure 4.8 Time-dependent morphology transition of 432 helicoid I. (a) Schematic illustration of time-dependent evolution of 432 helicoid I. All models are viewed along $[110]$ direction. Starting from $\{321\}$ -indexed nanoparticle with the same ratio of R and S region, different R/S boundaries are split, thickened, and distorted. (b) SEM images of 432 helicoid I at different growth times. Developed chiral components in 432 helicoid I are highlighted with red.

One of the most interesting features is that the addition of L-glutathione (L-GSH) induces a completely different chiral morphology by shifting another convex R/S boundary (Figure 4.9). A change in the four outer boundaries of rhombus $ABA'B'$ is observed instead of that in the inner \overline{AC} and $\overline{A'C}$ observed in the case of L-Cys. Note that \overline{AC} and $\overline{A'C}$ are convex, while \overline{BC} and $\overline{B'C}$ are concave. Both \overline{AB} and $\overline{A'B'}$ expanded outward and the other boundaries of $\overline{AB'}$ and $\overline{A'B}$ moved inward, creating the distorted boundary of rhombus $ABA'B'$ (Figure 4.9a). Distinctive edge growth was only observed after 40 min in the case of GSH (Figure 4.10). During this stage, as the distortion edge thickened, the chiral components became more distinguishable. Consequently, a pinwheel-like chiral structure with clockwise rotation and four-fold symmetry was manifested along the [100] direction (Figure 4.9b, 4.9c). This helicoid morphology is referred hereafter as '432 helicoid II'. The low-magnification SEM image shows uniformly synthesized 432 helicoid II particles (Figure 4.11).

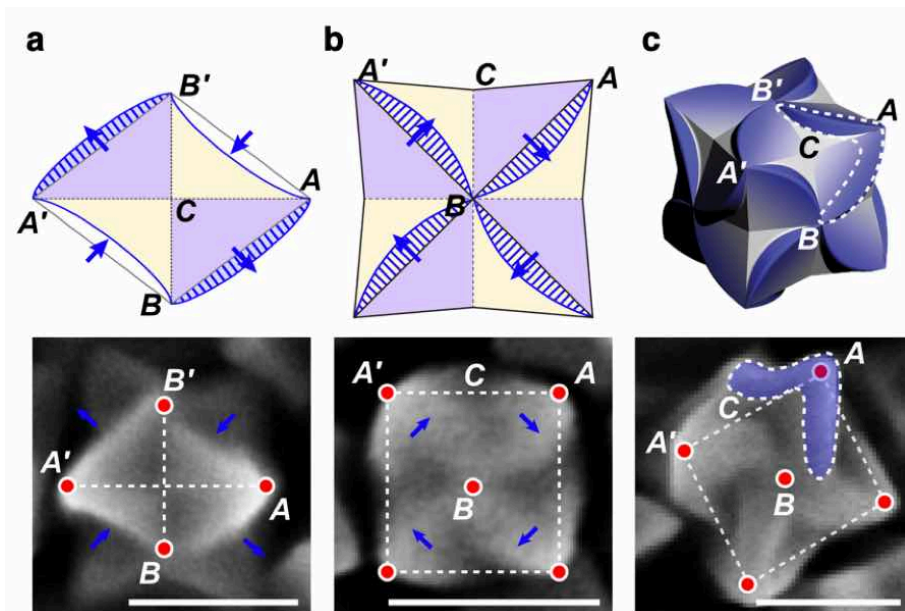


Figure 4.9 Mechanism of chirality evolution for 432 helicoid I. (a, b) Morphological development of 432 helicoid II in the presence of L-GSH viewed along the [110] (a) and [100] (b) directions. (c) Corresponding final chiral shape. Newly formed boundaries and pinwheel-like chiral elements of the final shape are colored in blue. Scale bar, 100 nm.

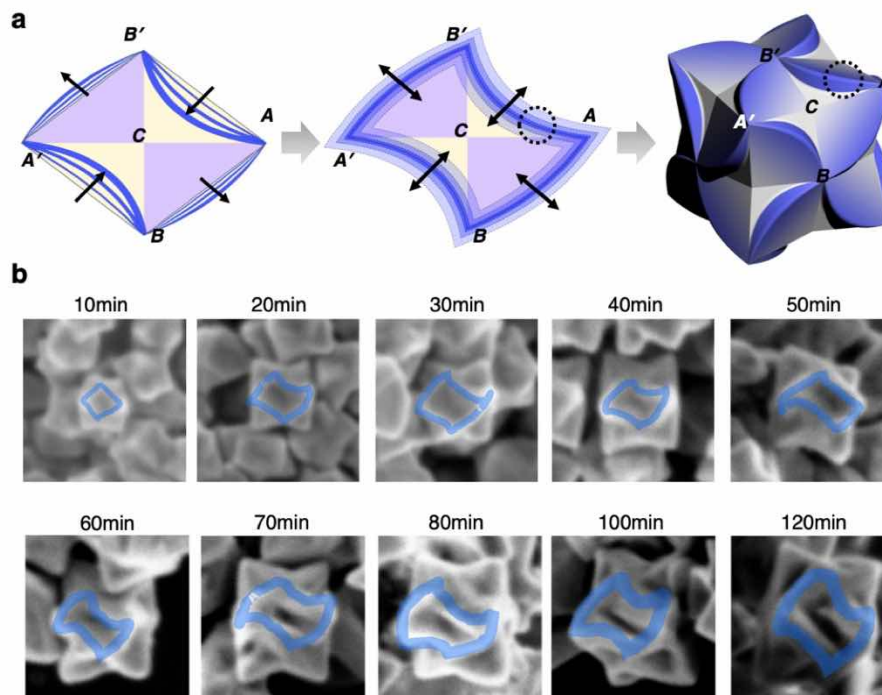


Figure 4.10 Time-dependent morphology transition of 432 helicoid II. (a) Schematic illustration of time-dependent evolution of 432 helicoid II. All models are viewed along $[110]$ direction. Starting from $\{321\}$ -indexed nanoparticle with the same ratio of R and S region, different R/S boundaries are split, thickened, and distorted. (b) SEM images of 432 helicoid II at different growth times. Developed chiral components in 432 helicoid II are highlighted with blue.

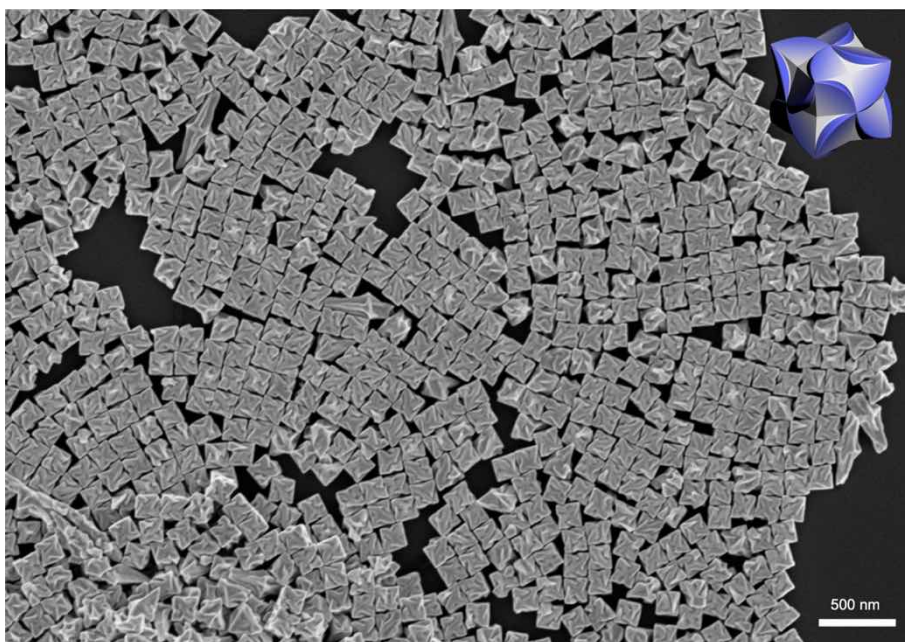


Figure 4.11 Large-area SEM image of 432 helicoid II synthesized with L-GSH.

4.2.2 Mechanism of chirality evolution

In high-resolution TEM (Figure 4.12), various steps and terraces of the subfacets of the chiral nanoparticle at an early stage of growth (20 min) reveal the peptide adsorption on the high-index plane. The TEM data is directly evidence for the involvement of high-index planes in the process of morphological chirality development in 432 helicoid I. Increased adsorption energy demonstrated by temperature-programmed desorption and electrochemical desorption studies further suggest the binding of molecule to a high-index surface (Figure 4.13). Although the intensity is small due to low coverage of Cys on the surface of helicoid I, distinctive peak was observed in Figure 4.13a around 635 K, whereas no peak exists in the case of cube. According to previous studies by the Gellman group,^{16,32} this characteristic feature suggests that L-Cys is attached to high-index planes via stronger interactions compared low-index planes. Additionally, the reductive desorption potentials of Au-S bonding with cube, high-index nanoparticles (stellated octahedron with differentiated {321} subfacets), and helicoid I nanoparticles were analyzed after further saturation of L-Cys. The cyclic voltammetry results in Figure 4.13b show that cathodic peaks were observed near -1.5 V for the high-index and helicoid I and -1.28 V for the cube, which were interpreted as the reductive desorption of thiol at high-index and Au (100) surfaces, respectively.^{33,34} This electrochemical study also supports the strong interaction of L-Cys with kink sites.

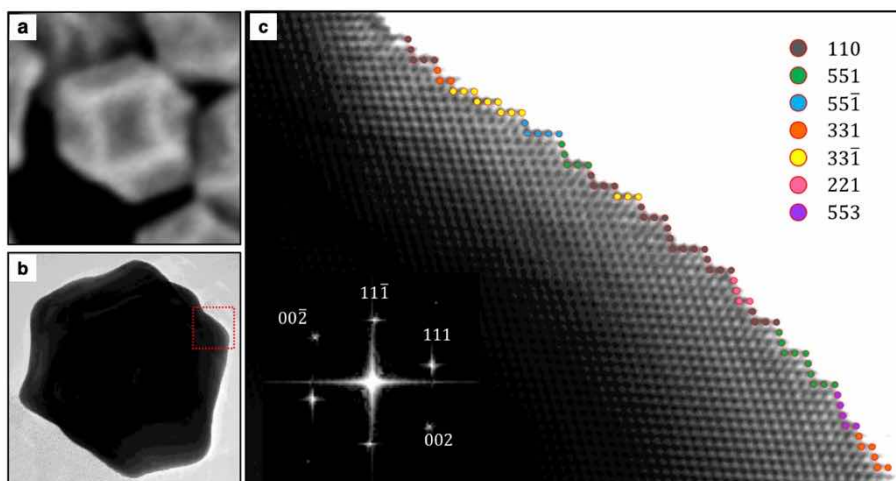


Figure 4.12 Atomic structure of chiral nanoparticle at initial stage. (a-c) SEM image (a) and TEM images (b, c) of chiral nanoparticle after 20-min growth. As the nanoparticle was oriented along $\langle 110 \rangle$ direction, the projected boundaries in TEM image consist of chirally distorted edges. HRTEM image of distorted edge corresponding to the red dotted box in (b). Atoms of microfacets are marked with colored spheres, and different colors are assigned to the Miller index of each microfacet. Based on microfacet nomenclature, the microstructure of (551) can be divided into three units of (111) and two units of $(11\bar{1})$. Inset: Corresponding FFT showing typical patterns along $[1\bar{1}0]$ zone.

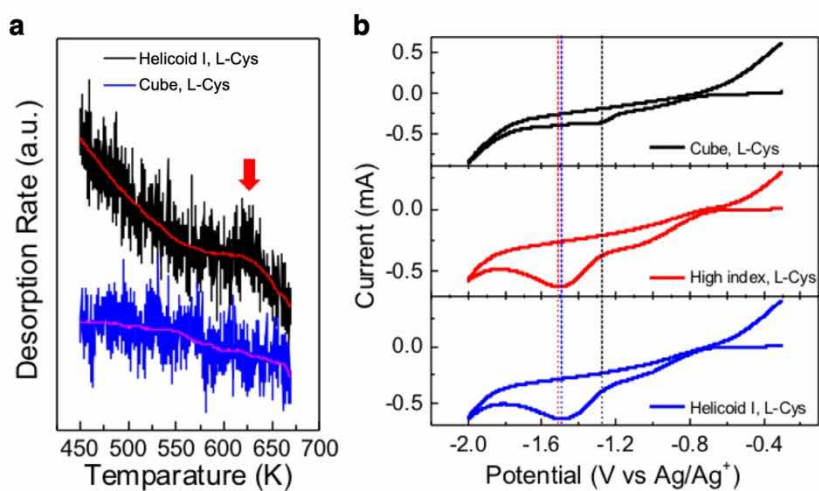


Figure 4.13 Adsorption energy difference of L-cysteine depending on the Miller index of surface. (a) Temperature-programmed desorption (TPD) spectra of L-Cys of helicoid I and low-index cube nanoparticle, monitoring of CO₂ (m/q=44 amu). As the temperature was raised at a heating rate of 3 K/min, helium carrier gas flowed over the dried nanoparticle sample. (b) Cyclic voltammograms for cube, high-index (stellated octahedron with differentiated {321} subfacets), and helicoid I with L-Cys measured in 0.1 M KOH-ethanol solution at a scan rate of 0.1 V/s. Negative peaks in $-1.8 \sim -1.1$ V originate from reductive desorption of L-Cys, and peaks at more negative potential indicates higher adsorption energy.

To experimentally confirm the involvement of -NH_2 and -COOH in selective interaction, an alkyl group was incorporated as a blocker at each N- and C-terminal of L-Cys molecule (Figure 4.14). When the N-terminal is blocked, chirality disappears completely in the morphology during the synthesis, and the g-factor (see Methods) is 0. This means that thiol and amine groups bind with the kinks on $\{321\}$, and the activity of the NH_2 group is critical for the enantioselective interaction at the kink site. This mechanism is also supported by previous studies, showing that the relative location of an amine group with respect to a thiol is the major determinant of the different binding affinities to *R* or *S* kink sites.³⁵⁻³⁷ Meanwhile, when the C-terminal is blocked, the g-factor decreases noticeably, and the chiral morphology becomes irregular and ill-defined. This means that COOH does not bind specifically to the kink site, but bulky group causes the interference for crystal growth direction due to steric hindrance. Therefore, the preferred interaction of L-Cys with the $\{321\}$ planes of *R* regions leads to slower growth in the vertical direction on the *R* regions compared to the *S* regions (Figure 4.15). For this reason, the *R/S* boundary shifts from the *R* to *S* region, accompanied by asymmetrical overgrowth.

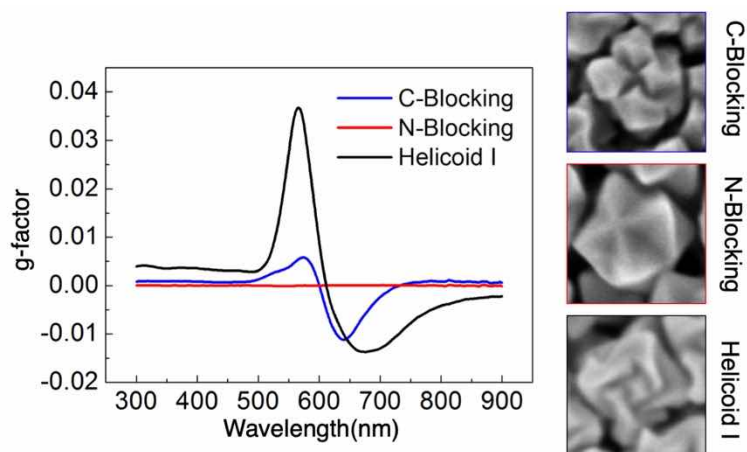


Figure 4.14 Effect of functional group change in L-Cys. Comparison of g-factor and SEM image of synthesized nanoparticles with C-terminal blocked L-Cys (L-cysteine ethyl ester) (top), N-terminal blocked L-Cys (N-acetyl-L-cysteine) (middle), and L-Cys (bottom). C-blocked L-Cys changed the chiral morphology and decreased the CD intensity of the resulting nanoparticles. Nanoparticles produced with N-blocked L-Cys showed achiral morphology without observable CD signal.

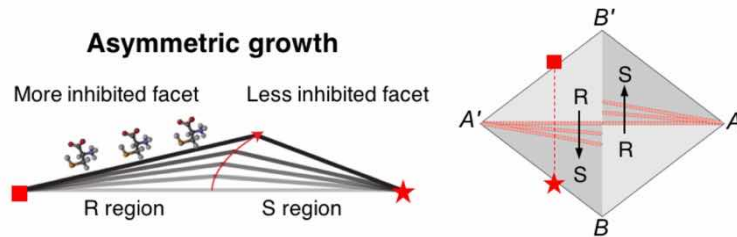


Figure 4.15 Schematic illustration showing asymmetric growth of R and S regions. Left: With the selective attachment of L-Cys in the R region, growth of the surface is inhibited, and the reduced growth results in a gradual increase of the area of the R region. Right: Corresponding surface region of the cross-section is indicated on rhombus ABA'B'.

It is worth mentioning that there were optimum concentrations for amino acid and peptide to achieve a highly twisted morphology (Figure 4.16). For example, in the case of cysteine (L-Cys), the optimum concentration in the growth solution (1.53×10^9 particles/mL) is 100 nM (500 pmol). At lower concentrations, high-index planes are still shown but without observable chirality. At concentrations higher than 100 nM, random and achiral structures were generated by losing specificity. A similar trend was also observed for the glutathione (L-GSH) case, which exhibited the highest g-factor at an optimal range, despite the concentration needed are 25 times higher than L-Cys case (2.5 μ M, 12.5 nmol). For both molecules, a fluorometric assay using a thiol-selective dye was performed to quantify the surface coverage that maximizes the specific chirality control (see Methods). Specifically, after complete growth in the growth solution (100 nM L-Cys), the 432 helicoid I particles were centrifuged and washed for further quantification. The adsorbed L-Cys on 432 helicoid I was separated through Au-S bond cleavage by adopting the previously known desorption method based on NaBH₄ reduction (Figure 4.17).^{38,39} From the schematic 3D model, the surface areas of 432 helicoid I and II were estimated. The surface densities of L-Cys and L-GSH were calculated to be 0.028 and 0.103 nmol/cm², respectively (Figure 4.17c). These values correspond to 0.01 ML and 0.22 ML respectively.^{40,41} Based on the surface density estimation, the average intermolecular distance for L-Cys and L-GSH is expected to be 2.5 nm and 1.3 nm, respectively. Therefore, it can be concluded that under optimized conditions, both molecules have enough room for binding of multiple functional groups. The low coverage seems to be necessary for enantioselective binding and chiral-selective growth because a weak binding motif such as amine and carboxylic groups would be interfered at high concentrations.

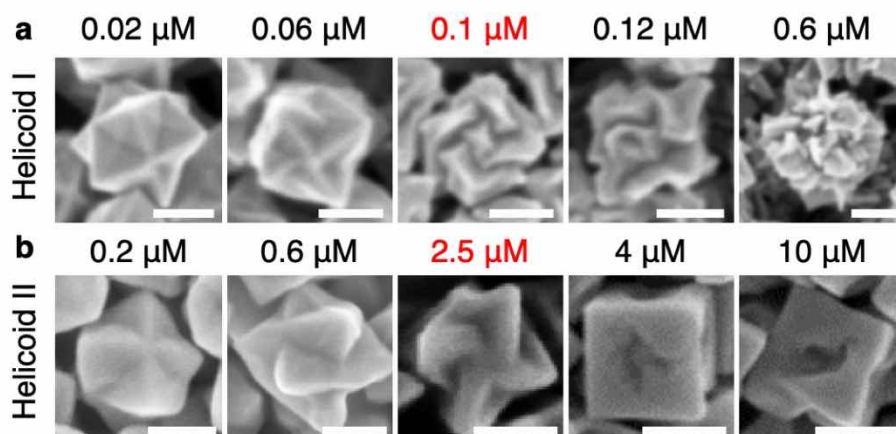


Figure 4.16 Effect of L-Cys and L-GSH concentrations on chiral morphology. (a, b) SEM images of chiral nanoparticles synthesized with different concentrations of Cys (a) and GSH (b). Highest g-factor was observed at optimum amino acid and peptide concentration (red color). At low concentration, only achiral nanoparticles were formed, but with incremental addition, chiral edges started to appear. An excess amount of molecule results in the overgrowth of edges and a significantly decreased CD signal, indicating that an optimal concentration exists for chirality formation. Scale bar, 100 nm.

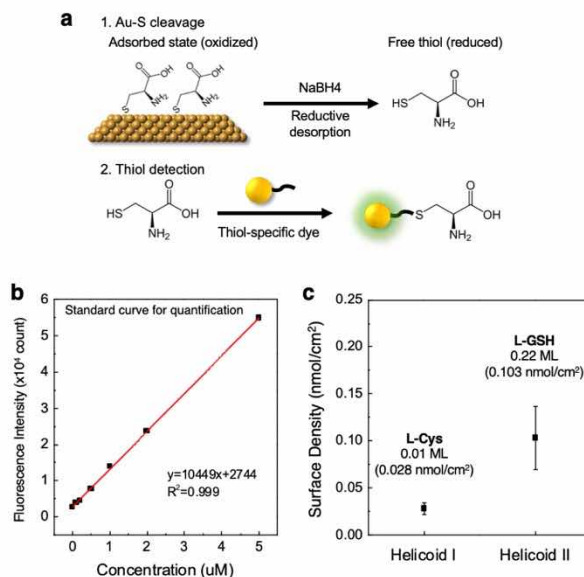


Figure 4.17 Quantification of adsorbed thiol molecule on helicoid nanoparticles. (a) Schematic experimental procedure for thiol quantification on Au surface. The reduction of thiolate by NaBH_4 cleaved Au-S bond, and the thiol group of the released molecule spontaneously reacted with thiol-specific dye, producing a fluorescent derivative. Excitation and emission wavelengths were 405 nm and 535 nm, respectively. (b) Concentration curve from 0 to 5 μM for fluorometric assay of L-Cys. Linear fitting and corresponding R^2 value show good linearity within the measured range. (c) Measured surface density of L-Cys and L-GSH for 432 helicoid I and II, respectively. Surface coverage is calculated by previously reported surface density of L-Cys and L-GSH at the fully saturated monolayer condition.

The different growth directions of 432 helicoid I and II can be understood at the atomic level by looking at $(321)^R$ surrounded by $(312)^S$ and $(231)^S$ in the $[111]$ direction (Figure 4.18). $(321)^R$ is composed of (111) terrace and alternating (100) and (110) microfacets. Different orders of (100) and (110) alternation results in opposite chirality such as $(312)^S$ and $(231)^S$. \overline{AC} , which is important for 432 helicoid I, is the boundary of $(321)^R$ and $(231)^S$, and \overline{AB} , which is important for 432 helicoid II, is the boundary of $(321)^R$ and $(312)^S$. This indicates that L-Cys and L-GSH induce the shift of \overline{AC} boundary in $[\bar{1}01]$ direction and \overline{AB} boundary in $[01\bar{1}]$ direction, respectively. On the $\{321\}$ surface, the Au atoms attach to the microfacets (100) and (110) at the kink, generating a new kink. We propose that the orientation of the adsorbed L-Cys and L-GSH may determine the specific growth direction of the kinks.

From the screening experiment with several peptide sequences, we found that the functional groups of thiol-containing peptide play a key role in determining the chiral morphology. Such substantial morphological differences may arise from alterations in the binding sites and the spatial arrangement of functional groups, as shown in the previous L-Cys blocking experiments (Figure 4.14). Compared to L-Cys, L-GSH has an elongated N-terminus owing to the specific γ -Glu group. We believe that the enantioselective interaction of L-GSH can be additionally benefited from the flexibility of the γ -peptide linkage. When γ -Glu is replaced with α -Glu (E-C-G) (Figure 4.19a), the chiral morphology was noticeably degraded. In addition, NP synthesis using γ Glu-Cys (γ E-C) produced a different morphology with a certain level of chirality (Figure 4.19a), whereas other N-terminal additions to L-Cys, such as Ala-Cys (A-C), Pro-Cys (P-C), Cys-Cys (C-C), and Tyr-Cys (Y-C), resulted in achiral morphology (Figure 4.19b). These results support the idea that the γ -Glu group plays an important role in chirality evolution.

Another difference between L-Cys and L-GSH was the effect of C-terminal modification on chirality evolution. Substitution of the C-terminus resulted in different types of shape evolution owing to changes in the spatial arrangement of functional groups related to the oriented attachment of amino acids and peptides.^{18,30} When L-Cys ethyl ester with a blocked carboxylic acid group was used in the synthesis, the g-factor was reduced by a factor of approximately ten (Figure 4.14). Blocking of the C-terminal carboxylic acid of L-GSH (γ -E-C-G) generated only achiral structures (Figure 4.19a). In addition, a different chiral morphology was developed by replacing Gly with Ala, probably as a result of the steric hindrance near the C-terminal side. According to a previous report,⁴² the -COOH of the Gly moiety in L-GSH is involved in binding onto the gold surface, along with the thiol and amine groups. The different chiral structure that is induced by the exchange of sequence at the C-terminus suggests that more diversified chiral structures may be synthesized by changing the C-terminal sequence (Figure 4.19a). Considering these results and the known molecular size, L-GSH on the Au (321)^R surface seems to interact with multiple kink sites, while L-Cys only interacts with a single kink site.³⁵⁻

37

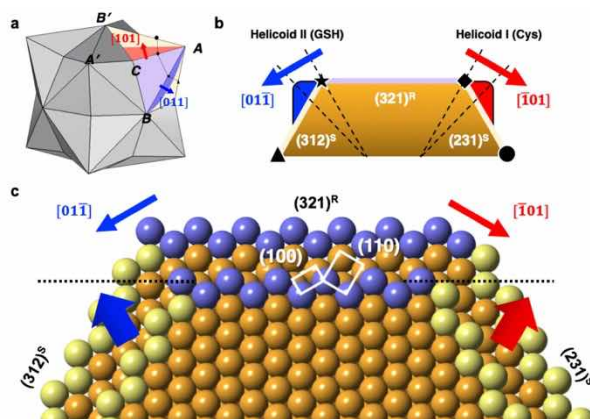


Figure 4.18 Differential growth direction of 432 helicoid I and II at atomic level. (a) Schematic illustration of chirality formation on $\{321\}$ nanoparticle. Boundary shifts of 432 helicoid I (L-Cys) and II (L-GSH) are indicated in red and blue, respectively. (b) Schematic (111) cross-section of $(312)^S$ - $(321)^R$ - $(231)^S$ facets. Original and newly shifted R/S boundaries are indicated with dashed lines. (c) Atomic arrangement of $(312)^S$ - $(321)^R$ - $(231)^S$ facets in (111) cross-section view. $\{321\}$ surface consists of (111) terrace and alternating $\{100\}$ and $\{110\}$ microfacets. \overline{AC} for 432 helicoid I shift in $[\overline{1}01]$ direction and \overline{AB} for 432 helicoid II shift in $[01\overline{1}]$ direction, respectively. The differentiated growth directions at $(312)^S$ and $(231)^S$, indicated with thick arrows, resulted in contrasting morphology of the chiral nanoparticles.

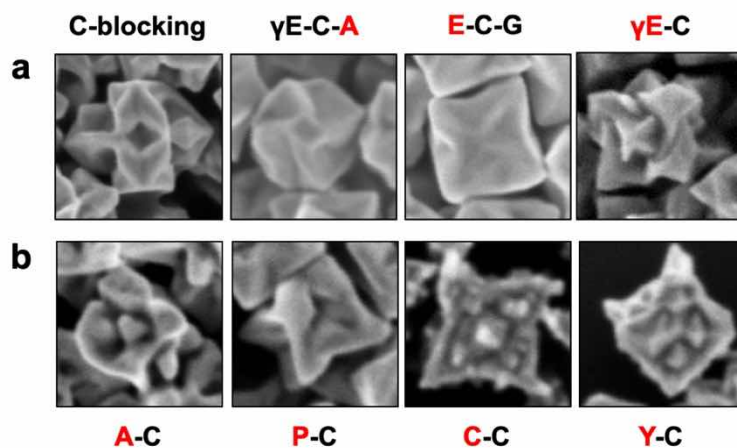


Figure 4.19 Effect of functional group change in L-GSH. (a) SEM image of synthesized nanoparticles prepared with L-glutathione ethyl ester (C-blocking), γ E-C-A, E-C-G, and γ E-C sequences. (b) SEM images of nanoparticles synthesized with different dipeptide sequences. Alanine (A), proline (P), cysteine (C), and tyrosine (Y) were added to the N-terminus of L-Cys, which dramatically modified the morphology of the resulting nanoparticle.

The different molecular features of L-Cys and L-GSH collectively influenced the morphological development and thus led to notable changes in the final chiral morphology. To obtain a detailed comparison of chiral evolution, we analyzed the temporal growth of 432 helicoids I and II in terms of SEM (Figure 4.8 and 4.10), g-factor (Figure 4.20a) and the amount of L-GSH in a nanoparticle (Figure 4.20b).

In the case of 432 helicoid I, the AC and A'C boundaries between the R and S planes started to develop and shift slightly to the S-plane direction, forming the split edges (Figure 4.8, stage I). In stage I, the g-factor is still low because the chiral components have not developed yet. After 20 min, protruded edges (R–S boundary) split more and these tilted edges grow laterally as the overall size of the particle increases (Figure 4.8, stage II). As the chiral components of the tilted edges developed, the g-factor increased rapidly (Figure 4.20a).

In the case of 432 helicoid II, the evolution direction of the chiral components is completely different. For the initial 30 min (Figure 4.10, stage I), the AB and A'B' edges of the rhombus ABA'B' expand with distortion. The distortion takes place gradually as a result of the increase in the R region. Distinctive edge growth was observed only after 40 min (Figure 4.10, stage II). During stage II, as the distorted edges became thicker, the chiral components were more distinguishable, increasing the g-factor (Figure 4.20a). According to the quantification result (Figure 4.20b), the amount of adsorbed L-GSH also increased at this growth stage. The increasing trend of adsorbed peptides with growth time is similar to that of g-factor (Figure 4.20a). This finding implies that the evolution of chirality is closely related to the adsorption of L-GSH on the gold surface. Furthermore, different increasing trends in the g-factor between 432 helicoids I and II indicate that contrasting binding kinetics between L-Cys and L-GSH on the gold surface. For the comparison of

adsorption kinetic, various concentrations of L-Cys and L-GSH were added to {321}-enclosed nanoparticles, and the adsorbed molecules on the nanoparticles were quantified (Figure 4.21). Given the concentration, a larger amount of L-Cys was attached to the high-indexed surface compared to L-GSH. Owing to this fast loading of L-Cys, only 0.1 μM is required for 432 helicoid I, whereas molecules that are 25 times larger are needed for 432 helicoid II to achieve a chiral morphology (Figure 4.16).

We suppose that differing growth directions of Au atoms are determined by the preferred molecular orientation of L-Cys and L-GSH at the kink sites. The interplay among the relative orientations of molecules adsorbed at the kink and the dynamic movement of the kink during crystal growth may determine the final morphology. Thiol is known to be anchored at the kink, and the relative positions of amine and carboxylic acid seem to make a difference. Considering the length of molecule, L-GSH should interact with at least two neighboring kinks, probably located on different terraces. In contrast, L-Cys should bind with a single kink.³⁵⁻³⁷ Using a 3D model of atomic arrangement and molecular structure, L-Cys and L-GSH on the Au (321)^R surface were displayed in Figure 4.22. We simply tried to fit the L-Cys and L-GSH molecules around the kink in a known conformation based on the preliminary DFT calculation. We found that L-Cys interacted with a single kink, but the larger L-GSH molecules should interact with multiple kinks on different terraces. We believe that these differential adsorption behaviors determine the preferred molecular orientation of L-Cys and L-GSH on the Au surface and make a difference in directing the specific growth direction and final structures of 432 helicoid I and II.

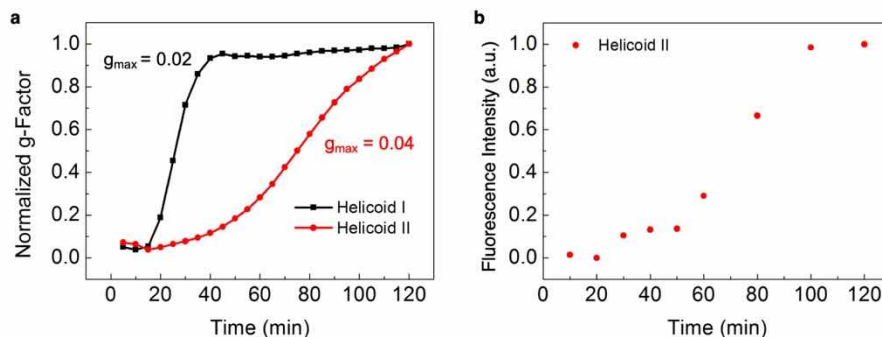


Figure 4.20 Temporal evolution of 432 helicoid I and II. (a) Increase in g-factor of 432 helicoid I (L-Cys) and II (L-GSH) with time. CD signal was measured, and normalized g-factor was displayed every 5 min during growth. (b) Amount of GSH adsorbed on 432 helicoid II at different growth times. For detailed quantification experiment of GSH on nanoparticle, see Method.

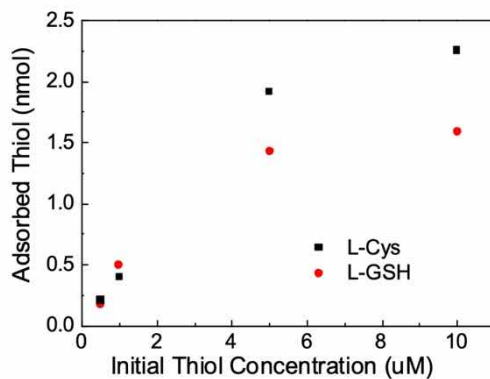


Figure 4.21 Adsorption study of L-Cys and L-GSH on {321} nanoparticles. Different concentrations of L-Cys and L-GSH were added and aged for 2 h, and the amount of adsorbate was measured by subtracting the L-Cys concentration in the supernatant from the initial concentration.

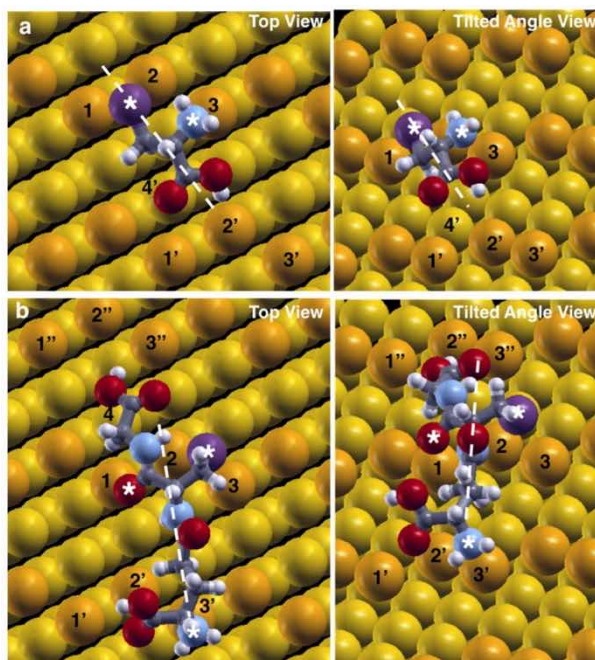


Figure 4.22 3D atomic model of L-Cys and L-GSH on Au (321)^R. (a, b) Molecular configuration of L-Cys (a) and L-GSH (b) anchored on the kinks of the Au (321)^R surface along the top view (left) and tilted angle view (right). Simple fitting of molecules around the (321)^R kink seems to indicate that L-Cys interacts with a single kink via two anchoring sites (Au-S*: 2.75 Å, Au-N*: 2.56 Å), whereas L-GSH interacts with multiple kinks located in different terrace layers via three anchoring sites (Au-S*: 2.72 Å, Au-N*: 2.62 Å, Au-O*: 2.64 Å). Color codes for each atom are Au (yellow, terrace; orange, kink), S (purple), N (light blue), O (red), C (gray), and H (white).

4.2.3 Highly-twisted chiral morphology: 432 helicoid III

The strongest chirality among the synthesized nanoparticles was displayed by a new type of chiral structure, designated as '432 helicoid III', which was synthesized utilizing an octahedron seed instead of a cube seed. The 432 helicoid III nanoparticles showed gammadion-like structures, consisting of four highly curved arms of increasing width, in all the six faces of the cubic geometry (Figure 4.23 and 4.24). Compared to 432 helicoid I and II, in 432 helicoid III, the chiral elements were twisted with a larger curvature, and gaps between them were carved more deeply in the central direction. Morphology at the initial stage (within 20 min) of synthesis revealed that chiral elements were already formed and that the edges were protruded (Figure 4.25). Compared with the case of cubic seed (432 helicoid II), the growth along the [100] direction is more rapid in the case of octahedron seeds, and thus vertices in [100] direction were more predominant during the synthesis. Therefore, the width and height of the four wings were increased and the pinwheel-like structure became more prominent in the final morphology.

Additional analysis regarding the 432 helicoid III morphology was performed using HAADF STEM imaging at different tilting angles (Figure 4.26). In particular, interior parts of the chiral structures carved toward the center of a particle can be visualized by comparing the contrast at different tilting angles. We also found that the depth of the chiral carved gap is about 50 nm, one-third of total length of a single particle. A consistent conclusion was also supported by the helium ion microscopy (HIM). Imaging after continuous ion milling using He⁺ ion shows the feature of the curved surfaces located inside the spacious gaps of pinwheel-like structures (Figure 4.27). From the morphological information regarding the 50-nm-deep chiral gap, a 3D model was newly constructed, and the distribution of the Miller Index was displayed by normal vector analysis (Figure 4.28). As shown in Figure

4.28c, high-index planes exist in the inner part of 432 helicoid III. The strong CD signal of this structure (Figure 4.29a) is largely attributed to these highly twisted chiral structures, which is roughly ten and four times larger than that of 432 helicoids I and II, respectively (Figure 4.29b).

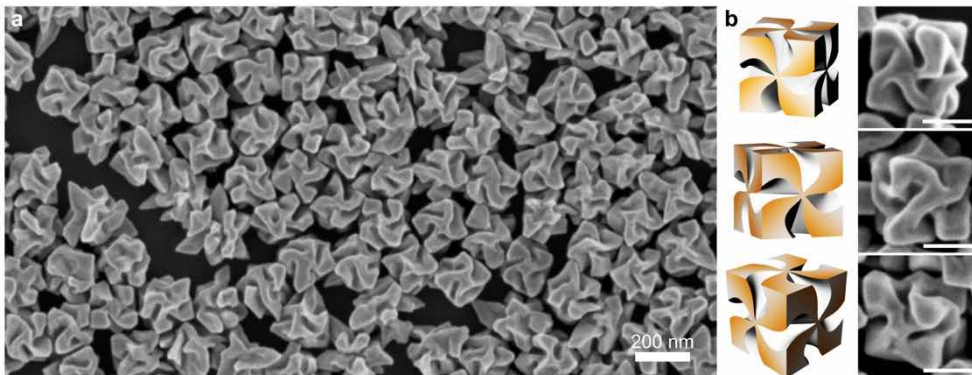


Figure 4.23 Morphology of 432 helicoid III. (a) SEM image of 432 helicoid III nanoparticles evolved from an octahedron seed. (b) 3D models and corresponding SEM images of 432 helicoid III oriented in various directions. Scale bar, 100 nm.

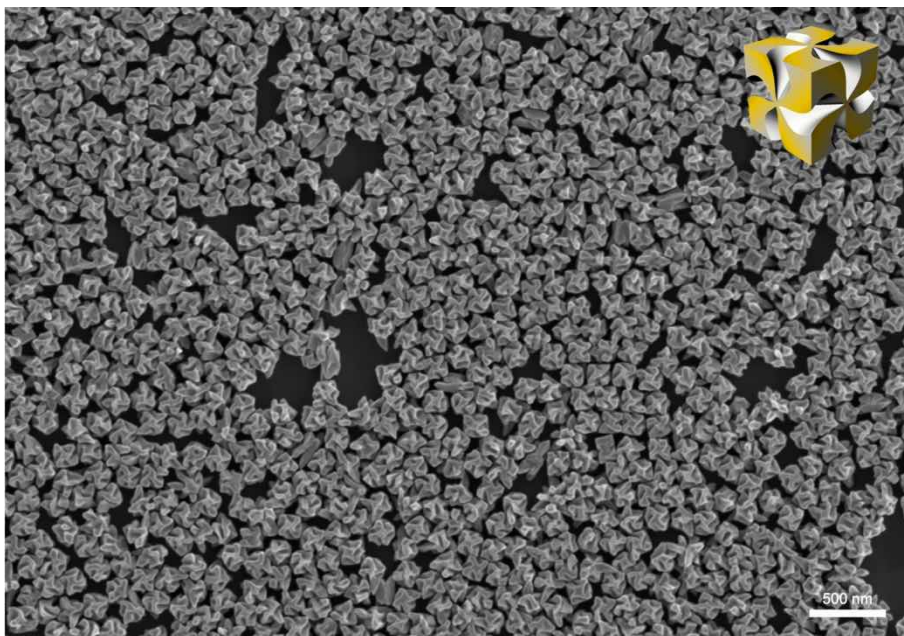


Figure 4.24 Large-area SEM image of 432 helicoid III nanoparticles synthesized using octahedral seed and L-GSH.

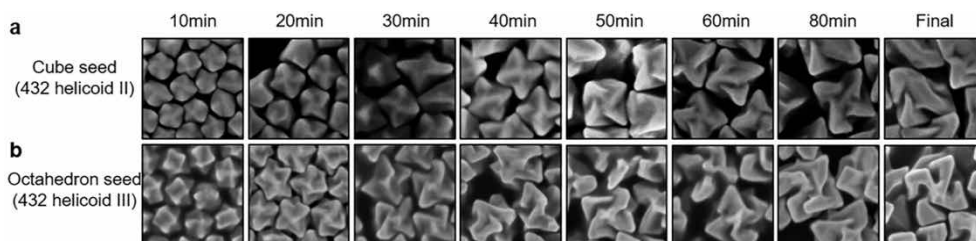


Figure 4.25 Effect of different seed shapes on chirality evolution. (a, b) SEM images of 432 helicoid II nanoparticles synthesized in the presence of L-GSH with cube seeds (a) or octahedron seeds (b) at different reaction times. In the case of octahedron seeds, more protruding edges of nanoparticles were created in the [100] direction compared to cube seeds in the early stages (10 and 20 min) of synthesis. The fast evolution of edges induces the formation of highly twisted arms and is a critical determinant of further growth.

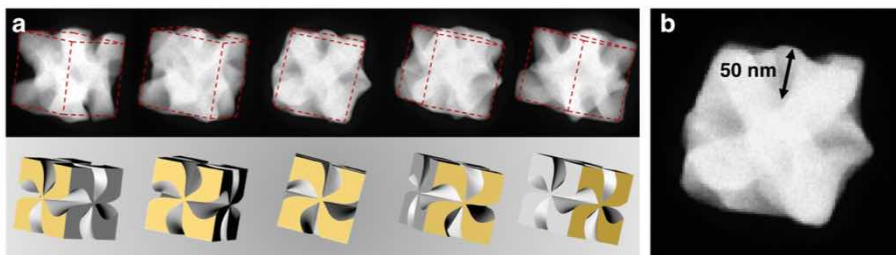


Figure 4.26 Tilt series of HAADF-STEM for 432 helicoid III. (a) HAADF-STEM images and corresponding 3D models of 432 helicoid III at different tilting angles. Front faces of 432 helicoid III are indicated with yellow in 3D models. Red dotted lines show the cubic outline. (b) Magnified STEM images showing the chiral carved gap with depth of about 50 nm.

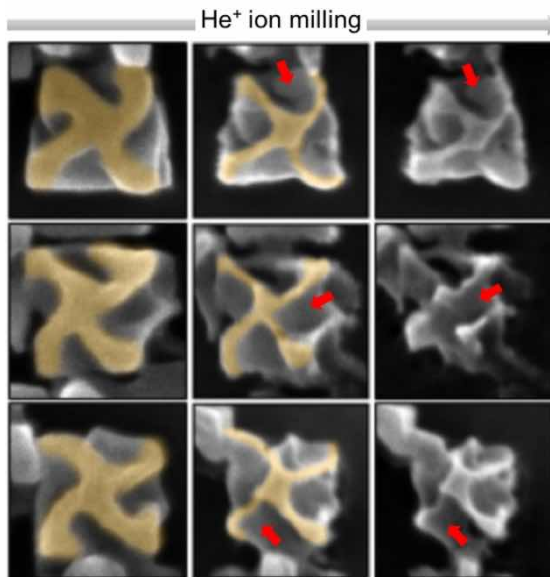


Figure 4.27 Characterization of interior gap using helium ion microscopy. Helium ion microscopy (HIM) secondary electron (SE) image of 432 helicoid III by He^+ -ion milling process. Original pinwheel-like structure of 432 helicoid III is highlighted in yellow. Exposure to He^+ ion beam with acceleration voltage of 30 keV and beam current of 0.733 pA allows visualization of the interior parts of the curved surfaces, as indicated by red arrows.

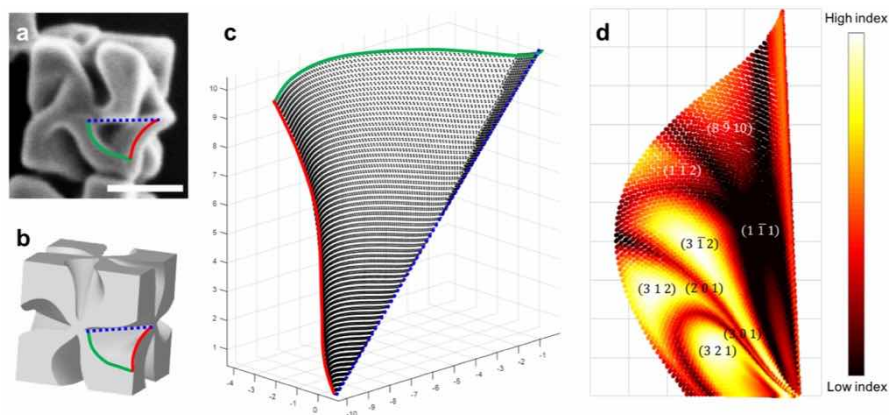


Figure 4.28 Miller-index analysis of 432 helicoid III based on 3D modeling. (a-c) Modeling of 432 helicoid III surface. Magnified SEM image of 432 helicoid III (a), corresponding 3D model (b), and interpolated curved surface (c) of 432 helicoid III. Curved outlines of chiral arm at the front and side face are indicated by green and red lines, respectively, and internal boundary is indicated by blue dotted line. 3D curved surface model of 432 helicoid III was constructed by the interpolation of surface outlines. (d) Distribution of Miller index on the modeled surface. Miller indices were calculated from a normal vector at each point of the surface.

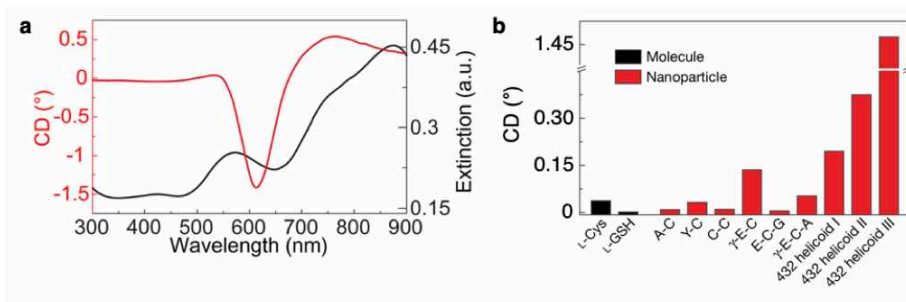


Figure 4.29 Optical activity of 432 helicoid III. (a) Measured CD and extinction spectra of 432 helicoid III. (b) Comparison of CD response of the synthesized helicoid structures and other nanoparticles.

Considering the mechanism of nanostructure formation, helicoid morphologies are a hybrid result of crystallographic control and enantioselective molecular recognition. Therefore, the chirality of these nanoparticles can be designed by manipulating both crystal growth parameters and the molecular binding property, and their combination provides a variety of morphology and chirality control. In addition to the nanostructure formation process, the three-dimensional geometries of helicoid morphologies are unique. Starting from the $\frac{4}{m}\bar{3}\frac{2}{m}$ (or full octahedral) point group symmetry of {321}-exposed NPs, the asymmetric growth breaks all mirror and inversion symmetry to finally produce helicoid morphology with 432 (or chiral octahedral) point group symmetry (Figure 4.30a). Remarkably, it is the first report for 432-symmetric nanostructures confined to the single nanoparticle level, even though similar symmetry can be found in periodic single-gyroid structures⁴³ and ferritin family proteins.⁴⁴ One of the unique geometric features of 432 helicoid is that in order to maintain chirality and 432-symmetry, chiral structures with opposite rotational directions coexist in individual nanoparticles along the {100} and {111} directions (Figure 4.30b). Therefore, the net chirality of a 432 helicoid NP is a result of combining two opposite rotation. From this perspective, we believe that if we can manipulate the weight factor of each rotation by controlling synthesis condition, handedness and overall degree of chirality can be manipulated.

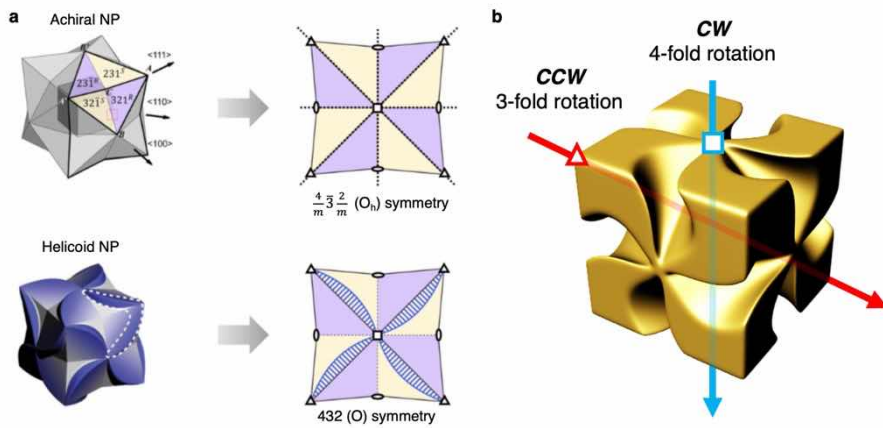


Figure 4.30 Symmetry aspect of 432 helicoid structure. (a) Comparison of symmetry elements for achiral hexoctahedral nanoparticle (top) and helicoid nanoparticle (bottom). (b) Rotation symmetry of 432 helicoid nanoparticle along $\langle 100 \rangle$ (blue) and $\langle 111 \rangle$ (red) directions.

4.3 Conclusion

We demonstrate a new paradigm- “from biological encoder to plasmonic chiral metamaterials”- which allows for the precise tuning of handedness and chiroptical response of metamaterials at the molecular sequence level. The peptide-encoding approach presented here for the evolution of chirality in a plasmonic helicoid has technological potential for the development of biologically responsive and tunable metamaterials. Based on the understanding of how atoms on a high-index plane can enantiospecifically interact with Cys-containing peptides, we revealed the mechanism of chirality evolution in gold nanoparticles. Using this approach, chiral elements were arranged within only about 100-nm cube-like structures, resulting in the three-dimensional chiral plasmonic metamaterials. We believe that the conformation control using long peptides or other chiral biomolecules will allow for the synthesis of other sets of chiral symmetry groups. The insights from this study will also aid in the theoretical guideline to design the artificial chirality and chiroptical properties in plasmonic metamaterials.

4.4 Methods

Chemicals

Hexadecyltrimethylammonium bromide (CTAB, 99%), L-ascorbic acid (AA, 99%) and tetrachloroauric(iii) trihydrate ($\text{HAuCl}_4 \cdot 3\text{H}_2\text{O}$, 99.9%) were purchased from Sigma-Aldrich. L-cysteine hydrochloride monohydrate (99%, TCI), D-cysteine hydrochloride monohydrate (99%, TCI), L-cysteine ethyl ester hydrochloride (99%, TCI), N-acetyl-L-cysteine (98%, TCI), L-glutathione (γ -E-C-G, 98%, Sigma-Aldrich), L-glutathione ethyl ester (90%, Sigma-Aldrich) and γ -L-glutamyl-L-cysteine (γ -E-C, 80%, Sigma-Aldrich) were obtained commercially and used without further purification. Di- and tri-peptides, L-alanyl-L-cysteine (A-C, > 98%), L-prolyl-L-cysteine (P-C, > 98%), L-cysteinyl-L-cysteine (C-C, > 98%), L-tyrosyl-L-cysteine (Y-C, > 98%), L-glutamyl-L-cysteinyl-glycine (E-C-G, > 98%) and γ -L-glutamyl-L-cysteinyl-L-alanine (γ -E-C-A, > 98%) were provided by GenScript and prepared in hydrochloride salt form before use. All aqueous solutions were prepared using high-purity deionized water ($18.2 \text{ M}\Omega \text{ cm}^{-1}$).

Synthesis of chiral nanoparticles

Cubic and octahedral seeds were synthesized as reported previously.^{24,45} Before use, both types of seed nanoparticle were centrifuged (6,708g, 150 s) twice and dispersed in aqueous CTAB (1 mM) solution. In a typical synthesis, a growth solution was prepared by adding 0.8 ml of 100 mM CTAB and 0.2 ml of 10 mM gold chloride trihydrate into 3.95 ml of deionized water to form an $[\text{AuBr}_4]^-$ complex. Au^{3+} was then reduced to Au^+ by the rapid injection of 0.475 ml of 100 mM AA solution. The growth of chiral nanoparticles was initiated by adding 5 μl of amino acid or peptide solution and 50 μl of seed solution into the growth solution. For the preparation of 432 helicoid I, cubic seed solution was added to the growth solution

and then, after a 20-min incubation, 100 μM cysteine was added. To prepare 432 helicoid II, 2 mM glutathione was added to the growth solution, followed by the addition of cubic seed solution. To prepare 432 helicoid III, 5 mM glutathione was added to the growth solution, followed by the addition of octahedral seed solution. The growth solution was placed in a 30 $^{\circ}\text{C}$ bath for 2 h, and the pink solution gradually became blue with large scattering. The solution was centrifuged twice (1,677g, 60 s) to remove unreacted reagents and was re-dispersed in a 1 mM CTAB solution for further characterization. To monitor the evolution of chirality, the growth reaction was stopped at different stages by centrifugation, after which we performed three repetitions of washing, re-dispersion, and centrifugation to remove the remaining chemicals.

Characterization

SEM images were taken with a SIGMA system (Zeiss). TEM images were captured using a JEM-3000F system (JEOL). Extinction and circular dichroism (CD) spectra were obtained using a J-815 spectropolarimeter instrument (JASCO). Kuhn's dis-symmetry factor (*g*-factor) is a dimensionless quantity that is useful for quantitative comparisons of chiro-optical properties among different systems and was calculated from the measured extinction and CD values using:

$$g - \text{factor} = 2 \frac{A_L - A_R}{A_L + A_R} \propto \frac{CD}{\text{extinction}}.$$

Temperature-programmed desorption spectra at a rate of 3 K min^{-1} were taken with monitoring of CO_2 ($m/q = 44$ amu), by using helium carrier gas. Cyclic voltammograms were measured in 0.1 M KOH-ethanol solution at a scan rate of 0.1 V s^{-1} . Desorption peaks at more negative potentials indicate the higher adsorption energy.

Quantification of amino acids and peptides

To quantify the amount of L-Cys and L-GSH on the 432 helicoids I and II, a fluorometric assay was performed. After complete growth in growth solution (100 nM L-Cys for 432 helicoid I and 2.5 μ M L-GSH for 432 helicoid II), the chiral nanoparticles were centrifuged and washed three times to remove the remaining chemicals in solution except the molecules adsorbed on the nanoparticle surface. By adding NaBH₄ to the nanoparticle solution, the reductive desorption reaction of adsorbed thiolate molecules (Au-SR) started immediately, and free thiol molecules (RS⁻) were released to the solution as follows: Au-SR + e⁻ → Au + RS⁻ (Figure 4.17a).^{38,39} The final concentration of NaBH₄ was 25 mM and the final volume of the solution was fixed to 100 μ l. After 5 min of incubation, the nanoparticles were centrifuged again and clear supernatant solutions containing the released L-Cys or L-GSH molecules were collected and incubated for 1 day in 25 °C to decompose the remaining NaBH₄. Quantification of L-Cys and L-GSH on the 432 helicoids I and II was carried out by using thiol-selective dye (Thiol detection assay kit, Cayman Chemical, 700340). The sample was diluted in the reaction buffer (10 mM phosphate buffer with 1 mM EDTA, pH 7.4). The thiol-selective dye reacted spontaneously with the free thiol of L-Cys or L-GSH in the sample solution, producing a fluorescent derivative (Figure 4.17a). The fluorescence signal of the sample was recorded by using an excitation wavelength of 405 nm and an emission wavelength of 535 nm. For the relative quantification, the standard solution was prepared under the same conditions and measured in the concentration range 0–5 μ M. The standard concentration curve showed good linearity, with R² = 0.999 (Figure 4.17b). The quantified amounts of L-Cys and L-GSH on the surface of 432 helicoids I and II were 98.9 \pm 22.6 pmol and 280.2 \pm 90.2 pmol, respectively. The adsorption amount of GSH during the synthesis of 432 helicoid II was monitored over time

(Figure 4.20b). To stop the growth at different stages, the particles were centrifuged out every 10 min. After the centrifugation was repeated three times to remove the remaining chemicals, the quantification experiment for L-GSH was performed as described above.

Calculation of surface coverage

To convert the measured concentration of molecules to the surface coverage, we estimated the total surface area of the 432 helicoid I and II samples. According to extinction measurements for the seed nanoparticles, the total number of nanoparticles in each sample batch was measured to be $N_{NP} = 1.53 \times 10^9 \text{ ml}^{-1}$. The surface area of a single 432 helicoid I nanoparticle was $A_{NP,H1} = 2.31 \times 10^{-9} \text{ cm}^2$, and that of helicoid II was $A_{NP,H2} = 1.78 \times 10^{-9} \text{ cm}^2$, approximated from the schematic three-dimensional models in Figure 4.3 and 4.11. Therefore, the total surface area of the nanoparticles in each sample was

$$A_{\text{total}} = N_{NP}A_{NP}, A_{\text{total}, H1} = 3.53 \text{ cm}^2, A_{\text{total}, H2} = 2.72 \text{ cm}^2.$$

The surface coverage of L-Cys and L-GSH in 432 helicoids I and II was calculated from the quantification results and the estimated total surface area of the nanoparticle samples, as shown in Figure 4.17c. The surface density of L-Cys and L-GSH was $0.028 \text{ nmol cm}^{-2}$ and $0.103 \text{ nmol cm}^{-2}$, respectively. These values correspond to 0.01 and 0.22 monolayers, respectively, calculated from the reported maximum coverage.^{40,41} On the basis of the surface density estimate, the average intermolecular distance for L-Cys and L-GSH is expected to be 2.5 nm and 1.3 nm, respectively. Therefore, we conclude that, under optimized conditions, both molecules have enough room to bind multiple functional groups, as is necessary for enantioselective recognition.

4.5 Bibliography

1. Hazen, R. M.; Sholl, D. S. Chiral Selection on Inorganic Crystalline Surfaces. *Nat. Mater.* **2003**, *2* (6), 367–374.
2. Zhang, S.; Zhou, J.; Park, Y.-S.; Rho, J.; Singh, R.; Nam, S.; Azad, A. K.; Chen, H.-T.; Yin, X.; Taylor, A. J.; et al. Photoinduced Handedness Switching in Terahertz Chiral Metamolecules. *Nat. Commun.* **2012**, *3* (1), 942.
3. Meinzer, N.; Barnes, W. L.; Hooper, I. R. Plasmonic Meta-Atoms and Metasurfaces. *Nat. Photonics* **2014**, *8* (12), 889–898.
4. Gansel, J. K.; Thiel, M.; Rill, M. S.; Decker, M.; Bade, K.; Saile, V.; von Freymann, G.; Linden, S.; Wegener, M. Gold Helix Photonic Metamaterial as Broadband Circular Polarizer. *Science* **2009**, *325* (5947), 1513–1515.
5. Pendry, J. B. A Chiral Route to Negative Refraction. *Science* **2004**, *306* (5700), 1353–1355.
6. Hendry, E.; Carpy, T.; Johnston, J.; Popland, M.; Mikhaylovskiy, R. V.; Laphorn, A. J.; Kelly, S. M.; Barron, L. D.; Gadegaard, N.; Kadodwala, M. Ultrasensitive Detection and Characterization of Biomolecules Using Superchiral Fields. *Nat. Nanotechnol.* **2010**, *5* (11), 783–787.
7. Soukoulis, C. M.; Wegener, M. Past Achievements and Future Challenges in the Development of Three-Dimensional Photonic Metamaterials. *Nat. Photonics* **2011**, *5* (9), 523–530.
8. Lee, H.-E.; Ahn, H.-Y.; Lee, J.; Nam, K. T. Biomolecule-Enabled Chiral Assembly of Plasmonic Nanostructures. *ChemNanoMat* **2017**, *3* (10), 685–697.
9. Kuzyk, A.; Schreiber, R.; Zhang, H.; Govorov, A. O.; Liedl, T.; Liu, N. Reconfigurable 3D Plasmonic Metamolecules. *Nat. Mater.* **2014**, *13* (9), 862–866.
10. Kuzyk, A.; Schreiber, R.; Fan, Z.; Pardatscher, G.; Roller, E.-M.; Högele, A.; Simmel, F. C.; Govorov, A. O.; Liedl, T. DNA-Based Self-Assembly of Chiral Plasmonic Nanostructures with Tailored Optical Response. *Nature* **2012**, *483* (7389), 311–314.
11. Ma, W.; Xu, L.; de Moura, A. F.; Wu, X.; Kuang, H.; Xu, C.; Kotov, N. A. Chiral Inorganic Nanostructures. *Chem. Rev.* **2017**, *117* (12), 8041–8093.

12. Che, S.; Liu, Z.; Ohsuna, T.; Sakamoto, K.; Terasaki, O.; Tatsumi, T. Synthesis and Characterization of Chiral Mesoporous Silica. *Nature* **2004**, *429* (6989), 281–284.
13. WEISSBUCH, I.; ADDADI, L.; LEISEROWITZ, L. Molecular Recognition at Crystal Interfaces. *Science* **1991**, *253* (5020), 637–645.
14. Sanchez, C.; Arribart, H.; Giraud Guille, M. M. Biomimetism and Bioinspiration as Tools for the Design of Innovative Materials and Systems. *Nat. Mater.* **2005**, *4* (4), 277–288.
15. Xiao, W.; Ernst, K.-H.; Palotas, K.; Zhang, Y.; Bruyer, E.; Peng, L.; Greber, T.; Hofer, W. A.; Scott, L. T.; Fasel, R. Microscopic Origin of Chiral Shape Induction in Achiral Crystals. *Nat. Chem.* **2016**, *8* (4), 326–330.
16. Horvath, J. D.; Koritnik, A.; Kamakoti, P.; Sholl, D. S.; Gellman, A. J. Enantioselective Separation on a Naturally Chiral Surface. *J. Am. Chem. Soc.* **2004**, *126* (45), 14988–14994.
17. Switzer, J. A.; Kothari, H. M.; Poizot, P.; Nakanishi, S.; Bohannon, E. W. Enantiospecific Electrodeposition of a Chiral Catalyst. *Nature* **2003**, *425* (6957), 490–493.
18. Kühnle, A.; Linderoth, T. R.; Hammer, B.; Besenbacher, F. Chiral Recognition in Dimerization of Adsorbed Cysteine Observed by Scanning Tunneling Microscopy. *Nature* **2002**, *415* (6874), 891–893.
19. Orme, C. A.; Noy, A.; Wierzbicki, A.; McBride, M. T.; Grantham, M.; Teng, H. H.; Dove, P. M.; DeYoreo, J. J. Formation of Chiral Morphologies through Selective Binding of Amino Acids to Calcite Surface Steps. *Nature* **2001**, *411* (6839), 775–779.
20. Sholl, D. S.; Asthagiri, A.; Power, T. D. Naturally Chiral Metal Surfaces as Enantiospecific Adsorbents. *J. Phys. Chem. B* **2001**, *105* (21), 4771–4782.
21. Ahmadi, A.; Attard, G.; Feliu, J.; Rodes, A. Surface Reactivity at “Chiral” Platinum Surfaces. *Langmuir* **1999**, *15* (7), 2420–2424.
22. McFadden, C. F.; Cremer, P. S.; Gellman, A. J. Adsorption of Chiral Alcohols on “Chiral” Metal Surfaces. *Langmuir* **1996**, *12* (10), 2483–2487.
23. Lee, H.-E.; Yang, K. D.; Yoon, S. M.; Ahn, H.-Y.; Lee, Y. Y.; Chang, H.; Jeong, D. H.; Lee, Y.-S.; Kim, M. Y.; Nam, K. T. Concave Rhombic Dodecahedral Au Nanocatalyst with Multiple High-Index Facets for CO 2

- Reduction. *ACS Nano* **2015**, *9* (8), 8384–8393.
24. Ahn, H.-Y.; Lee, H.-E.; Jin, K.; Nam, K. T. Extended Gold Nano-Morphology Diagram: Synthesis of Rhombic Dodecahedra Using CTAB and Ascorbic Acid. *J. Mater. Chem. C* **2013**, *1* (41), 6861.
 25. Sau, T. K.; Murphy, C. J. Room Temperature, High-Yield Synthesis of Multiple Shapes of Gold Nanoparticles in Aqueous Solution. *J. Am. Chem. Soc.* **2004**, *126* (28), 8648–8649.
 26. Tao, K.; Levin, A.; Adler-Abramovich, L.; Gazit, E. Fmoc-Modified Amino Acids and Short Peptides: Simple Bio-Inspired Building Blocks for the Fabrication of Functional Materials. *Chem. Soc. Rev.* **2016**, *45* (14), 3935–3953.
 27. Coppage, R.; Slocik, J. M.; Briggs, B. D.; Frenkel, A. I.; Naik, R. R.; Knecht, M. R. Determining Peptide Sequence Effects That Control the Size, Structure, and Function of Nanoparticles. *ACS Nano* **2012**, *6* (2), 1625–1636.
 28. Slocik, J. M.; Govorov, A. O.; Naik, R. R. Plasmonic Circular Dichroism of Peptide-Functionalized Gold Nanoparticles. *Nano Lett.* **2011**, *11* (2), 701–705.
 29. Dickerson, M. B.; Sandhage, K. H.; Naik, R. R. Protein- and Peptide-Directed Syntheses of Inorganic Materials. *Chem. Rev.* **2008**, *108* (11), 4935–4978.
 30. Weiner, R. G.; Skrabalak, S. E. Metal Dendrimers: Synthesis of Hierarchically Stellated Nanocrystals by Sequential Seed-Directed Overgrowth. *Angew. Chem. Int. Ed.* **2015**, *54* (4), 1181–1184.
 31. Liu, H.; Ye, F.; Yao, Q.; Cao, H.; Xie, J.; Lee, J. Y.; Yang, J. Stellated Ag-Pt Bimetallic Nanoparticles: An Effective Platform for Catalytic Activity Tuning. *Sci. Rep.* **2015**, *4* (1), 3969.
 32. Cheong, W. Y.; Gellman, A. J. Energetics of Chiral Imprinting of Cu(100) by Lysine. *J. Phys. Chem. C* **2011**, *115* (4), 1031–1035.
 33. Cho, F.-H.; Lin, Y.-C.; Lai, Y.-H. Electrochemically Fabricated Gold Dendrites with High-Index Facets for Use as Surface-Enhanced Raman-Scattering-Active Substrates. *Appl. Surf. Sci.* **2017**, *402*, 147–153.
 34. Arihara, K.; Ariga, T.; Takashima, N.; Arihara, K.; Okajima, T.; Kitamura, F.; Tokuda, K.; Ohsaka, T. Multiple Voltammetric Waves for Reductive

- Desorption of Cysteine and 4-Mercaptobenzoic Acid Monolayers Self-Assembled on Gold Substrates. *Phys. Chem. Chem. Phys.* **2003**, *5* (17), 3758.
35. Schillinger, R.; Šljivančanin, Ž.; Hammer, B.; Greber, T. Probing Enantioselectivity with X-Ray Photoelectron Spectroscopy and Density Functional Theory. *Phys. Rev. Lett.* **2007**, *98* (13), 136102.
 36. Greber, T.; Šljivančanin, Ž.; Schillinger, R.; Wider, J.; Hammer, B. Chiral Recognition of Organic Molecules by Atomic Kinks on Surfaces. *Phys. Rev. Lett.* **2006**, *96* (5), 056103.
 37. Kühnle, A.; Linderoth, T. R.; Besenbacher, F. Enantiospecific Adsorption of Cysteine at Chiral Kink Sites on Au(110)-(1×2). *J. Am. Chem. Soc.* **2006**, *128* (4), 1076–1077.
 38. Yuan, M.; Zhan, S.; Zhou, X.; Liu, Y.; Feng, L.; Lin, Y.; Zhang, Z.; Hu, J. A Method for Removing Self-Assembled Monolayers on Gold. *Langmuir* **2008**, *24* (16), 8707–8710.
 39. Ansar, S. M.; Ameer, F. S.; Hu, W.; Zou, S.; Pittman, C. U.; Zhang, D. Removal of Molecular Adsorbates on Gold Nanoparticles Using Sodium Borohydride in Water. *Nano Lett.* **2013**, *13* (3), 1226–1229.
 40. Bieri, M.; Bürgi, T. Adsorption Kinetics of L-Glutathione on Gold and Structural Changes during Self-Assembly: An in Situ ATR-IR and QCM Study. *Phys. Chem. Chem. Phys.* **2006**, *8* (4), 513–520.
 41. Arrigan, D. W. M.; Bihan, L. Le. A Study of L-Cysteine Adsorption on Gold via Electrochemical Desorption and Copper(II) Ion Complexation. *Analyst* **1999**, *124* (11), 1645–1649.
 42. Bieri, M.; Bürgi, T. L-Glutathione Chemisorption on Gold and Acid/Base Induced Structural Changes: A PM-IRRAS and Time-Resolved in Situ ATR-IR Spectroscopic Study. *Langmuir* **2005**, *21* (4), 1354–1363.
 43. Saranathan, V.; Osuji, C. O.; Mochrie, S. G. J.; Noh, H.; Narayanan, S.; Sandy, A.; Dufresne, E. R.; Prum, R. O. Structure, Function, and Self-Assembly of Single Network Gyroid (I4132) Photonic Crystals in Butterfly Wing Scales. *Proc. Natl. Acad. Sci.* **2010**, *107* (26), 11676–11681.
 44. He, D.; Marles-Wright, J. Ferritin Family Proteins and Their Use in Bionanotechnology. *N. Biotechnol.* **2015**, *32* (6), 651–657.
 45. Wu, H.-L.; Tsai, H.-R.; Hung, Y.-T.; Lao, K.-U.; Liao, C.-W.; Chung, P.-J.;

Huang, J.-S.; Chen, I.-C.; Huang, M. H. A Comparative Study of Gold Nanocubes, Octahedra, and Rhombic Dodecahedra as Highly Sensitive SERS Substrates. *Inorg. Chem.* **2011**, *50* (17), 8106–8111.

Chapter 5. Chiroptical Response of Plasmonic Helicoid Nanoparticles

5.1 Introduction

In this chapter, we present a detailed understanding of the optical property of 432-helicoid nanoparticles in far-field and near-field regime. In addition to the geometrical feature, the chirality of materials can be optically proved by creating a chiral state of light through different reactions to LCP and RCP. Since its first discovery by Pasteur, the optical properties of chiral materials have been regarded as effective tools for observing the three-dimensional structure of biomolecules by using a non-destructive spectroscopic method.¹⁻⁶ Structural changes of biomolecules in the nanometer range are related to their physiological function, which is of great importance in understanding life phenomena. Therefore, detecting molecular structures with polarization-based, "chiroptical", spectroscopy, such as circular dichroism (CD) and optical rotatory dispersion (ORD) is simpler, less invasive and cost-effective than conventional x-ray crystallography and electron microscopy methods. In addition, polarization tuning capability of the chiral materials can be further extended to the optical applications for light manipulation such as polarization-selective filter, optical diode, and anti-reflection coating. However, since the molecular signals originating from the chiral light-matter interaction are 10^{-6} to 10^{-2} times smaller than the original absorption, the detection of the signal itself is difficult, and large amount or high concentration of samples are required. Additionally, most of the chiroptical signal from biomolecules are generated in the ultraviolet region, which is a major hindrance for utilizing their chiral light-matter interactions in other interesting frequencies such as visible and IR regions.

In this respect, the integration of plasmonic material and chirality can maximize the chiroptical signals and push the limit of chiral light-matter interaction into an unnatural regime. Plasmonics deal with metallic nanomaterials and their unique optical properties. Metallic nanoparticles have a high density of quasi-free electrons which exhibit collective oscillation as a response to the external impinging light.⁷ This resonant oscillation confines far-field light in subwavelength scale, and large dipole strength of plasmonic nanoparticles can be manifested as large optical cross-sections. Those features of plasmonic materials can be adapted to the chiral nanostructures which have the stronger chiral light-matter interaction than that of molecular materials. The optical property of chiral plasmonic nanostructure can be measured by chiroptical spectroscopy such as CD or ORD, and furthermore can be directly used as a chiral medium to modulate the polarization state of incoming light and as polarization-selective applications such as polarizing filter,⁸ wavefront control,⁹ and even negative refractive index materials.¹⁰ In addition to the far-field property, the strong light confinement of the plasmonic nanostructure can lead to chiral near-field phenomena, suggesting the possibility of coupling with other plasmonic or molecular systems which is advantageous to the chiral sensing.^{11,12}

In the first part of this chapter, we studied the theoretical consideration for the optical property of metallic nanomaterial including localized surface plasmon resonance, plasmon hybridization model, and chiroptical response of plasmonic nanomaterials. To describe the electromagnetic response of chiral plasmonic material, the most simplified coupled oscillator model with two orthogonal dipoles was briefly explained to provide an intuition for understanding the material response originated in chiral geometry. Here, we highlighted the strong chiroptical response of the continuous chiral geometry in comparison with collective chiral assembly.

In the latter part of this chapter, we discussed the chiroptical property of chiral helicoid nanostructures synthesized in Chapter 4. Compared with the previously reported chiral plasmonic nanostructures produced by the bottom-up method, 432-helicoid nanoparticles showed a dramatic advance in optical dissymmetry between LCP and RCP: Dissymmetry g -factor of the randomly dispersed helicoid nanoparticle solution reached 0.2 at visible wavelengths. The underlying mechanism of strong optical dissymmetry was studied by the numerical simulation, and it was clarified that a large contrast in plasmonic resonance mode near the chiral gap structures causes strong chiroptical responses. Surprisingly, based on the wavelength-dependent polarization rotation ability, a solution of the helicoid gold nanoparticle can modulate the color of transmitted light in a wide range of visible wavelengths. This color transformation operates in real-time by rotating a polarizer and can be observed in naked-eye. Post-synthesis process by metal deposition further modulates the chiroptical response of the helicoid nanoparticles. Resonance coupling between the helicoid nanoparticle and metal thin-film enabled dramatic spectral tuning at the visible and NIR region, which is directly reflected in the color generation in cross-polarized condition. We believe that 432-helicoid nanoparticle will aid in the rational design of three-dimensional chiral nanostructures for use in advanced optical applications such as display and encryption technology.

5.2 Theoretical background

5.2.1 Dielectric function of metal

In order to explain the optical properties of metallic materials, it is necessary to understand the behavior of quasi-free electrons. Electrons in metallic materials represent a collective oscillation in the response of an incident electromagnetic wave. According to the simple plasma model, the behavior of electrons which is excited by the incident single frequency field is described as a damped harmonic oscillator as follows:

$$m^* \left(\frac{\partial^2 \mathbf{u}}{\partial t^2} + \gamma \frac{\partial \mathbf{u}}{\partial t} \right) = -e\mathbf{E}(t). \quad (4.1)$$

Here, oscillating electrons has coordination \mathbf{u} with charge e and effective mass m^* , and γ is collision frequency that quantifies the damping of free-electrons. The right side of equation (4.1) is driving force and can be expressed as $\mathbf{E}(t) = \mathbf{E}_0^{ext} e^{-i\omega t}$ by assuming harmonic time dependence, where \mathbf{E}_0^{ext} is the field amplitude of applied single frequency wave.

The solution for \mathbf{u} can describe the oscillation of electrons as

$$\mathbf{u} = \frac{e}{m^*} \frac{1}{\omega^2 + i\gamma\omega} \mathbf{E}_0^{ext}. \quad (4.2)$$

For N electrons per unit volume, polarization \mathbf{P} is defined as follows:

$$\mathbf{P} = -N e \mathbf{u}. \quad (4.3)$$

According to the electromagnetic constitutive equations[Ref], displacement \mathbf{D} can hold the following relation, $\mathbf{D} = \epsilon_0 \epsilon \mathbf{E} = \epsilon_0 \mathbf{E} + \mathbf{P}$, and combination of this relation

with equation (4.2) and (4.3) leads to the complex dielectric function of free-electron gas:

$$\epsilon_{Drude}(\omega) = 1 - \frac{\omega_p^2}{\omega^2 + i\gamma\omega}. \quad (4.4)$$

This is called Drude model for metallic materials with the isotropic property. In this model, the plasma frequency of electrons is given by $\omega_p = \sqrt{\frac{Ne}{\epsilon_0 m^*}}$.

According to this model, the negative values of $Re(\epsilon_{Drude})$ and non-vanishing $Im(\epsilon_{Drude})$ that appear below ω_p is characteristic metallic behavior. On the other hand, lossy dielectric behavior appears above ω_p with the positive value of $Re(\epsilon_{Drude})$, and for $\omega \gg \omega_p$ condition, $Im(\epsilon_{Drude})$ converges to 0 so the loss can be ignored. This means that at higher frequencies the movement of the electron does not follow the excitation of incident electromagnetic wave well.

This Drude model is an approximation that does not consider the restoring force of the electron. Therefore, resonance such as interband transition is neglected in this system, and it does not fit well over all regions of frequency when compared with the dielectric property measured in actual materials. Particularly in the wavelength region close to the interband transition, there is a large deviation in dielectric property between Drude model and the actual materials due to the contribution of the bound electron. An additional restoring force should be considered to account for this deviation, which is expressed in the Lorentz model as follows:

$$m^* \left(\frac{\partial^2 \mathbf{u}}{\partial t^2} + \gamma \frac{\partial \mathbf{u}}{\partial t} + \omega_0^2 \mathbf{u} \right) = -e\mathbf{E}(t). \quad (4.5)$$

Here, ω_0 is the resonance frequency due to the bound electron, and m^* is the effective mass for the bound electron.

The stationary solution and its complex dielectric function for Lorentz model are as follows:

$$\mathbf{u} = \frac{e}{m^*} \frac{1}{\omega_0^2 - \omega^2 - i\gamma\omega} \mathbf{E}_0^{ext}. \quad (4.6)$$

$$\varepsilon_{Lorentz}(\omega) = 1 + \frac{\omega_p^2}{\omega_0^2 - \omega^2 - i\gamma\omega}. \quad (4.7)$$

This Lorentz model describes the effect of one transition caused by the bound electron. However, the total dielectric function can be obtained by combining the terms for all transitions with the weighted factor to the free-electron oscillation by Drude model.

5.2.2 Polarizability of metal nanostructure

When a metallic material is confined at the nanometer level and becomes a nanoparticle with a finite dimension, it behaves like a cavity of plasma oscillation. In this case, a non-propagating plasmon localized to the nanoparticle can be formed by excitation of incident electromagnetic wave, showing a corresponding resonance, so-called localized surface plasmon resonance (LSPR), at the certain resonance frequency. When the dipole moment \mathbf{p} is induced in the nanoparticle by the initial electric field \mathbf{E}_0 , it is described as $\mathbf{p} = \alpha \mathbf{E}_0$ by the polarizability α . For the spherical nanoparticle with the sub-wavelength radius in a vacuum, the isotropic polarizability can be obtained by electrostatic approximation as follows:

$$\alpha = 4\pi\varepsilon_0 r^3 \frac{\varepsilon(\omega) - 1}{\varepsilon(\omega) + 2}. \quad (4.8)$$

Here, polarizability diverges at $\varepsilon(\omega) = -2$ condition, which corresponds to Fröhlich's condition for a spherical particle in the vacuum condition. Applying the complex dielectric function of the Drude model, the polarizability is given by

$$\alpha = 4\pi\varepsilon_0 r^3 \frac{\omega_{LSPR}^2}{\omega_{LSPR}^2 - \omega^2 - i\gamma\omega^2}. \quad (4.9)$$

This polarizability represents the Lorentzian line shape, where the LSPR frequency ω_{LSPR} is given by $\omega_{LSPR} = \omega_p/\sqrt{3}$. At the resonance condition ($\omega = \omega_{LSPR}$), the polarizability has a pure imaginary value, so the phase shift of $\pi/2$ appears between the incident electric field and the dipole. The exact peak position is observed at $\omega_{peak} = \sqrt{\omega_{LSPR}^2 - \gamma^2/2}$, which is not exactly the same as the resonance condition due to the damping term.

Interestingly, the resonance frequency of Drude metal particles with small and spherical shape is independent on the radius. However, as the size increases, the resonance can change depending on the radius due to the effect of the retardation, and as the geometry becomes more complex, the polarizability greatly changes including geometry contribution. Nevertheless, the resonance behavior of these localized plasmons maintains the Lorentzian lineshape, which can be described as a damped harmonic oscillator. In this case, induced dipole moment can be described as $\mathbf{p} = -e\mathbf{u}$, and in combination with the equation (4.6) and the relation $\mathbf{p} = \alpha\mathbf{E}_0$, polarizability can be given by

$$\alpha = -\frac{e^2}{m^*} \frac{1}{\omega_{LSPR}^2 - \omega^2 - i\gamma_{LSPR}\omega}. \quad (4.10)$$

Here, γ_{LSPR} do not represent material but damping of LSPR.

5.2.3 Qualitative model for complex plasmonic response

In the previous section, we discussed plasmonic resonance by individual metallic nanostructure. However, if two or more metal nanoparticles are located close enough, they can generate new collective resonance modes due to the coupling between plasmon resonance modes by Coulomb interaction. These phenomena have been known in solid-solid,¹³ inverse-inverse,¹⁴ and solid-inverse¹⁵ nanostructured systems. In these systems, the optical properties of the plasmonic nanostructure dramatically change due to strong coupling between the dipole or quadrupole plasmon modes. In order to intuitively understand coupling phenomena between plasmon modes, a plasmon hybridization model which is similar to the concept of hybrid orbital in molecular orbital theory can be introduced.¹⁶

For example, the simplest coupled dimer structure consisting of two nanorods can be used to qualitatively understand the plasmon hybridization phenomena (Figure 5.1a). In this structure, individual nanorods can be excited to dipole oscillation where each end of the nanorods are polarized to positive and negative charges, respectively. If two nanorods are separated by very short distances, these dipole oscillations can interact with each other by Coulomb interaction. In this case, two nanorods can oscillate either in-phase and out-of-phase. For the in-phase oscillation, two nanorods are symmetrically polarized to each other, and opposite charges are accumulated in the gap which can provide further stabilization of the system so that a low-energy bonding mode can be formed. On the other hand, for the case of anti-symmetric out-of-phase oscillation, the same charges are accumulated in the gap and generate additional electrostatic energy. Therefore, the high-energy anti-bonding mode is formed at this time. These bonding and anti-bonding modes have new resonance conditions at different resonance frequency from the individual plasmon modes. Using this model, we can provide an intuition

to interpret the optical response of plasmonic nanostructures with complex and coupled structures.

Interestingly, the concept of coupling two or more oscillators can help to understand the chiroptical behavior of chiral plasmonic nanostructures. According to the classical Born-Khun model for describing optical activity in chiral molecules, the simplest system for chiroptical response is a model for two orthogonally oscillating coupled electrons (Figure 5.1b).¹⁷ In this case, each individual oscillation can be excited by the horizontal or vertical polarization of exciting field, but potential energy due to one oscillation can be transferred to the other oscillation by Coulomb interaction between adjacent coupled electrons. It is intuitively clear that these coupling between two orthogonal oscillators will induce the rotation of polarization when incident linearly polarized light was irradiated. Let the polarization axis of incident linearly polarized light be aligned with the upper oscillator, which is confined to movement in the y-direction, and the orientation of the second oscillator be confined in the x-direction. When the incident light strikes the upper oscillator, the center-of-mass of this coupled system will be oriented in a different direction depending on the y-position, thus leading to the rotation of polarization. Thus, oscillation by these coupled electrons can be a single unit that can represent the chiroptical response.

The plasmonic analogue of this Born-Kuhn model can be implemented by two vertically displaced nanorods that have a 90° angle between them and are stacked at each corner side.¹⁷ To excite the resonance mode in the long axis direction for each nanorod, the polarization of the incident light field should be aligned parallel to the major axis direction. Since the distance between two nanorods is close enough, each plasmon resonance mode can be capacitively coupled to each other, or they can be conductively coupled assuming that two nanorods are connected to each

other. The chiral plasmonic resonance in the 90° -twisted nanorod dimer can be explained in the context of a conventional plasmon hybridization model (Figure 5.1b). For qualitative understanding, it was assumed that the vertical spacing between nanorods corresponded to a quarter-wavelength phase difference.

For the D-enantiomer structure of Figure 5.1b, when the circular polarization is incident in the $-z$ -direction, different resonance modes are excited because the rotating direction of the electric field vector for LCP and RCP is opposite. For RCP, it was assumed that the incident light traveling in the z -direction has its polarization axis aligned with the upper rod when the light strikes the topmost surface of the structure. Due to the quarter-wavelength spacing between nanorods, lower nanorod is excited by the clockwise-rotated polarization. As a result, the longitudinal plasmon mode of both nanorods is simultaneously excited in this situation. Due to the electric vector direction of the RCP, the two nanorods form an anti-symmetric configuration of dipoles. This configuration forms a high-energy anti-bonding mode by additional electrostatic energy. In contrast, in the case of LCP, two nanorods are symmetrically polarized to form a low-energy bonding mode. In other words, two hybrid resonance, bonding and anti-bonding, formed by the plasmon hybridization of 90° -twisted nanorod dimer, correspond to situations where RCP or LCP are incidents, respectively. Thus, RCP and LCP have plasmon resonance modes at different energies, and these differences cause chiroptical responses such as CD and ORD. These 90° -twisted nanorod dimer model can provide a useful insight to understand the chiroptical response of nanostructures, and more complex chiral nanostructures can be understood as a hybrid system containing multiple Born-Kuhn units.

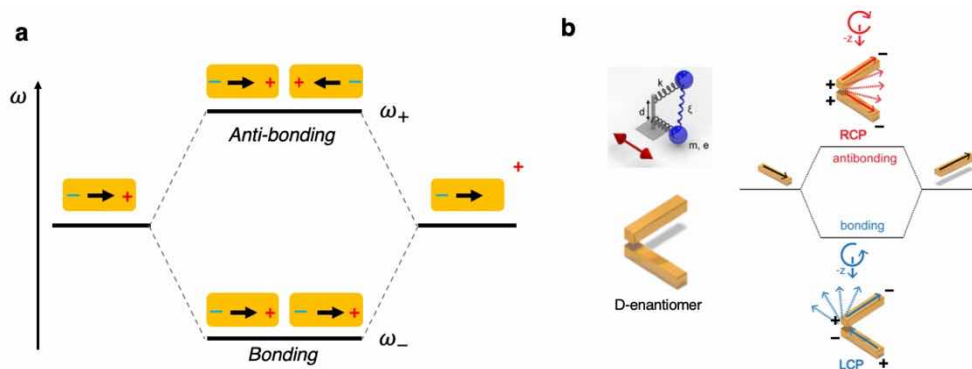


Figure 5.1 Plasmon hybridization scheme for complex and resonance-coupled plasmonic nanostructure. (a) Resonance coupling of end-to-end aligned Au nanorods dimer separated by a small gap. (b) Plasmonic Born-Kuhn model composed of 90°-twisted nanorods dimer. Hybridized plasmon mode excited by LCP and RCP corresponds to bonding and anti-bonding, respectively.

5.2.4 Electrodynamic description for chiral nanomaterial

Chiral plasmonic nanostructures can be used as the building blocks of plasmonic devices and metamaterials because of their strong chiroptical responses and subwavelength sizes. Therefore, it is also beneficial to have analytical guides for designing chiral nanostructure-based optical devices. Here, we briefly introduce the concepts of the analytic descriptions of a chiral plasmonic nanoparticle. For the chiral nanostructures which has sizes much smaller than the wavelength of interest, their scattering of light belongs to the Rayleigh regime. This leads us to describe the single chiral nanostructure as an effective homogeneous nanosphere composed of the chiral medium. In this effective approach, chiral morphology can be approximated with chiral material parameters. The effective description provides analytical benefits, allowing us to obtain an insight into the design of chiral plasmonic nanostructure with a high g-factor. Let us say the effective nanosphere is composed of a chiral medium with permittivity ε , permeability μ , and dimensionless chirality parameter κ related to the electromagnetic fields \mathbf{E} , \mathbf{B} , \mathbf{D} , and \mathbf{H} by the constitutive relations,

$$\mathbf{D} = \varepsilon\mathbf{E} + i\kappa\sqrt{\varepsilon_0\mu_0}\mathbf{H} \quad (4.11)$$

$$\mathbf{B} = \mu\mathbf{H} - i\kappa\sqrt{\varepsilon_0\mu_0}\mathbf{E} \quad (4.12)$$

The electric and magnetic dipole moments of the effective nanospheres are then respectively written as $\mathbf{p} = \alpha\mathbf{E} + i\mathbf{G}\mathbf{H}$ and $\mathbf{m} = \chi\mathbf{H} - i\mathbf{G}\mathbf{E}$, with the polarizabilities given by^{18,19}

$$\alpha = 4\pi\varepsilon_0 \frac{(\mu+2\mu_0)(\varepsilon-\varepsilon_0)-\kappa^2}{(\mu+2\mu_0)(\varepsilon+2\varepsilon_0)-\kappa^2} R^3 \quad (4.13)$$

$$\chi = 4\pi\mu_0 \frac{(\mu-\mu_0)(\varepsilon+2\varepsilon_0)-\kappa^2}{(\mu+2\mu_0)(\varepsilon+2\varepsilon_0)-\kappa^2} R^3 \quad (4.14)$$

$$G = 4\pi\varepsilon_0\mu_0 \frac{3\kappa}{(\mu+2\mu_0)(\varepsilon+2\varepsilon_0)-\kappa^2} R^3 \quad (4.15)$$

Where ε_0 and μ_0 are the permittivity and the permeability of the background medium, respectively. For two opposite circularly polarized light, the dipole moments \mathbf{p} and \mathbf{m} become

$$\mathbf{p}_{\pm} = \alpha_{\pm}\mathbf{E}_{\pm} = (\alpha \pm G)\mathbf{E}_{\pm} \quad (4.16)$$

$$\mathbf{m}_{\pm} = \chi_{\pm}\mathbf{H}_{\pm} = (\chi \pm G)\mathbf{H}_{\pm} \approx \pm G\mathbf{H}_{\pm} \quad (4.17)$$

for particles with weak magnetic responses, i.e., $\mu = \mu_0$. By the optical theorem, the extinction cross-section for circularly polarized light is given by $\sigma_{ext,\pm} \approx kIm(\alpha_{\pm})/\varepsilon_0$. Here, we neglect the interference effect between \mathbf{p} and \mathbf{m} by the non-magnetic response approximation.²⁰ Note that rigorous calculations are needed if the magnetic response χ is pronounced. The g-factor of the single chiral nanostructure can then be characterized by

$$g = \frac{\sigma_{ext,+} - \sigma_{ext,-}}{(\sigma_{ext,+} + \sigma_{ext,-})/2} = \frac{2Im(G)}{Im(\alpha)} \quad (4.18)$$

Thus, the polarizability α and G need to be respectively minimized and maximized to boost the g-factor. Based on this effective description, it is also possible to estimate the refractive index of the nanoparticle-dispersed medium using the Maxwell–Garnett formula adopted for chiral media,^{18,19} and it can provide a design rule for chiral nanostructure-based metamaterials exhibiting negative refraction.

The representative architectures of chiral nanostructures are categorized into two types: a chiral assembly of plasmonic nanoparticles^{21–24} and singular chiral nanostructure with continuous chiral morphologies.²⁵ Recently, it has become

known that the continuous chiral nanostructure can exhibit a much stronger chiroptical response than the chiral assembly counterpart by one order of magnitude.

Chiral assembly with multiple plasmonic building blocks generally suffers from retardation effect-mediated loss: the dephasing between the radiation from different plasmonic NPs in the helix structure.^{21,23} This originates from the fact that the dipolar oscillations of individual Au NPs in the helical clusters can be coupled with each other and cascaded along the larger helical geometry.²¹ Therefore, the retardation effect in the chiroptic response is inevitable in the chiral assembly, giving the origin of the relatively weaker chiroptic responses. For the helical assembly of spherical plasmonic nanoparticles, CD response of this helical cluster ($\Delta\sigma \equiv \sigma_+ - \sigma_-$) with an overall cluster size R is limited to the order of $\Delta\sigma \approx k^2 R^4$, while their absorption scales according to $\sigma \equiv (\sigma_+ + \sigma_-)/2 \approx kR^3$.^{26,27} This mismatching scale of kR between the CD and the absorption implies that the CD of the helical clusters comes from the retardation effect accompanying the small parameter kR .²¹ The dissymmetry factor (hereafter, g -factor), a typical measure of the chiroptical response using the ratio of the CD to the absorption ($g \equiv \Delta\sigma/\sigma$), is also bound to the order of kR or smaller orders. Owing to the intrinsic limitations resulting from this retardation effect, the experimentally obtained g -factor from helical clusters was limited to the order of 10^{-2} .^{21,23} In contrast, singular chiral nanoparticle avoid the retardation effect because the continuous chiral morphology of metal, rather than the discontinuously assembled Au NPs in helical clusters, is featured on the surface of a single particle.²⁵

5.3 Results and discussion

5.3.1 Chiroptical spectroscopy analysis of Au helicoid nanoparticle

Unique chiral geometry of helicoid nanoparticle offers strong chiral light-matter interactions which can be measured by CD spectroscopy. Figure 5.2 shows the SEM images and CD spectra of 432 helicoids I, II, and III. In the case of 432 helicoid I, twelve edges that constitute the cube are split in opposite directions to form a chiral geometry. On the other hand, the 432 helicoids II and III have chiral gaps along the twelve $\langle 110 \rangle$ -directions due to the formation of the pinwheel structure. This difference in morphology can be also manifested in the CD spectra. In case of 432 helicoid I, we can identify a spectrum with a positive wavelength at a short wavelength and a negative CD value at a long wavelength. However, in the case of 432 helicoid II and III, the opposite occurs at a short wavelength and a negative wavelength, although the chiral elements of all helicoid morphology rotated in the clockwise direction along the $\langle 100 \rangle$ -direction as rotation axis. According to the observation at Chapter 4, twisting of different crystal boundary for 432 helicoid II and III during the at the nanoparticle growth stage (Figure 4.7 and 4.9) is thought to be the cause of this opposite signal. In addition, the 432 helicoid II and III show similar spectral shape in CD spectra, but their CD intensity and the peak positions were different. This difference can be attributed that the depth of the chiral gap structure is deeper in helicoid III than that of helicoid II, which leads to increased capacitive coupling with stronger resonance at the longer wavelengths.¹⁶

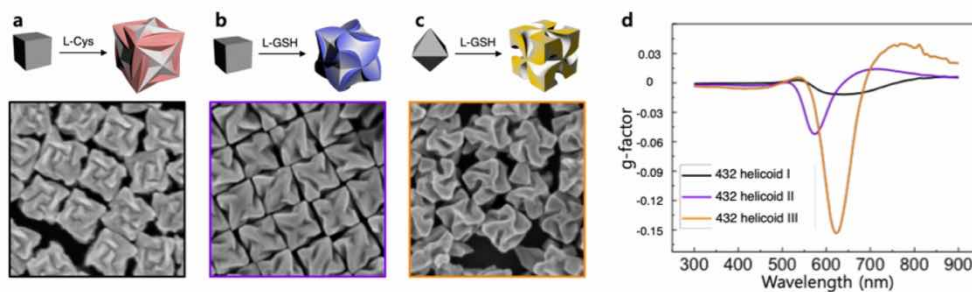


Figure 5.2 Chiroptical response of three 432 helicoid nanoparticles. (a) Schematic and SEM image of (a) 432 helicoid I, (b) 432 helicoid II, (c) 432 helicoid III nanoparticles. (d) Corresponding g-factor spectra of 432 helicoid I, II, and III solutions.

In order to confirm that this strong chiral light-matter interaction originates from chiral morphology defined in three-dimensional geometry, we confirmed the reciprocity of the CD response. In the case of two-dimensional quasi-chiral structures, which have been widely used in the field of chiral metamaterial, chiroptical signals appear in the far-field response only when the normal component of incident light is present. This is due to the existence of mirror planes parallel to nanostructures (substrates). In addition, when the incident light enters from the opposite direction, inversed chiroptical signal is measured along the opposite direction because of the presence of the mirror plane. Therefore, representing the same CD signal regardless of the incident direction of light can prove that the structure has three-dimensional chirality. To check this reciprocity, we measured helicoid III nanoparticle samples in solution and on the substrate in the forward and backward direction and confirmed the identical CD spectrum, as shown in Figure 5.3. This confirms that the CD signal of helicoid nanoparticles has reciprocity, and the huge chiroptical responses originate from the purely three-dimensional chiral geometry.

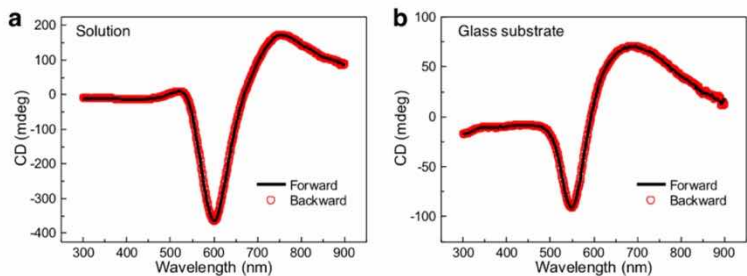


Figure 5.3 Reciprocity of CD measurement in 432 helicoid III. (a,b) CD spectra of 432 helicoid III nanoparticles dispersed in aqueous solution (a) and deposited on glass substrate (b). In both cases, CD measurements in forward and backward direction of samples produced identical responses.

For the 432 helicoid III, which show strongest chiroptical response among all 432 helicoid nanoparticles, we compared the circular dichroism and the optical rotation signals, which originate from the absorption difference and phase delay, respectively. As we have seen in the previous section, circular dichroism and optical rotation correspond to the imaginary part and real part of the chirality parameter κ and are proportional to the difference in extinction coefficient and refractive index for LCP and RCP, respectively. Figure 5.4 exhibited CD and ORD spectrum of the 432 helicoid III nanoparticle solution. The CD spectrum has a negative peak at 630 nm, crosses the zero-value at 700 nm, and shows a broad positive peak at 800 nm. On the other hand, the ORD spectrum shows a different spectral shape with a positive peak at 580 nm and a negative peak at 680 nm. In particular, at 630 nm, which was the peak in the CD, the ORD has a zero signal, which is consistent with the relationship between CD and ORD in the conventional chiral material showing Cotton effect.²

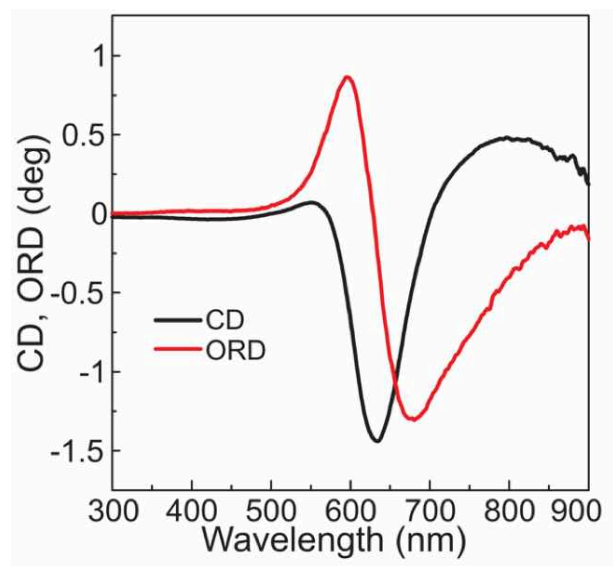


Figure 5.4 Circular dichroism (CD) and optical rotatory dispersion (ORD) spectra of 432 helicoid III nanoparticles.

We compared the degree of the chiral light-matter interaction of these helicoid nanoparticles with those of conventional chiral nanostructures. For the chiroptical response, Kuhn's dissymmetry factor (g-factor) can be a good criterion for comparing the effective difference between LCP and RCP at the same optical density. As we have mentioned in Chapter 4, the g-factor can be calculated by dividing CD by Absorption, $g = CD/Abs$, which has a value between -2 and $+2$. Using g-factor, we compared the size and wavelength range of the chiroptical response of 432 helicoid nanoparticles with conventional chiral plasmonic nanostructures synthesized by bottom-up method.

First, biomolecules such as amino acids, peptides, and proteins showed a g-factor around 10^{-4} to 10^{-3} at the UV region. This is because most of biomolecules absorb light only in the UV region, and their optical cross-section is small. On the other hand, when a chiral molecule is coupled to the surface of an achiral plasmonic nanoparticle, the chirality of the molecular dipole may represent a chiroptical response in the plasmon resonance region. This "plasmon-induced CD" response can be observed when using the simplest coupling of individual nanoparticles and chiral molecules, which shows chiroptical response at the visible plasmon resonance wavelength as well as in the UV signal. However, the g-factor is weak at the level of 10^{-4} to 10^{-3} at this time, which is similar to that of the molecule. As a way to increase chiroptical signals, a strategy for forming a hotspot through a nano-gap between plasmonic nanostructures was proposed, in which case the g-factor could be improved to 10^{-2} level.

Using molecular self-assembly phenomena, chiral plasmonic assembly structure can be produced by using achiral building blocks to form a chiral geometry. Although the collective chiral assembly may cause a loss of chiroptical response due to the retardation effects mentioned in the previous section, an increased g-factor of

10^{-2} level was usually achieved. For the case of the twisted rod structure with tiny spacing, g-factor of 0.07 has been reported.

Compared to those various cases, helicoid nanoparticles can be categorized as a continuous chiral nanostructure, which is a new class of geometry in bottom-up synthesis of chiral plasmonic nanoparticles. In particular, 432 helicoid III nanoparticles exhibited a g-factor of 0.2 even though the nanoparticles are randomly dispersed in solution, and it is worth noting that the g-factor value is higher than that of any other chiral nanostructures fabricated by bottom-up approaches. Owing to this g-factor value, the difference in optical response by LCP and RCP can be visually observable and provide a possibility to be used in polarized selective optical applications.

Table 5.1 Comparison of the g-factor of various chiral structures

	Structure	Wavelength	g-factor	Ref.	
Amino acid and peptide	L-cysteine	215 nm	5×10^{-3}	this work	
	L-glutathione	210 nm	2×10^{-4}	this work	
	α -helical protein	190 nm	3×10^{-3}	28	
Chiral molecule on achiral nanoparticle	Au nanoparticle coated with peptide	530 nm	3×10^{-4}	29	
	Ag nanoparticle coated with assembled chiral supramolecule	530 nm	2×10^{-3}	30	
	Nanogapped Au-Ag nanoparticle	430 nm	1×10^{-2}	31	
Chiral arrangement of multiple nanoparticles	Au-Ag nanoparticle heterodimer with antibody-antigen bridge	400 nm	2×10^{-2}	32	
	Au nanoparticle tetrahedral superstructure with DNA-nanoparticle conjugate	525 nm	2×10^{-2}	22	
	Au nanoparticle helical superstructure with DNA origami bundle	700 nm	3×10^{-2}	23	
	Au nanorod helical superstructure with bifacial DNA origami sheet	800 nm	2×10^{-2}	33	
	Twisted Au nanorod dimer with reconfigurable DNA origami bundle	750 nm	2×10^{-2}	34	
	Twisted Au nanorod oligomer with electrostatic side-by-side assembly	600 nm	7×10^{-2}	35	
	Chiral single nanoparticle	432 helicoid I	565 nm	3×10^{-2}	this work
		432 helicoid II	575 nm	5×10^{-2}	this work
432 helicoid III		620 nm	2×10^{-1}	this work	

5.3.2 Electrodynamic simulation of Au helicoid nanoparticle

The morphology of nanostructure is major determinant for the optical property of plasmonic materials. It can determine the frequency and amplitude of the resonance formed on the plasmonic nanoparticles, as well as alter the plasmon oscillation mode itself, such as the formation of higher-order and hybridized resonance mode.^{16,36} Therefore, investigating the plasmon resonance mode and microscopic electromagnetic field formed on the nanoparticle is critical for understanding the correlation of geometry and optical properties. In order to fundamentally understand the strong chiroptical response, we reproduced the experimental results and investigated the near-field phenomena through electromagnetic simulation using finite-difference time-domain (FDTD) method.

Based on the observed morphology, we attempted three-dimensional modeling of 432 helicoid III nanoparticles. According to the microscopic observation using SEM (Figure 4.23) and STEM (Figure 4.26), helicoid III nanoparticles have a chiral gap at the twelve $\langle 110 \rangle$ -direction of cubic form. Interestingly, the HIM result (Figure 4.27) shows that the internal structure of this gap is a twisted curved surface. From these observations, we modeled the morphology of the nanoparticles as shown in Figure 5.5a. Indeed, 432 helicoid III nanoparticles are randomly dispersed in the solution and can have orientation in all directions. To consider this situation in the FDTD simulation, we calculated the optical response in the 756 discrete orientations by rotating the nanoparticles with adjusting the angle of Θ and Φ , respectively, after fixing the propagation direction of the incident electromagnetic wave in the $-z$ -direction. Then, all calculated optical responses were averaged, which is shown in (Figure 5.5b). Figure 5.6a shows the CD spectrum and extinction spectrum obtained from the simulation, and Figure 5.6b was experimentally measured results. The calculated CD spectrum exhibited similar

spectral trend with the experiment, featuring negative and positive CD values at visible and NIR regions, respectively. In particular, peak positions at 620 nm with the largest chiroptical response were well matched with each other. However, the results at the longer wavelengths were not exactly consistent in both CD and Extinction, suggesting that the three-dimensional model currently in use does not fully reproduce the actual morphology of 432 helicoid III structures. Further refining of the structure and direct measurement of 432 helicoid III morphology using electron tomography or x-ray imaging will be beneficial to completely reproduce the actual morphology and chiroptical response.

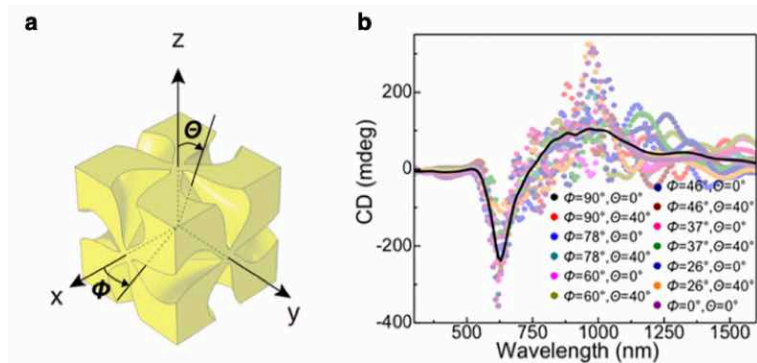


Figure 5.5 Finite-difference time-domain (FDTD) simulation. (a) 3D model and orientation of 432 helicoid III. (b) Orientation-averaged CD spectrum ($\langle CD \rangle_{\Omega}$, black solid line) and CD spectra calculated at selected orientations (dots). $\langle CD \rangle_{\Omega}$ is averaged over 756 discrete orientations. CD spectrum at a single orientation resembles $\langle CD \rangle_{\Omega}$ with some deviations.

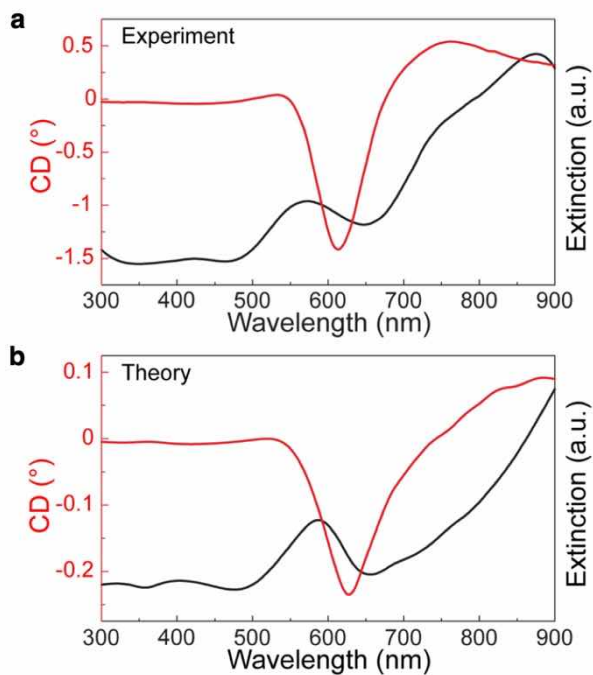


Figure 5.6 (a) Experimental CD and extinction spectra of 432 helicoid III. (b) Theoretical calculation of CD and extinction spectra of 432 helicoid III based on finite-difference time-domain method.

To understand the origin of this strong chiroptical response can be created, near-field plasmonic behavior was investigated. For the given helicoid III morphology, extinction and CD response were calculated when the incident circularly polarized light was excited in normal direction (Figure 5.7a), and subsequently, the electric field distribution was visualized (Figure 5.7b, upper). In the normal incidence condition, the strongest negative CD response occurred at 650nm, which is slightly red-shifted position compared with the extinction peak around 600 nm. At this wavelength, strong electric field was applied near the surface of helicoid nanoparticle and focused into the subwavelength areas between two chiral arms, called chiral gap. Differential electric field distribution between LCP and RCP excitation condition shows that strong near-field dissymmetry appears at the chiral gap region, and the far-field CD response is derived from the chiral plasmonic resonance mode (Figure 5.7c). Chiral patterns of magnetic field distribution and corresponding differential field between LCP and RCP excitation also support the generation of chiral plasmonic resonance (Figure 5.7d,e)

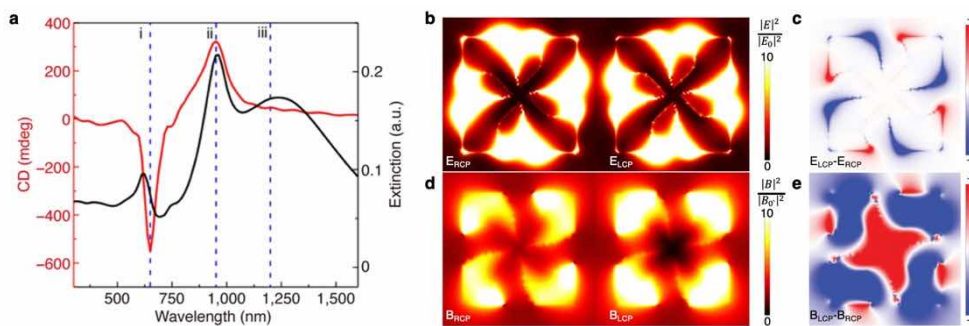


Figure 5.7 (a) CD and extinction spectra calculated for the helicoid III nanoparticle with a normal incidence of circularly polarized light. (b) Electric- and (c) magnetic-field intensities on an illuminated helicoid surface upon normal incidence of LCP and RCP light at 650 nm. The asymmetric field distribution of the (d) electric and (e) magnetic fields are displayed by the differences in these fields under excitation by left circularly polarized (LCP) and right circularly polarized (RCP) light.

It is well known that larger particles can support stronger dipole moments and higher-order modes, which can lead to stronger extinction and chiral responses. Figure 5.8 supports this claim, with chiral nanoparticles (samples 1–3) with increasing edge lengths (size of particle) in the same geometry showing increasing g -factors. However, to function as a metamaterial, the meta-atom, or chiral nanoparticle, should be smaller than the wavelength of the incident light; hence, the size of the chiral nanoparticle is limited to some extent.

Remarkably, the optical properties of the chiral nanoparticles (both extinction and chirality) depend strongly on their subwavelength plasmonic gap. Generally, chiral nanoparticles with narrower and deeper chiral gaps exhibit a stronger and red-shifted extinction and chiral response. The results are summarized in Figure 5.8, in which chiral nanoparticles (samples 4–7) with increasing gap widths have decreasing g -factors and those (samples 8–14) with increasing gap depths have increasing g -factors of more than 0.7. These stronger and red-shifted features may originate from a stronger dimeric coupling between the two domains separated by the chiral gap. This could be explained by the plasmon hybridization model, which explains the behavior of closely coupled plasmonic nanostructures due to the electrostatic dipole-dipole interaction resulting in an enhanced and stabilized (red-shifted in wavelength) response.¹⁶ We also found an enhanced electric field near the plasmonic gaps in Figure 5.9, which can result in enhanced dipole moments. This field enhancement increased as the plasmonic gap became narrower and deeper. We also studied chiral nanoparticles (samples 16–19) with different gap angles, which is essential for the broken parity symmetry and chiral response. An achiral nanoparticle with a gap angle of 0° or 90° will not exhibit any chiral response; however, it is still difficult to quantify the structural chirality of the other chiral nanoparticles studied here.

We also simulated chiral nanoparticles with more complex geometries (Figure 5.10). The difficulty in correlating structural chirality to the observed chiral properties is also addressed by the decreasing g-factor of chiral nanoparticles with increases in certain curvatures in samples 20–22. As stated above, structural chirality cannot be directly quantified, and we generally rely on numerical methods or experiments to predict chiral properties. In samples 23–26, the extinction of elongated chiral nanoparticles showed noticeable changes due to an increase in size, but their g-factors remained similar despite large changes in their aspect ratio and size, of up to a factor of three. The four-fold symmetry of our chiral nanoparticle gets broken, and the orientation dependence of responses becomes larger. In sample 32, the triangular plate also showed noticeable orientation-dependent responses. This anisotropic response has commonly been observed in canonical chiral systems, such as helices, twisted-nanorods and helical arrangements of nanoparticles, and is responsible for the lowering of the average chiral response. In samples 27–31, different chiral particle designs, such as hollow chiral nanoparticles, were constructed by removing cubic domains inside the chiral nanoparticle. In samples 27 and 28, which have small void sizes, the particles did not exhibit noticeable change in their responses. However, chiral nanoparticles with large voids (samples 29–31) had g-factors of more than 0.9—the strongest g-factor of these simulations. These hollow chiral nanoparticles have very thin outer shells and exposed insides. Interestingly, strongly enhanced and redshifted responses were observed despite the greatly reduced volume.

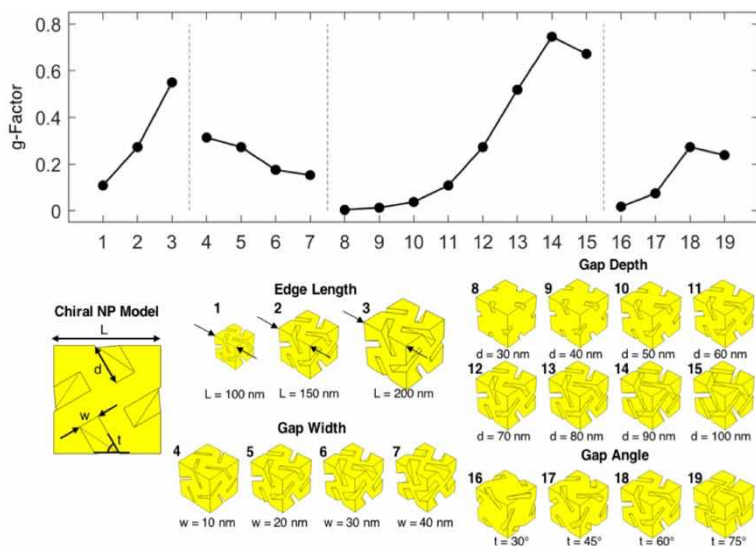


Figure 5.8 FDTD simulation on 432 helicoid III with different chiral gap geometry. Calculated g-factors of chiral nanoparticles corresponding to models (sample 1–19) using parameterized chiral nanoparticles. Chiral nanoparticles with different (sample 1–3) edge lengths (L) of 100–200 nm; (sample 4–7) gap widths (w) of 10–40 nm; (sample 8–15) gap depths (d) of 30–100 nm; and (sample 16–19) gap angles (t) of 30–75°. Default parameters are edge length of 150 nm, gap width of 20 nm, gap depth of 70 nm, and gap angle of 60°.

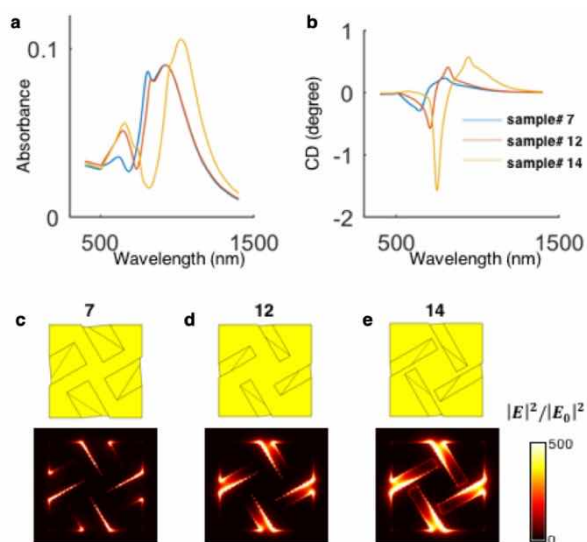


Figure 5.9 Correlation of chiroptical response and gap width. (a, b) Calculated absorbance and CD of chiral nanoparticles (sample 7: L150, w40, d70, t60), (sample 12: L150, w20, d70, t60), and (sample 14: L150, w20, d90, t60) using $N = 10^{15} \text{ m}^{-3}$ and $l = 10^{-3} \text{ m}$. (c–e) Calculated electric field intensity on the illuminated face ($z = -75 \text{ nm}$) at RCP illumination at the first CD peak of 600 nm, 670 nm, and 720 nm, respectively.

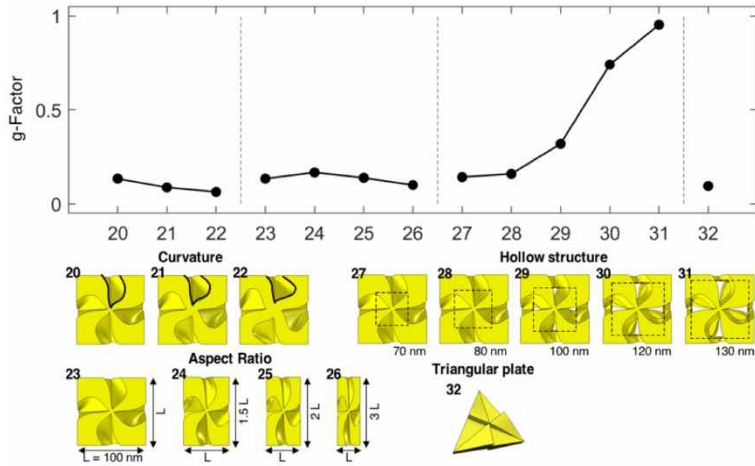


Figure 5.10 FDTD simulation on differently modified 432 helicoid III. Calculated g-factors of chiral nanoparticles corresponding to models (sample 20–32) using chiral nanoparticles with various geometry changes. (sample 20–22) Chiral nanoparticles with increasing curvatures from (sample 20) to (sample 22); (sample 23–26) Chiral nanoparticles with aspect ratio of (sample 23) 1 to (sample 26) 3; (27–31) chiral nanoparticles with hollow structures constructed by removing cubic domains with side lengths of (sample 27) 70 nm to (sample 31) 130 nm. Default size of chiral nanoparticles in (sample 20–31) is 150 nm. (sample 32) Planar-triangle-based chiral nanoparticle with edge length of 150 nm.

Based on the electromagnetic simulation study, we have developed some general guidelines for designing chiral nanoparticles with high g-factors. First, both the extinction (absorbance) and chiro-optical response (CD, g-factor) depend on the size of chiral nanoparticles. This is because a larger particle supports stronger dipolar modes and even higher-order modes, resulting in stronger extinction and chiro-optical responses. Second, in general, the chiro-optical properties of chiral nanoparticles depend strongly on their ‘gap’. Although the feature size of these gaps is much smaller than the wavelength, plasmonics allows considerable changes in response with subtle morphology differences. Narrower and deeper gaps allow stronger and redshifted chiroptical responses as well as extinction, which could originate from stronger dimeric plasmon coupling. The high-performance plasmonic chiral systems reported so far often have discrete particles that are coupled to achieve the enhanced responses. These chiral systems have linker molecules, such as DNA, to maintain their conformations. A single continuous chiral nanoparticle could have a similar property owing to the gaps that are deep and long. Therefore, designing chiral nanoparticles with high performance requires control over gap formation. Third, hollow chiral nanoparticles could achieve highly enhanced chiro-optical properties with g-factor of 0.9. In addition, the redshifted response without an increase in particle size could be beneficial because it decreases the particle-size-to-wavelength ratio, which brings this particle medium closer to the definition of a metamaterial.

In terms of structure-related optical activity, morphological integrity of chiral structure is indeed important for high g-factor. As an imperfect morphological deviation, structural change at the end of the curved arm is arbitrarily generated in our synthesis. To evaluate the effect of this change on the g-factor, a numerical simulation was performed on the two representative structures, as shown in Figure 5.11. When a bump was added to the end of the chiral arm (Figure 5.11a), slight change in CD signal was only observed. On the other hand, a bump located on the gap side of the chiral arm (Figure 5.11b) decreased the chirality, thus reducing CD intensity. Based on the simulation results, we concluded that maintaining the chiral gap is important for achieving high optical activity.

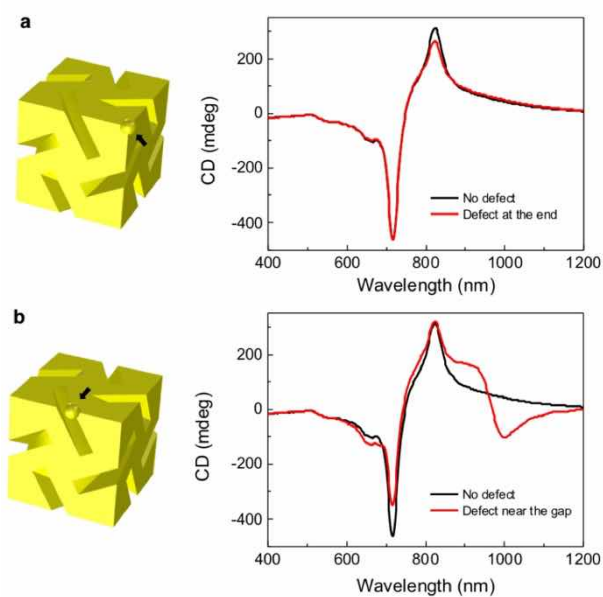


Figure 5.11 Effect of structure deviation on optical activity. Calculated CD signals of chiral nanoparticles with morphological deviation. With the addition of a spherical bump, changes in chiral structure were created, and the model with different bump locations was analyzed.

5.3.3 Polarization-based color modulation

As a result of the high g -factor of the helicoid nanoparticles, macroscopically distinguishable color change was possible by controlling the polarization. The CD spectrum and corresponding optical rotatory dispersion (ORD) spectrum of the 432 helicoid III nanoparticle solution are presented in Figure 5.4, and the output polarization state was directly measured by the rotating-waveplate polarimetry at four wavelengths using a linearly polarized incident light (Figure 5.12a). The largest ellipticity ($\chi = -28.7^\circ$, left circular polarized) was observed at 635 nm, and the azimuthal rotation (ψ) gradually changed from -7.9° to $+29^\circ$ as the wavelength was increased (Figure 5.12b). The conversion from linear to elliptically polarized light by the 432 helicoid III is clearly displayed under cross-polarized condition. Although the achiral nanoparticles did not exhibit any transmission (Figure 5.12c, left), a solution of 432 helicoid III showed bright yellow colored cross-polarized transmission, which reflects the pronounced polarization rotating ability that functions at visible wavelengths (Figure 5.12c, left). Changing the size of 432 helicoid III by controlling the initial seed concentration caused a resonance shift of the resulting nanoparticles, with the λ_{\max} increasing from 552 to 668 nm (5.13a, 5.13b). This modification also allows for a gradual tuning of the transmitted colors under cross-polarized conditions (0° , dotted box in Figure 5.13c). In addition, rotation of the analyzer reversibly generated various transmitted colors, thereby providing a versatile route for color modulation reflecting the ORD response (Figure 5.13c). In contrast to the symmetrical pattern of achiral nanoparticles, the color transition of 432 helicoid III was continuous and asymmetric, forming elliptical traces on the chromaticity diagram (Figure 5.13d). The color transformation of 432 helicoid III was dynamic and covered a wide area in the color space.

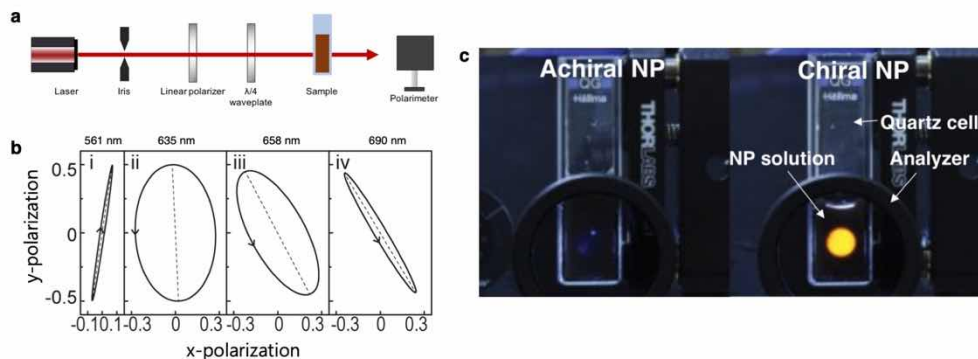


Figure 5.12 Visible light polarization control by 432 helicoid III solution. (a) Experimental setup used for polarimeter measurements with 561, 635, 658, and 690 nm laser source. (b) Polarization ellipses at each wavelength are expressed by ellipticity (χ) and azimuthal rotation (ψ); $\chi = 1.7^\circ$, $\psi = -7.9^\circ$ at 561 nm; $\chi = -28.7^\circ$, $\psi = 2.6^\circ$ at 635 nm; $\chi = -20.7^\circ$, $\psi = 26.6^\circ$ at 658 nm; and $\chi = -4.8^\circ$, $\psi = 29.0^\circ$ at 690 nm. (c) Photographs of achiral (left) and 432 helicoid III (right) solutions showing transmitted light under cross-polarized conditions.

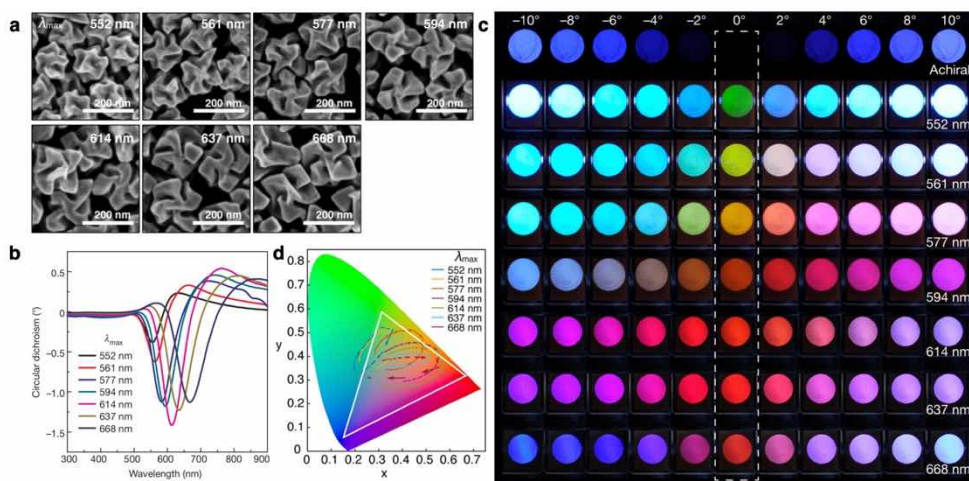


Figure 5.13 Transmitted color modulation by a dispersed solution of 432 helicoid. (a) SEM images and (b) corresponding CD spectra of 432 helicoid III nanoparticles with different sizes controlled by seed concentrations. Increasing nanoparticle size resulted in a red shift in plasmon resonance. The wavelengths λ_{\max} at maximum CD intensity are indicated in the images. (c) Polarization-resolved colors of light transmitted through seven different 432 helicoid III solutions containing different λ_{\max} values. The rotational angle of the analyzer was increased from -10° to 10° (see Methods). Angle 0° , which is indicated by a dashed box, represents cross-polarized conditions. (d) Color transition patterns of 432 helicoid III nanoparticles traced on CIE 1931 color space. The white triangle indicates the RGB boundary.

5.3.4 Spectral tuning of metal-coated helicoid nanoparticles

Control of the absorption and reflection of materials is essential for the optical application in various fields such as photovoltaic and photothermal devices,³⁷⁻³⁹ detectors for sensing and imaging materials,⁴⁰ and display materials.⁴¹ Metamaterial using plasmonic material is very efficient for this purpose because it can control the electromagnetic field through structural design. In particular, the optical properties of chiral plasmonic materials are specialized to control the polarization,⁸ allowing more convenient and active control for the absorption and reflection properties. However, controlling chiroptical properties is challenging to achieve because it requires precise control of the complex nanostructure. In the conventional metamaterial, the production of chiral nanostructures and the change of their optical properties were difficult due to the passive nature of the nanolithography technique. Here, we have developed a method to precisely control the chiroptical response of the chiral helicoid nanoparticles, which was synthesized in solution state via peptide-directed approach. Starting from the Au helicoid nanoparticle coated on the substrate, the CD response in visible and NIR region was greatly changed by depositing the nanometer-level metallic layer. These changes modulated the transmission color at cross-polarization conditions and covered wide areas in color gamut. In order to understand this phenomenon, we performed electromagnetic simulation and found that a new resonance mode caused by the coupling between metal thin-film and helicoid nanoparticles enable the dramatic tuning of the CD response. We believe this metal deposition approach will be useful as a new methodology for tailored chiroptical response.

To modulate the chiroptical response of the chiral nanoparticle, a metal layer was coated on the nanoparticle on a quartz substrate (Figure 5.14a). For this research, we chose 432 helicoid III nanoparticles due to their strong dissymmetric

signal. Au helicoid III nanoparticles were uniformly coated on the substrate by electrostatic interaction. The quartz substrate is positively charged by air-plasma treatment and subsequent poly(allylamine) treatment, and Au helicoid III nanoparticles have a slight negative charge due to the modification of mPEG-SH ($M_w = 5000$) on the surface. According to the TEM imaging, it was confirmed that the thickness of this PEG layer on the nanoparticles is about 4.7 nm (Figure 5.14b). Then, Au and Ag layers were deposited from 10 nm to 50 nm thick on the nanoparticle-coated substrate, using a thermal evaporator. During the metal deposition, the PEG ligand on the nanoparticle surface, which has been widely used as a low-fouling surface, was expected to induce the formation of a nanogap between the nanoparticles and the metal thin-film.^{31,42} Figure 5.14c and 5.14d is an SEM and TEM image of a nanoparticle surface coated with metal layers. In the magnified SEM and TEM images, the chiral structure on the top surface of helicoid III nanoparticles remained well, and we observed that the metal layer was continuously deposited on the upper part of original nanoparticles despite the PEG layer. In contrast, the nanoparticles can be separated from the substrate without damage in metal thin-film layer at the lower side of the nanoparticle, and after the separation, it was observed that a hole of the metal thin-film was formed. According to these observations, the evaporated metal atoms directly approached to the Au surface of the nanoparticle in the normal direction regardless of PEG layer. However, in the lateral direction, the penetration of the metal atoms through PEG layer was restricted, forming the nanogap structure between the nanoparticle and metal thin-film surrounding the lower part of the nanoparticle.

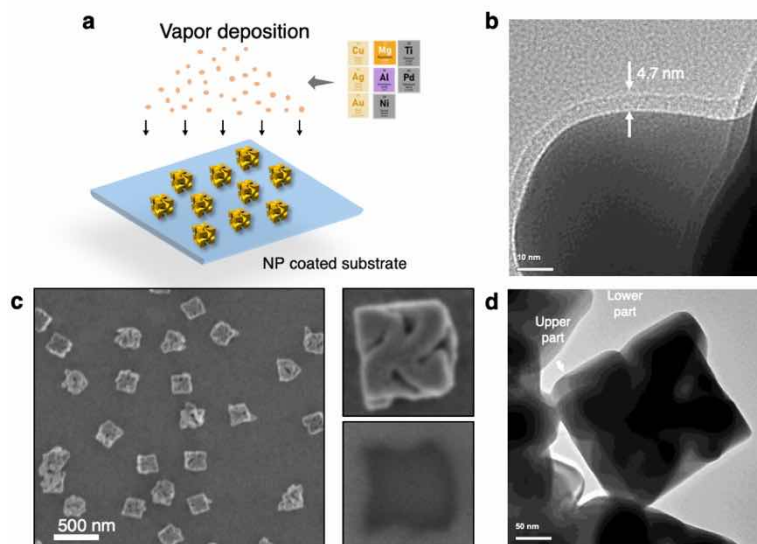


Figure 5.14 Fabrication of metal-deposited helicoid III nanoparticle. (a) Schematic of metal deposition process on the nanoparticle-coated substrate. (b) TEM image of mPEG-SH (MW=5000) modified helicoid III nanoparticle. (c) SEM images of Au deposited helicoid nanoparticle with a thickness of 30 nm. Upper right: SEM image of topmost surface of Au coated helicoid III nanoparticle. Lower right: SEM image of a hole of the metal thin-film was formed at the lower side of the nanoparticle, captured after the detachment of nanoparticle. (d) TEM image of Ag deposited helicoid nanoparticle (Ag thickness: 30 nm).

To investigate the chiroptical properties of the metal-deposited helicoid nanoparticles, CD response of the solid substrate was measured at normal incidence of light. Figure 5.15a is CD spectra which were measured when 10 nm to 50 nm thick Au layer is coated on helicoid III nanoparticles. In the absence of metal deposition layers, CD spectra of helicoid III showed typical spectral trends, featuring the bisignate shape with negative and positive CD values at visible and NIR regions, respectively. However, as Au coating thickness increased to 30 nm, a new signal in negative direction was gradually generated at around 800 nm. In the case of 30 nm coating, the two peak positions with the negative value can be found at both 550-600 nm region and 800 nm region, and thus the bisignate feature disappeared. The spectral tuning of CD in the negative direction became more apparent as the thickness of Au layer further increased. As the thickness of Au coating increased to 50 nm, the peak position was gradually blue-shifted with increased CD value, as well as the shorter wavelength peak was continuously red-shifted. As a result, two negative peaks were merged, resulting in a broad CD signal in 500-900 nm region. Figure 5.15b shows the results of coating Ag layer from 10-nm to 50-nm thickness. Similar to the case of using Au, the spectral tuning in negative direction was also observed around 700-800 nm region as the coating thickness was increased. Slight difference in the wavelength region is considered that intrinsic material properties of Ag and Au are different, because the plasma frequency of Ag is higher than that of Au, so that resonance occurs in the shorter wavelength region. As the coating thickness increased up to 50 nm, the negative tuning was further increased, and two negative peaks were overlapped and formed a broad resonance in the visible region. These spectral tuning results in both Au and Ag case indicate that the metal deposition gradually tunes the chiroptical response in the visible and NIR regions, providing a new tunability that the intensity and sign of the chiroptical response can be tailored by the post-synthesis process.

To understand this spectral tuning phenomenon, we adopted electromagnetic simulation. Absorption cross-section (σ_{Abs} , Figure 5.16a) and CD ($\Delta\sigma_{\text{Abs}}$, Figure 5.16b) were obtained for the helical nanoparticles placed on glass and surrounded by metal thin-film with 5 nm gap. For this case, CD was defined as the differential absorption cross-sections between the case of LCP and RCP excitation. While the absorption band at 700 nm was red-shifted and enhanced, we found that a new absorption peak appeared at 850 nm as increasing the Au thickness. This peak corresponded to the resonance mode that is newly generated in the negative direction on the $\Delta\sigma_{\text{Abs}}$ spectrum. Analysis of the electric field distribution at 850 nm showed that the difference between the case of LCP and RCP excitation was not significant in individual helicoid III nanoparticles and metal holes, respectively (Figure 5.16c). However, when the nanoparticle and hole were coupled, it was found that electric fields were formed at totally different positions in the case of LCP and RCP excitation. (Figure 5.16c). Therefore, the formation of the dissymmetric resonance mode at this wavelength may be attributed to the CD spectral tuning in the negative direction in the NIR region.

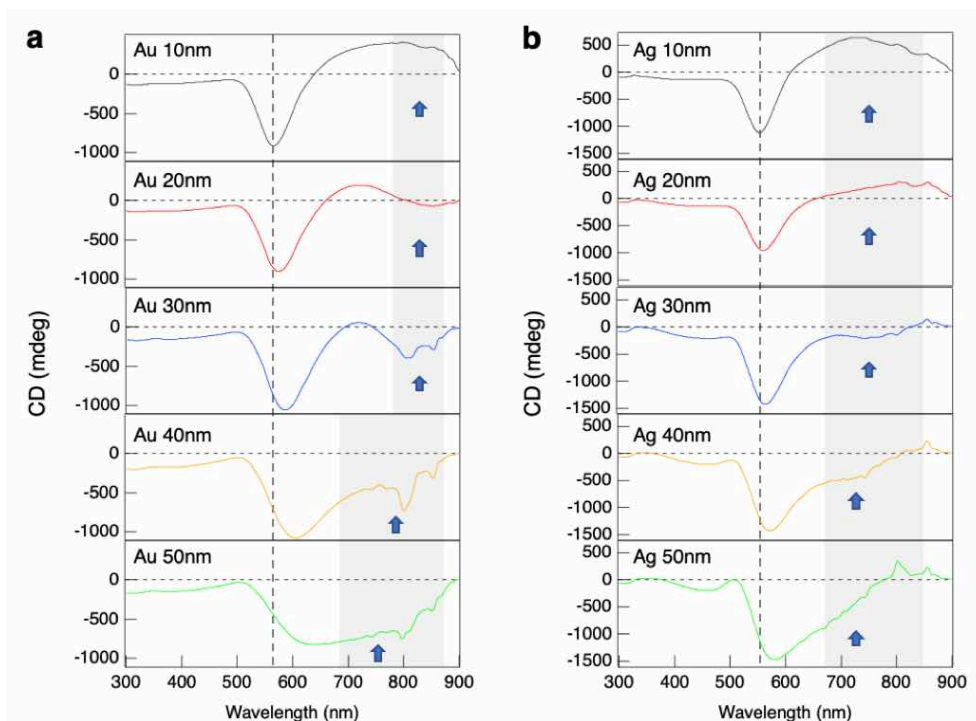


Figure 5.15 Chiroptical spectral tuning of 432 helicoid III nanoparticles. CD spectra of (a) Au-deposited and (b) Ag-deposited helicoid III nanoparticle substrate with metal thickness of 10 nm to 50 nm.

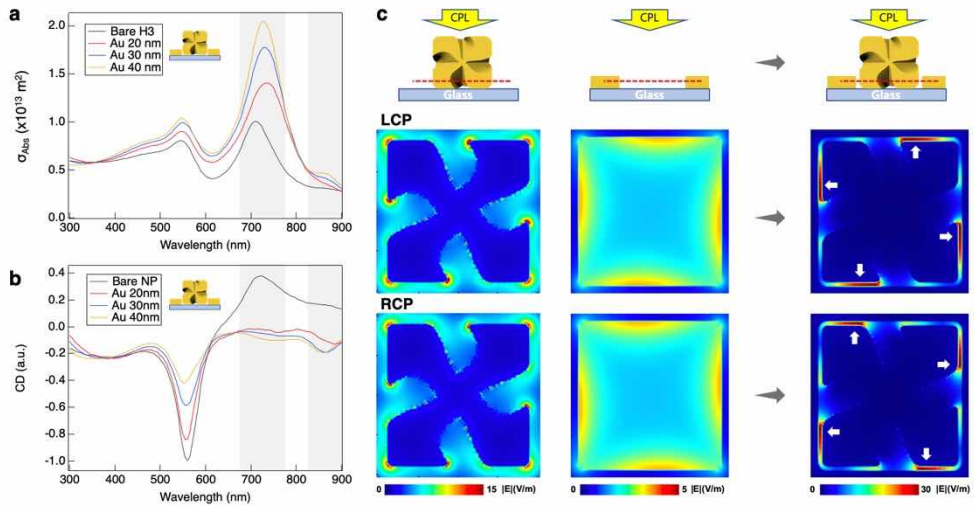


Figure 5.16 FDTD simulation of metal-deposited helicoid nanoparticle. (a,b) Absorption cross-section (a) and differential absorption cross-section between the case of LCP and RCP excitation (b). (c) The difference of nearfield distribution in the case of LCP and RCP excitation, at 850 nm. Time-averaged electric field was measured at nanogap region ($z = 20 \text{ nm}$).

Spectral tuning of CD caused by metal deposition was directly used to produce various transmission colors through polarization control. We utilized a cross-polarization condition using two linear polarizers to separate only the light from which the optical rotation occurred, thereby generating a unique transmission color. In particular, rotation of the polarizer angles further enables a dynamic modulation of the transmission color in real-time.⁴³

Bare and metal-deposited helicoid nanoparticles exhibit absorption in the visible and NIR regions due to plasmonic resonance, resulting in strong CD responses closely related to the absorbance bands, so-called Cotton effect. In this case, the ORD response has a zero-value where the wavelength of maximum CD value and exhibit a bisignate dispersion of optical rotation around this point. These CD and ORD responses can be derived from the chirality parameter κ , which is an electromagnetic response function, and can be measured by experiment or mutually converted to one another by Kramer-Kronig relation.⁴⁴ The ORD response represents the angle and direction of rotation of the linear polarization axis at a specific wavelength, and by assuming a cross-polarization condition, we can obtain the filtered transmittance by simple Malus's law as follows:

$$T = \cos^2(\varphi(\lambda) + \eta)$$

Here, $\varphi(\lambda)$ is the wavelength-dependent ORD angle, and η is the angle between the axis of the two polarizers. Finally, the calculated transmittance was converted into the corresponding color and their color coordinates on the colorspace by applying CIE1931 color matching function. Figure 5.17a is the calculated transmission color according to the Au coating thickness and polarizer angle, and Figure 5.17b is the trajectory of the corresponding color coordinate. As the thickness of the coating increase, the range of color modulation dramatically changed from bluish-green to orange, red, and purple. Compared with a result of bare 432 helicoid

III solution, the color of bluish-green and purple region, which are both ends of the color range, has been never achieved using bare helicoid III nanoparticles. It is worth to note that this wide area of color modulation was achieved in the identical geometry and size of nanoparticles by only using the post-synthesis control.

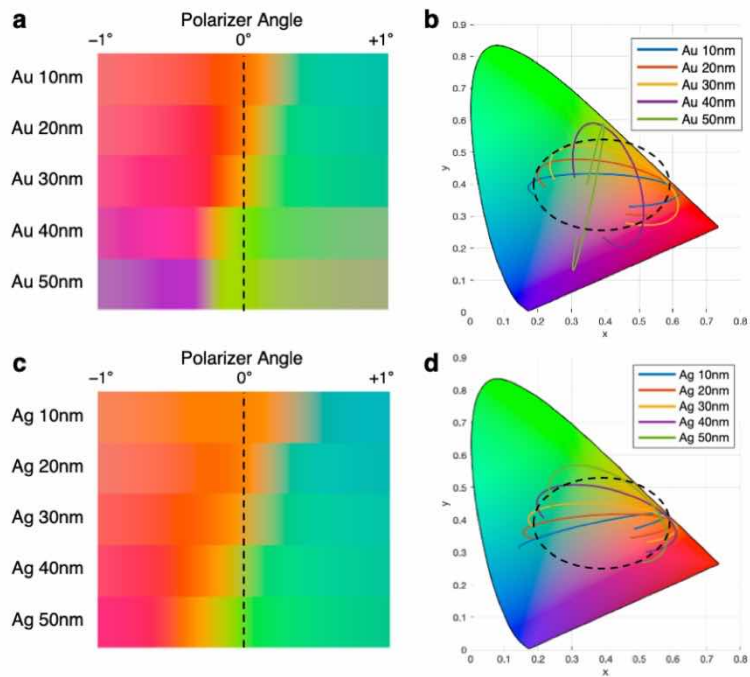


Figure 5.17 Transmitted color modulation by metal-deposited 432 helicoid III substrate. (a) Calculated polarization-resolved color transition and (b) corresponding trajectory on CIE 1931 color space for the light transmitted through Au-deposited 432 helicoid III substrate. (c) Calculated polarization-resolved color transition and (d) corresponding trajectory on color space for Ag-deposited 432 helicoid III substrate. The black dotted line indicates color coverage for bare 432 helicoid III solution.

5.4 Conclusion

We studied chiroptical response of 432 helicoid nanoparticles on the basis of experimental and theoretical analysis method. The highly twisted feature of chiral components in the helicoid gold nanoparticles gave rise to remarkably strong plasmonic optical activity; dissymmetry factor of the randomly dispersed nanoparticle solution reached 0.2 at visible wavelengths. Theoretical calculation clarified that this optical activity is associated with the formation of strong chiral nearfield at chiral gap structure. Using electromagnetic simulation for systematic geometrical variation of helicoid morphology, we have developed some general guidelines for designing chiral nanoparticles with high g-factors. Based on the wavelength-dependent polarization rotation ability, a solution of the helicoid III gold nanoparticle can modulate the color of transmitted light in a wide range of visible wavelengths. This color transformation operates in real-time by rotating a polarizer and can be observed in naked-eye, suggesting the possibility of optical applications such as display. Chiroptical response of 432 helicoid nanoparticles was further manipulated by the resonance coupling with metal thin-film layer. Dramatic spectral tuning in visible and NIR region render the wide coverage of color modulation by post-synthesis deposition process. This research may increase an understanding of plasmonic chiroptical phenomena and provide a principle to construct active devices and chiral sensors.

5.5 Methods

Characterization

Extinction and circular dichroism (CD) spectra were obtained using a J-815 spectropolarimeter instrument (JASCO), and optical rotatory dispersion (ORD) spectra were measured using an additional ORD attachment. To check the Lorentz reciprocity, we prepared solutions of nanoparticles and particles attached on the substrate. The CD spectrum of each sample condition was measured in the forwards and backwards directions by changing the direction of the sample relative to the incident light. Kuhn's dis-symmetry factor (*g*-factor) is a dimensionless quantity that is useful for quantitative comparisons of chiro-optical properties among different systems and was calculated from the measured extinction and CD values using:

$$g - \text{factor} = 2 \frac{A_L - A_R}{A_L + A_R} \propto \frac{CD}{\text{extinction}}.$$

SEM images were taken with a SIGMA system (Zeiss). TEM images were captured using a JEM-3000F system (JEOL).

The polarization-rotating ability of 432 helicoid III was evaluated from polarization- state measurements using an optical configuration consisting of a laser source, iris, linear polarizer, quarter-wave plate, sample and polarimeter. The output polarization state was measured using a PAX5710VIS-T rotating-wave plate Stokes polarimeter (Thorlabs). Laser sources with center wavelengths of 561 nm (CNI MGL-FN-561, DPSS Laser), 635 nm (Hitachi HL6321G laser diode), 658 nm (Hitachi HL6501MG laser diode) and 690 nm (Hitachi HL6738MG laser diode) were used. For the measurements, a solution of randomly dispersed 432 helicoid III nanoparticles was added to a quartz cell with a path length of 10 mm and was then irradiated with a vertically polarized incident beam. A quarter-wave plate was used

with a linear polarizer to compensate for any polarization interference caused by other optical parts of the system.

Macroscopic color changes in transmitted light were detected by polarization- resolved transmission measurements with an optical configuration consisting of a white-light illumination source, iris, linear polarizer, sample, linear polarizer (analyzer) and digital camera. The sample was placed between two crossed linear polarizers (0° represents cross-polarized conditions) and was irradiated with a collimated cold white-light source. The angle of the analyzer was changed from -10° (clockwise) to $+10^\circ$ (anticlockwise) in steps of 1° from the orthogonal configuration, which enables different wavelengths of light to propagate, rendering different colors of transmitted light. While rotating the analyzer, the color transition of the transmitted light was observable by the naked eye and was recorded with a digital camera (D90, Nikon).

Numerical calculations

Optical activity of the chiral nanoparticles was analyzed by using a three-dimensional full-wave numerical simulation using a commercial-grade simulator (Lumerical). The calculations were based on the finite-difference time-domain (FDTD) method. The geometry of the simulation model was deduced from SEM images and a mesh was constructed non-uniformly, with a mesh size of less than 10 nm near the nanoparticles. The refractive index of water was assigned a value of 1.33 and the optical properties of gold were taken from a previous study⁴⁵.

The FDTD simulation calculates the scattering (C_{sca}) and absorption (C_{abs}) cross-sections of a given particle. The extinction cross-section ($C_{ext} = C_{abs} + C_{sca}$) is used to estimate the macroscopic absorption. According to the Beer–Lambert law, the transmission T and absorbance A through a medium of thickness l and filled with particles to a number density N is represented by $T = I/I_0 = \exp(-NlC_{ext})$ and

$A = -\log_{10} T$. A chiral-particle medium exhibits different absorbance to left (LCP) and right (RCP) circularly polarized light (A_L and A_R); the CD calculated from this absorbance difference is approximated as

$$CD \approx (A_L - A_R) \frac{\log 10}{4} \text{ radian} = (A_L - A_R) \frac{\log 10}{4} \frac{180}{\pi} \text{ deg.}$$

Here, the orientation average over 756 directions was used to account for the random orientation of the chiral nanoparticles in a water medium. The incident illumination of an electromagnetic wave travels in the +z-direction. Under this fixed-illumination condition, nanoparticles were rotated in three-dimensions; the polar angle (Θ) was changed from 0° to 180° and the azimuthal angle (Φ) was simultaneously changed from 0° to 360° . Therefore, the orientation-averaged extinction ($\langle C_{ext} \rangle_\Omega$) and CD ($\langle CD \rangle_\Omega$) could be calculated. The electromagnetic field near the plasmonic helicoid was calculated at a normal incidence ($\Theta = 0^\circ$ and $\Phi = 0^\circ$) with a uniform mesh size of 2 nm. The electric- and magnetic-field distributions on the illuminated surface were displayed at selected wavelengths (650 nm, 950 nm and 1,200 nm); the field differences, $(|E_{RCP}|^2 - |E_{LCP}|^2)/E_0^2$ and $(|B_{RCP}|^2 - |B_{LCP}|^2)/B_0^2$, are representative of the microscopic asymmetric responses, where E_0 (B_0) indicates an amplitude of the initial electric (magnetic) field.

To estimate the chiral spectra of chiral nanoparticles, we first calculated the scattering cross-section and absorption cross-section of a single chiral nanoparticle at LCP and RCP incidences using FDTD with a total-field scattered-field formalism and perfectly matched layer (PML) absorbing boundaries in a water medium ($n = 1.33$). We considered random orientations of the colloidal chiral nanoparticles by rotating them to discrete orientations and averaging the results. Because the simulation of many particles with different orientations is time consuming, we simulated using a uniform 4-nm mesh. However, for some chiral nanoparticles with

small feature sizes (< 20 nm), a 3-nm mesh was used. We checked some of the results against those calculated with a 1-nm mesh and found no substantial differences, although the responses obtained with a 1-nm mesh were slightly stronger.

Absorbance (abs), CD and g-factor are characterized as follows:

$$abs = \frac{Nl\sum C}{2\log 10},$$

$$CD = \frac{Nl\Delta C}{4},$$

$$g - factor = 2 \frac{\Delta C}{\sum C},$$

where $\sum C \equiv \langle C_{ext,LCP} \rangle_{\Omega} + \langle C_{ext,RCP} \rangle_{\Omega}$, $\Delta C \equiv \langle C_{ext,LCP} \rangle_{\Omega} - \langle C_{ext,RCP} \rangle_{\Omega}$; $\langle \dots \rangle_{\Omega}$ represents an average over all orientations, $N = 1 \times 10^{15} \text{ m}^{-3}$ is the particle number density, and $l = 1 \times 10^{-3} \text{ m}$ is the optical path length. With this definition, the g-factor is constrained between -2 and 2.

Fabrication of metal-deposition helicoid nanoparticle

To prepare metal-deposited nanoparticle substrate, helicoid III nanoparticles were initially dispersed in CTAB 1 mM solution, and an aqueous mPEG-SH (250 μM) solution was added dropwise to the nanoparticle solution under gentle mixing. After 30 min, the nanoparticle solution was centrifuged and washed twice by deionized water. Pristine quartz substrate with 10 mm \times 10 mm size was treated by air plasma for 10 min and was subsequently immersed in poly(allylamine) hydrochloride (5 mM with NaCl 1 M) solution. After 1 hour, the substrate was thoroughly washed by deionized water and dried by N_2 flow. To start nanoparticle coating, a 200-uL-droplet of the prepared nanoparticle solution was placed on the quartz substrate and left undisturbed. After 1 hour, the substrate was carefully

immersed in deionized water for 5 min and dried by moderate N₂ flow. Additional metal layer was deposited by using thermal evaporator. Au and Ag targets were evaporated under room temperature and UHV condition (1×10^{-8} torr) and the rates of deposition in both cases were 0.2 Å / sec. After the deposition, optical properties of the metal-deposited nanoparticle substrate were measured in normal incidence.

5.6 Bibliography

1. Mason, S. F. *Molecular Optical Activity and the Chiral Discriminations*; Cambridge University Press: Cambridge, 1982.
2. Barron, L. D. *Molecular Light Scattering and Optical Activity*; Cambridge University Press: Cambridge, 2004; Vol. 101.
3. Kelly, S. M.; Price, N. C. The Application of Circular Dichroism to Studies of Protein Folding and Unfolding. *Biochim. Biophys. Acta - Protein Struct. Mol. Enzymol.* **1997**, *1338* (2), 161–185.
4. Hargittai, M.; Hargittai, I. *Symmetry through the Eyes of a Chemist*; Springer Netherlands: Dordrecht, 2009.
5. Cahn, R. S.; Ingold, C.; Prelog, V. Specification of Molecular Chirality. *Angew. Chemie Int. Ed. English* **1966**, *5* (4), 385–415.
6. Kahr, B.; Arteaga, O. Arago's Best Paper. *ChemPhysChem* **2012**, *13* (1), 79–88.
7. Maier, S. A. *Plasmonics: Fundamentals and Applications*; Springer US: New York, NY, 2007.
8. Gansel, J. K.; Thiel, M.; Rill, M. S.; Decker, M.; Bade, K.; Saile, V.; von Freymann, G.; Linden, S.; Wegener, M. Gold Helix Photonic Metamaterial as Broadband Circular Polarizer. *Science* **2009**, *325* (5947), 1513–1515.
9. Yu, N.; Genevet, P.; Kats, M. A.; Aieta, F.; Tetienne, J.-P.; Capasso, F.; Gaburro, Z. Light Propagation with Phase Discontinuities: Generalized Laws of Reflection and Refraction. *Science* **2011**, *334* (6054), 333–337.
10. Pendry, J. B. A Chiral Route to Negative Refraction. *Science* **2004**, *306* (5700), 1353–1355.
11. Hendry, E.; Carpy, T.; Johnston, J.; Popland, M.; Mikhaylovskiy, R. V.; Laphorn, A. J.; Kelly, S. M.; Barron, L. D.; Gadegaard, N.; Kadodwala, M. Ultrasensitive Detection and Characterization of Biomolecules Using Superchiral Fields. *Nat. Nanotechnol.* **2010**, *5* (11), 783–787.
12. Tang, Y.; Cohen, A. E. Optical Chirality and Its Interaction with Matter. *Phys. Rev. Lett.* **2010**, *104* (16), 163901.
13. Jain, P. K.; El-Sayed, M. A. Plasmonic Coupling in Noble Metal

- Nanostructures. *Chem. Phys. Lett.* **2010**, *487* (4–6), 153–164.
14. Artar, A.; Yanik, A. A.; Altug, H. Multispectral Plasmon Induced Transparency in Coupled Meta-Atoms. *Nano Lett.* **2011**, *11* (4), 1685–1689.
 15. Hentschel, M.; Weiss, T.; Bagheri, S.; Giessen, H. Babinet to the Half: Coupling of Solid and Inverse Plasmonic Structures. *Nano Lett.* **2013**, *13* (9), 4428–4433.
 16. Prodan, E. A Hybridization Model for the Plasmon Response of Complex Nanostructures. *Science* **2003**, *302* (5644), 419–422.
 17. Yin, X.; Schäferling, M.; Metzger, B.; Giessen, H. Interpreting Chiral Nanophotonic Spectra: The Plasmonic Born–Kuhn Model. *Nano Lett.* **2013**, *13* (12), 6238–6243.
 18. Sihvola, A. H.; Lindell, I. V. Chiral Maxwell-Garnett Mixing Formula. *Electron. Lett.* **1990**, *26* (2), 118.
 19. Lindell, I. V., Sihvola, A. H., Tretyakov, S. A., & Viitanen, A. J. *Electromagnetic Waves in Chiral and Bi-Isotropic Media*; Artech House: Boston-London, 1994.
 20. Nieto-Vesperinas, M.; Gomez-Medina, R.; Saenz, J. J. Angle-Suppressed Scattering and Optical Forces on Submicrometer Dielectric Particles. *J. Opt. Soc. Am. A* **2011**, *28* (1), 54.
 21. Fan, Z.; Govorov, A. O. Plasmonic Circular Dichroism of Chiral Metal Nanoparticle Assemblies. *Nano Lett.* **2010**, *10* (7), 2580–2587.
 22. Yan, W.; Xu, L.; Xu, C.; Ma, W.; Kuang, H.; Wang, L.; Kotov, N. A. Self-Assembly of Chiral Nanoparticle Pyramids with Strong R / S Optical Activity. *J. Am. Chem. Soc.* **2012**, *134* (36), 15114–15121.
 23. Kuzyk, A.; Schreiber, R.; Fan, Z.; Pardatscher, G.; Roller, E.-M.; Högele, A.; Simmel, F. C.; Govorov, A. O.; Liedl, T. DNA-Based Self-Assembly of Chiral Plasmonic Nanostructures with Tailored Optical Response. *Nature* **2012**, *483* (7389), 311–314.
 24. Shen, X.; Zhan, P.; Kuzyk, A.; Liu, Q.; Asenjo-Garcia, A.; Zhang, H.; García de Abajo, F. J.; Govorov, A.; Ding, B.; Liu, N. 3D Plasmonic Chiral Colloids. *Nanoscale* **2014**, *6* (4), 2077.
 25. Fan, Z.; Govorov, A. O. Chiral Nanocrystals: Plasmonic Spectra and Circular Dichroism. *Nano Lett.* **2012**, *12* (6), 3283–3289.

26. Bohren, C. F.; Huffman, D. R. *Absorption and Scattering of Light by Small Particles*; Wiley: Weinheim, 1998.
27. Novotny, L.; Hecht, B. *Principles of Nano-Optics*; Cambridge University Press: Cambridge, 2006.
28. McPhie, P. Circular Dichroism Studies on Proteins in Films and in Solution: Estimation of Secondary Structure by g-Factor Analysis. *Anal. Biochem.* **2001**, *293* (1), 109–119.
29. Slocik, J. M.; Govorov, A. O.; Naik, R. R. Plasmonic Circular Dichroism of Peptide-Functionalized Gold Nanoparticles. *Nano Lett.* **2011**, *11* (2), 701–705.
30. Maoz, B. M.; van der Weegen, R.; Fan, Z.; Govorov, A. O.; Ellestad, G.; Berova, N.; Meijer, E. W.; Markovich, G. Plasmonic Chiroptical Response of Silver Nanoparticles Interacting with Chiral Supramolecular Assemblies. *J. Am. Chem. Soc.* **2012**, *134* (42), 17807–17813.
31. Hao, C.; Xu, L.; Ma, W.; Wu, X.; Wang, L.; Kuang, H.; Xu, C. Unusual Circularly Polarized Photocatalytic Activity in Nanogapped Gold-Silver Chiroplasmonic Nanostructures. *Adv. Funct. Mater.* **2015**, *25* (36), 5816–5822.
32. Wu, X.; Xu, L.; Liu, L.; Ma, W.; Yin, H.; Kuang, H.; Wang, L.; Xu, C.; Kotov, N. A. Unexpected Chirality of Nanoparticle Dimers and Ultrasensitive Chiroplasmonic Bioanalysis. *J. Am. Chem. Soc.* **2013**, *135* (49), 18629–18636.
33. Lan, X.; Lu, X.; Shen, C.; Ke, Y.; Ni, W.; Wang, Q. Au Nanorod Helical Superstructures with Designed Chirality. *J. Am. Chem. Soc.* **2015**, *137* (1), 457–462.
34. Kuzyk, A.; Schreiber, R.; Zhang, H.; Govorov, A. O.; Liedl, T.; Liu, N. Reconfigurable 3D Plasmonic Metamolecules. *Nat. Mater.* **2014**, *13* (9), 862–866.
35. Yan, J.; Hou, S.; Ji, Y.; Wu, X. Heat-Enhanced Symmetry Breaking in Dynamic Gold Nanorod Oligomers: The Importance of Interface Control. *Nanoscale* **2016**, *8* (19), 10030–10034.
36. Fan, J. A.; Wu, C.; Bao, K.; Bao, J.; Bardhan, R.; Halas, N. J.; Manoharan, V. N.; Nordlander, P.; Shvets, G.; Capasso, F. Self-Assembled Plasmonic Nanoparticle Clusters. *Science* **2010**, *328* (5982), 1135–1138.

37. Bermel, P.; Ghebrebrhan, M.; Chan, W.; Yeng, Y. X.; Araghchini, M.; Hamam, R.; Marton, C. H.; Jensen, K. F.; Soljačić, M.; Joannopoulos, J. D.; et al. Design and Global Optimization of High-Efficiency Thermophotovoltaic Systems. *Opt. Express* **2010**, *18* (S3), A314.
38. Hao, J.; Wang, J.; Liu, X.; Padilla, W. J.; Zhou, L.; Qiu, M. High Performance Optical Absorber Based on a Plasmonic Metamaterial. *Appl. Phys. Lett.* **2010**, *96* (25), 251104.
39. Li, W.; Valentine, J. Metamaterial Perfect Absorber Based Hot Electron Photodetection. *Nano Lett.* **2014**, *14* (6), 3510–3514.
40. Niesler, F. B. P.; Gansel, J. K.; Fischbach, S.; Wegener, M. Metamaterial Metal-Based Bolometers. *Appl. Phys. Lett.* **2012**, *100* (20), 203508.
41. Zheng, G.; Mühlenbernd, H.; Kenney, M.; Li, G.; Zentgraf, T.; Zhang, S. Metasurface Holograms Reaching 80% Efficiency. *Nat. Nanotechnol.* **2015**, *10* (4), 308–312.
42. Nam, J.-M.; Oh, J.-W.; Lee, H.; Suh, Y. D. Plasmonic Nanogap-Enhanced Raman Scattering with Nanoparticles. *Acc. Chem. Res.* **2016**, *49* (12), 2746–2755.
43. Lee, H.-E.; Ahn, H.-Y.; Mun, J.; Lee, Y. Y.; Kim, M.; Cho, N. H.; Chang, K.; Kim, W. S.; Rho, J.; Nam, K. T. Amino-Acid- and Peptide-Directed Synthesis of Chiral Plasmonic Gold Nanoparticles. *Nature* **2018**, *556* (7701), 360–365.
44. Moscovitz, A. Theoretical Aspects of Optical Activity Part One: Small Molecules. In *Advances in Chemical Physics*; 2007; pp 67–112.
45. Johnson, P. B.; Christy, R. W. Optical Constants of the Noble Metals. *Phys. Rev. B* **1972**, *6* (12), 4370–4379.

Chapter 6. Concluding Remarks

In this thesis, we developed a novel bottom-up route for nanoscale morphology and chirality control. The fundamental motivation of this research was inspired by two well-known bottom-up processes, the nanocrystal synthesis and the biological left-right asymmetry. As an alternative for complicated nanofabrication processes such as lithography and molecular self-assembly, we proposed that spontaneous growth of nanostructure via colloidal synthesis can be promising for morphology and chirality control of plasmonic nanoparticle. We focused on the efficient colloidal synthesis platform for the morphology control and chirality evolution of plasmonic nanoparticle. Strong chiroptical response in singular chiral nanoparticle was analyzed and further controlled.

For the morphology and chirality control in colloidal synthesis, we developed a universal platform for producing nanocrystal exposing crystal surface with desired Miller-index plane and resulting morphology. We described the mutual interaction of cetyltrimethylammonium bromide (CTAB) and ascorbic acid (AA) in controlling the shapes of gold nanoparticles. There are many previous works to obtain the various shapes of gold nanoparticles. But in many cases, the results still remain phenomenological and are hard to be predicted and translated into new synthesis developments. We have chosen the well-known ligand, CTAB, and the reducing agent, AA and studied the role of them thermodynamically and kinetically. We have found that the relative ratio of CTAB and AA is important to determine the relative growth of different crystallographic facet. By analyzing the role of ligands and controlling the growth kinetics, we have synthesized all the possible morphologies of gold nanoparticles. Based on the discoveries, the morphology diagram was constructed as a function of CTAB and AA concentration. Furthermore,

we successfully synthesized the rhombic dodecahedron and hexoctahedron for the first time without any additives. This work can provide a useful guideline to control the morphology simply by controlling the relative ratio of CTAB and AA.

Most of the numerous colloidal synthesis methods have produced highly symmetric and achiral nanoparticles due to the symmetric condition of nanoparticle growth. In this research, we suggested a new paradigm- “from a biological chiral encoder to plasmonic chiral nanoparticle”- that enable the strongest chirality at the individual nanoparticle. By understanding the chirality of inorganic crystal surface and their interfacing with biomolecules, we demonstrated the chirality formation mechanism in a single nanoparticle level. This research reveals the definitive role of enantioselective interactions between peptides and metal surfaces for driving chirality development. Importantly, we identified that the thiol group in cysteine and amine group in the N-terminus of peptides are vital parameters of chirality formation and suggest that other side chains served as chirality encoders. Also, for the first time, the concept of inorganic surface chirality defined at the crystalline high-index plane was adopted to account for the chirality transfer and asymmetric growth rate at the crystalline facet level. The mechanism proposed here newly emphasizes the importance of high-index planes, which is rarely exposed in general, but can be stabilized by organic ligands, such as peptides in the present case, and can be asymmetrically overgrown. The general strategy developed here can be directly applied to other plasmonic or catalytic materials, such as Ag, Cu, Pt, and Pd and can even be extended to other thiol-containing ligands.

The chiral helicoid nanoparticles identified in this research are three-dimensionally twisted from the basis of a hexoctahedron. The highly twisted chiral components, which arranged within cube-like structures with a side length of only about 100 nm, belong to the 432-symmetry group and thus exhibit the strongest

enhancement in Kuhn's dissymmetry factor (g-factor) than any other dispersable chiral nanostructure reported to date. Surprisingly, based on the wavelength-dependent polarization rotation ability, we demonstrated a color transformation that operates in real-time by rotating a polarizer and can be observed in naked-eye. Furthermore, through the combination of peptides and seed morphology, this chiro-optical property of the nanoparticles can be precisely controlled. Considering this exceptional optical response originating from the single nanoparticle, we expect that this material can be readily processed into thin-film or composite for the polarization-based application of metamaterial devices. As an example, post-synthesis process of metal deposition on the nanoparticle coated substrate was manifested the spectral tuning of chiroptical response in the visible and NIR range. This approach can build up an extra dimension in the manipulation of chiral light-matter interaction.

In conclusion, we developed bottom-up and biomolecular route for nanoscale morphology and chirality control. We believe that this approach will attract scientific interest for the understanding the interface of molecules and inorganic materials and has technological potential for the development of advanced optical devices with three-dimensional, angle-insensitive features. Insights from this study could provide theoretical guidelines for designing artificial chirality and chiro-optical properties for active color displays, holography, reconfigurable switching, chirality sensing, and all-angle negative-refractive-index materials.

국문 초록

나노 구조는 재료의 근본적인 특성을 새롭게 변화시킬 수 있어 나노 과학의 중요한 분야로서 연구되어 왔다. 원자 수준부터 벌크 수준에 이르는 영역에 걸쳐 형태 및 카이랄성을 제어하는 것은 특히 재료의 광학적인 특성과 밀접한 연관이 있다. 최근 수십 년 동안 나노 구조를 가진 다양한 재료들은 뛰어난 빛-물질 간 상호작용을 통해 나노 광학 분야를 이끌어왔지만, 여전히 원자 및 나노 미터 수준에서 원하는 형태와 카이랄성을 형성하는 것은 가장 도전적인 과제 중 하나이다. 지금까지 나노 미터 수준에서 구조를 제어하고 대칭성이 낮은 구조를 제작하기 위해서는 정밀한 리소그래피 기술 또는 분자 자기조립을 이용한 스캐폴드 등이 필요하였다. 그러나 이러한 기술들은 공정이 매우 복잡하고 해상도 및 안정성이 낮으며 특수한 설비 등을 필요로 하여 실제 응용에 주된 장애물로서 작용하였다. 따라서 나노 구조를 제어할 수 있는 대안 기술을 개발하는 것은 이러한 한계점을 해결하고 새로운 방향을 제시할 수 있다는 점에서 중요하다. 이에 우리는 본 연구를 통하여 콜로이드 합성과 같이 나노 구조의 자발적인 형성을 통해 앞서 언급한 한계점들을 극복할 수 있는 방법을 제안하였다. 본 학위 연구에서는 플라즈모닉 나노입자의 형태와 카이랄성을 체계적으로 조절하기 위한 생체 분자 기반의 새로운 상향식 방법을 연구하였다.

지금까지 콜로이드 합성 방법을 통해 플라즈모닉 나노 입자의 다양한 나노 구조들이 달성되었지만, 궁극적으로 나노 입자의 합성에

대한 열역학적 및 동역학적 효과에 대해 이해하고 이를 활용할 수 있는 보편적인 합성 시스템을 개발하는 것이 필요하다. 한편 대칭성의 측면에서, 대부분의 플라즈모닉 금속은 거울 대칭성의 결정 구조를 가지기 때문에 구조 자체가 카이랄성을 가지는 나노 결정 형태를 만드는 것은 불가능하다. 이에 플라즈모닉 나노입자에서 형태와 카이랄성을 조절할 수 있는 새로운 방법을 개발하기 위해, 제 2 장에서는 생체 분자를 이용하여 무기 물질에 카이랄성을 형성하는 것에 초점을 맞추고 상향식 방법을 통해 복잡한 나노 구조를 구현한 선행 연구들을 조사하였다. 이 과정을 통해 카이랄 형태의 나노 결정을 자발적으로 형성하기 위하여 생체 분자와 자연적으로 카이랄성을 가진 결정 표면 간의 상호작용이 매우 중요하다는 결론을 얻을 수 있었다. 원자 및 분자수준에서의 카이랄성 전달에 대한 교훈을 바탕으로 하여, 본 학위 연구에서는 나노 입자의 형태 조절과 카이랄성 발달을 위한 새로운 합성 플랫폼을 개발할 수 있었다.

제 3 장에서는 기존에 잘 알려진 시드 성장법을 기반으로 하여 표면 리간드인 cetyltrimethylammonium bromide (CTAB) 과 환원제인 ascorbic acid (AA) 간의 경쟁 효과를 이용해 금 나노 입자의 다양한 형태를 제작하였다. CTAB 과 AA 의 농도 비율은 결정 방향에 따른 상대적인 성장 속도를 바꿔 줌으로서 노출된 결정 표면의 밀러 지수를 결정하였다. CTAB 과 AA 의 농도를 체계적으로 조절한 결과, CTAB 과 AA 농도를 변수로 하는 금 나노 결정에 대한 형태 분포도 (morphology diagram) 를 만들 수 있었으며, 이를 통해 저밀러지수 결정면이 노출된 나노 입자의 형태들에 대한 합성 조건을 찾을 수 있었다. 특히 이러한 합성 플랫폼을 이용하여, 기존에는 CTAB-AA

조건에서 만들어진 바가 없었던 사방십이면체 (rhombic dodecahedron) 및 육팔면체 (hexoctahedron) 형태의 나노입자를 최초로 합성하였다. 이러한 연구는 나노 입자의 표면에서 저밀러지수 및 고밀러지수 결정면의 조절이 가능한 합성 플랫폼으로서 나노 입자의 다양한 형태를 구현하는 데 유용한 방법을 제공할 것이다.

제 4 장에서는 나노입자의 형태와 결정면을 조절하는 과정을 더 발전시켜 카이랄성 조절 인자로 작용하는 생체 분자를 도입한 결과 3 차원 카이랄 형태의 균일한 나노입자를 합성하는 화학적인 방법을 개발하였다. 본 연구에서는 펩타이드 분자를 카이랄성 자기 조립을 위한 템플릿으로서 사용하는 대신에, 고유의 카이랄성을 가지는 고밀러지수 결정면 상의 키크 (kink) 원자 위치와 티올 (thiol) 작용기를 함유한 펩타이드 분자 간의 카이랄성 선택적 상호작용을 이용하여 나노입자의 비대칭적 성장을 유도할 수 있었다. 카이랄 나노 구조의 발달은 R 방향과 S 방향의 카이랄성 원자배열을 가진 서로 다른 카이랄성의 고밀러지수 결정면들이 비대칭적으로 성장함으로써 가능할 수 있었다. 펩타이드가 없는 일반적인 나노입자 성장 조건에서는 {321}의 지수를 가지는 고밀러지수 결정면들이 노출되어 육팔면체 (hexoctahedron) 나노입자가 형성되며, 이때 나노입자 표면 전체에 걸쳐 분포한 R 과 S 방향의 카이랄 결정면으로 인해 분자와 무기 표면 간의 카이랄성 전달 현상을 이용할 수 있었다. 고밀러지수 결정 표면에 다량 분포한 키크 위치들은 시스테인 (cysteine) 또는 이를 함유한 다른 펩타이드들의 카이랄성에 따라 분자의 방향과 결합 에너지가 서로 다르게 나타나는 비대칭적 결합의 수용체로서 작용하였다. 본 연구에서는 고밀러지수 결정면과 분자 흡착에 대한 자세한 분석을 통하여 카이랄 형태가

발달하는 과정을 확인할 수 있었다. 합성 과정 중 순수한 거울상 이성질체의 첨가는 좌우 비대칭의 헬리코이드 (helicoid) 형태를 가진 나노입자를 발달시켰으며, R 과 S 방향 결정면 간의 경계 지점이 틀어지는 독특한 구조적인 특성을 나타내었다. 세부적으로 헬리코이드 나노입자 형태는 휘어진 정도가 극대화된 구조 요소들로 구성되어 있었다. 대칭성의 측면에서 헬리코이드 나노입자는 432-점대칭군에 해당하는 카이랄 나노 구조로서, 기존에 플라즈모닉 나노재료에서 다뤄진 바 없었던 새로운 구조 및 대칭성을 가지고 있다.

제 5 장에서는 헬리코이드 나노입자의 3 차원적인 카이랄 형태에서 비롯된 독특한 광학적 특성에 대하여 다루었다. 기존에 보고되었던 상향식 방식의 카이랄 나노구조들에 비하여 헬리코이드 나노입자는 현저하게 높은 플라즈몬 기반 광학 활성도를 나타냈다. 헬리코이드 III 나노입자의 광학적 비대칭성 인자를 계산한 결과 용액 상에 무작위로 분산되어 있는 상태에서도 가시광선 영역에서 0.2 의 높은 수치를 기록하였다. 이러한 높은 광학적 비대칭성 현상을 이해하기 위해 전자기 시뮬레이션 계산을 시도한 결과, 헬리코이드 나노입자에 발달한 깊은 갭 (gap) 구조에 인가되는 강한 카이랄성 근접장 형성이 높은 광학적 비대칭성을 나타내는 데 중요한 역할을 하는 것을 알 수 있었다. 한편 헬리코이드 나노입자는 파장에 따라 빛의 편광축을 다양하게 회전시키는 특성을 보였으며, 이러한 현상을 이용하여 간단한 교차 편광 조건 하에서 용액 상에 녹아있는 나노입자를 투과한 빛이 넓은 범위에 걸친 색깔을 나타낼 수 있다는 것을 입증하였다. 이러한 색 변화 실험은 편광판의 회전에 따라 실시간으로 작동하였으며 육안으로 관측될 수 있어 차세대 디스플레이 소재 등 광학적 응용 가치가 매우

높다. 또한 한 번 만들어진 헬리코이드 나노입자에 추가적인 금속 박막을 커플링 시킴으로써 광학적인 특성을 크게 변조할 수 있었다. 이를 통해 가시광선 및 근적외선 영역에 걸쳐 광학 스펙트럼의 형태를 크게 조절할 수 있었으며, 이러한 변화는 교차 편광 조건에서의 색 변화의 영역을 조절하는 데 이용될 수 있었다. 본 연구를 통하여 플라즈모닉 나노재료의 카이랄성 광학 특성 및 편광 기반의 광학 디바이스에 대한 이해가 증진될 것으로 예상된다.

본 학위 연구에서는 나노 수준의 형태와 카이랄성 제어를 위한 새로운 상향식 방법을 개발하였다. 본 연구에서 카이랄성을 발달시키기 위해 사용한 생체 분자를 이용한 접근 방법은 생체 분자의 반응에 민감하고 조절이 가능한 메타 물질의 개발로 이어질 기술적 가능성이 있다. 이러한 접근 방법을 이용함으로써 카이랄성 구조 요소들이 약 100 나노미터 수준의 입방체 구조에 432 대칭성을 유지한 상태로 정렬되기 때문에, 각도에 관계없이 유사한 특성을 가지는 3 차원의 플라즈모닉 메타 물질로서 활용될 수 있다. 또한 본 연구를 통해 생체 분자와 무기 물질간의 상호작용에 대한 이해를 증진시켰으며, 이는 카이랄성 나노재료를 설계하는 새로운 돌파구를 제공함으로써 플라즈모닉스, 메타물질, 나노구조 제작을 포함한 관련 분야의 발전에 기여할 것으로 기대된다.

주요어: 플라즈몬, 나노입자, 형태, 카이랄성, 펩타이드, 고밀리지수, 콜로이드 합성

학번: 2013-20607